

DESIGN AND DEVELOPMENT OF CELL BASED OSTEOCHONDRAL CONSTRUCTS

Dr. AMRITA NATARAJAN

Ph.D. THESIS

2022



**SREE CHITRA TIRUNAL INSTITUTE FOR MEDICAL SCIENCES
AND TECHNOLOGY, TRIVANDRUM**

An Institution of National Importance established by an Act of the Indian Parliament
(Act No.52 of 1980)

Department of Science and Technology, Govt. of India
www.sctimst.ac.in

**DESIGN AND DEVELOPMENT OF CELL BASED
OSTEOCHONDRAL CONSTRUCTS**

A THESIS SUBMITTED BY

Dr. AMRITA NATARAJAN

TO

**SREE CHITRA TIRUNAL INSTITUTE FOR MEDICAL SCIENCES AND
TECHNOLOGY, TRIVANDRUM**

IN PARTIAL FULFILMENT OF THE REQUIREMENTS

FOR THE AWARD OF

DOCTOR OF PHILOSOPHY

2022

DECLARATION BY THE STUDENT

CERTIFICATE

I, **Dr. Amrita Natarajan**, here by certify that I had personally carried out the work depicted in the thesis titled “**Design and Development of Cell Based Osteochondral Constructs**”, except where due acknowledgement has been made in the text. No part of the thesis has been submitted for the award of any other degree or diploma prior to this date.

Trivandrum
20.12.2022



Amrita Natarajan
Reg no: 2016/PhD/11



श्री चित्रा तिरुनाल आयुर्विज्ञान और प्रौद्योगिकी संस्थान, तिरुवनन्तपुरम- 11, केरल

**Sree Chitra Tirunal Institute for Medical Sciences and Technology,
Thiruvananthapuram- 11, Kerala**

(भारत सरकार के अधीन राष्ट्रीय महत्व का संस्था)

(An Institution of National Importance under Government of India)

दूरभाष सं./Telephone No. 0471-2443152 फाक्स/Fax 0471-24464332550728

ई-मेल/E-mail : sct@sctimst.ac.in वेबसाइट/ Website : www.sctimst.ac.in

CERTIFICATE BY THE RESEARCH GUIDE

Dr. Prabha D. Nair, FBAO, FRSC (UK)

Scientist G (Senior Grade) & Formed Head, Dept of Applied Biology

Division of Tissue Engineering and Regeneration Technologies

Biomedical Technology Wing,

Sree Chitra Tirunal Institute for Medical Sciences & Technology

Poojappura, Trivandrum, Kerala, India-695012

email: prabha49@gmail.com

This is to certify that **Dr. Amrita Natarajan**, Division of Tissue Engineering and Regeneration Technologies, Department of Applied Biology, of this institute has fulfilled the requirements prescribed for the Ph.D. degree of Sree Chitra Tirunal Institute for Medical Sciences and Technology, Trivandrum.

The thesis entitled “**Design and Development of Cell Based Osteochondral Constructs**”, was carried out under my direct supervision. No part of the thesis was submitted for the award of any degree or diploma prior to this date.

*Clearance was obtained from the Institutional animal ethics committee (Approval no: IAEC No: SCT/IAEC-286/September/2018/97 for carrying out this study.

Thiruvananthapuram

Dr. Prabha D. Nair
(Research guide)



श्री चित्रा तिरुनाल आयुर्विज्ञान और प्रौद्योगिकी संस्थान, तिरुवनन्तपुरम- 11, केरल

Sree Chitra Tirunal Institute for Medical Sciences and Technology,
Thiruvananthapuram- 11, Kerala

(भारत सरकार के अधीन राष्ट्रीय महत्व का संस्था)

(An Institution of National Importance under Government of India)

दूरभाष सं./Telephone No. 0471-2443152 फाक्स/Fax 0471-24464332550728

ई-मेल/E-mail :sct@sctimst.ac.in वेबसाइट/ Website : www.sctimst.ac.in

APPROVAL OF THE THESIS

The Thesis Entitled

DESIGN AND DEVELOPMENT OF CELL BASED OSTEOCHONDRAL CONSTRUCTS

Submitted by

Dr. Amrita Natarajan

for the degree of

Doctor of Philosophy

Of

SREE CHITRA TIRUNAL INSTITUTE FOR

MEDICAL SCIENCES AND TECHNOLOGY, TRIVANDRUM

is evaluated and approved by

Dr. Prabha D. Nair
(Research Supervisor)

Prof. Ashok Kumar
Thesis Examiner

In memory of

*My beloved Dad who taught me about dreams and how to catch
them*

Dedicated to

My guide, for her advice, patience and faith

My husband, for his infinite strength, love and encouragement

My mom, who made me who I am

My daughter, for emotional support

Fidus Achates

Science, enlightening us

God almighty

ACKNOWLEDGEMENTS

It is with a deep sense of gratitude, satisfaction and divine blessings from Supreme God Almighty that I submit this dissertation. I take this opportunity with great pleasure to thank all those who have contributed in one or the other way to the success of this study.

I express my deepest sense of gratitude and respect to my Guide, Dr. Prabha D. Nair, Scientist G Senior Grade, Division of Tissue Engineering and Regeneration Technologies, SCTIMST for her constant guidance, encouragement and incessant support provided to me throughout the study. She gave timely suggestions with kindness, putting in great effort to train me with scientific principles for tackling research problems and took significant effort for the successful completion of this endeavour.

The Director and former Director, SCTIMST, the Head, BMT Wing, Dr.H.K.Varma are greatly acknowledged for providing all the facilities for the successful completion of this work. I am thankful to the Dean, Dr. Sankara Sharma, Associate Dean, Dr. P.V Mohanan, Deputy Registrar, Mrs. Radha M, Registrar, Dr. Santhosh Kumar and all the members of academic division, Directors's office, Head BMT Wing's office, Research & Publication cell and Institute Library for their assistance.

I thank members of the Doctoral Advisory Committee, Dr. T.V Anilkumar, Scientist G, Division of Experimental pathology, Dr. R.S. Jayasree, Scientist G, Division of Biophotonics, Dr. Rekha M.R, Scientist F, Division of Biosurface technology, for their timely valuable suggestions and comments which helped in setting the study objectives, in planning experiments and improving the quality of this work. I also take this opportunity to thank all the Ph.D. coursework Coordinators: Dr. Maya Nandkumar A, Dr. Manoj Komath, Faculty members, BMT Wing, SCTIMST and all teaching faculty of my course work.

I wish to acknowledge SERB for JRF and ITR Division, ICMR for the prestigious Direct SRF and financial support from Indo Denmark project "MUSTER: Musculoskeletal Stem cells targeting". BT/IN/Denmark/08/JD/2016 during the course of the study.

I am extremely thankful to Dr. Sachin J Shenoy, Scientist 'F', Division of In Vivo Models and Testing, for extending his expertise and skilled surgical handwork in creating critical size defects in animals. I thank Dr.Harikrishnan V.S and all members of DLAS, especially Mr. Sharath, Mr. Manoj, Mr. Sunil and Mr. Pradeep for their sincere assistance throughout the animal experiments.

I take this opportunity to thank Dr. T.V AnilKumar and all staff of Division of Experimental pathology, especially Dr. Geetha C S, Dr. Purnima C and Mr. Pratheesh KV for their support rendered for tissue sectioning, providing with all sorts of support for carrying out special staining procedures and helping me with the histological analysis of tissue sections. I thank Dr. Manoj Komath and all staffs of Division of Bioceramics Laboratory, for ESEM analysis and Dr Rekha M.R, and all staffs of Division of Biosurface Technology for providing with Nanodrop facility. I express my gratitude to Dr. Roy Joseph, Division of Polymeric Medical Devices for mechanical testing and Mrs. Jasmin Joseph, Dr. Chandrashekar and Mrs. Reshmi for helping me with the mechanical studies of samples. I express my sincere gratitude

to Dr. Radhakumary C, Dr. Renjith S, Ms. Nimi N, Dr. Sasikala, Central Analytical Facility for TG/DTG analysis and technical assistance in using the cold centrifuge. I am thankful to Mr. Ramesh Babu, Mr. Prathyush, Mr. Reji from Precision Fabrication Lab for fabricating different sizes of biopsy punch used for the study. Dr. Sabareeshwaran, Dr. Arya Anil, Mr. Joseph Sebastian and Mrs. Sandhya of Division of Histopathology, Dr. Anugya Bhatt, Mrs. Priyanka, Mr. Ranjith S, from the Division of Thrombosis Research, Dr. P.R. Anilkumar, Dr. Naresh Kasoju, Dr. Senthil and all staff and students of Division of Tissue Culture are greatly acknowledged for helping with their facilities during the course of the study.

I express my sincere gratitude to the Director of Rajiv Gandhi Centre for Biotechnology, Thiruvananthapuram, for providing the flow cytometry and confocal imaging facility. I also thank Ms. Indu Ramachandran and Ms. Arya V S of RGCB for the technical assistance in performing flow cytometry and Mr. Gopikrishnan, Ms. Bindhu, Mrs. Soumya for confocal images, RGCB and Mrs. Soumya, Kerala University for the technical assistance in taking confocal microscopic images.

I express my sincere gratitude to all my fellow students from other departments of our campus, the Security officer and other staffs, Stores and Purchase Division, the administrative and accounts section for their assistance support throughout the course of the study. I am extremely grateful to Dr Arun Anirudhan, Mr. Sajithlal, Mr. Binu and all other staff of Network Services for providing the uninterrupted online services for conducting Ph.D Seminars and presentations.

I owe a deep sense of gratitude to Dr. Lynda V. Thomas for her keen interest in giving skilled training on 3D printing, her prompt inspirations and timely guidance at every stage of my research. I am deeply indebted to my labmates at Division of Tissue Engineering and Regeneration technologies (DTERT).; Ms. Jijo Wilson, Dr. Sivadas V.P, Dr. Dhanesh. V. K., Dr. Babitha.S., Dr. Neelima.T, Dr. Merlin, Dr. Soumya, Ms. Evelyn, Mr. Dipin Das for their support, encouragement and friendship.

I owe a huge debt of gratitude to all my dear friends on the campus especially Dr. Lakshmi V, Mrs. Nimi N, Dr Naresh Kasoju, Mr. Roopesh, Mrs. Charulatha, Mrs. Treesa, Dr. Shanthi, Dr. Eva C Das, Dr. Amita Ajith, for their friendship and always encouraged me to move forward by overcoming the hurdles.

I have no words to express gratitude to my family members who provided the most precious support. I am indebted to my husband Dr Revish. V.R, my dad Col. Dr. M. Natarajan (Late), my mom Mrs. M.S. Rita, my daughter Anika Revish, my sister Dr. Aparna, my co brother Dr Akhilesh, my in laws Dr Vishnurajan & Mrs Retna Kumari for always being my side, for their love, sacrifices, endless support and continued encouragement throughout my life who have enabled me to complete this Ph.D. research and thesis submission.

Dr. Amrita Natarajan

TABLE OF CONTENTS

ACKNOWLEDGEMENTS	v
TABLE OF CONTENTS	vii
LIST OF FIGURES	xiv
LIST OF TABLES	xvi
ABBREVIATIONS	xvii
SYNOPSIS	xviii
CHAPTER 1	1
1 INTRODUCTION	1
1.1 Osteochondral tissue and its defects.....	1
1.2 Current treatment methods	2
1.3 Osteochondral tissue engineering.....	4
1.3.1 Structure and composition of osteochondral unit.....	4
1.3.2 Importance of the structural design of an osteochondral scaffold.....	6
1.3.3 Techniques for fabricating OC scaffolds.....	7
1.3.4 Composition of the scaffolding biomaterial	8
1.3.5 Cells.....	9
1.4 Definition of the problem	11
1.5 Hypothesis.....	11
1.6 Aims Objectives	12
1.7 Significance.....	12
CHAPTER 2	14
2 REVIEW OF LITERATURE	14
2.1 The anatomical structure of the osteochondral unit	14
2.1.1 Articular cartilage.....	14
2.1.1.1 Zones	14
2.1.1.2 Regions.....	15
2.1.1.3 Chondrocytes.....	16
2.1.1.4 Extracellular Matrix	16
2.1.2 Calcified Cartilage.....	17
2.1.3 Subchondral Bone	18
2.2 Osteochondral defect classification.....	19
2.3 Osteoarthritis (OA) and the molecular mechanism of OA.....	19
2.4 Current osteochondral repair strategies and challenges thereof	22
2.4.1 Palliative treatment.....	22

2.4.2	Reparative treatments	23
2.4.3	Restorative treatment.....	23
2.5	Osteochondral Tissue engineering	24
2.5.1	Scaffolds for osteochondral tissue regeneration and its preparation strategies	25
2.5.1.1	Architectures of the scaffolds.....	26
2.5.1.1.1	Monophasic scaffolds.....	26
2.5.1.1.2	Biphasic scaffolds	27
2.5.1.1.3	Triphasic and multiphasic scaffolds.....	28
2.5.1.1.4	Multiphasic gradient and continuous gradient scaffolds.....	29
2.5.1.2	Choices for the fundamental material composition.....	30
2.5.1.3	Different types of scaffolds in osteochondral tissue engineering.....	33
2.5.1.4	Scaffold fabrication techniques	35
2.5.2	Other key elements in osteochondral tissue engineering	42
2.5.2.1	Tissue forming cells	42
2.5.2.2	Biochemical signaling factors	45
2.5.2.3	Physiochemical and physical signaling factors	47
2.6	Tissue engineered articular cartilage products	48
CHAPTER 3	50
3	MATERIALS AND METHODOLOGY	50
3.1	Materials.....	50
3.2	Development of biphasic scaffolds (BPS) mimicking osteochondral architecture.	51
3.2.1	System A - BPS fabricated via Combinatorial approach	51
3.2.1.1	Fabrication of biphasic scaffold	51
3.2.1.2	Characterization of biphasic scaffold.....	53
3.2.1.2.1	Analysis of morphological features.....	53
3.2.1.2.2	Analysis of wettability features	53
3.2.1.2.3	Analysis of chemical features	53
3.2.1.2.4	Analysis of thermal features.....	54
3.2.1.2.5	Analysis of mechanical features.....	54
3.2.1.2.6	Analysis of degradation features	54
3.2.1.2.7	Assessment of <i>in vitro</i> bioactivity	55
3.2.1.2.8	Assessment of <i>in vitro</i> cytocompatibility	55
3.2.2	System B - BPS fabricated via 3D printing and dissolution adhesion technology.....	56
3.2.2.1	Fabrication of 3D-printed biphasic scaffolds	56
3.2.2.2	Characterization of biphasic scaffolds	58

3.2.3	System C - BPS fabricated via 3D printing.....	59
3.2.3.1	Fabrication of Biphasic scaffold.....	59
3.2.3.2	Characterization of biphasic scaffolds	61
3.3	Isolation and characterization of adipose-derived mesenchymal stem cells (MSCs) .	62
3.3.1	Isolation and characterization of Rat MSCs.....	62
3.3.1.1	Isolation of Rat MSCs	62
3.3.1.2	Characterization of rat MSCs	63
3.3.1.2.1	Morphology	63
3.3.1.2.2	Surface marker analysis	64
3.3.1.3	Multilineage differentiation assay	65
3.3.2	Isolation and characterization of Rabbit MSCs.....	66
3.4	In Vitro culture of MSCs and evaluation of production of ECM.....	66
3.4.1	Evaluation of chondrogenesis in 2D culture and production of ECM	66
3.4.2	Evaluation of osteogenesis in 2D culture and production of ECM	67
3.5	In vitro differentiation potential of MSCs on the biphasic scaffold (BPS)	68
3.5.1	System A- BPS fabricated via Combinatorial approach	68
3.5.1.1	<i>In Vitro</i> cytocompatibility with Rat ADMSCs.....	68
3.5.1.2	Cell Adhesion/ attachment and morphology	68
3.5.1.3	MSC proliferation on biphasic 3D scaffolds	69
3.5.1.4	Differentiation of rat MSCs on 3D scaffolds into cartilage and bone lineages.....	70
3.5.1.4.1	Cell Seeding and Cell-scaffold Construct Culture.	70
3.5.1.4.2	Evaluation of <i>in-vitro</i> chondrogenesis	70
3.5.1.4.3	Evaluation of the <i>invitro</i> osteogenesis.....	72
3.5.1.4.4	Immunostaining for cartilage and Bone markers	72
3.5.1.4.5	Gene expression analysis by real-time PCR.....	73
3.5.2	System B - BPS fabricated via 3D printing and dissolution adhesion technology.....	75
3.5.2.1	<i>In Vitro</i> cytocompatibility with rabbit MSCs.....	75
3.5.2.2	Cell attachment and proliferation.....	75
3.5.2.3	Differentiation of rabbit ADMSCs on 3D scaffolds into cartilage and bone lineages	75
3.5.2.3.1	Evaluation of <i>invitro</i> chondrogenesis.....	76
3.5.2.3.2	Evaluation of osteogenesis	76
3.5.2.3.3	Immunostaining for cartilage and bone markers	76
3.5.2.3.4	Gene expression analysis using qRT-PCR.....	76
3.5.3	System C - BPS fabricated via 3D printing.....	77
3.5.3.1	<i>In Vitro</i> cytocompatibility with rabbit ADMSCs.....	77
3.5.3.2	Cell attachment and proliferation.....	77

3.5.3.3	Differentiation of rat ADMSCs on 3D scaffolds into cartilage and bone lineages	78
3.5.3.3.1	Evaluation of <i>in vitro</i> chondrogenesis.....	78
3.5.3.3.2	Evaluation of osteogenesis.....	78
3.5.3.3.3	Immunostaining for cartilage and bone markers	78
3.5.3.3.4	Evaluation of cell morphology and distribution of cell and ECM using ESEM	79
3.5.3.3.5	Gene expression analysis RT-qPCR	79
3.6	Tissue engineering an osteochondral construct and its <i>in vivo</i> evaluation.....	80
3.6.1	Comparative study.....	80
3.6.1.1	Mechanical properties	80
3.6.1.2	Cell activity by proliferation studies using Pico green method.....	81
3.6.1.3	<i>In vitro</i> differentiation of Rat MSCs and Functionality assessment.....	81
3.6.2	<i>In vivo</i> repair of osteochondral defect.....	81
3.6.2.1	Animal Surgery: <i>In vivo</i> surgical procedure of Rat osteochondral defect model and Implantation of developed biphasic scaffolds into defects.	82
3.6.2.2	Gross morphological assessment.....	83
3.6.2.3	Histological assessment.....	85
3.6.2.3.1	Haematoxylin and Eosin (H&E) staining.....	86
3.6.2.3.2	Safranin O-staining	86
3.6.2.3.3	Alcian blue staining.....	87
3.6.2.3.4	Trichrome staining	87
3.7	Statistical analysis	87
CHAPTER 4.....		88
4 RESULTS.....		88
4.1	Development of biphasic scaffolds (BPS) mimicking osteochondral architecture	88
4.1.1	System A - BPS fabricated via combinatorial approach	88
4.1.1.1	Fabrication of biphasic scaffold	88
4.1.1.2	Characterization of biphasic scaffold	93
4.1.1.2.1	Analysis of morphological features.....	93
4.1.1.2.2	Analysis of wettability features.....	94
4.1.1.2.3	Analysis of chemical features	95
4.1.1.2.4	Analysis of thermal features.....	96
4.1.1.2.5	Analysis of mechanical features.....	98
4.1.1.2.6	Analysis of degradation features	99
4.1.1.2.7	Assessment of <i>invitro</i> bioactivity.....	100
4.1.1.2.8	Assessment of <i>in vitro</i> cytocompatibility	101
4.1.2	System B – BPS fabricated via 3D printing and dissolution adhesion technology ...	102

4.1.2.1	Fabrication of biphasic scaffolds (BPS) by 3D printing:	102
4.1.2.2	Characterization of individual scaffolds and biphasic scaffolds:	106
4.1.2.2.1	Analysis of morphological features.....	106
4.1.2.2.2	Analysis of chemical features	108
4.1.2.2.3	Analysis of thermal features.....	108
4.1.2.2.4	Analysis of wettability features.....	110
4.1.2.2.5	Analysis of mechanical features.....	110
4.1.2.2.6	Analysis of degradation features	110
4.1.2.2.7	Assessment of <i>in vitro</i> bioactivity	112
4.1.2.2.8	Assessment of <i>in vitro</i> cytocompatibility	112
4.1.3	System C – BPS fabricated via 3D printing	114
4.1.3.1	Fabrication of biphasic scaffolds (BPS) by 3D printing:	114
4.1.3.2	Characterization of scaffolds.....	117
4.1.3.2.1	Analysis of morphological features.....	117
4.1.3.2.2	Analysis of chemical features	119
4.1.3.2.3	Analysis of thermal features.....	120
4.1.3.2.4	Analysis of wettability features.....	121
4.1.3.2.5	Analysis of mechanical features.....	122
4.1.3.2.6	Analysis of degradation features	123
4.1.3.2.7	Assessment of <i>in vitro</i> bioactivity	123
4.1.3.2.8	Assessment of Chondroitin sulfate (CS) leach out study:	124
4.1.3.2.9	Assessment of <i>in vitro</i> cytocompatibility	125
4.2	Isolation and characterization of MSCs	126
4.2.1	Rat adipose-derived MSCs.....	126
4.2.1.1	Isolation of rat MSCs	126
4.2.1.2	Characterization of rat MSCs	126
4.2.2	Rabbit adipose-derived MSCs.....	128
4.3	In Vitro culture of MSCs and evaluation of production of ECM.....	130
4.3.1	Evaluation of chondrogenesis in 2D culture and production of ECM	130
4.3.2	Evaluation of osteogenesis in 2D culture and production of ECM.	131
4.4	In vitro differentiation potential of MSCs on the biphasic scaffold (BPS)	132
4.4.1	System A- BPS fabricated via Combinatorial approach	132
4.4.1.1	<i>In Vitro</i> cytocompatibility with rat ADMSCs	132
4.4.1.2	Cell adhesion/Attachment and morphology	133
4.4.1.3	Cell proliferation studies	134
4.4.1.4	Differentiation of rat ADMSCs on 3D scaffolds into cartilage and bone lineages ...	136

4.4.1.4.1	Evaluation of chondrogenesis	137
4.4.1.4.2	Evaluation of the osteogenesis	137
4.4.1.4.3	Immunostaining for cartilage and Bone markers	139
4.4.1.4.4	Gene expression analysis qRT-PCR:	140
4.4.2	System B - BPS fabricated via 3D printing and dissolution adhesion technology....	144
4.4.2.1	<i>In Vitro</i> cytocompatibility evaluation with rabbit MSCs	144
4.4.2.2	Cell attachment and proliferation	144
4.4.2.3	Differentiation of rabbit MSCs on 3D scaffolds into cartilage and bone lineages....	145
4.4.2.3.1	Evaluation of chondrogenesis	145
4.4.2.3.2	Evaluation of osteogenesis	145
4.4.2.3.3	Immunostaining for cartilage and bone markers	147
4.4.2.3.4	Gene expression analysis using qRT-PCR.....	147
4.4.3	System C - BPS fabricated via 3D printing.....	149
4.4.3.1	<i>In Vitro</i> cytocompatibility evaluation of the 3D printed scaffolds with rat ADMSCs: Cell Viability by Live dead assay	149
4.4.3.2	Cell proliferation studies	151
4.4.3.3	Cell morphology.....	151
4.4.3.4	Differentiation of rat ADMSCs on 3D scaffolds into cartilage and bone lineages ...	153
4.4.3.4.1	Evaluation of chondrogenesis	153
4.4.3.4.2	Evaluation of osteogenesis	154
4.4.3.4.3	Immunostaining for cartilage and bone markers	155
4.4.3.4.4	Gene expression analysis using qRT-PCR.....	157
4.5	Tissue engineering an osteochondral construct and its in vivo evaluation.....	159
4.5.1	Comparative study.....	159
4.5.1.1	Mechanical studies	159
4.5.1.2	Proliferation studies.....	160
4.5.1.3	Functional estimation	160
4.5.2	In vivo repair of osteochondral defect.....	162
4.5.2.1	Gross morphological analysis	162
4.5.2.2	Histological examination of the retrieved construct and regenerated osteochondral tissue from rat knee joint.....	165
4.5.2.2.1	H&E staining.....	166
4.5.2.2.2	Trichrome staining	166
4.5.2.2.3	Safranin-O staining	167
4.5.2.2.4	Alcian blue staining.....	168

CHAPTER 5	170
5 DISCUSSION	170
5.1 Development of biphasic scaffolds (BPS) mimicking osteochondral architecture ...	170
5.1.1 System A- BPS fabricated via Combinatorial approach	170
5.1.2 System B - BPS fabricated via 3D printing and dissolution adhesion technology....	176
5.1.3 System C - BPS fabricated via 3D printing.....	179
5.2 Isolation and characterization of Mesenchymal stem cells (MSCs)	188
5.2.1 Mesenchymal stem cells (MSCs) from rat and rabbit adipose tissues	188
5.3 In Vitro 2Dculture of MSCs and evaluation of production of ECM	189
5.4 Invitro differentiation potential of MSCs on the biphasic scaffold (BPS)	190
5.4.1 System A- BPS fabricated via Combinatorial approach	190
5.4.2 System B - BPS fabricated via 3D printing and dissolution adhesion technology....	197
5.4.3 System C - BPS fabricated via 3D printing.....	199
5.5 Tissue engineering an osteochondral construct and its in vivo evaluation.....	206
6 SUMMARY AND CONCLUSION	214
FUTURE DIRECTIONS	219
REFERENCES	220
LIST OF PUBLICATIONS	234
AWARDS	234
SYLLABUS AND SEMINAR TOPICS	235
CURRICULUM VITAE	236
APPENDIX	237

LIST OF FIGURES

Figure 1.1: The schematic representation of osteochondral tissue.	5
Figure 4.1.1: Fabrication of biphasic scaffold via combinatorial approach..	92
Figure 4.1.2: Biphasic scaffold.	92
Figure 4.1.3: Analysis of morphological features.	94
Figure 4.1.4: Analysis of wettability by contact angle measurements of scaffolds.	95
Figure 4.1.5: Analysis of chemical features.	96
Figure 4.1.6: Analysis of thermal features by thermogravimetric analysis (TGA/DTG)..	97
Figure 4.1.7: Analysis of mechanical features.	98
Figure 4.1.8: <i>In vitro</i> degradation of the scaffolds and <i>invitro</i> bioactivity study of the bone phase..	100
Figure 4.1.9: In vitro cytocompatibility assessment	Error! Bookmark not defined.
Figure 4.1.10: Invitro Cytocompatibility assessment of scaffolds on L929 cells by MTT assay.	102
Figure 4.2.1: BPS fabricated via 3D printing and dissolution adhesion technology.	105
Figure 4.2.2: Analysis of morphological features by SEM.	107
Figure 4.2.3: Analysis of chemical and thermal features.	109
Figure 4.2.4: Analysis of wettability and mechanical features.	111
Figure 4.2.5: Analysis of <i>in vitro</i> degradation of developed scaffolds.	111
Figure 4.2.6: Assessment of <i>invitro</i> bioactivity.	112
Figure 4.2.7: Assessment of <i>in vitro</i> cytocompatibility assessment.	113
Figure 4.2.8: Analysis of cytotoxicity.	113
Figure 4.3.1: BPS fabricated via 3D printing.	117
Figure 4.3.2: Analysis of morphological features.	118
Figure 4.3.3: Analysis of chemical features.	120
Figure 4.3.4: Analysis of thermal features.	121
Figure 4.3.5: Analysis of wettability and mechanical features.	122
Figure 4.3.6: <i>Invitro</i> degradation of developed scaffolds, chondroitin sulfate leach out study for cartilage phase, and in vitro bioactivity of bone phase..	125
Figure 4.3.7: Assessment of cytocompatibility.	125
Figure 4.4.1: Isolation and characterization of rat MSCs.	127
Figure 4.4.2: Flow cytometric analysis of surface markers of rat MSCs.	128
Figure 4.4.3: Isolation and characterization of rabbit MSCs.	129
Figure 4.4.4: Flow cytometric analysis of surface markers of rabbit MSCs.	130
Figure 4.4.5: 3D pellet culture of MSCs and evaluation of chondrogenesis.	131
Figure 4.4.6: Evaluation of osteogenesis and production of ECM in vitro.	132
Figure 4.5.1: <i>In vitro</i> cytocompatibility assessment using MSCs.	136
Figure 4.5.2: Cell adhesion and proliferation study of scaffolds using MSCs..	136
Figure 4.5.3: Study on cell morphology.	136
Figure 4.5.4: Biochemical assessment of chondrogenic and osteogenic differentiation of MSCs.	138
Figure 4.5.5: Immunofluorescence confocal microscopic images of cartilage markers.	139
Figure 4.5.6: Immunofluorescence confocal microscopic images of osteogenesis markers.	140
Figure 4.5.7: Assessment of expression of the chondrogenesis-specific genes. (.....	142
Figure 4.5.8: Assessment of expression of the osteogenesis-specific genes.	142
Figure 4.6.1: <i>In vitro</i> cytocompatibility assessment of BPS using MSCs.	144
Figure 4.6.2: <i>Invitro</i> proliferation and differentiation studies.	146

Figure 4.6.3: Immunohistochemical analysis for specific markers of chondrogenesis and osteogenesis.	147
Figure 4.7.1: <i>In vitro</i> cytocompatibility assessment at day 7.....	150
Figure 4.7.2: <i>In vitro</i> cytocompatibility assessment at day 28.....	150
Figure 4.7.3: Cell adhesion, proliferation and morphology.	152
Figure 4.7.4: Evaluation of differentiation of rat ADMSCs on 3D scaffolds into cartilage and bone lineages on respective phases by biochemical analysis.	155
Figure 4.7.5: Immunohistochemical analysis for specific markers of chondrogenesis and osteogenesis.	156
Figure 4.7.6: Assessment of marker genes for chondrogenesis.....	158
Figure 4.7.7: Assessment of expression of the osteogenesis-specific genes.....	158
Figure 4.8.1: Comparative study among the three BPS fabricated.....	161
Figure 4.8.2: Surgical procedure of osteochondral defect creation and scaffold implantation.....	163
Figure 4.8.3: Gross appearance scores of knees in three different groups at 1 and 3 months.	164
Figure 4.8.3: Gross images of knee joints from each experimental group.	169
Figure 4.8.6: Histological examination of regenerated osteochondral tissue.	169

LIST OF TABLES

Table 1: Primer sequences used for qPCR.....	74
Table 2: Primer sequences used for qPCR.....	77
Table 3: Primer sequences used for qPCR.....	79
Table 4: Experimental groups for the in vivo study.....	83
Table 5: Scoring criteria.....	84
Table 6: Printing parameters of BPS: System A.....	91
Table 7: The distribution of pores in cartilage and bone phases.....	94
Table 8: Printing parameters of BPS: System B.....	104
Table 9: Printing parameters of BPS: System C.....	115
Table 10: The distribution of pores in cartilage and bone phases.....	118

ABBREVIATIONS

PCL	:Poly (ϵ -caprolactone)
PLGA	:Poly (lactic-co-glycolic acid)
PVP	:Polyvinylpyrrolidone
CS	:Chondroitin sulfate
β TCP	:Beta Tricalcium phosphate
ECM	:Extra cellular matrix
MSC	:Mesenchymal stem cells
SEM	:Scanning electron microscopy
FTIR	:Fourier-transform infrared spectroscopy
TG/DTG	:Thermogravimetric and derivative thermogravimetry
PBS	:Phosphate-buffered saline
BSA	:Bovine serum albumin
DMEM- HG	:Dulbecco's minimal essential medium -high glucose
FBS	:Fetal bovine serum
ABAM	:Antibiotic-Antimycotic
EDTA	:Ethylene diamine tetra acetic acid
FITC	:Fluorescein isothiocyanate
ISCT	:International society for cellular therapy
IAEC	:Institutional Animal Ethics Committee
2D	:Two Dimensional
3D	:Three Dimensional
ACI	:Autologous Chondrocytes Implantation
DMSO	:Dimethyl Sulphoxide
GAGs	:Glycosaminoglycans
RT	:Room temperature
SD	:Standard Deviation

SYNOPSIS

Human diarthrodial joint consists of osteochondral tissue, comprising superficial articular cartilage layered on the surface of subchondral bone. Osteochondral defects (OCDs), caused by multifactorial pathology which include lesions that penetrate the entire thickness of the articular cartilage, extend beyond the calcified zone, and into the subchondral bone. The condition may progress to osteoarthritis if not treated, which is the third most common musculoskeletal disease in the world, resulting in chronic physical disabilities. OCDs are difficult to treat because of the avascular nature and poor inherent regenerative capacity of the cartilage layer. The current treatment methodologies including osteochondral grafts have various limitations. Thus, simultaneous regeneration of dual tissues with disparate biomechanical properties for potential applications in treating OCDs is a target in regenerative medicine and an unmet clinical need.

In this scenario, osteochondral tissue engineering (OCTE) has emerged as a promising alternative, which attempts to bioengineer osteochondral tissues by combining relevant cells, three-dimensional (3-D) scaffolds, and biomolecules. For regenerating osteochondral defects by mirroring complex native tissue structures exhibiting anisotropic properties, a dual-zonal scaffold material-cell combination was proposed. Ideally, the composition, design/ fabrication methods, mechanical behavior, and degradation pattern of the biological substitute (scaffold) persuades the other components of OCTE; associated progenitor cells and growth factors/biomolecules. The 3D-printing technique can mitigate the drawbacks of conventional techniques by providing tailored design as well as Spatio-temporal control over the overall volumetric porosity and pore size.

The study aimed to develop biphasic scaffolds with a microarchitectural pattern similar to native tissue that can support the viability and differentiation of adipose-derived stem cells to chondrocytes in the upper cartilage layer and bone-like cells in the lower bone layer and maintain its functionality with stable phenotype. The thesis entitled “*Design and Development*

of Cell-Based Osteo-Chondral Constructs” is divided into six chapters. The introduction and background of the study are elaborated in chapter 1, which discusses about the pathophysiology of osteochondral tissues, current treatment methodologies and their limitations, concept of biomaterial-based OCTE, highlighting the various approaches to fabricating biphasic matrices for OCTE. The study hypothesis “*biomaterials based biphasic scaffolds which recapitulates osteochondral structure could favor differentiation of MSCs to respective lineages*”, is put forward in this chapter. To this end, the major objectives of the study were set as:

1. Development of biphasic scaffolds (BPS) mimicking osteochondral architecture.
2. Further characterization of developed biphasic scaffolds (BPS)
3. Isolation, culture, and characterization of adipose-derived mesenchymal stem cells (ADMSCs) and evaluation of its in-vitro differentiation into chondrogenic and osteogenic lineage in 2D culture.
4. Assessing the A differentiation potential of MSCs on the biphasic scaffold (BPS) capturing distinct layers of Osteochondral tissues.
5. Tissue engineering an anatomically shaped osteochondral construct and its in vivo evaluation.

The second chapter constitutes a systematic and comprehensive review of literature in the context of OCTE. Mainly, various reports in the field of OCTE are reviewed to understand the most appropriate and relevant study designs that mimic the native osteochondral tissues. The limitations of conventional fabrication techniques and the advantages of additive manufacturing technologies for fabricating customizable biphasic scaffolds are emphasized. Also, the impact of 3D printed scaffold designs on cellular behavior, native interfacial tissue properties, and the ability to adapt to the biological environment are reviewed. Besides, the chapter discusses various concepts and literature on mesenchymal stem cells (MSCs) and their differentiation into the desired lineage, followed by a discussion on biological cues including

the role of chondroitin sulfate and calcium and phosphate ions on chondrogenic and osteogenic differentiation respectively. The availability of suitable small animal models and surgical techniques with minimal trauma to the animals were also reviewed.

Chapter 3 describes the experimental design, a detailed description of materials, and experimental protocols. The chapter is further divided into four subsections. **Section 1** describes the development of three novel biphasic systems named as System A, B, and C. Section 1 is further divided into (1), (2) and (3). **Section 1 (1)** elaborates on the experiments designed for **System A** including biphasic scaffold fabrication (the components of cartilage and bone layer and its physicochemical, mechanical and biological characterization. The same experiment design is followed for **System B and System C** and is described in **Section 1 (2) and (3)** respectively.

Briefly, in system A, a blend of PCL/Gelatin is used to develop the upper cartilage phase with gradient pores via solution-based 3D printing whereas freeze-dried PCL/CaSO₄ represents the bone phase. The two phases are adhered using a medical-grade sealant to get the biphasic scaffold. In System B, solution-based 3D printing of materials with biomimetics is adopted where the printing ink contains the dispersion of cartilage ECM mimicking chondroitin sulfate (CS) and osteogenesis favoring β TCP along with the biocompatible polymers PCL and PLGA. Here, we conceived the dissolution-adhesion technology to intricately link the two phases effectively. In System C, a blend of PCL/PVP/CS and PCL/PVP/BTCP is used to fabricate the cartilage and bone phase respectively via 3D printing. Before printing, the respective solutions were mixed with Polyacrylic acid (PAA) for interpolymer complexation intending to improve the printing and prevention of z-axis collapse of printed layers. Here, the biphasic scaffold is fabricated via continuous printing. The scaffolds are characterized by thermal analysis, Fourier transform IR spectroscopy (FTIR), contact angle measurements, surface morphology analysis, pore characteristics, mechanical properties, degradation pattern,

bioactivity, and cytotoxicity. Further, using L929 cells, the cytocompatibility of developed biphasic scaffolds was determined by cell viability assays.

Section 2 (1) and (2) describe the isolation and characterization of rat and rabbit adipose-derived MSCs (ADMSCs) including multilineage differentiation assay and evaluation of extracellular matrix synthesis. **Section 3** describes the *invitro* differentiation potential of MSCs on the biphasic scaffold (BPS) mimicking the osteochondral architecture, which is further divided into 1, 2 & 3 representing System A, B & C.. In this section, the cell viability by live dead staining, morphology and attachment pattern by F actin staining, and proliferation ability of the scaffolds by Pico green assay using ADMSCs are determined. After this study, the method of differentiation of ADMSCs into chondrogenic and osteogenic lineages on 3D scaffolds was described. The *in vitro* cultured constructs are further evaluated for osteochondrogenesis by biochemical assays, Immunostaining, and Gene expression analysis. **Section 4** describes tissue engineering an osteochondral construct and its *in vivo* evaluation. Firstly, a comparative study was done among the three systems fabricated with respect to mechanical tests, proliferation, and biochemical assays. Among the three, the system that appeared the best is selected for *in vivo* study in the rat osteochondral defect model (Wistar rat). The second half of this section describes in detail, the *in vivo* evaluation of the PCL/PVP/PAA-based 3D printed biphasic scaffold with a specific design (System C) in a rat osteochondral defect model. The study groups were divided into three namely **Group 1: Biphasic scaffolds (BPS), Group 2: Biphasic scaffolds (BPS) +Cells, and Group 3: Sham**. The surgical procedure, post-implantation tissue retrieval, grossing, tissue processing, sectioning for histology, and staining of the defect site are elaborated in this chapter.

Chapter 4 categorically presents the results of various experiments described in chapter 3, substantiated with adequate and relevant figures, tables, and graphs. The first section elaborates on the results of the fabrication process and its characterization of three novel

biphasic osteochondral constructs. In system A, PCL/Gelatin-based cartilage phase with gradient pores was fabricated via 3D printing in a rectilinear pattern and freeze-dried PCL/CaSO₄ with random pores as the bone phase. In System B, 3D printed cartilage phase had oriented pores with cubical patterns in a tapering fashion to recreate the microarchitecture of hyaline cartilage. While the 3D printed bone part had pores in a honeycomb pattern to mimic its counterparts for enhancing osteogenesis. In System C, interpolymer complexation using PAA improved the printing process and prevented the z-axis collapse of the printed layer. The cartilage phase was printed in a cubical pattern and bone layer with a star pattern. SEM analysis of all systems revealed well-controlled and interconnected porous structures. Physico-chemical characterization confirmed the thermal stability and improved surface hydrophilicity with comparable compressive strength and is hence suitable for further biological studies. The degradation rate was higher for blended scaffolds. *In vitro* bioactivity studies confirmed the ability of the bone layer to undergo biomineralization. *In vitro* cytotoxicity results confirmed the non-cytotoxicity of the scaffolds.

In the second section, the methodology followed for the isolation of ADMSCs was successful in establishing a healthy population of cells. Further, the isolated MSCs were characterized and confirmed the presence of cytoskeletal and characteristic surface markers. Functional characteristics of MSCs were confirmed by a multi-lineage differentiation assay. ADMSCs could be induced to differentiate into chondrocytes and bone-forming cells and form the ECM *in vitro* 2D culture. In the third section, the results of biological studies confirmed that the scaffolds provide a good microenvironment for cell adhesion, spreading, and proliferation of MSCs, thus acted as excellent cell affable assemble. Further, upon evaluation of the differentiation potential of cartilage and bone phases, indicates that the cells were able to maintain their functionality tested through biochemical analysis. Immunostaining and Gene expression analysis confirmed that the respective layers showed greater potential to

differentiate ADMSCs to chondrogenic and osteogenic lineage and production of ECM. In section 4, from the comparative study, System C showed greater functionality and comparable mechanical properties and hence was selected for further implantation in Rat osteochondral defects. The biphasic scaffolds were implanted and no signs of rejection, infection, inflammation or extensive fibrosis were seen. Upon Grossing, in groups of Biphasic scaffolds (BPS) and Biphasic scaffold (BPS) + Cells, neo-formed tissues were whitish to translucent, smooth (heterogeneous) and intact surface with less irregularity was observed. Histologically, in the BPS and BPS +Cells groups, defect sites were mostly covered with new cartilage tissue with distinct defects in the SHAM; the thickness of the new tissue was similar to that of the surrounding normal cartilage layer. The chondrocyte concentration and ECM deposition were enhanced with visibly lined chondrocytes and increased production of proteoglycans in the BPS + Cells group.

In chapter 5, a thorough discussion of the results obtained is carried out with the existing literature. It is shown that scaffold design has a hierarchical pattern with great precision and control over the zonal organization of layered cartilage and could successfully stimulate the attachment and proliferation of ADMSCs. Moreover, the presence of bioactive ingredients induces the chondrogenic and osteogenic differentiation of MSCs in respective layers and produces matrix for osteochondral repair. The *in vitro* results were correlated with the *in vivo* results, suggesting their translational potential in osteochondral tissue regeneration.

Chapter 6 briefly summarizes the results of the study, which are analyzed to draw appropriate conclusions. The limitations of the study are identified and future perspectives regarding the potential of these 3D printed osteochondral scaffolds in personalized tissue engineering and its clinical translation are proposed.

CHAPTER 1

1 INTRODUCTION

1.1 Osteochondral tissue and its defects

In the human diarthrodial joint, articular cartilage and subchondral bone together constitute the load-bearing system known as an osteochondral unit. The primary role of articular cartilage is to protect the underlying bone from excessive stresses by distributing complex loads evenly. It also improves joint congruence and enables a wide range of low-friction movement with excellent lubrication. Very often, articular cartilage and subchondral bone develop defects and related disorders following long-term wear or acute trauma or osteochondritis dissecans. Thus, osteochondral defects (OCDs) are injuries or lesions that penetrate the entire thickness of the articular cartilage, extend beyond the calcified zone, and into the subchondral bone (Lopa and Madry, 2014). Defects in the highly structured matrix can progressively deteriorate through mechanisms of stress concentration and cell signaling cascades. If not treated, the condition may progress to degenerative disorders like osteoarthritis which is the third most common musculoskeletal disease in the world (Martel-Pelletier et al., 2016). With rising life expectancy and an aging population, the prevalence of such a chronic condition is estimated to increase. The complex condition affects the whole joint and ultimately, the tissue's mechanical integrity and cushioning function are lost resulting in bone-to-bone contact. In its pathogenesis, mechanical deterioration of articular cartilage and subchondral bone alteration plays a key role. Clinically, the patients present the condition with severe pain, joint deformity, and diminished mobility leading to chronic physical disabilities (Li et al., 2015). Eventually, the multifactorial pathology leads to a condition that causes enormous medical costs with less economic productivity as the consequent effect. Of note, OCDs are critical clinical problems and are difficult to treat as the human body has poor inherent repair/regenerative capacity of the

cartilage layer because of its avascular nature, lack of reparative cells and bioactive factors, and necessitate surgical procedures for the treatment of OCD including total joint replacement.

1.2 Current treatment methods

The International Cartilage Regeneration & Joint Preservation Society (ICRS) has recommended the Outerbridge classification score and evaluation score system and described a four-grade classification system (Slattery and Kweon, 2018) to accurately assess the severity of articular cartilage lesions for appropriate clinical treatment and scientific study. A wide range of therapeutic therapy techniques, including palliative, reparative, and regenerative treatments (Kwon et al., 2019), have been developed and deployed to prevent and treat early osteoarthritis characterized by the loss of articular cartilage.

Palliative treatments such as arthroscopic lavage or washout and debridement, aim to relieve patients' symptoms such as articular pain, but they rarely result in the restoration of injured tissue (Redman et al., 2005). However, risks of osteonecrosis, injury to the surrounding cartilage, and advancement of partial-thickness lesions are all possible side effects of chondroplasty. Reparative therapies such as arthroscopic abrasion arthroplasty, Pridie drilling (Martin and Jakob, 2022), and microfracture (Steadman et al., 2001) aim to promote subchondral bone bleeding, blood clot formation, and subsequent recruitment of bone marrow cells and fibrocartilage filling to achieve a spontaneous and natural cartilage repair. These current surgical treatments have poor persistent results.

Autologous chondrocyte implantation (ACI) has evolved over numerous generations as the clinically acknowledged regenerative therapy approach for cartilage defects (Vasiliadis et al., 2010). In ACI, passaged articular chondrocytes are used, which possess the greater innate potential to form hyaline-like cartilage when compared to multipotent marrow cells homed into the site in microfracture. The immature neocartilage fill formed by ACI may have a better ability to integrate and conform to the defect. However, ACI commonly resulted in a

fibrocartilaginous or fibrous fill, which may have arisen from cell passaging, patient age, and surgical discrepancies (Harris et al., 2011). Also, the procedure is inconsistent concerning the number of cells retained in the defect site, where they adhere, and how they form neocartilage. As the depth of the defect often extends to the subchondral bone, limited success is observed with microfracture and ACI as this address only cartilage defects and showed the inability to regenerate subchondral bone. Further, the inferior quality of repair tissue leads to failure and alterations of the subchondral bone. Hence regeneration efficacy for osteochondral defects involving subchondral bone injury is still a challenge.

Osteochondral auto/allografts offer better clinical results than microfracture or ACI. Thus, grafting is the frequently adopted clinical therapy to treat OCD, with cylindrical autografts for smaller defects (diameter <3 cm²) and allografts for larger defects (diameter >3 cm²) (Tamaddon et al., 2018). However, both strategies suffer from a lack of graft availability. Graft failure has been attributed to the failure of graft at the osseous region, lateral integration, deterioration of graft margins, and delamination from surrounding tissue, as well as the risk of donor site morbidity for autografts and disease transmission/rejection for allografts (Frank et al., 2017). Another gold standard treatment surgical approach for painful osteoarthritic cartilage is a total joint arthroplasty (Steinhaus et al., 2017), where the diseased cartilage and the underlying healthy bone are removed and prosthetic replacement of the joint with metal or ceramic components which has acceptable short-term but potentially poor long-term results. Over a million total joint arthroplasties are performed each year. The loosening of implants or eventual migration of prosthetic components is a major drawback (Aprato et al., 2016) and results in major loss of tissue. However, due to the limited lifespan of implant materials, younger patients delay receiving their first joint replacement, resulting in multiple physician visits for more conservative treatment options and an increase in the overall costs related to treating painful osteoarthritis. Moreover, as life expectancy has increased, more patients need

revision surgeries to replace worn and damaged implants. Addressing the loss of larger volumes of osteochondral tissue, coupled with the inherently limited regenerative capacity of osteochondral tissue, and the intricacies of articular cartilage composition makes osteochondral regeneration and reconstruction a significant clinical challenge worldwide and an unmet clinical need. Thus, regenerative engineering has emerged as a promising option to treat OCD.

1.3 Osteochondral tissue engineering

Tissue engineering is a promising strategy to develop biological substitutes that restore, maintain, or improve functions of damaged tissue or a whole organ. Osteochondral tissue/regenerative engineering (OCTE) intends to bioengineer damaged osteochondral tissues by combining relevant cells, three-dimensional (3-D) scaffolds instead of the native extracellular matrix (ECM), with a complex structure and appropriate biomechanical properties, and biomaterials in a harmonious manner. Ideally, several requirements from different perspectives like the composition (biocompatibility, degradation pattern, and stable physicochemical properties upon implantation), fabrication methods favoring design/ structure (porosity and nutrient transfer), and desired functionality (phenotypic stability of cells, biochemical and mechanical behavior) need to be considered when designing and fabricating the osteochondral scaffold. As a result, these biological substitutes (scaffolds) persuade the other OCTE components, such as related progenitor cells and growth factors/biomaterials, to recreate the microstructural properties of desired tissue, thereby healing or replacing damaged tissue or organs.

1.3.1 Structure and composition of osteochondral unit

To design a biomimetic scaffold, a thorough understanding of the OC unit's composition, structure, and function is required. Native osteochondral tissue consists of varying zones named as superficial, middle, deep, calcified, and a base of subchondral bone, as depicted in Figure 1. Each zone has a specific composition of extracellular matrix (ECM)

molecules and cellularity with collagen fiber orientation and organization of cells, resulting in remarkable biomechanical stability. The compressive modulus of superficial, middle, and deep zones is 0.079, 2.1, and 320 MPa (Keeney and Pandit, 2009), respectively, indicating the significant differences in stiffness of this tissue. The bone tissue is highly vascularized, and predominantly consists of water (20–30%), collagen type I, and hydroxyapatite crystals, and the latter two account for providing the tissue’s stiffness and compressive strength.

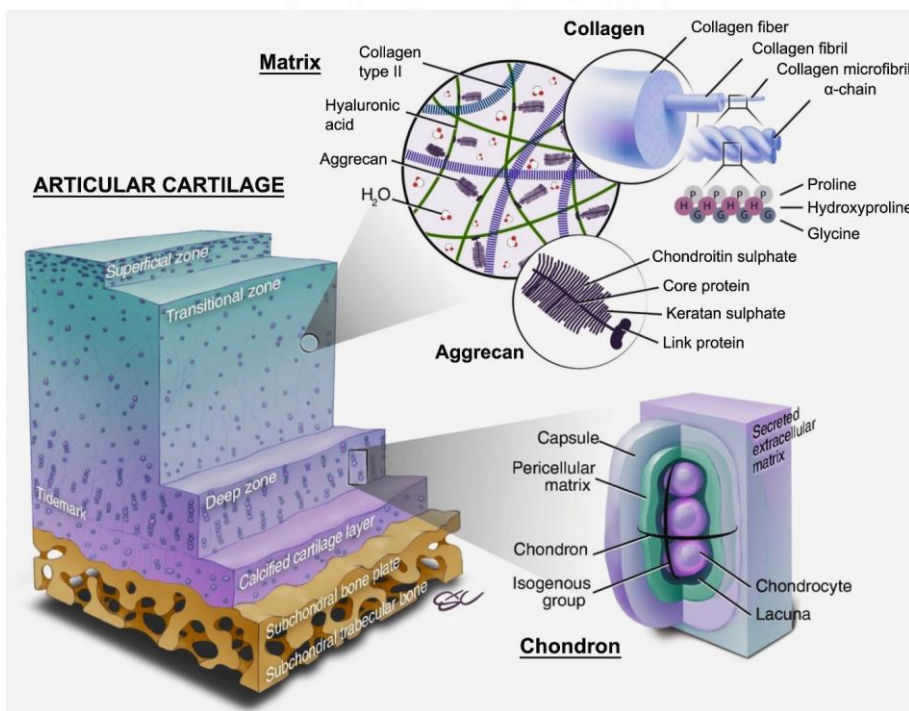


Figure 1.1: The schematic representation of osteochondral tissue. The extracellular structure of the osteochondral unit and its main individual components including the collagen and aggrecan in the matrix, and chondron are depicted in the figure (Wei and Dai, 2021)

The compressive modulus of subchondral bone (5.7 GPa) is higher than that of cartilage. The components of osteochondral cartilage include dense ECM of primarily collagen and glycosaminoglycans (GAGs) (15–35% wt) but with a much higher fluid content (water and electrolytes, (60–80% wt) and sparse distribution of native cells, chondrocytes (5% wt) responsible for the synthesis of ECM components required to maintain the cartilaginous matrix (Tatari, 2007). Unlike self-regenerative bone tissue, the small percentage of chondrocytes embedded in the dense ECM affects both cell mobility and migration. The disparate

biomechanical properties of bone and cartilage indicate the complexity of this dual tissue, which is in part why the restoration of the bio functionality of damaged osteochondral tissues remains an unsolved clinical need, making it challenging for the design and fabrication of tissue engineering scaffolds. In this context, the choice of the appropriate fabrication method, chemical nature of the scaffolding biomaterial, biodegradability, and long-term biocompatibility, is a prime necessity to foster cellular attachment, proliferation, and desired differentiation towards specific cells phenotypes.

1.3.2 Importance of the structural design of an osteochondral scaffold

The 3D scaffolds with specific structure/design play a pivotal role by interacting with the cells and reinvigorating appropriate signals at the tissue, cellular, and molecular scales. The structure of osteochondral tissue demands a complex spatiotemporal delivery of exogenous growth factors to achieve a sustained release and is associated with high costs and off-target tissue responses. Thus, an instructive material-based regenerative engineering without exogenous growth factors relies exclusively on scaffold morphology, modulus, chemical functionality, and wettability, to foster recruited or seeded cells to proliferate and eventually tissue regeneration. Moreover, high porosity and interconnectivity are considered beneficial for nutrient diffusion and neo-tissue infiltration. In most cases, the cartilage lesion spreads to the underlying subchondral bone, resulting in an osteochondral defect. As cartilage and subchondral bone tissues have different lineage-specific biological properties and a heterogeneous intermediate region (calcified cartilage) between them, producing discrete cartilage and subchondral bone tissues simultaneously within a single homogeneous scaffold remains difficult. Thus, instructive osteochondral scaffolds with biphasic embraced designs, often created as cylindrical plugs can provide two unique milieus for multipotent cells to differentiate into osteoblastic or chondrogenic lineages. So, for regenerating osteochondral

defects by mirroring complex native tissue structures exhibiting anisotropic properties, a dual-zonal scaffold material-cell combination was thus proposed.

The scaffold design has been proven to be extremely important for the success of OCTE, and there are certain parameters for scaffold design that must be followed. Firstly, the scaffolds must closely resemble the intricate and hierarchical structure of native tissue, with discrete yet integrated layers for simultaneous repair of cartilage and subchondral bone. Second, scaffolds should have sufficient mechanical strength at the cartilage/bone interface to withstand the high loading requirements of human joints, as well as gradient mechanical properties from cartilage to the underlying bone. Third, to allow for cell migration and nutrient transfer, scaffolds must have a structure with interconnecting pores and internal channels.

1.3.3 Techniques for fabricating OC scaffolds

A variety of manufacturing techniques (Frassica and Grunlan, 2020) have been used to meet the above parameters for osteochondral scaffolds, including solvent casting, freeze-drying, phase separation, and fiber bonding. These traditional production procedures, on the other hand, have little control over scaffold geometry and porosity (Cheng et al., 2019). The technology revolution of additive manufacturing is gaining ground in the development of patient-specific tissue engineering scaffolds, well with the recent report on the fabrication of osteochondral scaffolds utilizing three-dimensional (3D) printing. The 3D-printing technique (Li et al., 2018) can mitigate the drawbacks of conventional fabrication techniques by providing tailored design as well as spatio-temporal control over the overall volumetric porosity and pore size. The scaffolds used in regenerative therapies should integrate with existing native tissue and 3D printing technologies have unquestionably proved their potential to fabricate customizable, biomimetic scaffolds from a variety of biomaterials. Here, the internal architecture of the scaffold can be tuned with micrometer resolution and thickness of struts separating the pores, which in turn can decide the porosity of the scaffold. Porosity (Yu et al.,

2008) is a major decisive factor, which can greatly affect the nutrient transferring capability of the scaffold and further decide the cell survival and differentiation. Generally, biphasic were obtained by deposition of two different materials and architectures and were even integrated with a poly- ϵ -caprolactone (PCL) framework for higher compressive strength.

1.3.4 Composition of the scaffolding biomaterial

The selection of appropriate scaffolding material, when combined with fabrication technologies, is critical for achieving the requisite physical and biological qualities, as well as the successful creation of desired tissue. Biomaterials an indispensable integrand, serve as a temporary framework with initial mechanical function, and provide architectural scaffolding to augment tissue regeneration (Nooeaid et al., 2012). Likewise, the biomaterial should degrade at a rate that is comparable to the growth of new tissues at the implantation site. Polymers (Natural and synthetic), metallic materials and inorganic materials such as ceramics and bioactive glasses, ECM-based materials, and the composites (Deng et al., 2019) made up of a variety of the aforementioned materials are the major categories of biomaterials proved their efficacy in various biomedical applications because of the greatest diversity and most striking resemblance to natural ECMs. The two distinct tissues, cartilage and bone consist of heterogeneous composite material arranged in an orderly fashion. Hence, composites of synthetic or natural polymeric substances are found to be more effective for developing scaffolds with improved biomimetic properties over conventional single-component systems and its appropriate selection determines the success of the strategies. Thus, multicomponent systems can be designed to produce high-performance composites. Natural polymers (Zhao et al., 2021) such as polysaccharides (typically hyaluronic acid (HA), chondroitin sulfate, alginate, agarose, chitosan, and gellan gum) and protein-based materials (commonly collagen, gelatin, and silk fibroin) (Wei and Dai, 2021) have received much interest due to their structural similarity to native ECM and the resulting biocompatibility, biodegradability, and low

inflammatory response. However, issues like as purification difficulty, poor mechanical characteristics, unpredictable degradation time, and batch-dependent performance remain unsolved. Scaffolds made of synthetic polymers (Frassica and Grunlan, 2020) such as poly(ethylene glycol) (PEG), poly(lactic acid-co-glycolic acid) (PLGA), polycaprolactone (PCL), poly(vinyl alcohol) (PVA), etc have also been widely used in osteochondral tissue engineering because of their improved controllability and reproducibility in terms of molecular weight, degradation rate, and industrial-scale manufacture. Synthetic polymers, on the other hand, confront difficulties such as low bioactivity and complicated structural design and preparation methods. Poly (ϵ -caprolactone) (PCL) (Siddiqui et al., 2018), an FDA-approved low-cost biodegradable polyester, is a well-known candidate material to fabricate the scaffolds . However, lack of hydrophilicity and cell recognition sites, extremely slow degradation rate, and lack of flexibility limit its usage in the regeneration of tissues like the diarthrodial joint, where excessive loading forces are exerted. Bioceramics (Deng et al., 2019) have been extensively reported to be incorporated with natural or synthetic polymers and serve as components in promoting subchondral bone regeneration due to their biocompatibility, bioactivity, and mechanical strength as the most ubiquitous and generally accepted type of materials for the replacement and reconstruction of damaged bone tissues.

1.3.5 Cells

The use of cells with the ability to differentiate into chondrogenic and/or osteogenic cells in scaffolds is prevalent in tissue engineering for the development of an engineered osteochondral unit. In contrast to the variety of biomaterials employed to construct a biomimetic 3D architecture in OCTE, the availability of cell populations is limited. The quality of regenerated tissue and deposition of ECM depends on the incorporated cells. The most commonly used cells include chondrocytes, chondroprogenitor cells and osteoblasts, multipotent stem cells (BMSCs, adipose-derived stem cells (ADMSCs)), and pluripotent

embryonic stem cells (ESCs) and induced pluripotent stem cells (iPSCs) (Fu et al., 2022). To simulate the contrasting environments in the two regions, chondrocytes in the cartilage layer were combined with preosteoblasts in the subchondral layer for osteochondral defect repair (Cao et al., 2003). Chondrocytes confront several challenges, including low isolation efficiency, reduced proliferation capability, and the frequent tendency of dedifferentiation in culture (Nukavarapu and Dorcemus, 2013). Thus, a fundamental need in OCTE is progenitor cells that could differentiate into preferred lineages to replace the need for autologous cells in sufficient numbers to build 3D structures.

The use of stem cells can be a possible option to mitigate the drawbacks of articular chondrocytes and are considered to be promising cellular approaches for tissue engineering strategies. Mesenchymal stem cells (MSC) have a high ability for self-renewal, multilineage differentiation upon stimulation by appropriate signaling molecules/factors, immunomodulatory capabilities, and manipulation ease, making them an appealing tool for research and clinical use. ADMSCs are relatively easy to isolate and culture and have higher proliferation capacity and abundance than BMSCs, and have demonstrated the ability to perform both chondrogenesis and osteogenesis in a variety of biomaterial settings, according to recent report (Mellor et al., 2015). MSCs being the most commonly employed cells, at present, the main limitation in the clinical use of MSCs for cartilage repair is its tendency to differentiate into hypertrophic chondrocytes and after transplantation, the implants may undergo mineralization and become bone (Somoza et al., 2014). MSC properties vary greatly based on a variety of factors like tissue source, isolation procedure, and medium composition. Also, the type of material influences MSC chondrogenesis and hypertrophy, and the induced lineages are regulated by the scaffold's design, which includes different pore sizes, interconnectivity, and metabolic conditions. Thus, the selection of an appropriate cell source with high proliferation capacity and differentiation potential is very crucial in OCTE.

1.4 Definition of the problem

Osteochondral defects (OCDs) include lesions or degeneration of cartilage, subchondral bone, and bone-cartilage interfaces resulting from traumatic injuries, disease, or aging. The current treatment methodologies like microfracture, autologous chondrocyte implantation, and osteochondral grafts have various limitations. Thus, treating OCDs is a major clinical need and a target in regenerative medicine as it requires simultaneous regeneration of both bone and cartilage. The recent successful paradigms/models of Osteochondral Tissue Engineering (OCTE) involve the combination of mesenchymal stem/progenitor cells, scaffolds, and biomaterials to mimic the crucial aspects of physiological niche. To overcome the bottlenecks of osteochondral tissue engineering and considering the spatial hierarchy and complexity of osteochondral units in composition, structure, and functions, key challenges remain to be overcome in regenerating damaged osteochondral tissues. Another ongoing problem in osteochondral tissue engineering is graft and implant integration with the surrounding tissue. There are numerous studies available on multiphasic and gradient scaffolds developed with emerging innovative technologies. However, research into fabricating gradient scaffolds that mimic the morphological, biological, physicochemical, and mechanical heterogeneities exhibited in osteochondral tissue is still in its infancy. Despite the significant advances made in the fields of biomaterials and biological research, this remains a difficult goal to fulfill. Hence, this Ph.D. dissertation attempts to provide a viable answer to the lack of artificial matrices for therapeutic use in osteochondral tissue regeneration.

1.5 Hypothesis

It was hypothesized that biomaterials-based biphasic scaffolds that replicate osteochondral structure could favor differentiation of MSCs to corresponding lineages.

1.6 Aims and Objectives

1. To develop biphasic scaffolds (BPS) that mimic the hierarchical nature of native osteochondral tissues.
2. To study the *invitro* differentiation potential of adipose-derived MSCs cultured on biphasic scaffolds towards chondrogenic and osteogenic lineage in respective phases of BPS
3. To study the effect of bioengineered biphasic osteochondral constructs to repair or regenerate the critical size defects *in vivo*.

To achieve the aims, the following objectives are set for the work,

1. *Development of biphasic scaffolds (BPS) mimicking osteochondral architecture.*
2. *Further characterization of developed biphasic scaffolds (BPS)*
3. *Isolation, culture, and characterization of adipose-derived mesenchymal stem cells (ADMSCs) and evaluation of its in-vitro differentiation into chondrogenic and osteogenic lineage in 2D culture.*
4. *Assessing the invitro differentiation potential of MSCs on the biphasic scaffold (BPS) capturing distinct layers of Osteochondral tissues.*
5. *Tissue engineering an anatomically shaped osteochondral construct and its in vivo evaluation.*

1.7 Significance

Osteochondral tissue is one of the most complex connective tissues with a gradient structure in terms of type, number and size of resident cells as well as the compositional variation of the extracellular matrix (ECM). Mimicking such an extraordinary hierarchical tissue architecture poses a technological challenge in the field of osteochondral tissue engineering. Therefore, innovative 3D scaffold fabrication strategies with an ability to recapitulate the continuous gradients are needed to bioengineer the osteochondral substitutes

for critical-size defects. In this doctoral work, we for the first time present the design, development and evaluation of three novel 3D printed biphasic scaffolds with a biomimetic gradient tissue architecture. Specifically, the scaffold was fabricated with a great control over process parameters in order to have a hierarchical pore organization, wherein the pore networks were created with a gradient of pore sizes. Further, the scaffold was functionalized by incorporating bioactive cues to promote the osteo-chondro genesis. The study established that the biphasic scaffolds with biomimetic gradient pore architecture and bioactive cues successfully promotes the differentiation of mesenchymal stem cells (MSCs) towards chondrogenic and osteogenic lineage in respective phases. Thus, the structural hierarchy be considered as an imperative element in the scaffold for addressing the spatial complexity of osteochondral units. Further, we were able to show for the first time *in vivo* that the hierarchical structure could aid in the efficient regeneration of the osteochondral tissues, and the customization offered by 3D printing could be explored in personalized tissue engineering.

CHAPTER 2

2 REVIEW OF LITERATURE

2.1 *The anatomical structure of the osteochondral unit*

The human diarthrodial joints consists of the osteochondral unit which forms the supportive and protective connective tissue in the musculoskeletal system. It consists of articular cartilage in zonal organization, osteochondral interface/calcified cartilage and subchondral bone, having disparate biomechanical properties that together facilitates the easy dissipation of forces with low coefficient of friction.

2.1.1 *Articular cartilage*

The surface of movable joints consists of articular cartilage which is hyaline type, about 2 to 4 mm thick with a translucent smooth appearance at fresh state (Nooeaid et al., 2012). The tissue is tough, durable and flexible and unlike most tissues it is devoid of blood vessels, nerves, or lymphatics. Structurally, the cartilage consists of dense extracellular matrix with sparsely distributed highly specialized cells called chondrocytes (F. H. Chen et al., 2006) which is responsible for the homoeostasis and remodeling of all ECM components.

The unique organization of chondrocytes and ECM proteins showing regional variations in the structure and composition, physiologically divides the cartilage into four zones: the superficial/tangential, middle/ transitional, deep/ radial and calcified cartilage zones (Goldring, 2012) and constitutes 10–20%, 40–60% and 30–40% of the articular cartilage thickness respectively (Buckwalter et al., 1994). Three regions are found within each zone named as the pericellular, the territorial, and the interterritorial region.

2.1.1.1 **Zones**

The thin superficial layer encompasses well-organized tightly packed type II collagen fibrils arranged parallel to the articular surface with relatively high number of flattened chondrocytes resident in the ECM fibrils. The integrity of this layer is crucial in the protection of the deeper

layers from shear, tensile, and compressive stresses while joint articulation with ease. Also, this zone provides lubrication through direct contact with the synovial fluid and is responsible for the lubrication and tensile properties of cartilage (Sophia Fox et al., 2009). The middle (transitional) zone lies immediately below the superficial zone, consisting of spherically shaped chondrocytes at low density and, proteoglycans and obliquely arranged thicker collagen fibrils. The specific structure provides the first line of resistance to compressive forces and acts as a functional bridge between the superficial and deep zones (Deng et al., 2019). In the deep zone, large diameter collagen fibrils are arranged perpendicular to the articular surface and provides the greatest resistance to compressive force and represents 30 % of articular cartilage volume. Also, rich in proteoglycan content, but lowest in water concentration. The chondrocytes are arranged parallel to the collagen fibres in columnar alignment. Due to greater proteoglycan content and unique patterned arrangement, the deep zone provides the highest amount of resistance to compressive forces (Quinn et al., 2005).

2.1.1.2 Regions

There are distinct regions in the ECM of articular cartilage in addition to the zonal variations concerning to the composition, proximity to the chondrocytes, and collagen fibril diameter and organization. They are pericellular, territorial, and interterritorial regions. The thin layer of pericellular matrix (Chung et al., 2001) consisting of proteoglycans, glycoproteins and non-collagenous proteins completely surrounds the chondrocyte and plays a pivotal role in initiation of signal transduction within cartilage on substantial loads. The pericellular matrix is surrounded by the thicker territorial matrix (Guilak and Mow, 2000) which forms a basketlike network of fine collagen fibrils around the cells. The matrix protects the chondrocytes against load induced mechanical stresses, adding resiliency to the articular cartilage structure. The interterritorial matrix (Mow and Guo, 2002, p.) being the largest region contributes utmost biomechanical properties where proteoglycans are abundantly present. The alignment of

collagen fibres in each zone in the interterritorial region varies, in which the superficial zone consists of randomly oriented bundles of large collagen fibrils that are arranged parallel to the surface, obliquely in the middle zone, and perpendicular in the deep zone.

2.1.1.3 Chondrocytes

Chondrocytes are highly specialized, metabolically active resident cells in articular cartilage that originate from mesenchymal stem cells and constitute about 2% of the total volume of articular cartilage (Buckwalter and Mankin, 1998a). These cells vary in shape, number, and size, depending on the anatomical regions of the articular cartilage. The chondrocytes are arranged in lacunae as isogenous group and surrounded by narrow pericellular matrix (PCM), together referred to as a chondron. They can sense the changes in local environment by expressing integrins (Loeser, 2014). Each chondrocyte establishes a specialized microenvironment and is responsible for the turnover of the ECM in its immediate vicinity. This microenvironment prevents migration of cells to adjacent areas of cartilage. The cell-to-cell contacts for direct signal transduction and communication between cells are rare. However, they respond to a variety of stimuli, piezoelectric forces, and hydrostatic pressures. Unfortunately, chondrocytes have limited potential for replication, a factor that contributes to the limited intrinsic healing capacity of cartilage in response to injury. (Bhosale and Richardson, 2008).

2.1.1.4 Extracellular Matrix

The ECM of articular cartilage mostly consists of tissue fluid (water), collagen, proteoglycan and noncollagenous proteins, glycoproteins lipids and phospholipids (smaller amounts). The water forms 65–85% of total wet weight, consisting dissolved inorganic ions. The relative water concentration decreases from about 80% at the superficial zone to 65% in the deep zone. The water flow facilitates nutrient transport to the chondrocytes and provides lubrication on the articular surface (Gao et al., 2014). The cartilage ECM is rich in collagens which constitutes

60–85% of dry weight. Type II collagen represents 90% to 95% of the total collagen and are intertwined with proteoglycans (Shoulders and Raines, 2009).

Proteoglycans represent the second-largest group of macromolecules in the ECM and are heavily glycosylated protein monomers that account for 15–40 % of dry weight. It consists of a protein core with covalently attached linear and negative charged glycosaminoglycan (GAGs) chains extending out from the protein core. They interact with hyaluronan chains through link proteins to form larger aggregates and aggrecan is the major proteoglycan whereas different GAGs like hyaluronic acid, chondroitin sulfate, keratan sulfate and dermatan sulfate are seen in articular cartilage. The osmotic properties of the articular cartilage are due to the sulphated GAGs in the aggrecan that attract cations in water.

The fibrillar collagen II network and proteoglycans in the ECM attributes to the unique viscoelastic properties of the articular cartilage and dissipate the mechanical loads deep into the underlying subchondral bone during compression and reestablish original state when the pressure is relieved. The noncollagenous proteins and glycoproteins such as fibronectin and CII, a chondrocyte surface protein plays a pivotal role in the organization and maintenance of the macromolecular structure of the ECM (Sophia Fox et al., 2009).

2.1.2 Calcified Cartilage

Calcified cartilage forms the transitional zone between the flexible uncalcified cartilage and the rigid subchondral bone and act as a physiological barrier between these two different tissues. The calcified cartilage (CC) layer spans from thin wavy basophilic border known as tide mark at the bottom of the deep zone to the cemental line just above the subchondral bone (Lyons et al., 2006). The CC layer is interlocked tightly with the cartilage above and the lower subchondral bone plate and distribute mechanical loadings during joint motion. The tide mark separates the deep zone from the calcified cartilage and prevents the articular cartilage from the invasion of vasculature and nerves. The collagen fibrils are arranged perpendicular to the

articular cartilage. The interface is permeable to low molecular weight nutritional solutes. Chondrocytes are scarcely distributed and exhibit a hypertrophic phenotype in this layer and can produce type X collagen to calcify the ECM. The collagen fibers of articular cartilage are in continuous with the calcified zones and convert shear into compressive and tensile forces (Goldring and Goldring, 2016).

2.1.3 Subchondral Bone

The highly innervated, stiffened and less pliable subchondral bone lies just beneath the cement line of calcified zone and has an effect on the viscoelasticity and nutritional metabolism of articular cartilage, and at the same time it contributes to the pain in disease (Li et al., 2013). The zone can be anatomically divided into subchondral cortical bone plate (SBP) and cancellous/trabecular bone (STB). The SBP is impenetrable thin lamellae lying immediately beneath the mineralized cartilage with low porosity and limited blood vessels. This bony layer maintains the shape of articular bone and a suitable biomechanical environment for the differentiation and development of cartilage. STB has randomly aligned trabeculae which is porous with lower density and stiffness, highly vascularized and metabolically active (Madry et al., 2010). Subchondral bone consists of osteocytes embedded in hydroxyapatite and rich ECM. The bone tissue comprises of organic and inorganic based extracellular bone matrix where three types of cells including osteoblasts, osteocytes and osteoclasts are found. The organic contents are collagen type I (90% of bone matrix), the proteoglycans (osteonectin, osteopontin, and osteocalcin) and glycoproteins (type I and V collagen, fibronectin and laminin) rich amorphous interfibrillar matrix (Furuya et al., 2018). The inorganic components are predominantly needle-like crystals of calcium hydroxyapatite (HAp, $\text{Ca}_{10}(\text{PO}_4)_6(\text{OH})_2$) (~50% of the dry weight of the matrix) and others include bicarbonates, citrate, magnesium, potassium and sodium ions. The cells of bone tissue are involved in bone metabolism and direct or indirect mechanical transduction through solid matrix (Pouran et al., 2017).The collagen

fibers along with inorganic elements contribute to the ultimate hardness and resistance of the bone tissue.

2.2 *Osteochondral defect classification*

The maintenance of articular cartilage is extremely dependent on preserving its organized architecture. Any defects that penetrate deep into the articular cartilage, osteochondral interface and subchondral bone are known as osteochondral defects, where these three tissues exhibit anisotropic properties. Outerbridge classification score system is the most accepted classification system recommended by the International Cartilage Regeneration & Joint Preservation Society (ICRS) which describes a four grades classification system in 1961 according to the macroscopic aspects, depth, location, and the condition of the surrounding cartilage (Slattery and Kweon, 2018). Thus, for suitable clinical treatment and scientific study, cartilage lesions are classified as Grade 0 (normal cartilage), Grade I where the softening and swelling of the articular cartilage are present. In Grade II; partial thickness chondral defect, the damage is confined only to the articular hyaline cartilage zone without affecting the calcified cartilage where fissuring or fragmentation of the cartilage surface in an area up to half an inch in diameter is observed. Grade III denotes a fully thickness chondral defect causing damage to the calcified cartilage layer where lesions with the same fissuring and cracks extending in an area more than half an inch. In Grade IV, osteochondral defect, when the subchondral bone is totally exposed and the structure of the whole osteochondral tissue is destroyed (Wei and Dai, 2021).

2.3 *Osteoarthritis (OA) and the molecular mechanism of OA*

Articular cartilage and subchondral bone are subjected to constant biomechanical stresses and react accordingly where reparative process is a part of joint homeostasis. However, articular cartilage can be damaged under pathological conditions like trauma and osteoarthritis (OA), where there is abnormal mechanical loading. Osteoarthritis (OA) is a age related degenerative

condition characterized by slow deterioration of articular cartilage and subchondral bone in response to insult or injury (Loeser et al., 2012). The homeostatic or reparative processes cannot compensate for destructive mechanisms, resulting in sequential events that affect the integrity of ECM. During the early stages of OA, the molecular composition and organization of the extracellular matrix is altered first (Maldonado and Nam, 2013). The articular chondrocytes, in response to change in ECM composition exhibit a transient proliferative response characterized by chondrocyte cloning and an increased matrix synthesis (Col2, aggrecan etc.) is observed (Pearle et al., 2005). Also, greater expression of hypertrophic markers such as Runx2, Col X, and MMP13 are observed. This alteration of cellular configuration further changes the structure and composition of the ECM secreted by the cells, characterized by the changes of aggrecan towards nonaggregated form.

The reduced proteoglycan content decreases the compressive modulus of cartilage and the tissue is subjected to greater strains. But the collagen synthesis rate increases and the composition of collagen type changed from collagen type II to type I (Xia et al., 2014). Collagen type I has inferior properties and affects the mechanical stability of the ECM network. The cartilage cannot no longer withstand tension or shear and predisposes the cartilage to splitting or fibrillation. The collective deterioration in the structural integrity and composition of ECM progressively alters the microenvironments of chondrocytes and modulates its activities. The stimulated chondrocytes produce more catabolic factors involved in cartilage degradation, accompanied by the elevated biochemical markers. Chondrocytes possess receptors for these intrinsic and extrinsic growth factors, cytokines and other inflammatory mediators (Goldring and Marcu, 2009). The activated integrins, when fibronectin (FN) and type II collagen (COL2) fragments binds to the integrin receptors, can stimulate the production of matrix-degrading proteinases and inflammatory cytokines and chemokines in chondrocytes(Pulai et al., 2005) .

The articular chondrocytes will then undergo apoptosis, leading to irreversible cartilage degeneration and the articular cartilage will eventually be completely lost. The reduced joint space resulting from total loss of cartilage will cause friction between bones, leading to clinical symptoms such as pain and limited joint mobility. Other signs of OA, including subchondral sclerosis, bone eburnation, osteophyte formation, as well as loosening and weakness of muscles and tendons will also appear (A. R. Sharma et al., 2013).(Thambyah and Broom, 2009). Also, a higher level of alkaline phosphatase (ALP), osteocalcin, osteopontin, IL-6, IL-8, and progressive ankylosis protein homolog (ANKH), urokinase plasminogen activator (uPA), prostaglandin and insulin growthfactor-1 (IGF-1) are present in subchondral bone, attributed to its boosted bone anabolic activity of resident osteoblasts (Sanchez et al., 2008; Truong et al., 2006). But the newly formed bone is not necessarily accompanied by equivalent mineralization leads to many osteoids in the subchondral bone resulting in detrimental effects on bone properties.

Signaling mechanisms is the major phenomenon to maintain the stable phenotype for articular cartilage and subchondral bone, extracellular matrix (ECM) synthesis and bone remodeling process. An imbalance in the signalling pathway leads to deterioration of cartilage quality and thickening of the subchondral bone contributing to the progression of OA.

WNT signaling plays an essential role in cartilage, bone and joint development. Though WNT signaling acts as a survival signal by inhibiting apoptosis of chondrocytes, increase in WNT signaling induces the expression of catabolic factors such as MMPs and aggrecanase, contributing to cartilage damage. WNT signaling is essential for bone homeostasis, but increased WNT signaling induces sclerosis in bone through knock down of WNT antagonists. This causes an increased bone formation and thickening of subchondral end plate which contribute to deterioration of cartilage under altered mechanical load (A. R. Sharma et al., 2013).

BMP signaling regulates the endochondral bone formation through canonical Smad molecules and are involved in all phases of chondrogenesis (Retting et al., 2009, p. 1). BMP-2, -4 and -5 play significant roles in protection and repair of cartilage through chondrocytes proliferation and regulating the synthesis of aggrecan and proteoglycan. (Zhao et al., 2017). Along with BMPs, TGF- β also plays an indispensable role in articular maintenance, metabolic homeostasis and structural integrity. (Blaney Davidson et al., 2007).

2.4 Current osteochondral repair strategies and challenges thereof

The treatment of osteochondral lesions is a great challenge in clinics due to the unique and complex structure of osteochondral tissue and the limited capacity of articular cartilage for intrinsic healing. Current clinical treatment methods for osteochondral treatment can be categorized as palliative treatment, reparative treatment and regenerative/restorative treatment.

2.4.1 Palliative treatment

Palliative treatment for osteochondral defects includes arthroscopic debridement, abrasion arthroplasty and chondroplasty (Howell et al., 2021). In arthroscopic lavage and debridement procedure, cartilage or bone debris are removed from the damaged area and then the pathological structures are resected. This provides a short-term symptomatic relief of the knee pain by reducing the inflammatory response and improve the functional status. Chondroplasty aims to produce a smooth edge macroscopically without damaging the surrounding cartilage by using mechanical tools or radiofrequency energy. However, due to the high temperature during chondroplasty treatment, risks of osteonecrosis, damage to the surrounding cartilage and progression of the partial-thickness lesions and are not suitable for patients who have lesions smaller than 0.0127- 0.0254 m² (Upmeier et al., 2007).

2.4.2 Reparative treatments

The reparative treatment are invasive methods includes arthroscopic abrasion arthroplasty, Pridie drilling, microfracture and mosaicplasty (ŻYLIŃSKA et al., 2018). Arthroplasty emphasizes on superficial abrasion and exposure of the viable bone. Pridie drilling is a modification to debridement procedure where multiple deep holes into the subchondral bone marrow are created by a quarter-inch drill. The procedure focusses on repairing the osteochondral defect areas by drilling subchondral bone to foster the haemorrhage from the site, subsequent blood clot formation, recruitment of bone marrow cells and fibrocartilage filling. These events favour spontaneous and natural cartilage repair. In microfracture, multiple perforations which are 3–4 mm apart and 2–4 mm in depth, are made using arthroscopic awl after removal of the overlying calcified cartilage (Martin and Jakob, 2022). Though microfracture technique is considered as the gold standard for knee cartilage repair, the filled fibrocartilage possesses inadequate biomechanical features. Mosaicplasty involves osteochondral transplantation with autograft and allograft and reported to offer superior clinical results than microfracture (Hangody and Füles, 2003).

2.4.3 Restorative treatment

Autologous chondrocyte implantation (ACI), matrix-assisted chondrocyte implantation and DeNovo natural tissue/engineered tissue are well known restorative methods. ACI being the widely recognized regenerative strategy for cartilage defect, has evolved with several generations (Vasiliadis et al., 2010). The neocartilage formed by ACI have a better ability to integrate and conform to the defect site, and thus, have shown positive outcomes in terms of functionality and biomechanics. To overcome the associated complications, second generation ACI are introduced wherein the synthetic collagen membrane are used to cover the treated defects (Minas et al., 2016). Further, a third-generation ACI known as matrix-assisted autologous chondrocytes are transplanted into the defect/lesion (Schuette et al., 2017) (Kon et

al., 2009). The enhanced proliferation, stable phenotype and the uniform distribution of the chondrocytes are the known benefits.

Although these strategies are current standard methods for osteochondral defect management, the secondary traumatization, long recovery time and slow tissue maturation time limit their application in clinics. Hence, there is need to develop a clinically compliant treatment strategy which facilitates complete healing of articular cartilage, osteochondral interface and subchondral bone simultaneously.

2.5 Osteochondral Tissue engineering

Regenerative medicine seeks to develop alternative solutions for organ transplantation using various approaches. In this regard, cell-based therapies and tissue engineering are the two most studied methods. The aforementioned cell-based treatments strategies showed limited success in long-term repair and also exhibit undesirable side effects. The treatments are usually restricted to small lesions, making the overall outcome generally inadequate.

Tissue engineering is a newly emerged interdisciplinary field, that joins the latest developments in cell/molecular biology, materials science and engineering, chemistry and medical sciences towards the development of biological hybrid substitutes (combining biodegradable supports, cells and signalling molecules, such as growth factors) that restore, maintain, or improve tissue function or a whole organ (Langer and Vacanti, 1993). It involves understanding the components of the organism and principles of tissue growth through natural signalling pathways and applying this to produce functional replacement tissue for clinical use. It was once categorized as a sub-field of biomaterials, now having grown in scope, it emerged as a separate field. The three principal components are scaffolds, cells and signaling factors to build implantable tissues *in vitro* settings. The past few decades have witnessed the booming development in the study of both bone and cartilage tissue engineering. ***Osteochondral tissue engineering (OCTE) aims at recreating a hyaline-like tissue to restore the articular surface***

and subchondral bone beneath as similar as possible to the physiological one, both biologically and biomechanically (Pereira et al., 2018). The critical requirements of OCTE are the right choice of the materials combinations, the design of the scaffold structure influencing the effect of porosity (porosity content, pore size distribution and interconnectivity), adequate cell sources and the unsurpassed delivery strategies for growth factors (Fu et al., 2022). But the osteochondral constructs need specific attention because of complicated structure with different specifications for each layer. Consequently, the most difficult challenge for osteochondral regeneration is to regenerate articular cartilage, subchondral bone and osteochondral interface simultaneously.

In regenerative approaches, scaffolds play a crucial role in defining the 3-D anatomical shape and microenvironment for regenerative cells, while maintaining space, favoring regeneration of new bone, and preventing soft tissue migration in the bony lesion (Nooeaid et al., 2012). A variety of materials have been explored as scaffolds for bone tissue regeneration.

2.5.1 Scaffolds for osteochondral tissue regeneration and its preparation strategies

Biomaterials based 3D construct provides architectural framework that structurally and functionally imitate the native osteochondral tissue and support suitable microenvironment for the restoration of the multifaceted tissue. Hence scaffold being the integral component in osteochondral tissue engineering that augment cell growth and eventual tissue regeneration forms the principal research focus for material scientists (Nukavarapu and Dorcemus, 2013). The requirements that need to fulfilled from different perspectives while designing and fabricating the osteochondral scaffold includes (1) Compositionally, appreciable biocompatibility and biodegradability of the scaffold with negligible immune rejection and stable physicochemical properties when implanted into the body (2) Structurally, a stratified orientation of pores providing suitable microenvironment for ensuing formation of the damaged tissue (3) Functionally, the phenotypic stability and the biomechanical properties

withstanding the stresses, and the integration with the surrounding cartilage and bone (Yang et al., 2017).

2.5.1.1 Architectures of the scaffolds

Combined with the composition of the scaffolding material, the architecture of the scaffold is a crucial factor for determining the success of any tissue engineered construct. The technology revolution has witnessed the development of osteochondral scaffolds through decades from the simplest homogenous (monophasic) to heterogenous scaffolds including biphasic, triphasic and multiphasic ones. Recently, the gradient scaffolds in terms of composition and architecture have attracted thoughtfulness to replicate the natural heterogeneity seen in native osteochondral tissue.

2.5.1.1.1 Monophasic scaffolds

The single-phased osteochondral implants, the first investigated strategies consist of uniform material composition and structure. Though homogenous, the combinations of different natural and synthetic materials are used to get a well-blended single component and uniform structural designs are explored. The easy processing of scaffolds and seeding autologous chondrocytes in the top of the 3D scaffold to form a cell–scaffold construct for *in vivo* implantation outlines the concept of this architecture. There are several studies related to monophasic scaffold and its potential for osteochondral regeneration. Chen et.al fabricated two types of monophasic collagen-based scaffolds with radial and random orientation separately and measured the effects on *in vitro* MSCs migration and *in vivo* osteochondral defect regeneration. The radially oriented scaffolds with aligned channels horizontally and vertically performed better in both cell migration promotion and osteochondral defect healing results. (Chen et al., 2015) Another study involves preparation of tannic acid mediated dual peptide-functionalized monophasic scaffolds and presented the satisfactory biological performance in MSCs recruitment and simultaneous regeneration of cartilage and subchondral bone (Zhang et al., 2020). Bunpetch et

al. fabricated a silicon-based bioceramic (silicon-calcium-phosphate) monophasic scaffold with dual-lineage regeneration bioactivities for osteochondral defects (Bunpetch et al., 2019). For osteochondral applications, scaffolds can be fabricated from single component with a specific design. To fabricate reproducible and porous architectures, the two sides of the osteochondral construct with distinct structures and shapes can be fabricated via Fused deposition modelling (Hutmacher, 2001) (Cao et al., 2003).

Though many studies related to monophasic scaffolds showed satisfactory outcome in effective regeneration, the majority of these studies are far from the requirements to regenerate osteochondral lesions efficaciously.

2.5.1.1.2 Biphasic scaffolds

The natural heterogeneity of osteochondral tissues consisting of two different lineage specific cells with disparate biomechanical properties, necessitates the development of biphasic substitutes. Thus, led to the alternative strategy of designing bi-layered/biphasic structures resembling the stratified anatomical architecture to provide a favourable environment that guides cartilage regeneration on the upper phase and foster bone formation on the lower part. The cartilage phase should be more ductile and facilitates fluid uptake capability to ensure a cushion effect. Meanwhile, the bone-side layer should display higher stiffness with good affinity to the ceramic constituent of bone and encourage vascularization, especially for large defects. The two cells interact differently with the same material and structural design. Hence pore morphology and size along with the composition should be tuned independently, so that chondrocytes and osteoblasts may perform accordingly (Stewart and Kawcak, 2018)

The biphasic scaffolds can be from two independent layers or integrated bilayered scaffolds. In the former one, the two layers are independently fabricated and joined prior the implantation using a fibrin glue, sutures or press fitting. Here, both chondrogenic and osteogenic cells are cultivated in separate environmental conditions. A biphasic construct was fabricated by

Malafaya et.al, where the bone-layer was produced from chitosan–HA composite particles and the cartilage layer from chitosan alone. The two layers are glued using fibrin sealant (Malafaya et al., 2005). The main drawback is the lack of effective integration between the two layers. The second type of biphasic scaffolds are well integrated ones' prior to cell culture, fabricated through different strategies. Chang *et al.* developed biphasic scaffolds by soaking gelatin solution into one of the extremities of ceramic cubes derived from cancellous bone of calf femoral condyles. The gelatin is impregnated through diffusion upon soaking which was further crosslinked with glutaraldehyde to get the biphasic construct (Chang et al., 2004). Another strategy is based on using common materials for upper and lower layers and integrated via different techniques likes compression moulding or 3D printing technique (G. Chen et al., 2006). Zhu et al. developed sodium alginate (SA)/agarose composite hydrogel containing BMSCs and articular chondrocytes depicting cartilage phase while SA/bioglass hydrogel with BMSCs for subchondral bone regeneration. A stable integration in the stratified structure was provided by the SA phase through crosslinking. Hyaline cartilage and subchondral bone were observed to be stimulated simultaneously after the injection of the stratified scaffold into the rat model (Zhu et al., 2019). Liu et al. incorporated two stem cell differentiation inducers, kartogenin and alendronate, separately into the HA-based cartilage layer and the HAp-based bone layer which were bound by semi-immersion (Liu et al., 2020, p.). The MSCs in the biomimetic biphasic scaffold can differentiate into both chondrocytes and osteoblasts, promoted by the layer-specific release of the two drugs. However, in biphasic scaffolds the calcified cartilage, the natural chondral-osseous interface which is a primary determinant in maintaining the microenvironment of the two distinct tissues is ignored.

2.5.1.1.3 Triphasic and multiphasic scaffolds

Considering that the native osteochondral tissue consists of articular hyaline cartilage with three distinct zones having varying structures and compositions and a calcified interface,

significant advances have occurred in fabricating scaffolds that mimics the hierarchical organization of the osteochondral physiological structure. Thus, the strategy of triphasic scaffold has been employed in osteochondral tissue engineering. Tampieri et al. developed a trilayered scaffold based on HA, type I collagen and Hap consisting of upper cartilaginous layer made of hyaluronan charged collagen and the lower subchondral bone layer composed of the biom mineralized collagen (70 wt% Hap; nucleation of HAp nanocrystals onto the collagen fibers during their self-assembling), an intermediate region with the same biom mineralized collagen but a lower percentage of mineral (40 wt % HAp) was incorporated to resemble the calcified zone. The triphasic scaffold was later demonstrated to exhibit good mechanical and biological behaviour in treating the chondral and osteochondral lesions in horse and sheep models as well as clinical trials, which is now commercially available as MaioRegen® for clinical applications (Tampieri et al., 2008).

2.5.1.1.4 Multiphasic gradient and continuous gradient scaffolds

To translate the complicated natural paradigm in design pattern, multiphasic gradient scaffolds have been explored which are superior to monophasic and biphasic ones in regenerating osteochondral defects. The gradients can be achieved through varying chemical compositions and structural characteristics as in arrangement, distribution, dimension and orientation. A variety of techniques are adopted to incorporate multiphasic and continuous gradients into the cartilage and osteochondral scaffolds such as 3D printing especially extrusion printing and selective laser sintering, sequential layering of hydrogel solutions at partial gelation, microfluidic-based method, electrospinning etc. Chemical compositional gradients involve the changes in the fundamental materials and the encapsulated bioactive molecules. Du et.al studied on an acellular seven-layered gradient scaffold consisting of PCL and HAp microspheres prepared through selective laser sintering technique. The content of HAp increased from 0 to 30% from upper cartilage layer to lower bone part. The *in vitro* cellular

evaluation and *in vivo* implantation results verified its capability in tissue regeneration (Du et al., 2017). Guo et.al fabricated a bioinspired gradient silk protein-based composites coupled with biosilica selective peptide-R5 having three regions consisting of high, medium and low concentrations of the R5 peptide. The gradient composites exhibited continuous transitions, supported tunable mineralization and mechanical properties, and regulated osteogenic differentiation of human mesenchymal stem cells *in vitro* (Guo et al., 2017). Di Luca et al. 3D printed a multiphasic pore size gradient scaffold and evaluated the effect on the proliferation and differentiation of the seeded MSCs and the ECM deposition. An increased expression of chondrogenic markers and ECM deposition was observed upon decreasing the pore size in the gradient scaffold (Luca et al., 2016). Despite the difficulty in achieving continuous structural variations, the creation of those multiphasic structural gradient scaffolds offers another strategy to obtain an accurate mimicry of native tissues and also serves as a great tool for improving our understanding of the interactions between cells and biomaterials with different pore structures. The multiphasic gradient and continuous gradient scaffolds fabricated by emerging new technologies and traditional methods have been achieved both in chemical compositions and structural characteristics.

2.5.1.2 Choices for the fundamental material composition

A successful strategy in osteochondral tissue engineering embraces the design of the scaffold structure and the appropriate choice of biomaterials. Scaffolds play a crucial role and hence advances in biomaterials and fabrication techniques led to the development of biomimetic scaffolds. Large diversity of bioactive materials with unique characteristic are available and well-studied in the field of OCTE. In view of the components and structures of OC tissue, most of the materials used for its regeneration include natural and synthetic polymers, and the composites of several kinds of the aforesaid materials.

a. Natural polymers

Natural polymers are widely used in scaffold fabrication due to their inherent biomimetic properties and mimic the native environment of the tissue. Natural polymers sourced from polysaccharide (hyaluronic acid (HA), chondroitin sulfate, alginate, agarose, starch, chitosan and gellan gum), protein-based materials (collagen, glycosaminoglycan, gelatin and silk fibroin), polypeptides and poly(hydroxyalkanoates) have attained extensive explorations due to the structural similarity to the ECM and the subsequent biocompatibility, biodegradability and insignificant inflammatory response (Wei and Dai, 2021). Many natural polymers contain specific domains that send signals to guide cells at various developmental stages and facilitate the proliferation and differentiation of tissue specific as well as progenitor cells. However, they possess low stiffness, weak biomechanics, issues of antigenicity, processing difficulty and uncontrollable degradation time. HA being abundant GAGs in native cartilage, scaffolds based on HA reported to be beneficial one for cartilage and osteochondral regeneration upon modification (Yamanlar et al., 2011) through additional polymer networks or by chemically at the hydroxyl and carboxyl functional groups using methacrylate, thiol and amino acid (Chen et al., 2021). Chondroitin sulfate (CS) has greater role in fundamental, structural and biological processes like HA and thus many studies related to CS suggested improved mechanical and signaling properties in variety of composite materials for OCTE (Meghdadi et al., 2019). Similarly, alginate (Balakrishnan et al., 2014), chitosan (Suh and Matthew, 2000), agarose (Zarrintaj et al., 2018), and gellan gum (Zia et al., 2018) are all natural polysaccharides with similar structures to GAGs and thus have been extensively explored in OCTE. Collagen (Levingstone et al., 2016) and its derivative gelatin (Gao et al., 2019), and silk fibroin (Hong et al., 2020) due to its excellent resemblance to the native ECM and processibility, they can be used as reinforcing fibers and then incorporated into hydrogels to improve the mechanical strength. Concerning to its inferior mechanical strength and low bioactivity, these polymers are

usually blended with proven polymers for tuning its innate properties without comprising its known beneficial properties.

b. Synthetic polymers

Synthetic polymers are extensively used in osteochondral tissue engineering for their better processability, regulated mechanical properties, reproducibility over the molecular weight, controlled degradation kinetics and large-scale production. The most popular biodegradable synthetic polymers include poly (alpha-hydroxy acids), especially poly (lactic acid) (PLA), poly (glycolic acid) (PGA) and their co-polymers (PLGA), poly (ethylene glycol) (PEG), poly(ε-caprolactone), poly (propylene fumarate), poly(dioxanone), polyorthoesters, polycarbonates, polyanhydrides poly (vinyl alcohol) (PVA), poly (L-glutamic acid) and polyphosphazenes (Mano and Reis, 2007). The poly (D, L-lactic-co-glycolic acid)(Critchley et al., 2020) , poly (caprolactone) (Du et al., 2017; Woodruff and Hutmacher, 2010), poly (ethyleneglycol) (B. Sharma et al., 2013) and poly (glycolic acid) (Okamoto and John, 2013) are commonly used polymers for osteochondral regeneration. However, an immune response or toxicity with certain polymeric combinations, the weak bioactivity, complicated structural design and preparation processes led to blending natural and synthetic polymers to bring together the advantages of the two kinds of materials, offering more possibilities to produce superior scaffolds (Frassica and Grunlan, 2020) .

c. Bioceramics

Bioceramics are extensively used for the reconstruction of damaged bone tissues for their biocompatibility, excellent osteoconductivity, bioresorbability and mechanical strength. Both crystalline and amorphous inorganic biomaterials such as hydroxyapatite ($\text{Ca}_5(\text{PO}_4)_3(\text{OH})$), tricalcium phosphate (TCP, $\text{Ca}_3(\text{PO}_4)_2$), calcium silicate, calcium sulphate and amorphous bioactive glass (BG) are well explored (Ma et al., 2018; Vallet-Regi and Salinas, 2021). However, due to the poor elasticity and high stiffness, a mixture of natural or synthetic polymers /bioceramics have been widely reported over the years in promoting subchondral

bone regeneration and to improve their elasticity modulus. Zhou et al. developed a stratified biphasic scaffold consisting of collagen and collagen/HAp representing upper layer and lower layer respectively. The studies demonstrated that the lower collagen/ HAp layer promoted better osteogenic induction of seeded MSCs than the collagen layer or pure Hap (Zhou et al., 2011). β -TCP is widely acknowledged in bone tissue engineering because of its better structural, similar chemical composition, bioactivity, mechanical and biological performances. Hence β TCP is used in many studies related to the bone compartment in the osteochondral scaffold (Kosik-Kozioł et al., 2019). Calcium silicate is known for its osteogenic and angiogenic abilities and these beneficial properties are due to the released silicon ions. Chen et al. studied on lithium calcium silicate-based 3D printed osteochondral scaffold which exhibited good mechanical strength, biodegradability and favoured simultaneous regeneration of both cartilage and subchondral bone in rabbit osteochondral defects (Chen et al., 2019).

2.5.1.3 Different types of scaffolds in osteochondral tissue engineering

Structural and functional requirements are the most significant criteria to be met by OCTE scaffolds intended for clinical applications. Different types of scaffolds that have a structural and compositional resemblance to natural ECM are well studied for OCTE and include porous, fibrous, hydrogels, microspheres, metals and composites, and ECM-based matrices.

a. Porous Scaffolds

Porous scaffolds can guide the seeded cells to proliferate, infiltrate and direct further differentiation towards specific and diverse lineages through their interconnected pore networks. The different types of porous scaffolds include sponge, foam, mesh, microfibers and nanofibers, etc. The formation of extracellular matrix and further tissue formation is dependent on the suitable microenvironment like macro- and micropores that promote nutrient supply, stimulate effective cell-cell and cell-matrix communications, and crucial channels for blood vessel and nerve growth. The effects of pore size on the efficacy of in vivo osteochondral tissue repair are well studied (Duan et al., 2014).

b. Hydrogel Scaffolds

Natural and synthetic hydrogel scaffolds are widely used in OCTE due to their biocompatibility, biodegradability, and cell interaction. Also, the extracellular matrix of osteochondral tissue is gelatinous in nature with fibrous components and thus hydrogel provides the microenvironment for the adhesions of cells and further tissue repair. Decellularized ECM, collagen, chitosan, and hyaluronic acid are natural materials used in hydrogels, with acceptable biocompatibility, whereas synthetic polymers are easier to process and control (Naahidi et al., 2017).

c. Microsphere Scaffolds

Microspheres (MSs) are widely used in tissue engineering as it provides biomimetic structural support, improved mechanical strength and bioactivity, therapeutic effect and regulates cell metabolism. Hence MS showed promise for the development of osteochondral tissue engineering (He et al., 2020). The two types of MSs are well studied, including MS-leached scaffolds where MSs work as porogens to produce porous structure whereas, in the MS-incorporated scaffolds, these can modify the superior biological functions through biological regulation, controlled release of biomolecules and drugs, and cell delivery in vivo. A study on MS leached scaffolds reported better cell infiltration and tissue invasion. PLGA, chitosan and Hydroxyapatite, etc. can be used for preparing MS. A study based on bi-layered scaffold incorporating MSs loaded with TGF- β 1 and BMP-2 showed induced chondrogenic and osteogenic differentiation. This microsphere scaffold was reported to induce a high degree of tissue repair based on histological evidence (Reyes et al., 2014).

d. Composite Scaffolds

To incorporate the properties of two materials, polymers and ceramics are integrated to produce various scaffold fabrications. Ceramics have better mechanical stiffness and corrosion resistance but inherent features, such as fragility, inelasticity and difficult processing limit their applications. Bioceramics are categorized into bioinert materials (e.g., alumina and zirconia),

semi-inert surface reactive materials (e.g., bioactive glass and dense hydroxyapatite) and biodegradable materials (e.g., calcium phosphate and tricalcium phosphate) (Pina et al., 2018). Hence composite scaffolds based on polymers and ceramics provide enhanced mechanical and degradation properties. A bilayered scaffold with a gradient transition zone consisting of chitosan/hyaluronic acid (HA) based cartilage layer and chitosan/alginate/ hydroxyapatite nanorod (HAp) bone layers was fabricated via a thermally induced phase separation process. The seeded cells in both layers maintained excellent viability and differentiated into chondrogenic and osteogenic lineages, respectively. The bone-cartilage interface regulates the mechanical properties of the composite structure, enhances the integration and inhibits unexpected infiltration, and provides an independent microenvironment for differentiation.

2.5.1.4 Scaffold fabrication techniques

A variety of technologies have sprung up for fabricating 3D scaffolds in osteochondral tissue engineering research over the past few decades to improve scalability, sustainability and spatial control. These include traditional methods such as lyophilization, freeze-drying, gas foaming, sol-gel process, electrospinning, phase separation, solvent casting, compression molding and particulate leaching (Cheng et al., 2019).

With the development of manufacturing technologies, the electrospinning process has been applied to produce functional scaffolds with spatially complex properties in osteochondral tissue engineering. It is a simple and efficient method to produce fibers in nano or micrometer-scale from charged threads of polymer solutions or melts using an externally applied electric field. The thin jets from the capillary tube forms fibers and gets deposited sequentially towards a collector plate to create a scaffold. The technique creates scaffolds from composite materials with a large surface area for cell attachment. (Castaño et al., 2012). Many studies related to the fabrication of biphasic scaffolds via electrospinning were well explored that conveniently showed the ability to synergistically support the chondrogenic and osteogenic growth (Kim et

al., 2020; M et al., 2017). Considering the insufficient mechanical properties, poor cell infiltration of electrospun structure and less feasibility to incorporate bioactive molecules during scaffold fabrication due to the use of organic solvents, a variety of other methods for addressing these issues have been proposed.

The phase separation process can be induced thermally or by a nonsolvent method, where the latter results in scaffolds with heterogeneous pore structures which is not suitable for the fabrication of tissue engineering scaffolds, that generally need a uniform pore structure. Thermally-induced phase separation is a widely adopted procedure to fabricate porous scaffolds with uniform pore structures (Da et al., 2013) where the temperature change (cooled in a controlled manner) induces demixing of a homogeneous melt blend cast into the desired scaffold shape and separates into a polymer-rich and a polymer-less (solvent-rich) phase. Upon removal of solvent through extraction, evaporation, or sublimation producing a micro/nano porous scaffold. The de-mixing can be solid-liquid (usually for binary polymer-solvent mixtures), or liquid-liquid (usually for ternary polymer/solvent/non-solvent mixtures) (Akbarzadeh and Yousefi, 2014). As compared with electrospinning, phase separation has a great potential for the development of 3D nano/micrometer structures. The limitations include inadequate resolution and limited material choice.

With the advantage of environmental protection, freeze-drying is a suitable option to fabricate 3D scaffolds. Freeze-drying (Fereshteh, 2018) involves three major steps where it starts with the freezing of a polymer solution at a low temperature (-70°C to -80°C) and subsequent formation of solvent ice crystals surrounded by polymer aggregates. Through vacuum, the surrounding pressure is reduced to a level (to a few millibars) lower than the equilibrium vapor pressure of the frozen solvent (P_0). The solvent ice in the material then gets completely sublimated into the gas from the solid phase known as the primary drying process, producing a dry polymer scaffold with an interconnected porous structure. The unfrozen water

in the material is removed through desorption in a secondary drying process. Emulsification freeze-drying involves dissolving polymers/ceramics in a solvent and an emulsion is obtained when mixed with water. The mixture in a mold separates into two phases when frozen. Upon freeze-drying, the solvent and dispersed water are removed from the frozen emulsion, creating pores in a solidified scaffold. A bilayered gelatin/ β -tricalcium phosphate (GT) sponges were fabricated through freeze-drying technology (Seo et al., 2013) and these scaffolds showed more cartilage-like tissue with no adverse effects. However, fabricating scaffolds with hierarchical structures that mimic osteochondral tissue via freeze-drying is very difficult.

Sol-gel is a method that involves gentle reaction temperature, and it is suitable for scaffold fabrication. However, the small size and low porosity of scaffolds limit their application in osteochondral tissue areas (Balamurugan et al., 2007).

The process of solvent casting/particulate leaching is widely used in fabricating porous scaffolds where porogens are dispersed in a polymeric solution obtained by the dissolution of a polymer in an organic solvent. The polymeric mixture is poured into a moulded structure and when the solvent evaporates, the polymer gets hardened or set. Subsequently, the porogen which is often a salt such as sodium chloride is dissolved in water, resulting in the creation a hardened polymer scaffold with a porous network. The disadvantage includes difficulty to control pore shape and pore interconnectivity of scaffolds. Wu et al. evaluated the efficacy of bilayered silk scaffolds loaded with TGF- β 3/BMP-2 for osteochondral defect repair in rabbits aided by the solvent casting/particulate leaching technology (Wu et al., 2021). The lyophilized silk powder was first mixed with hexafluoroisopropanol (HFIP) solution with or without sucrose particles in a silicone mold. Then, 10% silk- HFIP solution was poured onto the mold and kept for crosslinking. The demolded scaffolds were treated with methanol (100% w/v) and running water to remove the HFIP and particles. After the process above, the top and bottom layers of scaffolds served as the cartilage and subchondral bone layers, respectively.

In gas foaming method, the use of solvents deployed in solvent casting/particulate leaching methods are eliminated. The methodology involves chemical foaming or mechanical foaming to generate gas where nucleation and growth of gas bubbles dispersed throughout a polymer creates a porous structure (Garg and Goyal, 2014). Solid discs of a scaffold material are created through compression moulding, followed by exposure to high pressure CO₂ gas (5.5 MPa) at room temperature. When CO₂ pressure is reduced to atmospheric levels (P₀CO₂), the solubility of the gas in the polymer rapidly decreases, causing CO₂ gas to clump together and subsequently creating pores. The technique can produce scaffolds with ~93% porosity and pore sizes of ~100 nm. The advantages are simple and inexpensive technique and the shape and density of scaffolds are controllable, whereas the disadvantages include low porosity, disconnected pores, difficult to control pore connectivity and poor mechanical property hinder their application in osteochondral tissue engineering. Reyes R et al. developed the PLGA based porous structure by gas foaming technique and studied the effects on inducing repair by TGF-β₁/BMP-2 loaded segmented polyurethane/poly(lactic-co-glycolic) (SPU/PLGA) scaffolds in osteochondral lesions (Reyes et al., 2014).

The complicated gradient heterogeneity of the native osteochondral tissue and inability to biologically mimic the original microstructure of cartilage and subchondral bone led to the low efficiency of traditional methods.

a. 3D printing

There is a growing need for developing patient-specific scaffolds that recapitulate the native mechanical strength, collagen architecture, surface contour, and morphology of the patient's native joint. Over time there has been an improvement in the ability to spatially control scaffold microarchitecture and content as newer technologies have emerged. To imitate the natural paradigm and translate such design motifs, 3D printing, state-of-the-art technology was

adopted to fabricate biological constructs with hierarchical architecture similar to the anisotropic nature of osteochondral tissue (Do et al., 2015).

The printing process allows proper positioning of biomaterials, patterning heterogeneous cells in high densities and distribution of signaling factors, through an automated dispensing system to form tissue engineering constructs. This ensures the cells are held together with uniform cell distribution and better cell-cell communication when dispensed in biocompatible materials to form desired 3D functional structures.

The structure of a 3D printed object depends on the model created by a computer-aided design (CAD), which describes 3D objects in a series of cross-sectional layers. The models are physically reproduced through an additive process when CAD models are fed into a 3D printer. CAD models of the patient defect data are created from the data obtained through computed tomography (CT) or magnetic resonance imaging (MRI), which are converted into STL formats and further sliced using specific software into G-code and fed into a 3D printer. The G-code encodes 3D CAD models in a format that can control 3D printers where layer-by-layer processing of powder, liquid or solid material substrates and each newly formed layer is adhered to the previous layer, resulting in the creation of a construct of gradually increasing size. The printing parameters such as print speed, layer height, print head temperature and pressure can all be modified and optimised through G-code (Murphy and Atala, 2014).

The technology is categorized as scaffold-based printing and scaffold-free printing. Scaffold-based printing is further classified into cellular and acellular 3D printing, depending on whether the ink contains living cells or not. Besides, cellular 3D printing can be extrusion-based printing, laser-based printing, droplet-based printing and stereolithography, and acellular 3D printing can be divided into fused deposition modelling, melt electrospinning writing and selective laser sintering (Daly et al., 2017). The 3D printed scaffolds have shown the potential

in the regeneration of osteochondral defects by generating both cartilage and subchondral bone tissues in the defect regions (Du et al., 2017).

The first 3D printer was based on the technology of inkjet printer and known as binder jetting or drop-on-powder. The printing process uses a liquid binder solution dispensed through the printer nozzle in the designated powdered bed areas directed by the CAD. The excess powder is removed after the binder solution and powder are selectively combined. The new powder layers are deposited by lowering the build platform (Saunders and Derby, 2014). In Stereolithography (SLA), a solidified 3D object is fabricated via layer-by-layer photo polymerization of liquid UV curable resin using a laser which solidify the model's cross-section as per CAD design, allowing rapid fabrication of a 3D object with controlled architecture and micrometre-level resolution. Zhou X et.al. fabricated and studied the potential of 3D-printed scaffold with biomimetic biphasic structure for improved osteochondral regeneration (Zhou et al., 2019). Fused deposition modelling (FDM) technique is used to fabricate 3D structures by layer-by-layer deposition of thermoplastic filament material of appropriate diameter onto a platform using a temperature controlled printhead. Polymers like polycaprolactone are frequently printed for various application via FDM. In BTE, FDM is an extensively used method for fabricating synthetic scaffolds, but the high temperatures restrict the incorporation of growth factors and biomolecules (C. Wang et al., 2020). In Selective laser sintering (SLS), a computer-controlled laser beam is used to sinter the powder material together which is printed sequentially in a layer-by-layer pattern as per the design. But the elevated temperature is a major drawback for the cells and biomolecules (Kamboj et al., 2020, p.).

The 3D bioprinting uses biomaterials, cells (encapsulated or seeded), and biomolecules, typically referred to as a bioink, which are precisely deposited in a layer-by-layer process to build-up a 3D structure. The ability to print multiple cells and biocompatible materials with greater design freedom compared with conventional fabrication techniques has enabled the

development of 3D structures that resemble the complex 3D biophysical and biochemical environment in tissues. The use of 3D bioprinting within osteochondral tissue engineering is becoming widespread as an enabler technology to fabricate complex multimaterial structures that mimic the biological and mechanical properties of tissue. Printing resolution, structure fidelity, material viscoelasticity are crucial parameters in determining the printability of bioinks and its relationship to the final mechanical and biological properties of the structure.

Based on the working principle, 3D bioprinting strategies are categorized namely inkjet-based bioprinting, laser-assisted bioprinting (LAB), pressure-assisted (extrusion) based bioprinting, acoustic bioprinting, stereolithography (SLA)-based bioprinting, and magnetic bioprinting. In inkjet bioprinting, picolitre volume (1-100 pL) droplets of bioink holding 10^4 - 30^4 cells per droplet, are deposited on a substrate under computer control (Boland et al., 2006). Laser-assisted bioprinting (LAB) systems print bioinks comprising of cells or molecules in liquid or gel solution over the initial print material known as ribbon assembly. The incident pulsed laser beam of 5 kHz produces a high-pressure bubble, which propels the bioink droplets (cell-containing materials) from the ribbon toward a collector substrate (Matai et al., 2020). Keriquel et al. used LAB to 3D print mesenchymal stromal cells incorporated with collagen and nano-hydroxyapatite, onto a mouse cranial defect to aid bone regeneration (Keriquel et al., 2017). The heat-induced potential damage to cells, high system costs and the time-consuming procedure are concerning demerits. Extrusion bioprinters deposit continuous filaments of materials, where highly viscous bioinks placed in plastic syringes are dispensed through a nozzle pneumatically or mechanically (piston or rotating screw) onto sterile substrates. The printed filaments are then cross-linked by light (mostly UV), enzymes, chemicals, or heat to form mechanically durable structures (Ning and Chen, 2017). Acoustic bioprinting uses surface acoustic wave technology to fabricate intricate 3D structures by depositing cell encapsulated picolitre droplets from an open-pool of bioink in the presence of a gentle acoustic field (Guo

et al., 2016). Stereolithography (SLA) bioprinting is a light-assisted direct printing method, where light-sensitive bioinks are cured plane-by-plane to build-up materials with micro/nano architecture (Chan et al., 2010). In microvalve bioprinting (Ng et al., 2017), fluids under a constant pneumatic pressure are dispensed from cartridge tips by opening and closing a small valve which is controlled mechanically, electrically or magnetically. This droplet-based system can print cells including MSCs with high viability and functionality, with biomaterials like collagen and bone morphogenic protein.

2.5.2 Other key elements in osteochondral tissue engineering

2.5.2.1 Tissue forming cells

For successful regeneration of desired tissues that mimics the complex heterogeneities with respect to anatomical and biological properties, the cells and growth factors are equally important components for osteochondral tissue engineering strategies. The dual tissue consisting of cartilage and bone has entirely different properties despite deriving from common progenitor cells. The appropriate choice of an adequate cell source is critical in any TE strategy as the incorporated cells are generally considered to improve the ECM deposition and eventual tissue regeneration. The adequacy in source, ease of manipulation and safety in implantation makes the chosen cells an ideal candidate for tissue engineering purposes. These include, those existed in the host tissue such as chondrocytes, chondroprogenitor cells and osteoblasts, and multipotent stem cells like BMSCs, adipose stem cells (ASCs) and pluripotent embryonic stem cells (ESCs) and induced pluripotent stem cells (iPSCs) (Fu et al., 2022).

Tissue-specific cells and progenitor cells (stem cells from various sources) are two commonly recommended cell types for osteochondral defect repair. The most direct cell source is obtained from the isolation of mature cells (osteoblasts and chondrocytes) through biopsies taken from the patients, followed by an expansion *in vitro*. Chondrocytes, being the predominant cells in articular cartilage, are the widely used cell types in restoring

osteocondral defects. Numerous OCTE studies are based on tissue-specific cells, i.e. chondrocytes embedded in a variety of biomaterials that could produce more functional cartilaginous tissue formation and high integration into the surrounding matrix. To mimic the dual environment, chondrocytes in the cartilage layer were used in combination with preosteoblasts in the subchondral layer for osteochondral defect repair (Korpayev et al., 2020). Nevertheless, chondrocytes are faced with several notable challenges like limited quantity in the native tissue leading to low isolation efficiency, reduced proliferation potential and dedifferentiation phenomenon during culture and expansion. Osteoblast cells are widely used for the subchondral bone part, where osteoblast-derived VEGF promotes bone repair and homeostasis (Hu and Olsen, 2016).

The use of stem cells is a promising solution to circumvent the drawbacks related with tissue-specific cells. The progenitor cells commonly used are

1) bone marrow derived Mesenchymal stem cells (BM-MSCs), the most widely studied ones in osteochondral tissue engineering due to their advantages like rapid proliferation, multipotency, the secretory, immunomodulatory functions (MSC) and better tissue survival *in vivo* (Lee and Kang, 2020). But, the procedure is highly invasive and the frequency, proliferation efficiency and differentiation potential decline with age. Diverse biomaterials encapsulated with MSCs are broadly studied and Zhou et al. investigated the proliferation and differentiation of BMSCs into chondrocytes and osteoblasts on two distinct layers of a collagen-HAp biphasic scaffold in the presence of chondrogenic and osteogenic chemical factors (Zhou et al., 2011). The chondrogenesis and hypertrophy of MSCs are material-dependent, and the induced lineages can also be inspired by the scaffold's architecture, that has different pore sizes, interconnectivities, and metabolic environments. Co-culture of MSCs and chondrocytes in tissue engineering scaffolds has also been explored to enhance the cartilage

regeneration, when the chondrogenic phenotype of chondrocytes can be maintained and the chondrogenic differentiation of BMSCs can be promoted (Zhu et al., 2019).

2) Umbilical cord derived mesenchymal stem cells (UC-MSCs), possess many merits including unlimited supply, noninvasive procurement and high purity with faster proliferation rates, greater expansion capability, broad multipotency and negligible immune response. They are more primitive and express both MSC and ESC markers (Marmotti et al., 2017)

3) Adipose -tissue derived MSCs (AT-MSCs) from lipoaspirates possess higher proliferation potential and larger abundance than BMSCs and have showed the ability of both chondrogenesis and osteogenesis in a variety of biomaterial environments. However, their chondrogenic potential is relatively lower than BMSCs and the cell differentiation is greatly dependent on the optimal culture system and scaffold architectures (Nour-Eldeen et al., 2020)

4) Synovium-derived MSCs presented better proliferation and chondrogenic differentiation performance (Sasaki et al., 2018) than BM-MSCs and AT-MSCs, but a less osteogenic capability than BM-MSCs. Also, these cells favoured enhanced ECM deposition and inhibited hypertrophy of chondrocytes (H. Li et al., 2016).

5) Amniotic fluid-derived stem cells (AFSCs), can be a promising alternative for the reconstruction of articular cartilage when associated with scaffolds owing to their multipotentiality and plasticity (Zuliani et al., 2021).

6) Urine-derived stem cells (USCs) are recently reported cell types with osteogenic and chondrogenic potentials. The simple isolation procedure and culture methods along with non-invasive, easy obtainment, low-cost and high efficiency makes these cell types as a candidate for seed cells in tissue engineering (Zhang et al., 2021).

Upon chondrogenic stimulation, MSCs showed greater tendency towards hypertrophy leading to calcified cartilage, which has prompted researchers to study into pluripotent embryonic stem cells (ESCs) and induced pluripotent stem cells (iPSCs) for osteochondral

repair. ESCs have the potential to offer unlimited number of chondrogenic cells. But lack of control in the lineage-specific differentiation along with immune rejection and ethical issues have limited their extensive utility (Wei and Dai, 2021). Hence, iPSCs isolated from somatic cells such as fibroblasts provided greater promise in regenerative medicine because of the similar capabilities of chondrogenic and osteogenic differentiation like MSCs for restoring cartilage and bone defect both *in vitro* and *in vivo*. Ko et al. investigated the chondrogenic differences between iPSCs and BMSCs and discovered that chondro-induced iPSCs had higher GAG contents and better chondrocytic features *in vitro* than chondro-induced BMSCs (Ko et al., 2014).. However, many hurdles still need to be overcome including protocols of isolation, differentiation and purification and the potential tissue malformations *in vivo*.

2.5.2.2 Biochemical signaling factors

Natural growth factors (transforming growth factor (TGF)- β , bone morphogenetic proteins (BMPs), and small synthetic molecules (dexamethasone (DEX) and kartogenin (KGN)) can provide an appropriate microenvironment for osteochondral tissue ingrowth. Besides the embedded tissue forming cells, the right choice of biochemical signalling factors is critical. They can mediate growth, proliferation, and differentiation by activating specific pathways and increasing the expression of specific proteins.

TGF- β upon binding to its membrane-bound receptors type I and type II receptors, can initiate the cell signaling and further affects the cell behaviors (Travis and Sheppard, 2014). Bone consists of abundant TGF- β and bind to the TGF- β receptors present on the surface of osteoblasts in high concentration. The three isoforms of TGF- β plays an important role in chondrocyte maturation and endochondral ossification by regulating the expression of transcription factors Sox-9 and Runx2. The different zones of the osteochondral unit and during different growth phases, the expression of TGF- β 1, 2 and 3 varies. They promote the synthesis of proteoglycans and type II collagen in chondrocytes. The chondrogenic and osteogenic

differentiation of MSCs depends on the dosage of TGF- β 1. Also, TGF- β 2 and TGF- β 3 are extensively used to induce the chondrogenic differentiation of stem cells and production of aggrecan and type II collagen (Guo et al., 2010).

BMPs are involved in cartilage and bone formation during skeletal morphogenesis, hence these are effective tissue engineering growth factors for cartilage and bone regeneration (Bessa et al., 2008). BMP-2, 3, 4, 6, 7 and 9 are the most extensively studied ones. The endogenous BMPs are involved in protecting the cartilage from damage and activate the regenerative processes. BMP-2 are either used alone or combined with other growth factors for the differentiation of MSCs towards chondrogenic and osteogenic lineage. BMP-4 has major role in bone formation but also promotes the chondrogenesis of stem cells and the regeneration of hyaline cartilage(Deng et al., 2018) .

The common routes of administration of growth factors are direct injection and systemic administration. However, due to short half-life in blood circulation, scaffolds that can control growth factors release in a sustained fashion facilitate formation of osteochondral tissue. But challenges faced includes burst release, difficulty in storage and easy inactivation.

Clinically, dexamethasone (DEX), is a widely used synthetic glucocorticoid to treat inflammatory diseases and for osteoarthritis. Several studies suggested its potential for growth-factor-induced differentiation of stem cells towards chondrogenic and osteogenic lineages in vitro in a dose dependent manner. The activity of the molecule in deciding the differentiation lineage of MSCs depends on the dose and exposure stage during differentiation (Florine et al., 2013). Also, when used in combination with growth factor such as TGF- β and BMPs, DEX showed very positive results depending on tissue origin of MSCs and the culturing microenvironment.

Kartogenin (KGN) a small molecular synthetic compound, which showed enhanced repair of damaged cartilage and osteochondral defect regeneration. The studies showed a dose-

dependent stimulation of the lineage-specific differentiation of MSCs to chondrocytes. Also, this organic molecule could protect the articular chondrocytes when used as direct intra-articular injection for osteoarthritis. These are used in diverse strategies includes incorporation in particle or thermogel drug delivery systems, and encapsulation in cartilage and osteochondral tissue engineering scaffolds (X. Li et al., 2016).

2.5.2.3 Physiochemical and physical signaling factors

The biological processes involved in osteochondral regeneration involves physiochemical (oxygen tension, pH and carbon dioxide concentration) and physical factors (temperature, mechanical cues etc).

The varying oxygen tension from superficial (~7%) to deep zone (~1 %) within articular cartilage are mediated by hypoxia-inducible factors which is known to have significant effects on development of cartilage. Hence, the hypoxic condition is commonly used in combination with scaffold and/or biochemical signaling factors to induce the chondrogenic differentiation of stem cells and matrix synthesis by chondrocytes (Meretoja et al., 2013).

The physiochemical stimuli and the biomechanical cues required for the repair and restoration of damaged osteochondral tissues can be provided by the environmental culturing system in the bioreactors. The types of bioreactors mimicking the biomechanical characteristics of articular cartilage includes stir, perfusion, rotating wall vessel, stretch, compression, hydrostatic pressure and combined ones, *etc* (Darling and Athanasiou, 2003). Based on the media which transmit the forces, mechanical cues can be categorized as those mediated through liquid (hydrostatic pressure, fluid shear stress), solid (compression and its combination with shear stress) and other noncontact media (electromagnetic field, microgravity, ultrasound, *etc.*) (Du et al., 2019).

2.6 Tissue engineered articular cartilage products

A plethora of research published in osteochondral tissue engineering, but one of the most important issues faced is the inability to move technologies into the clinic.

BioCartilage®, Cartiform® and CarGel™ are augmentation strategies to restore the damaged cartilage and are based on decellularized ECM/ allograft/mixed with patients' whole blood. TruFit™ from Smith & Nephew is a synthetic resorbable biphasic implant to treat osteochondral lesions. Though the reports suggest favorable one-year outcomes, the pain and knee swelling and repeated surgeries could be the reason for the nonavailability of the product (Bekkers et al., 2013). MaioRegen™ (Tampieri et al., 2008) is a three-layer multiphasic gradient composite scaffold that mimics native osteochondral structures. In randomized controlled clinical trial, it showed complete defect filling of both bone and cartilage as well as a good integration with the border. But the regenerated cartilage tissue had a limited quality, showing slight hypertrophy and fibrous-like cartilage in a prospective study (Kon et al., 2011). ChondroMimetic® is a collagen, GAGs and calcium phosphate biphasic scaffold, demonstrated significant improvement in the clinical symptoms as well as function and activity level of the knee joint (Getgood et al., 2012). Agili-C™ is a biphasic scaffold from CartiHeal consisting coralline aragonite representing the subchondral bone phase, HA impregnated aragonite for the cartilage phase (Matta et al., 2019). The porous and resorbable scaffold revealed its ability to stimulate the regeneration of hyaline cartilage and deposition of cartilage ECM and help the patient return to sports.

BioCart™ II marketed by Histogenics, is a fibrinogen/hyaluronic acid scaffold seeded with expanded autologous chondrocytes. A Phase I trial (n=8) demonstrated the feasibility of BioCart™ II for treating femoral lesions and osteochondritis dissecans. Phase II trial results have not yet been published (Nehrer et al., 2008). Cartipatch® is an agarose-alginate hydrogel seeded with expanded autologous chondrocytes. A prospective multi-center study showed

positives results and because the operation involved removal of subchondral bone, the hydrogel was used mainly to treat osteochondritis dissecans (Selmi et al., 2008). Chondrospheres® (ACT3D-CS or ARTHROCELL 3D®) are neocartilage based on autologous chondrocytes derived small spheroids and their associated matrix. At a 2-year follow-up, Chondrosphere ® treatment was reported to improve range of motion, pain levels, excellent integration, and a smooth repair tissue surface (Schubert et al., 2009). Hyalograft® C marketed by Anika Therapeutics is an autologous chondrocytes seeded hyaluronic acid-based scaffold (Marcacci et al., 2007). The treatment showed improved patient evaluation scores. Scaffold degradation happened within ten months in majority of patients. Commercialization was stopped in 2013.

ACI-Maix™ by Matricel, a bilayer structured type I/III collagen membrane derived from decellularized porcine peritoneal tissue that consists of collagen and elastin. These are seeded with autologous chondrocytes and used for matrix-induced autologous chondrocyte implantation (MACI) technique (Edwards et al., 2013). The scaffold possess a porous side which faces the defect bed to allow cell infiltration and a non-porous side for cell retention. The implantation studies revealed redifferentiation, such as rounded cell morphologies and increased collagen II and aggrecan. NOVOCART® 3D by TETEC consists of a biphasic type I collagen scaffold seeded with autologous chondrocytes. The bilayer scaffold contains dense, cell-impermeable membrane on one side derived from bovine pericardium (Zak et al., 2014). The two layers are firmly connected by lyophilizing the membrane with a collagen sponge layer consisting of type I collagen and chondroitin sulfate with pores 130-200 μm in diameter.

RevaFlex™/DeNovo® ET from Isto Technologies, St. Louis, MO is a scaffold-free neocartilage disc composed of allogeneic juvenile chondrocytes and their associated matrix. (Adkisson et al., 2010). CaReS® marketed by Arthro Kinetics Biotechnology consists of a type I collagen hydrogel embedded with primary autologous chondrocytes (Schneider et al., 2011).

CHAPTER 3

3 MATERIALS AND METHODOLOGY

3.1 Materials

The common reagents and chemicals used for the study are described below.

All reagents were used without further purification. Poly (ϵ -caprolactone) (PCL) (Cat No: 440744, average M_n 80,000) pellets, Gelatin Type A from porcine skin, Bloom 300, Calcium Sulphate, Poly (D, L-lactide-co-glycolide) (PLGA) lactide: glycolide 75:25, (Cat No: P1941, Mol wt.: 66,000-107,000), β -tri-Calcium phosphate (β TCP), puriss. p.a., \geq 98% β -phase basis (sintered Powder) (Cat No 13204), Chondroitin 4-sulfate sodium salt, from the bovine trachea (Cat No: C9819), β Glycero phosphate disodium salt hydrate (Cat No: G9422), Bicinchoninic acid (BCA) reagents (Cat Numbers C2284 AND B9643), Alkaline Phosphatase Yellow (p-nitro phenol phosphate) liquid substrate (Cat No: P7998), Dexamethasone (D4902), Dimethyl sulphoxide (D8418), Methanol (179337), Ethanol (1.00983.0511), 2-PhosphoL-Ascorbic acid (49752), L-Cysteine (C7477), Methyl thiazolyl diphenyl-tetrazolium bromide (MTT, M5655) L-Proline (P5607) and 1,9-Dimethylmethylene blue zinc chloride double salt (DMMB) assay kit (341088) were purchased from Sigma-Aldrich Merck, St.Louis, Missouri, United States. 1,4 dioxane (Mw of 119.38 g/mol), acetic acid, and ethyl acetate (Merck, India), whereas Type II collagenase (Cat# 17101-015, 230 U/mg), Fetal Bovine Serum (FBS) (10270-106), Dulbecco's modified Eagle's medium (DMEM-High Glucose, 12800017), antibiotic-antimycotic (100X, 15240062), Non-essential amino acids (NEAA, 100X, 11140-050), Trypsin-EDTA, 0.25% (25200072), DAPI (Di amidimo-2-phenylindole, D1306), Dulbecco's phosphate-buffered saline (21600010), sodium pyruvate (11360070), L-glutamine (25030081), DNazol Reagent (10503027), LIVE/DEADTM Viability/ Cytotoxicity Kit (L3224) and High-Capacity cDNA Reverse Transcription Kit (4368814) were purchased from Thermo Fisher Scientific, USA. Insulin-Transferrin-Selenium (ITS-G, 41400045), Bone morphogenic protein (BMP) -2. Papain (RM058) was purchased from HIMEDIA Laboratories, India; Sircol

Collagen Assay kit (Biocolor systems); Transforming Growth Factor β 3 (009-001-W27) was obtained from Rockland, USA; RNAiso Plus (Cat No: 9108) from Takara Bio Inc, Japan; and Takyon No Rox SYBR Master Mix dTTP Blue (UF-NSMT-B0710) was purchased from Eurogentec, Belgium. Antibodies: Endoglin/CD105 antibody (P3D1, sc-18838, Santa Cruz), CD90/Thy-1 antibody (202501, Biolegend), Anti-CD73 antibody (ab175396, Abcam), CD45 antibody (120401, Biolegend), and CD34 antibody (151602, Biolegend). Power up TM SYBR TM Green master mix (Applied Biosystems TM, A25742), Formaldehyde (Sigma Aldrich, St.Louis, USA) was used for fixing cells before analyzing samples for immunostaining.

3.2 Development of biphasic scaffolds (BPS) mimicking osteochondral architecture

3.2.1 System A – BPS fabricated via Combinatorial approach

3.2.1.1 Fabrication of biphasic scaffold

The fabrication methodology involves 3D printing of directional cartilage phase whereas bone phase by freeze-drying technique represented as 3D Printed PCL/Gelatin (3DPG) and freeze-dried PCL/CaSO₄ (P/C) respectively. The two phases are further glued together to get the osteochondro mimetic biphasic scaffold. In the first step, fabrication of the cartilage phase via 3D printing was done after optimizing the solution concentration (PCL/Gelatin solution) and printing parameters like needle gauge size, infill density, nozzle diameter, feed rate, flow rate, layer height, and speed of the printer. The 123D design, a 3D-printing model creating tool by Autodesk, was used to create customized models. The created designs were then exported in STL format and fed to a 3D printer (Maker City, India) for fabricating the scaffolds. To get a gradient scaffold with desired porosity and thickness, different concentrations of PCL/Gelatin solution were tried and finally, a turbid solution containing PCL and Gelatin in the ratio 79:21 was selected and used to develop the cartilage phase at room temperature (25°C), using a nozzle tip with an inner diameter of 0.33mm. Briefly, a solution of 40 weight percent of PCL and Gelatin was prepared in ethyl acetate: acetic acid solvent system with continuous stirring using

a magnetic stirrer for 4hrs at a temperature of 40°C. Adequately blended PCL/Gelatin solution taken in a 10 ml syringe was extruded through a 23 gauge needle via 3D plotting, to produce strands of filaments. These stands were dispensed layer by layer, with a Z-axis interlayer increment of 150µm. The movement of the nozzle along the X, Y, and Z-axis were controlled using a Repetier Host software and the nozzle speed was set at 10 mm/s to ensure the layer height (150 µm) and to enable the immediate partial solidification of the PCL-Gelatin blend in a rectilinear pattern. The first 10 layers of the scaffold were printed with 40 % infill density, whereas the following 15 layers were printed at 30%, and the final 10 layers at 20% infill density. Once the stereoscopic 3D scaffolds of designed height were obtained, they were air-dried for 48 hours. to eliminate any residual solvents. The printed scaffold sheets measuring 50 × 50 × 2 mm (width x breadth x height) were then punched into circular discs of 8mm diameter using cylindrical disc cutters. All scaffolds were then disinfected with 70 % ethanol for 30 minutes, followed by additional 30-minute sterilization under UV light. All the scaffolds were rinsed twice with sterile 1X DPBS before further use.

Secondly, fabrication of the bone zone/calcified phase by the freeze-drying process was done. To fabricate PCL polymer scaffolds and CaSO₄/PCL composite scaffolds, a homogeneous solution of 10-weight percentage PCL was prepared in 1,4 Dioxane with continuous stirring for 6 hours at 45°C in a water bath. Exactly, 0.5 g of Calcium sulfate was dispersed onto the polymer matrix and vigorously stirred using a homogenizer for overnight to produce 5% CaSO₄ in a 10% w/v CaSO₄/PCL composite scaffold. PCL and CaSO₄/PCL solution were then immediately poured into precooled polypropylene vials and frozen at -80°C for 24 hours to solidify the solution. The frozen solution was lyophilized at -70°C for 8 hours to remove the solvent. The obtained scaffold samples were of dimension 0.8 cm x 10 cm (diameter X height). The scaffolds of desired height were cut from each lyophilized segment,

ETO sterilized, and rinsed twice with 1X DPBS before further use. Scaffolds of dimensions 8mm in diameter and 3mm in height were used for characterization and analysis.

Finally, these two phases are glued together by using a medical-grade sealant - Tissel, a fibrin glue to get the osteochondro-mimetic constructs. It was then air-dried for 48 hours to ensure effective sealing. This is followed by sterilization of biphasic scaffolds with 70% ethanol and UV irradiation. Constructs of dimension 8mm diameter x 4mm height (height of the chondral layer is 1mm and that of the bone layer is 3mm) were used for further studies.

3.2.1.2 Characterization of biphasic scaffold

3.2.1.2.1 Analysis of morphological features

The morphology and pore size of fabricated scaffolds (freeze-dried PCL alone, PCL/CaSO₄, 3D printed PCL, 3D printed PCL/Gelatin) were characterized using a Scanning Electron Microscopy (SEM) (Hitachi S 2400 (Japan)). Scaffolds were cut into 1cm (D) x 2 mm (H) pieces and were coated sputter-coated with gold using JEOLJFC 1600 for 2 minutes at 10 mA before imaging.

3.2.1.2.2 Analysis of wettability features

Static water contact angles of the scaffolds (PCL alone, PCL/CaSO₄, PCL/Gelatin) were measured using the sessile drop technique at room temperature. The images of the contact angle of water droplet on scaffold surface were visualized through the video-based contact angle (OCA15 plus, Optical Contact Angle System; Data Physics, Germany). An average of six measurements at six different sites on the scaffolds was taken and reported.

3.2.1.2.3 Analysis of chemical features

FTIR spectra of four groups of scaffolds (freeze-dried PCL alone, PCL/CaSO₄, 3D printed PCL alone, PCL/Gelatin) were characterized using an ATR-FTIR spectrometer (Alpha II, Bruker, Germany). The IR spectra of the scaffolds were then analyzed in the range of 400- 4000 cm⁻¹.

3.2.1.2.4 Analysis of thermal features

Thermogravimetric analysis (TGA) and derivative thermogravimetry (DTG) (TG/DTG) of the samples, (3D printed PCL, 3D printed PCL/Gelatin, freeze-dried PCL, freeze-dried PCL/CaSO₄) were analyzed by using SDT Q600, simultaneous DTA-TGA Analyzer (TGA). The temperature calibration was performed using alumina as reference material. The samples (4–7 mg) were placed in the pan and were run in the temperature range of 25 °C – 600 °C (for TG) at a rate of 10 °C/min under nitrogen purge (30 ml/min). From TG/DTG, the thermal stability of the composite material and compositional analysis can be done.

3.2.1.2.5 Analysis of mechanical features

The compressive mechanical properties of four groups of cylindrical samples (3D printed PCL, 3D printed PCL/Gelatin, freeze-dried PCL, freeze-dried PCL/CaSO₄), of dimension 16 mm X 8 mm (height X diameter) were determined using an Instron mechanical tester (Instron 5848, USA). The samples were wet in PBS for 24 hours before the compressive mechanical properties were evaluated. All samples (n=6 for each group) were compressed with a 2.0 kN load cell and at a crosshead speed of 1 mm/min with a pre-load of approximately 0.05N until the machine protection distance was reached. The analyses were performed at room temperature, providing the same conditions for each measurement. The compressive modulus was determined from the slope of linear region of stress-strain curve before failure.

3.2.1.2.6 Analysis of degradation features

In vitro degradation studies for four groups of scaffolds (freeze-dried PCL alone, PCL/CaSO₄, 3D-printed PCL alone, PCL/Gelatin) of dimension 10 (D) X 2 (H) mm were performed in triplicate, by immersing specimens in Phosphate buffered saline (1X DPBS, pH 7.4) at 37° C with shaking for 3 months. At the end of time points, the scaffolds were removed, rinsed thoroughly with deionized water, kept in a blotting paper for 5 minutes, and weighed on an

electronic balance for evaluating the wet weight change. After equilibrium in PBS, all scaffolds were weighed and recorded as W_0 . At various intervals, scaffolds were recovered and weighed (W_t). The degradation rate of scaffolds was calculated using the equation: Degradation ratio = $(W_0 - W_t)/W_0 \times 100\%$. The degradation pattern was observed by SEM analysis.

3.2.1.2.7 Assessment of *in vitro* bioactivity

To investigate the apatite mineralization ability of the bone phase of BPS *invitro*, stimulated body fluids were prepared according to previous methods (Oyane et al., 2003). The scaffolds (PCL alone and PCL/CaSO₄, n=3) were soaked in 10 ml 1X SBF at 37°C, refreshed after soaking for 1, 3, 7, 10, 14, and 28 days respectively. The scaffolds were collected from SBF solution after soaking for 14 days, rinsed with distilled water thrice, dried at 60°C overnight and the bioactivity was assessed by the standard protocol equation. Weight retained = $(W_t - W_i) / W_i \times 100$ where W_t is the weight of the scaffold after an incubation period in SBF and W_i is the initial weight of the sample after saturation in SBF. The apatite formation on the surfaces of scaffolds was observed by SEM and EDS.

3.2.1.2.8 Assessment of *in vitro* cytocompatibility

Scaffolds of dimension 0.8 cm (D) X 2 mm (H) were sterilized in a 70% ethanol aqueous solution for 2hr, dried under a sterile biosafety cabinet for 2 hours, followed by overnight UV sterilization, extensively washed with phosphate-buffered saline (PBS) to remove residual ethanol and then rinsed with complete medium (CM). Scaffolds were then incubated in CM at 5% CO₂ until cell seeding.

For cell viability studies, the scaffolds (n=3 for each phase) were seeded with 40 μ L of L929 cell solution (0.5×10^6 cells/scaffold) and were assessed using the LIVE/DEAD Viability kit for mammalian cells (Invitrogen Life Technologies, USA), according to the manufacturer's instructions. Before adding 1ml of fresh medium to the cell-seeded scaffolds, they were

incubated for 2 hours to allow for initial cell attachment. The culture medium was changed every 2 to 3 days. The cells/scaffolds composites were washed twice in PBS and incubated with 100µl PBS containing 4 µM ethidium homodimer-1 and 2 mM calcein-AM for 5 min at ambient temperature in the dark. The scaffolds were rinsed twice in PBS and the distribution pattern of the Live/Dead stained cells on the scaffolds was visualized under a confocal laser (Olympus IX 81, Japan)/fluorescence microscope (Olympus 1X 71) with 494 nm (green, Calcein) and 528 nm (red, EthD-1) excitation filters the image stacking software /confocal microscopy. The living cells were stained green, and the dead cells as red. Non-seeded scaffolds were also stained as blank control to avoid background effect.

MTT assay was performed to assess the cytocompatibility of developed scaffolds. The L929 cells were seeded (3×10^3 cells/well) in triplicates in a 96-well plate for cell attachment. The media was removed and replaced with scaffold leaching solution (experimental group; leachate was collected after the scaffolds were immersed for 24 and 48 hr in DMEM, or DMEM alone (negative control), or with DMSO (positive control; 5% in media) to the cultures 24 hours post cell seeding. The DMEM+10%FBS was added to the cultures only during the initial 24 hours for achieving proper cell attachment, which was removed by washing with 1XDPBS. After 1, 2, and 3 days of incubation with respective groups, 10 µL of MTT solution (0.5 mg/mL) was added to each well, followed by another 4 hours of incubation. Finally, 100 µL of DMSO was added for 10 min to dissolve the formazan crystal completely. The absorbance was measured using the microplate reader at a wavelength of 570 nm. The experiment was done in triplicate and cell viability $\geq 80\%$ is regarded as non-cytotoxic.

3.2.2 System B - BPS fabricated via 3D printing and dissolution adhesion technology

3.2.2.1 Fabrication of 3D-printed biphasic scaffolds

The fabrication methodology involves 3D printing of directional cartilage and bone phases represented as 3D Printed PCL/PLGA/CS (3DPPLGCS) and PCL/PLGA/βTCP (3DPPLGT)

respectively. Finally, composite scaffold fabrication via dissolution adhesion technology. Main steps are involved in fabrication of biphasic scaffolds using 3D printing, as given below.

Bone zone/calcified phase:

Initially, the bone/calcified phase of the biphasic scaffold was created by the 3D printing technique using a 3D printer (Maker City, India). Different concentrations of PCL/PLGA solution were also explored to get the best porosity and thickness in the gradient layer. Finally, a turbid solution containing PCL, PLGA, and β TCP in the ratio 62.5: 31.25: 6.25 was selected and used to develop a calcified phase at room temperature (25°C), using a nozzle tip with an inner diameter of 0.33mm. The speed of printing was set at 10 mm/s to ensure the layer height (100 μ m) and to enable the immediate partial solidification of the PCL-PLGA blend in a honeycomb pattern. The first 10 layers of the scaffold were printed with 50 % infill density, whereas the following 8 layers were printed at 40%, then 8 layers at 30% infill density, and the final 9 layers at 20% infill density. Once the stereoscopic 3D scaffolds of designed height were obtained, they were air-dried for 48 hours. to eliminate any residual solvents.

Cartilage phase:

Secondly, the cartilage phase was also fabricated by 3D printing using the 3D printer, Maker city. Based on the ease of printing, a turbid solution containing PCL, PLGA, and Chondroitin sulfate in the ratio 65:30:5 was chosen. Different infill densities were used to create a gradient cartilage phase (25 %, 30 %, 40 %, and 50 % from top to bottom layers). The plotter's speed was set to 10mm/s and was printed in a cubical pattern as per the model design. The initial 10 layers of the scaffold were printed with a 50% infill density, followed by 8 layers at 40% infill density, then 8 layers at 30% infill density, and finally 7 layers at 25% infill density. The printing was done at 25°C (room temperature).

Cartilage-bone biphasic scaffold (BPS):

An organic solvent (1,4 dioxane) was applied to the bottom of the cartilage phase and the top of the bone scaffold, to dissolve both layers slightly. The cartilage phase was then lightly

pressed onto the bone scaffold. Hence, the biphasic scaffold has PCL/PLGA/CS on the upper layer and PCL/PLGA/ β TCP on the lower half (hereafter represented as BPS). It was then air-dried for 48 hours inside a fume hood to ensure that the solvent is completely removed. The biphasic scaffolds were sterilized with 70% ethanol followed by UV irradiation for 2 hours. The excess ethanol was allowed to evaporate, and any residual ethanol was removed by PBS wash (3 times, 5 minutes each).

3.2.2.2 Characterization of biphasic scaffolds

The surface chemistry of each phase of biphasic scaffolds (PCL, PCL/PLGA, PCL/PLGA/CS, and PCL/PLGA/ β TCP) was analyzed in attenuated total reflection (ATR) mode using an ATR-FTIR spectrometer (Alpha II, Bruker, Germany). FTIR spectra of four groups of scaffolds were collected from 4000 to 400 cm^{-1} at ambient temperature. The structural morphology and microstructure of the printed phases of the biphasic scaffold were analyzed using Scanning Electron Microscopy (SEM) (Hitachi S 2400 (Japan)). SEM micrographs of designed pore channels, struts, and the surface of scaffolds were obtained. Pore sizes ($n=6$) of the scaffolds were measured from SEM micrographs using ImageJ software. The surface wettability of the scaffolds was assessed by measuring the water contact angle using the sessile drop method.

The thermal stability and compositional analysis of each composite phase of biphasic scaffolds (PCL/PLGA, PCL/PLGA/CS, PCL/PLGA/ β TCP) were determined by TG/DTG and DTA, and the thermal behavior upon incorporating the bio factors into the 3D printed scaffolds was evaluated by differential scanning calorimetry using SDT Q600, simultaneous DTA-TGA Analyzer (TGA) & Differential Scanning Calorimeter (DSC). The temperature calibration was performed using alumina as reference material. Thermal characteristics of the 3D scaffolds and the effect of each component on the thermal behavior were evaluated by using differential scanning calorimetry. Samples of 8 mg were heated from 25 to 200°C at 10°C/min under a nitrogen atmosphere (50 ml/min) by using aluminum cells. Change in

thermal response among the scaffolds and the melting temperature (T_m) was evaluated from the peak of the melting endotherms. The compressive modulus of the scaffolds, PCL/PLGA, PCL/PLGA/CS, and PCL/PLGA/ β TCP was measured Using an Instron mechanical tester (Instron 5848, USA) with a 2.0 kN load cell and compressed at a crosshead speed of 1 mm/min. The compressive stress and strain at maximum load are then calculated and plotted. The compressive modulus was calculated from the initial linear region of stress-strain curves. Average values were obtained from testing six scaffolds of each variation.

In vitro degradation studies (both qualitative and quantitative) were carried out for three months on two groups of scaffolds (10 (D) X 4 (H) mm) in size (PCL/PLGA and BPS consisting of PCL/PLGA/CS in the upper part and PCL/PLGA/ β TCP in the lower part). The degradation rate was determined and the degradation pattern of the scaffolds was observed by SEM analysis. The apatite mineralization ability of the bone phase of BPS *invitro* was investigated by immersing the samples (PCL/PLGA and PCL/PLGA/ β TCP, n=3) in simulated body fluids. The apatite formation on the surfaces of scaffolds was observed by SEM and EDS.

To evaluate potential toxicities *invitro*, cell viability and cell distribution within the scaffolds (PCL/PLGA/CS and PCL/PLGA/ β TCP and BPS) were assessed using L929 cells at 3 days of culture following the same protocol described in section 3.2.1.2.8. The cytocompatibility of these 3D printed scaffolds was tested quantitatively using an MTT assay. The study groups were the scaffold leaching solution, the media alone (DMEM, negative control), or with DMSO (positive control, 5% in media).

3.2.3 System C - BPS fabricated via 3D printing

3.2.3.1 Fabrication of Biphasic scaffold

The fabrication methodology involves 3D printing of directional cartilage and bone phases represented as 3D Printed PCL/PVP/CS/PAA (3DPPCS) and PCL/PVP/ β TCP/PAA (3DPPPT) respectively. Finally, composite scaffold fabrication via continuous printing.

Biphasic osteochondral constructs were developed by a two-step process. Firstly, the bone phase was printed, followed by the printing of the cartilage phase on the bone phase which was upturned with the face having 60% infill density or with the smallest pores, using a single head customized 3D printer. Biphasic osteochondromimetic scaffolds were fabricated as previously described in sections 3.2.1.1 and 3.2.2.1. Cartilage and Bone phases were fabricated from an adequately blended solution of PCL/PVP/CS and PCL/PVP/ β TCP in optimized concentration, 72:24:4 and 72:25:3 respectively. In the fabrication process, the created 3D models exported to STL files were sliced and the G-code is then fed into the 3D printer (Maker city) where the printing process is carried out using the ink containing biomaterials and biomolecules.

Before printing, the solution is mixed with 50% polyacrylic acid for interpolymer complexation to enhance printing. For the cartilage phase, the printing solution is dispensed using a 22 Gauge needle probe (0.413 mm inner diameter) at a feed rate of 182 with a print speed of 10mm/s in the best-suited cubical pattern as a close-packed array separated by a strut width (filling distance between adjacent pores in the topmost layer) of 0.5mm. The scaffolds are generated with a wall thickness (layer height) of 0.2mm with varying infill density (ID) from top to bottom. To mimic the hierarchical architectural pattern of native tissues, each layer is printed with a different infill density where the topmost layer is printed with 25% ID, followed by increasing the ID; 30, 40, 50, and 60 % for subsequent bottom layers. Based on our studies, the specific infill density at the top was selected to support easy cell seeding, whereas at the bottom to prevent cell leakage during the seeding. Thus, overall, 30 layers are printed with a total scaffold thickness of 3mm.

For the bone phase, a 22 Gauge needle probe (0.413 mm inner diameter) is used to dispense the ink with a feed rate of 170 at a print speed of 10mm/s. The layers are printed in a star pattern as a close-packed array separated by a strut width of 0.3 mm and a wall thickness of 0.18 mm. For better cell attachment and proliferation in a precise pattern, each layer is

printed with different infill densities where the topmost layer is printed with 25% ID, followed by increasing the ID; 30, 40, 50, and 60 % for subsequent bottom layers. Based on our studies, the specific infill density at the top was selected to support easy cell seeding, whereas at the bottom to prevent cell leakage during the seeding. Thus, a total of 30 layers are printed with a total scaffold thickness of 3mm. Three groups of cylindrical scaffolds (PCL/PVP/PAA, PCL/PVP/CS/PAA, PCL/PVP/BTCP/PAA) of the same dimensions, 50 (L) X 50 (W) X 3 (H) mm were constructed through 3D printing. A 1 cm diameter punch is used to cut the scaffolds of dimension 10 (D) X 3 (H) mm for further studies. The scaffolds were collected and washed sequentially in 80% ethanol and three cycles of sterile distilled water. They were stored in sealed packages at room temperature until use.

3.2.3.2 Characterization of biphasic scaffolds

For surface chemistry and compositional analysis, FTIR spectra of scaffolds (PCL, PCL/PVP, PCL/PVP/PAA, PCL/PVP/CS/PAA, and PCL/PVP/ β TCP/PAA) were collected using an ATR-FTIR spectrometer from 4000 to 400 cm^{-1} at ambient temperature. The structural morphology, microstructure, pore design, and struts of each sputter-coated printed phase of the biphasic scaffold (PCL/PVP/PAA, PCL/PVP/CS/PAA, and PCL/PVP/ β TCP/PAA) were analyzed using Scanning Electron Microscopy (SEM) (Hitachi S 2400 (Japan)). The surface wettability of the scaffolds was assessed by measuring the water contact angle using the sessile drop method, at room temperature as mentioned in previous sections. The thermal stability and decompositional analysis of each composite phase of biphasic scaffolds were determined by thermogravimetric analysis (TGA/DTG). The compressive modulus of scaffolds (n=6), PCL/PVP/PAA, PCL/PVP/CS/PAA, and PCL/PVP/ β TCP/PAA was measured using an Instron tester (Instron 5848, USA) with a 2.0 kN load cell and compressed at a crosshead speed of 1 mm/min.

In vitro degradation studies (both qualitative and quantitative) were carried out for three months on three groups of scaffolds, PCL/PVP/PAA, PCL/PVP/CS/PAA,

PCL/PVP/BTCP/PAA of dimension 10 (D) X 3 (H) mm. Also, to study the effect of interpolymer complexation using PAA in the degradation pattern of scaffolds, degradation studies were performed among the scaffolds with and without interpolymer complexation and the degradation rate was determined. The degradation pattern of the scaffolds was observed by SEM analysis. The apatite mineralization ability of the scaffolds (PCL/PVP/PAA and PCL/PVP/ β TCP/PAA, n=3) was investigated *invitro* in SBF following the same protocol described in previous sections. The apatite formation was also observed by SEM and EDS.

The *in vitro* release study of chondroitin sulfate (CS) from the cartilage phase of BPS was also assessed over 28 days. At 37°C, scaffolds with dimensions of 10 (D) X 4 (H) mm (n=6) were incubated in 1 mL of PBS. They were transferred to fresh PBS at each endpoint (1 h, 3 h, 5 h, 24 h, day 2, day 3, day 7, day 14, and day 28). The amount of CS released into PBS at each time point was measured using a DMMB assay kit (Sigma-Aldrich,341088). The percentage cumulative release (g/ml) was calculated, and the mean value is graphically represented. The cytocompatibility of the scaffolds (PCL/PVP/PAA, PCL/PVP/CS/PAA and PCL/PVP/ β TCP/PAA) were assessed by MTT assay using L929 cells, following the same protocol described in section 3.2.1.2.8.

3.3 Isolation and characterization of adipose-derived mesenchymal stem cells (MSCs)

3.3.1 Isolation and characterization of Rat MSCs

3.3.1.1 Isolation of Rat MSCs

The experimental protocols were approved by the Institutional animal ethical committee (IAEC), and the current study's methodologies were carried out following SCTIMST's ethical principles after receiving IAEC approval (IAEC, Number: SCT/IAEC-286/SEPTEMBER/2018/97). Wistar rats weighing 250-350 gms were used to harvest adipose-derived mesenchymal stem cells (ADMSCs). The isolation, culture, and characterization of ADMSCs were performed according to a standard methodology developed in our lab

(Aloysious and Nair, 2013), with minor modifications. Briefly, adipose samples from retroperitoneal and subcutaneous fat pad were collected aseptically from the euthanized animal in Dulbecco's phosphate-buffered saline (DPBS) containing 10X antibiotic-antimycotic (Gibco, USA). 2 gm of adipose tissue was sliced into smaller pieces using sterile scalpel blade (No.24). The cut tissue pieces were washed thrice in DPBS containing 1% antibiotic/antimycotic inside a Forma Class II, A2 biological safety cabinet (Thermo Fisher Scientific) and were digested in a 20 ml syringe filtered Dulbecco's modified Eagle's medium-High Glucose (DMEM-HG, (Gibco, USA-12800017) containing 0.15 % (1.5 mg/ml) collagenase type 2 (Gibco, USA) for 40 minutes at 100rpm in orbital shaker set at 37°C. A white buffy coat was obtained, the supernatant was removed to another falcon tube and the floated lipid layer was discarded. The collagenase was inactivated by adding an equal amount of pre-warmed complete media containing 10% FBS, and 1% antibiotic-antimycotic solution (Ab/Am) (Gibco, USA). The suspension was centrifuged at 1800 rpm for 10 minutes at 4°C to get a pellet and resuspended in fresh complete media. The isolated cells were seeded onto a 25cm² cell culture flask (Thermo Scientific™ Nunc™, India) in 3 ml complete media, and cultured in a humidified incubator at 37°C with 5% CO₂. After 24 hours, the morphology of the cells was observed under phase-contrast microscopy (Olympus 1X 71) and the non-adherent cells were discarded by washing PBS twice and a fresh medium was added to the flask. The media was changed every 2-3 days and the confluent monolayer was trypsinized using 1ml of 0.25% trypsin-EDTA (Gibco, USA) solution, the cells were sub-cultured at a density of 2x10⁴ cells/cm² and expanded up to passage 3 and used for further studies.

3.3.1.2 Characterization of rat MSCs:

3.3.1.2.1 Morphology

F-actin staining of ADMSCs cultured on 24 well tissue culture plates was carried out by using FITC-conjugated phalloidin (Invitrogen, USA). Cells were fixed with 4% paraformaldehyde

for 20 minutes, permeabilized with 0.1% Triton X-100 for 10 min, and blocked with 2% BSA for 30 min. The stock solutions of FITC-phalloidin dissolved in DMSO were added to 1% BSA in PBS for a final concentration of 1 µg phalloidin/1 µl PBS. Cells on coverslips were placed upside down on a 25 µl phalloidin solution/1 cm² area for 30 minutes at room temperature in dark. The staining of vimentin antigen, the intermediate filament protein of MSCs were tested by permeabilizing the fixed cells, subsequently blocked and incubated with the specific vimentin antibodies (anti-vimentin mouse monoclonal, sc-373717; 1:200) for 60 min at 37°C. The cells were further incubated with Alexa fluor 488 conjugated goat anti-mouse secondary antibodies (Invitrogen A32723.; 1:200;). The nucleus was counterstained using DAPI for 5 min. The stained cells were washed with PBS and imaged using a fluorescence microscope (Olympus1X71, USA).

3.3.1.2.2 Surface marker analysis

To confirm the phenotype of isolated MSCs, the expression of a characteristic set of mesenchymal stem cells surface markers, such as the cluster of differentiation (CD)73, CD90, and CD105, while lacking expression of CD34, CD45, are tested through immunophenotyping and via flow cytometry as per the guidelines of Mesenchymal and Tissue Stem Cell Committee of the International Society for Cellular Therapy (ISCT) (Dominici et al., 2006). ADMSCs cultured on coverslips as monolayers were fixed with 4% (w/v) paraformaldehyde at 4°C for 20 min, blocked in 1% (w/v) bovine serum albumin and incubated with the specific primary antibodies for 60 min at 37°C such as CD73 (rabbit polyclonal, Invitrogen Cat #PA5-81614; 1:500); endoglin (CD105) (mouse monoclonal (P3D1), SC 18838; 1:200), CD90 (Thy-1.1) (mouse Monoclonal Antibody, Invitrogen eBioscience™ 14-0900-81; 1:200), CD 45-PE/CD 34-FITC (BD biosciences ab83465; 1:200). Subsequently, cells were incubated with Alexa fluor 488 conjugated goat anti-mouse secondary antibodies (Invitrogen A32723.; 1:200;) for CD 105, 90 and Alexa fluor 488 conjugated goat anti-rabbit secondary antibodies (Invitrogen

A32731.; 1:200;) for CD 73, incubated for 60 minutes at 37°C in the dark. Cells were counterstained with DAPI (Sigma-Aldrich; Merck) for nuclear staining. Images were captured using an inverted fluorescence microscope (Olympus IX 71) with an attached Nikon ZE-1-C1 3.70 digital camera system (Nikon Corporation, Tokyo, Japan).

The phenotypic analysis of isolated MSCs was further confirmed by flow cytometry using BD FACS Aria Cell Sorter (Becton and Dickinson, USA) with specific antibodies mentioned above. The medium was removed from flasks, cells were washed with DPBS twice, and trypsinized to form single-cell suspension using 0.25% trypsin-EDTA. Further, trypsin was inactivated by adding the basal medium, centrifuged, washed thrice with DPBS, and cells were counted. $0.1-1 \times 10^6$ cells were resuspended in 100ul of DPBS in a cytometry tube and 10 μ l of each antibody (CD 105, CD 90, CD 73, CD 45, CD 34) is added, incubated for 1 hour at room temperature. After incubation, cells were washed and incubated with secondary antibodies for 60 minutes at 37°C in the dark. 10^4 cells were counted and recorded for each measurement and analyzed by gating using Flowing software.

3.3.1.3 Multilineage differentiation assay

For the trilineage differentiation assessment for ADMSCs (Bunnell et al., 2008), the cells were seeded at a density of 1×10^4 cells per well in a 6 well plate and cultured in a normal DMEM medium containing 10% FBS and antibiotics. After the cells reached 90% confluency, the media was changed to adipogenic induction media (containing 0.5 mM Isobutyl methyl xanthine (IBMX), 50 μ M Indomethacin, 0.5 μ M dexamethasone, 10% FBS and 100u Penicillin/ streptomycin/mL) for assessing adipogenic differentiation potential, Osteogenic induction media (DMEM medium supplemented 10^{-8} M Dexamethasone, 10mM Beta glycerophosphate, 0.05 mg/ml L-ascorbic acid, 10% FBS, 100 U penicillin/streptomycin/mL) for assessing osteogenic differentiation potential and chondrogenic induction medium (DMEM-HG supplemented with 10 % FBS, 100U penicillin/streptomycin, 20 ng/ml

recombinant human TGF- β 1 protein, 10 ng/ml recombinant human TGF- β 3 protein (R&D Systems, Minneapolis, MN, USA), 25ng BMP2, insulin transferrin selenium solution (ITS-G; Gibco), 1mM sodium pyruvate (Gibco), 10^{-7} M dexamethasone (Sigma-Aldrich), 50 mg/L-Ascorbic acid-2 phosphates and 40 μ g/ml L-proline (Sigma-Aldrich)). After the culture periods of 14, and 28 days, the cells were fixed with 4% paraformaldehyde, stained with Oil Red O solution for lipids (adipogenic differentiation), Alizarin red S for calcium deposition (osteogenic differentiation), safranin-o-solution for GAGs, Sirius red stain for collagen (chondrogenic differentiation) and Mayer's hematoxylin counterstain for nuclei.

3.3.2 Isolation and characterization of Rabbit MSCs

Seven-month-old adult New Zealand white rabbits were chosen for the isolation of adipose tissue. The collection of Adipose tissue and all further experiments were carried out according to the ethical guidelines of our institute after obtaining approval from ICSCR (Institutional stem cell research committee) and the Institutional animal ethical committee (SCT/IAEC/062/August/2013/81). The same protocol adopted for isolating rat ADMSCs was followed for the isolation of rabbit ADMSc. The phenotypic characterization of isolated MSCs was done by immunostaining and flow cytometric analysis as per the guidelines of the Mesenchymal and Tissue Stem Cell Committee of the International Society for Cellular Therapy (ISCT). To substantiate the results of phenotypic characterization, the trilineage differentiation potential of cells was also assessed (Szepesi et al., 2016).

3.4 In Vitro culture of MSCs and evaluation of production of ECM

3.4.1 Evaluation of chondrogenesis in 2D culture and production of ECM

For pellet formation, rat ADMSCs were seeded at a density of 5×10^5 cells/well in a 24-wells plate and were cultured in a chondrogenic induction medium (CIM) Medium. Media changes were carried out at 3-day intervals, and the chondrogenic pellets were collected on day 21. The sGAG content from the spheroid was quantified by dimethyl methylene blue (DMMB) assay

to assess the chondrogenic ECM production. The pellets were digested in 1ml digestion buffer containing 20U/mL papain by incubating at 65°C for 2.5 hours. The total sGAG concentration per spheroid was quantified by measuring the absorbance at 595 nm against the standard curve with chondroitin sulfate (Sigma).

Aggrecan can be used as an indicator for cartilage formation and is stained dark blue using the copper-containing dye, Alcian Blue. For histology and immunostaining, pellet samples were washed twice with phosphate-buffered saline (PBS) and fixed in 4% paraformaldehyde (PFA) for 2 hours at ambient temperature and washed twice with PBS. The pellets were cryosectioned and Alcian blue staining (1% Alcian blue (Sigma-Aldrich) in 3% glacial acetic acid solution) and immunostaining for Collagen 2 and aggrecan were performed to observe chondrogenic differentiation.

For determining the *in vitro* chondrogenesis, RT PCR analysis was further performed to confirm the expression of marker genes. The transcript levels of chondrocyte-specific genes [ACAN, COL2a1, and Sox9] were assessed by quantitative reverse transcription-polymerase chain reaction (qRT-PCR). Complementary deoxyribonucleic acid (cDNA) was then synthesized from 750 ng of the total RNA using a High-Capacity cDNA Reverse Transcription Kit (Thermo Fisher Scientific, USA). The quantitative PCR analysis i.e, the cDNA was amplified using qPCR Master Mix (Takara) TB Green® Premix Ex Taq™ II (Tli RNase H Plus, Cat No: RR820B) using the qTOWER³ G real-time PCR machine (Analytik Jena, Germany). The relative expression level of each target gene was then calculated using the $2^{-\Delta\Delta Ct}$ method and representative outcomes were illustrated as target gene expression normalized to the reference gene GAPDH.

3.4.2 Evaluation of osteogenesis in 2D culture and production of ECM

For assessing osteogenic differentiation potential to induce osteogenesis and production of ECM, ADMSCs were seeded at a density of 5×10^5 cells/well in a 24-well plate and were

cultured in an Osteogenic induction medium. After 28 days of culture, Alizarin red staining and Calcium estimation were done to confirm the production of ECM *in vitro*. The calcium content was quantified by Calcium assay using Total Calcium estimation kit, OCPC method (Coral Clinical Systems) as per manufacturers instruction. The absorbance of the standard and test sample was measured in a microplate spectrophotometer at 570nm.

For histology, 2D cultured cells were washed twice with phosphate-buffered saline (PBS) and fixed in 4% paraformaldehyde (PFA) for 20 min at room temperature and washed twice with PBS and stained with Alizarin red, a commonly used stain to identify calcium-containing osteocytes in differentiated culture of mesenchymal stem cells (MSCs). The cells are stained with Alizarin Red S solution (2g Alizarin Red S (Sigma, Cat No: A5533) in 100 ml ddH₂O) and incubated at room temperature in the dark for 45 min.

The transcript levels of osteogenic specific genes [Bone sialoprotein (BSP), Osteocalcin (BGLAP), Osterix] were assessed by quantitative reverse transcription-polymerase chain reaction (qRT-PCR) to determine the expression of marker genes for osteogenesis.

3.5 Invitro differentiation potential of MSCs on the biphasic scaffold (BPS)

3.5.1 System A- BPS fabricated via Combinatorial approach

3.5.1.1 In Vitro cytocompatibility with Rat ADMSCs

The effect of polymer, fabrication methodology and presence of residual solvents on cell viability and cell distribution in the scaffolds was assessed at 7-day and 28- days (n=3 for each phase) post-seeding. The scaffolds were seeded with 40 µL of ADMSC solution (0.5×10^6 cells/scaffold) and were assessed using the LIVE/DEAD Viability kit.

3.5.1.2 Cell Adhesion/ attachment and morphology

For assessing the cell adhesion rate, 20µl of MSC cell suspension (5×10^5 cells/ ml) was seeded onto the bone and cartilage phases and incubated scaffolds at 37°C in an atmosphere of 5% CO₂. After 0, 4, 8, 12, and 24 hours of culture, the cells were detached from the scaffolds by

using 0.25% trypsin for 30 minutes followed by the addition of 0.1 % Collagenase I for 1.5 hrs. A cell-count plate was used to determine cell numbers and thereby analyzed cell adhesion% on scaffolds. Further, the morphology of cells in scaffolds cultured in a growth medium for 3 days was studied by staining against F-actin using FITC-conjugated phalloidin (Invitrogen, USA). Briefly, the scaffolds were washed with PBS and fixed with 4% paraformaldehyde for 30 min. After permeabilization of cell membrane with 0.1 % Triton X-100 for 10 minutes, the cytoskeleton was stained by FITC-phalloidin for 30 minutes at 37 °C and nuclei were stained with DAPI for 7 minutes at room temperature. Once successfully stained, the morphology of ADMSCs on the scaffolds was observed by a laser confocal microscope (Carl Zeiss LSM 710) and epifluorescence microscope (Olympus IX70 inverted fluorescence microscope).

3.5.1.3 MSC proliferation on biphasic 3D scaffolds:

The amount of DNA in the cells attached to the scaffolds was determined using Quant-iT PicoGreen dsDNA Reagent and Kits (Invitrogen™) according to the manufacturer's instructions. The proliferation of ADMSCs on 3D scaffolds (freeze-dried and 3D printed) compared to PCL alone was determined after 1,3,5-, 7- and 14-day culture. Disc scaffolds of 8 (D) x 3 (H) mm were fabricated for *in vitro* cell culture for quantitative estimation of proliferation. The ADMSCs seeded scaffolds (2×10^5 cells/scaffolds) within 24 well plates and cell culture plates used as the blank group were quantified for the DNA content. At the indicated time points, the scaffolds were rinsed with PBS three times and submerged in 1 mL of cell lysis buffer. To release the DNA, the samples were vortexed for 30 min on ice throughout the entire process and were homogenized using a 21-gauge needle. 100 uL of sample was mixed with 100 uL of DNA-binding fluorescent dye solution, and the fluorescence intensity was measured at an excitation wavelength of 485 nm and an emission wavelength of 535 nm using the Microplate Reader (BioTek, Winooski, USA), supported by the Gen5 data

analysis software. The samples (n = 3) were prepared in triplicate. The DNA concentrations were calculated according to DNA standard curve plotted using Calf Thymus DNA.

3.5.1.4 Differentiation of rat MSCs on 3D scaffolds into cartilage and bone lineages

3.5.1.4.1 Cell Seeding and Cell-scaffold Construct Culture.

The scaffolds (n=6) were initially incubated with a culture medium for 3 hours, followed by drop-wise seeding of cells (20 μ L of ADMSCs suspension at a cell density of 1.0×10^6) onto the top of the scaffold after removing the culture medium used for the initial wetting of the scaffolds. The cell-seeded scaffolds were kept at 37°C in a humidified incubator for 4 hours in stationary conditions for initial cell attachment. After 4hr the scaffolds were fed with an additional culture medium.

The chondrogenic differentiation induction potential of the 3D printed gelatin incorporated chondral layer and the osteogenic differentiation promoting efficiency of the calcium sulfate containing bone layer was compared with that of bare PCL scaffolds. Both composite and bare PCL scaffolds seeded with rat ADMSCs were cultured in osteogenic and chondrogenic differentiation medium to evaluate the respective induction potential. The scaffolds fed only with DMEM-HG served as negative controls.

3.5.1.4.2 Evaluation of *in-vitro* chondrogenesis

a. Sulfated glycosaminoglycan (sGAG) Quantification by DMMB assay:

To quantify cartilaginous ECM production by cells within the chondrogenic phase of the BPS (PCL, PCL/Gelatin, and 2D cultures as control) after 7, 14, 21, and 28 days of culture in CIM, the proteoglycan content was determined from the glycosaminoglycan (sGAG) content spectrophotometrically, using a 1, 9-dimethyl methylene blue (DMMB; Sigma, St. Louis, MO, USA) dye-binding assay. In brief, the cell-seeded scaffolds were digested in 1ml digestion buffer containing papain [20U/mL papain (RM058, Himedia), L-Cysteine (5 mM), Disodium hydrogen phosphate (125 mM) and Disodium-EDTA (5 mM)] by incubating at 65°C for 2.5

hours. 50 μ l of the sample was mixed with 200 μ l of DMMB reagent. The total sGAG concentration per construct was quantified by measuring the absorbance at 525 nm against the standard curve with chondroitin-6-sulfate (Sigma, St. Louis, MO, USA) using Asys UVM 340 Microplate Reader (BioChrom, UK). and the results were represented graphically. The total sGAG content was normalized to the scaffold wet weight and the total DNA content. sGAG content in non-cell-seeded scaffolds, digested in the same manner, were detected and the values were subtracted (OD of test samples-OD of non cell-seeded scaffolds) to avoid any interference with the assay. Three replicates were made per sample.

A fluorometric assay was used to determine the DNA content using Quant-iT PicoGreen dsDNA Reagent and Kits. The specimens were then digested for 2.5 hours at 65 °C in a papain solution. 100 μ L of sample was mixed with 100 μ L of fluorescent dye solution. After that, the fluorescence intensities were measured at 485 nm for excitation and 535 nm for emission. The DNA content was normalized using a calf thymus DNA standard.

b. Total Collagen estimation

Quantification of total collagen content was performed using Bicolor Sircol soluble collagen (Sirius Red) assay kit as per the protocol provided by the manufacture. In this assay, recently synthesized immature biochemical collagen which can be solubilized by acid-pepsin digestion is quantified. All the scaffolds were digested using acid-pepsin (0.1mg/ml in 0.5 M acetic acid) in the ratio 1:20 and overnight incubation at 4^oC with mechanical stirring to completely release collagen into the solution where it can be subsequently quantified by sircol protocol. This was followed by centrifugation for 10 minutes and the supernatant was used for the estimation of total collagen. 200 μ l of sample was mixed with 500 μ l of Sircol reagent. The standards were prepared using the collagen standard (0.5 mg/ml) available in the kit. The optical density was measured at 540nm and the concentrations of total collagen in the scaffolds were calculated from the calibration plot of the standards.

3.5.1.4.3 Evaluation of the *invitro* osteogenesis

a. Assessment of Alkaline Phosphate activity

The cell-seeded scaffolds (PCL, PCL+CaSO₄, 2D culture) were cultured in an osteogenic induction medium for 7, 14, 21, and 28 days. After each time point, the cell lysates were prepared by treating with Triton X-100 for 1h followed by sonication. ALP substrate (Alkaline Phosphatase Activity kit (calorimetric, ab83369) and cell lysate in the ratio of 1:1 was taken in a microplate reader and incubated in dark for 30 minutes at 37°C. The enzymatic reaction was stopped by using 3M NaOH and the absorbance was taken at 405 nm. The ALP activity in the cell lysates was quantitatively determined from the standard graph plotted using the p-nitrophenol. Also, the values were normalized to the total protein content in cell lysate, which was measured by the BCA assay.

b. Calcium estimation

In vitro mineralization on scaffolds (PCL, PCL/CaSO₄, 2D culture), suggestive of the differentiation of ADMSCs to osteoblast was quantified by Calcium assay using Total Calcium estimation kit, OCPC method (Coral Clinical Systems). Here, the cell lysates were prepared by treating the cultured scaffolds with Triton X-100. To 20µl of sample lysate and standard (10 mg/dl), 500µl of both reagents (L1 and L2) were added and incubated for 5 minutes at room temperature. The absorbance of the standard and test sample was measured in a microplate spectrophotometer at 570nm against the blank, which contains only distilled water (20µl) and reagents. The absorbance of test samples was normalized with the absorbance obtained from non-cell-seeded scaffolds digested in the same manner.

3.5.1.4.4 Immunostaining for cartilage and Bone markers:

To evaluate the extent of chondrogenesis, the chondrogenic markers, type II collagen, and Aggrecan link protein expression were detected after 28 days of chondrogenic culture by immunofluorescence. Correspondingly, the differentiation of ADMSCs towards osteogenic

lineage and production of extracellular matrix proteins in cell-scaffold constructs cultured in the osteogenic differentiation medium was estimated by assessing early and late osteogenic markers osteonectin, osteocalcin, and ALP by immunofluorescence. Briefly, constructs were fixed with 4% paraformaldehyde for 30 min, rinsed with PBS twice and were incubated with 2% bovine serum albumin (BSA) (Sigma Aldrich, A3294) for 1 hr at 37 °C to avoid nonspecific binding of antibodies. The samples (cartilage phase and respective control) were further incubated with mouse anti-collagen type 2 A1 primary antibody (1:300 in 1% BSA; SC-52658) or mouse anti-aggrecan antibody (1:200 in 1% BSA; SC-73693) and bone phase were incubated with mouse anti-TNAP antibody (1:200 in 1% BSA; SC-137213) or mouse anti-SPARC (osteonectin) (1:200 in 1% BSA; SC-73472) or mouse anti-osteocalcin ((1:200 in 1% BSA; SC-365797) for 24hours at 4 °C. After thorough washing with PBS, the samples were incubated with respective secondary antibodies; Alexa fluor 488 goat anti-mouse or Alexa Fluor 647 goat anti-mouse secondary antibodies (Invitrogen) in 1:200 (1% BSA) for 1 h at room temperature, washed with PBS, and the nuclei were counterstained with DAPI. The stained samples were visualized and recorded using the confocal microscope.

3.5.1.4.5 Gene expression analysis by real-time PCR:

For determining the *in vitro* differentiation potential of ADMSCs seeded on to 3D printed scaffolds, the transcript levels of chondrocyte-specific genes [ACAN, COL2a1, HAS1, Sox9, and COL10] and osteoblast-like cells specific genes [Sox9, RunX2, BGLAP, ALP, and COL1A2] was assessed by quantitative reverse transcription-polymerase chain reaction (qRT-PCR). Total messenger RNA (mRNA) of ADMSCs embedded in fabricated scaffolds, PCL/Gelatin (cartilage phase), PCL/CaSO₄ (Bone phase), and its respective control at different times was isolated using Trizol (Invitrogen). The purity and quantity of isolated RNA were estimated using NanoDrop200c, Thermo Fisher Scientific, USA. 750 ng of the total RNA was reverse-transcribed into cDNA using a High-Capacity cDNA Reverse Transcription Kit

(Applied biosystem), according to the manufacturer's instructions. Quantitative reverse transcription-polymerase chain reaction (qRT-PCR) was performed i.e, the cDNA was amplified using POWER up SYBR green master mix (Applied Biosystems TM, A25742) following the manufacturer's instructions using the qTOWER³ G real-time PCR machine (Analytik Jena, Germany). The qPCR cycles consisted of 40 rounds of amplification of the cDNA template with primers annealing at 57 °C; Gene expression levels for chondrogenesis (ACAN, COL2A1, HAS1, Sox9, and COL10) and osteogenesis [Sox9, RunX2, BGLAP, ALP, and COL1A2] were normalized to the housekeeping gene Glyceraldehyde 3-phosphate dehydrogenase (GADPH) and showed as fold change relative to the value of embedded MSCs at day 3. The relative expression level of each target gene was then calculated using the $2^{-\Delta\Delta Ct}$ method. Each qPCR was done on at least three distinct experimental samples and representative outcomes were illustrated as target gene expression normalized to the reference gene GAPDH. Error bars are represented as SD from the mean of technical replicates.

Table 1: Primer sequences used for qPCR.

Gene	FORWARD PRIMER (5'-3')	REVERSE PRIMER (5'-3')
SOX9	5'- CTCCTACTACAGCCACGCAG-3'	5'-AGCTGTGTGTAGACGGGTTG-3'
HAS1	5'- TCTATGGGGCGTTCCTCAGT -3'	5' -AAGTGGGGTCCTCCTGGTAG-3'
ACAN	5'-AGCCCTTGTCTGAATGGAGC -3'	5'-GGTCGGGAAAGTGGCGATAA -3'
COL2A1	5'-GGCCAGGATGCCCGAAAATTA-3'	5'-ACCCCTCTCTCCCTTGTCAC-3'
COL 10A1	5'-AAGGTGATCCTGGAGTGGGA-3'	5'-TGGGATACCTGGTGGTCCAAT-3'
RUNX 2	5'-GCGGTGCAAAC TTTCTCCAG -3'	5'-TCACTGGACTGAAGAGGCTG -3'
BGLAP	5'-GGCGCTACCTCAACAATGGA-3'	5'-GGCAACACATGCCCTAAACG-3'
ALP	5'-GCCCCTGACTGAAATTCCTCG -3'	5'-CACTGGGAAGATAACAAGCCCC-3'
COL1A2	5'-AATGTTGGCCAGCTGGTAAAG-3'	5'-AGGTTTGCCAGGATCACCAGAG-3'
GAPDH	5'-AGTGCCAGCCTCGTCTCATA-3'	5'-AACTTGCCGTGGGTAGAGTC-3'

3.5.2 System B - BPS fabricated via 3D printing and dissolution adhesion technology

3.5.2.1 In Vitro cytocompatibility with rabbit MSCs

The cell viability and distribution of ADMSCs in the scaffolds were assessed at 28- days (n=3 for each phase) post-seeding, where 40 μ L of cells solution (0.5×10^6 cells/scaffold) were seeded onto the scaffolds. The live and dead cells on the scaffolds were assessed by following the same protocol mentioned in 3.2.1.2.8, using the LIVE/DEAD Viability kit.

3.5.2.2 Cell attachment and proliferation:

For studying the cell adhesion morphology, the spreading pattern of ADMSCs on the 3D printed scaffolds was evaluated by staining against F-actin with FITC-conjugated phalloidin. The proliferation of ADMSCs on 3D printed hybrid scaffolds compared to PCL/PLGA was determined by measuring the metabolic activity using a standard MTT assay (Li et al., 2018). Scaffolds (n = 3) were seeded with 2×10^5 ADMSCs/scaffolds in 12 well plates and the proliferation was evaluated at 1, 3, 5, and 7 days. Following culturing, scaffolds are transferred into new 24-well plates containing a 5:1 ratio of media and MTT solution (5 mg/ml in PBS), respectively, and incubated for 4 hours at 37°C as per previously standardized protocols (Baghaban Eslaminejad et al., 2010).

3.5.2.3 Differentiation of rabbit ADMSCs on 3D scaffolds into cartilage and bone lineages

The composite (PCL/PLGA/CS, PCL/PLGA/ β TCP and bare (PCL/PLGA) scaffolds of dimensions 10(D) X 2 (H) mm (n=6) were seeded with rabbit ADMSCs, cultured in the specific differentiation medium to evaluate the osteogenic and chondrogenic differentiation induction potential of 3D printed scaffolds with incorporated factors and compared with that of bare PCL/PLGA scaffolds. Qualitative and quantitative analyses of differentiation induction by the scaffolds at different time points were also performed.

3.5.2.3.1 Evaluation of *in vitro* chondrogenesis

The dimethyl methylene blue (DMMB) assay was used to determine the sGAG content in the cartilage layer of the 3D printed scaffold (PCL/PLGA, PCL/PLGA/CS) as well as monolayer after 7th, 14th, and 28th days of culture. The total collagen content was quantified using the Bicolor Sircol soluble collagen (Sirius Red) assay kit according to the manufacturer's protocol..

3.5.2.3.2 Evaluation of osteogenesis

The alkaline phosphatase (ALP) activity of ADMSCs cultured on different scaffolds (PCL/PLGA, PCL/PLGA/ β TCP, and monolayer culture in an osteogenic medium) was quantified for 7, 14, 21, and 28 days using an ALP liquid substrate according to the manufacturer's protocol. To assess ADMSC differentiation to osteoblast, *in vitro* mineralization on scaffolds (PCL/PLGA, PCL/PLGA/TCP, 2D culture) was analyzed and quantified by the OCPC method using the Calcium estimation kit (Coral Clinical Systems).

3.5.2.3.3 Immunostaining for cartilage and bone markers

Immunostaining for specific markers, type II collagen and Aggrecan, was used to assess the differentiation of ADMSCs towards chondrocyte lineage and the production of cartilage ECM. Similarly, the extent of ADMSC osteogenic differentiation was determined by immunostaining the osteogenic markers, Osteonectin, Osteocalcin, and ALP. For nuclear staining, DAPI was used. Using a confocal microscope, the stained sections were visualized and recorded.

3.5.2.3.4 Gene expression analysis using qRT-PCR

The transcript levels of osteogenic specific genes [Bone sialoprotein (BSP), Osteocalcin (BGLAP), Osterix] and chondrocyte specific genes [ACAN, COL2a1, HAS2 and Sox9] were assessed by qRT-PCR following the same protocol described in section 3.6.1.4.6. The quantitative PCR analysis i.e, the cDNA was amplified using qPCR Master Mix (Takara) TB

Green® Premix Ex Taq™ II (Tli RNase H Plus, Cat No: RR820B) using the qTOWER³ G real-time PCR machine (Analytik Jena, Germany).

Table 2: Primer sequences used for qPCR.

Gene	FORWARD PRIMER (5'-3')	REVERSE PRIMER (5'-3')
SOX9	5'-CTCAAGGGCTACGACTGGAC-3'	5'-TGTAGTCCGGGTGGTCCTTC-3'
HAS2	5'-TTTGCCTTTTTGGAGCACCG-3'	5'-TTCCCTGCCCATGACTTCAC-3'
ACAN	5'-GCCAGAGTTCAGTGGAAACAACA-3'	5'-AGAGACCCGCCTCTCCTGAA-3'
COL2A1	5'-TCAAGGATTTCAAGGCAACC-3'	5'-GGAACCACTCTCACCCCTTCA-3'
IBSP	5'-ACAACACTGGGCTATGGAGA-3'	5'-CCTTGTTTCGTTTTCATCCAC-3'
BGLAP	5'-ACTCTTGTCGCCCTGCTG-3'	5'-CTGCCCTCCCTCTTGGAC-3'
Osterix	5'-TGCTTGAGGAGG AAGTTCAC-3'	5'-AGGTCACTGCCACAGAGTA-3'
GAPDH	5'-GTTCCATGGCACAGTCAAGG-3'	5'-CCAGGGGGGCAAGCAGTTG-3'

3.5.3 System C - BPS fabricated via 3D printing

3.5.3.1 In Vitro cytocompatibility with rat ADMSCs

The viability of seeded MSCs (0.5×10^6 cells/scaffold) and their distribution within the scaffolds (PCL/PVP/PAA/CS and PCL/PVP/ β TCP/PAA) of dimension 10 (D) X 3(H) mm were assessed at 7 and 28 days of culture using the LIVE/DEAD Viability kit, following the same protocol described in section 3.2.1.2.8. Furthermore, the cytocompatibility of these 3D printed scaffolds was tested using an MTT assay.

3.5.3.2 Cell attachment and proliferation

The cell adhesion morphology and spreading pattern of ADMSCs on the 3D printed phases of BPS, was evaluated by staining against F-actin with FITC-conjugated phalloidin. The proliferation of ADMSCs on 3D printed hybrid scaffolds (PCL/PVP/PAA/CS and PCL/PVP/ β TCP/PAA) compared to PCL/PVP/PAA was determined by measuring the cell number inside the scaffolds in which the total DNA was quantified by using Quant-iT PicoGreen dsDNA Reagent and Kits.

3.5.3.3 Differentiation of rat ADMSCs on 3D scaffolds into cartilage and bone lineages

The methodology of cell seeding and induction protocol is mentioned in previous sections 3D printed cubical scaffolds of dimensions 10(D) X 3 (H) mm (n=6) (PCL/PVP/PAA/CS and PCL/PVP/PAA) were seeded with rat ADMSCs and cultured in differentiation medium.

3.5.3.3.1 Evaluation of *in vitro* chondrogenesis

The secretion of glycosaminoglycan (GAG) from differentiated ADMSCs to chondrocytes cultured on cartilage phase and control scaffolds ((PCL/PVP/PAA, PCL/PVP/CS/PAA, 2D culture) was measured by the DMMB method. The total collagen content was quantified using the Bicolor Sircol soluble collagen (Sirius Red) assay kit, described in previous sections.

3.5.3.3.2 Evaluation of osteogenesis

The alkaline phosphatase (ALP) activity of ADMSCs cultured on different scaffolds (PCL/PVP/PAA, PCL/PVP/BTCP/PAA, 2D culture) in the osteogenic medium was quantified for 7, 14, 21, and 28 days using an ALP liquid substrate. To assess the *in vitro* bone Matrix deposition of the bone phase of BPS and control scaffolds (PCL/PVP/PAA, PCL/PVP/BTCP/PAA, 2D culture), calcium deposition was quantified by the OCPC method using the Total Calcium estimation kit (Coral Clinical Systems).

3.5.3.3.3 Immunostaining for cartilage and bone markers

Immunostaining for specific markers, type II collagen, and Aggrecan, was used to assess the differentiation of ADMSCs towards the chondrocyte lineage and the production of cartilage ECM. Similarly, the extent of ADMSC osteogenic differentiation was determined by immunostaining the early and late osteogenic markers, Osteonectin, Osteocalcin, and ALP following the protocol mentioned in previous sections.

3.5.3.3.4 Evaluation of cell morphology and distribution of cell and ECM using ESEM

The morphology and distribution of cells attached to the scaffolds (PCL/PVP/CS/PAA and PCL/PVP/BTCP/PAA) cultured in respective differentiation mediums were evaluated after 28 days of culture scaffolds via scanning electron microscopy (SEM). 40 μ L of ADMSCs suspension were seeded (seeding density of 1×10^6 cells) dropwise onto the top of the 3D printed cubical scaffolds of dimensions 10(D) X 3 (H) mm (n=6), incubated at 37°C and were supplied with specific induction medium. After 28 days of culture, samples were washed with PBS and ESEM images were captured at different magnifications to obtain information regarding the cell morphology and overall distribution of cells and ECM molecules.

3.5.3.3.5 Gene expression analysis RT-qPCR

The osteogenic and chondrogenic differentiation ability of seeded MSCs in various scaffolds was assessed by measuring the expressions of osteogenic specific genes; SRY-Box Transcription Factor 9 (SOX 9), alkaline phosphatase (ALP), collagen type I (COL1A1), Bone Gamma-Carboxyglutamate Protein (BGLAP)/osteocalcin (OCN), and Runt-related transcription factor (Runx2) and chondrocyte specific genes; aggrecan (ACAN), collagen type 2 A1 (COL2A1), Hyaluronan Synthase 2 (HAS2), SRY-Box Transcription Factor 9 (Sox9) and collagen type 10 (COL10 A1) respectively. Gene expressions from the MSCs cultured in the scaffolds were detected by quantitative real-time polymerase chain reaction (Q-RTPCR), following the same protocol described in section 3.6.1.4.6.

Table 3: Primer sequences used for qPCR.

Gene	FORWARD PRIMER (5'-3')	REVERSE PRIMER (5'-3')
SOX9	5'- CTCCTACTACAGCCACGCAG-3'	5'-AGCTGTGTGTAGACGGGTTG-3'
HAS1	5'- TCTATGGGGCGTTCCTCAGT -3'	5' -AAGTGGGGTCCTCCTGGTAG-3'
ACAN	5'-AGCCCTTGTCTGAATGGAGC -3'	5'-GGTCGGGAAAGTGGCGATAA -3'
COL2A1	5'-GGCCAGGATGCCCGAAAATTA-3'	5'-ACCCCTCTCTCCCTTGTCAC-3'

COL 10A1	5'-AAGGTGATCCTGGAGTGGGA-3'	5'-TGGGATACCTGGTGGTCCAAT-3'
RUNX 2	5'-GCGGTGCAAACCTTTCTCCAG -3'	5'-TCACTGGACTGAAGAGGCTG -3'
BGLAP	5'-GGCGCTACCTCAACAATGGA-3'	5'-GGCAACACATGCCCTAAACG-3'
ALP	5'-GCCCCTGACTGAAATTCCTCG -3'	5'-CACTGGGAAGATACAAGCCCC-3'
COL1A2	5'-AATGTTGGCCCAGCTGGTAAAG-3'	5'-AGGTTTGCCAGGATCACCAGAG-3'
GAPDH	5'-AGTGCCAGCCTCGTCTCATA-3'	5'-AACTTGCCGTGGGTAGAGTC-3'

3.6 Tissue engineering an osteochondral construct and its *in vivo* evaluation.

In this section, a comparative study was done among the three systems fabricated with respect to mechanical tests, proliferation, and biochemical assays. Among the three, the system that appeared the best is selected for *in vivo* study in rat osteo chondral defect model (Wistar rat) followed by grossing and histological staining.

3.6.1 Comparative study:

To expand the application of the biphasic scaffolds for osteochondral tissue engineering, the three different scaffolds were selected (System A, B, and C) and compared for their ability to regenerate osteochondral tissue in the animal models with critical size osteochondral defects. In this comparative study, three osteochondral scaffolds with different structural patterns depicting specific pore structures (varying pore size and strut width) were fabricated according to the design created using 123 design software as mentioned in the previous sections. The structural analyses including compression test, cellular activity evaluation by proliferation studies, and biochemical analysis specific for chondrogenesis and osteogenesis were done to assess the functionality were performed as per the standardized protocol for comparative study.

3.6.1.1 Mechanical properties:

The compressive mechanical properties of each phase of three developed systems and their respective controls of dimension 16 mm X 8 mm (height X diameter) were determined using an Instron mechanical tester (Instron 5848, USA). The compressive stress and strain at

maximum load are calculated and plotted. The compressive modulus was calculated from the initial linear region of stress-strain curves.

3.6.1.2 Cell activity by proliferation studies using Pico green method:

Five different groups of PCL-based scaffolds (System A Chondral phase, System B Chondral phase, System C Chondral phase, System B Bone phase, and System C Bone phase) were fabricated using custom-made 3D printer at room temperature using the standardized setting parameters. System A Bone phase was fabricated by freeze-drying. MSCs were seeded into different types of scaffold systems (8 (D) x 3 (H) mm) for proliferation analysis at days 1, 3, 5, 7, and 14. The amount of DNA in the cells attached to the scaffolds was determined using Quant-iT PicoGreen dsDNA Reagent and Kits.

3.6.1.3 *In vitro* differentiation of Rat MSCs and Functionality assessment

The chondrogenesis ability of ADMSCs cultured on the cartilage phase of three biphasic scaffolds (System A, B, and C) was evaluated by quantifying the sGAG content spectrophotometrically by dimethyl methylene blue (DMMB) assay after the 7th, 14th and 28th days of culture. After quantifying, the results were compared among the scaffolds. To evaluate the osteogenic ability of seeded ADMSCs in bone phases of biphasic scaffolds, we compared the alkaline phosphatase (ALP) activity in 3 groups of constructs (bone phases of System A, B, and C) and their respective controls for 7, 14 and 28 days in osteogenic medium. The quantitative estimation was done according to the protocol mentioned in previous sections. From the results, the best one was further selected to get implanted in the knee joint of Wistar rats having osteochondral defects in medial femoral condyle.

3.6.2 *In vivo* repair of osteochondral defect

Animal experiments were approved by the Institutional Animal Ethical Committee of the Sree Chitra Tirunal Institute for Medical Sciences and Technology (IAEC No: SCT/IAEC-

286/September/2018/97). A total of 18 Wistar rats (both sexes), weight between 300 and 450 gms with the age of 3-4 months were used in the experiment for creating 36 defects and randomly divided into 3 groups namely Group1: BPS (Biphasic scaffold), Group II: BPS+Cells and Group III: SHAM, for two-time points. All surgical procedures were performed under general anaesthesia and strict sterile conditions.

3.6.2.1 Animal Surgery: *In vivo* surgical procedure of Rat osteochondral defect model and Implantation of developed biphasic scaffolds into defects.

Ten-week-old Wistar rats with a mean weight of 320 ± 20 g were used in this study and anesthetized with Ketamine (35–40 mg/kg)/Xylazine (2–5 mg/kg). Post sedation, isoflurane was delivered from a precision vaporizer (1.5–3%) in 100% O₂ via a face mask during the surgery. Following stable anesthesia, hair from the surgery site around each knee was shaved. The area was disinfected with alternate scrubs of betadine and 70% ethanol and then draped. The surgical procedure was performed under strict aseptic conditions. A lateral parapatellar longitudinal incision was made to expose the medial condyle of the femur. The tibia was lightly pushed to displaced laterally to allow the exposure of the medial femoral condyle. Using a dental micromotor with saline irrigation, osteochondral defects (1.5 mm diameter and 1.5 mm depth) were created through both the chondral and the subchondral bone layer of the medial femoral condyle in their right and left knee joint. The defect was then filled by press-fitting the biphasic matrices (either with or without cells) into the defect. To avoid graft displacement from occurring, the size of the implant was made slightly larger than the defect size to press-fit the implant. All rats were randomly allocated into three groups and two-time points described in Table 4 (1 month and 3 months): defects with bilayered scaffolds (n=6) designated as group 1, defects with MSCs seeded bilayered scaffolds (n=6; 2650 cells per scaffold) as Group 2, and the sham-operated group represents the third group (Group 3). The joint was then washed off debris with sterile saline, the patella and the femur relocated, and the articular

capsule and bursae were closed with absorbable suture and skin bound with a non-absorbable closure (Vicryl 3/0 suture & Mersilk 3/0 respectively). Each rat's conditions were monitored during anaesthesia and surgery by the staff. Upon recovery from anaesthesia, the rats were returned to their cages where they were allowed unconstrained movements and weight-bearing activity and were observed by the staff for signs of pain, infection, and proper activity post operatively. Antibiotics Ceftriaxone (10mg/kg) i/m and analgesic Meloxicam (0.5mg/kg) were given once daily for 5 days post operatively. Food was given after the animals moved on their own to prevent gut stasis.

Table 4: Experimental groups for the in vivo study

Group	No of knee joints for 1 months study period (A)	No of knee joints for 3 months study period (B)	Total no of knee joints (A+B)
Group I: Sham control (defect without implant)	6	6	12
Group II : Biphasic matrices (BM)	6	6	12
Group III: Biphasic matrices + differentiation cues (BM+D)	6	6	12
Total	18	18	36
Total no of animals used for 1 and 3 months of study period:18			

3.6.2.2 Gross morphological assessment

During treatment, the knee joints were routinely examined for any edema or change in surface temperature by gently touching the joints. Upon termination, each rat was sacrificed and an arthrotomy was performed to re-inspect the intraarticular structure. The surface of cartilage was carefully observed for any morphological changes by naked eyes and the knee joints were excised using the bone cutter. After investigation of the possibilities of rejection or infection, such as severe inflammation or extensive fibrosis, or any other abnormality, the degree of

cartilage repair was grossly assessed. The nature of regenerated tissue in the defect, its integration with adjacent tissue, and the percentage of defect repair were macroscopically evaluated. Coloration, luster, irregularity, presence of any depression or bulging of repaired tissues in the defect area and state of the border with adjacent normal cartilage tissue were carefully examined and gross appearance was scored following a modified Goebel and ICRS scoring system (Goebel et al., 2017). Harvested femoral condyles were also photographed so that a record of their gross appearance was obtained. Following this, the joints were put in 10% neutral buffered formalin (NBF) (Merck) and histological analysis was performed.

Table 5: Scoring criteria

S.NO	Category	Item	Points
1	Presence of blood vessels in the repair tissue (Goebel)	No	4
		Less than 25% of the repair tissue	3
		25 - 50% of the repair tissue	2
		50 - 75% of the repair tissue	1
		More than 75% of the repaired tissue	0
2	Macroscopic appearance (Goebel and ICRS)	Intact smooth surface	4
		Fibrillated surface	3
		Small, scattered fissures or cracks	2
		Several, small or few but large fissures	1
		Total degeneration of grafted area	0
3	Integration to border zone (ICRS)	Complete integration with surrounding cartilage	4
		Demarcating border <1 mm	3
		3/4 of graft integrated, 1/4 with a notable border >1 mm width	2
		1/2 of graft integrated with surrounding cartilage, 1/2 with a notable border >1 mm	1
		From no contact to 1/4 of graft integrated with surrounding cartilage	0
Total points			12

3.6.2.3 Histological assessment:

The joints were collected in 10 % Neutral buffered formalin (NBF) and after being thoroughly fixed, specimens were subjected to chelation-based slow and gentle decalcification before routine tissue processing to paraffin for histological evaluation. Decalcification describes the technique for removing minerals from bone or other calcified tissue so that good-quality paraffin sections can be prepared that will preserve all the essential microscopic elements. Chelating agents such as ethylene diamine tetraacetic acid (EDTA) work by capturing the calcium ions from the surface of the apatite crystal, slowly reducing its size.

The joints were incubated in 35 ml 12.5 % EDTA decalcifying solution, prepared by dissolving 125 gm Ethylene Diamine Tetra Acetic acid (EDTA) disodium salt dihydrate (Merck) (pH- 7) with 10 gm sodium hydroxide (NaOH) pellets (Merck) for the complete dissolution of EDTA with continuous stirring on the tabletop stirrer. The solution was changed on alternate days to ensure better penetration and to test for the degree of decalcification at regular intervals of 5days by grossing using a surgical blade (No.11). The grossed tissue was again put in fresh decalcifying solution for approximately 12- 16 days along with continuous stirring. At the endpoint of decalcification, the tissues were subjected to processing, embedding, sectioning, staining, and mounting. Sagittal cuts were made perpendicular to the surface from the area of the defect and processed for paraffin embedding.

Before processing decalcified samples were given a water wash for 2hrs, followed by short tissue processing in an automated semi-enclosed benchtop tissue processor, Leica TP1020 (Leica Biosystems, Germany). It consists of following steps: (i) dehydration in series of alcohol (50, 70, 80, 95 and 100% - 2 changes); (ii) clearing in xylene (Merck) (2 changes) and (iii) paraffin impregnation. Then the tissues were embedded in paraffin using an embedder (Leica EG1150H) to make tissue blocks. Multiple sections were taken and the required number of sections for various staining were obtained using a semi-automated rotary microtome

(RM2255, Leica Biosystems, Germany) (RM2550, Leica, Germany). The sections (4 μm) were cut using Leica disposable blade, put in the water bath at 45°C, and carefully placed on albumin-coated slides (Starfrost). These slides were used for further staining procedures as described below. For the rest of procedures, staining and mounting were done manually.

3.6.2.3.1 Haematoxylin and Eosin (H&E) staining

The slides with sections were stained with H&E to determine cellular organization in the hyaline cartilage and subchondral bone. Deparaffination was performed on the obtained slides with sections by placing them in a hot air oven at 60°C for 1 hour. The deparaffinized sections were cleaned twice in xylene, then rehydrated in a descending series of alcohols (100, 95, 70 %), each for 5 minutes with two changes in 100 %. The slides were then immersed in Hematoxylin (Sigma, USA) for 20 minutes, washed in running tap water for 10 minutes, and then immersed in Eosin (Sigma, USA) for 2 minutes before being washed in running tap water for 10 minutes. The sections were dehydrated in an ascending series of alcohol concentrations (70, 95, 100%) for 5 minutes each, with two changes in 100 %. After staining, the slides were mounted and images were captured using a light microscope (Nikon E 600, Nikon, Japan).

3.6.2.3.2 Safranin O-staining:

Safranin O stains sulfated glycosaminoglycans in a semiquantitative manner. The paraffin sections are deparaffinized and slides were hydrated using xylene and graded ethanol (100%, 95%, 80%, 70%, and 50%) to distilled water. Further, stained with Wiegert's iron hematoxylin working solution for 10 minutes, washed in running tap water for 5 minutes, and destained in 1% acid alcohol. The washed slides were stained with 0.05 % fast green (FCF) solution for 5 minutes, quickly rinsed with 1% acetic acid solution, and stained in 0.1% safranin O solution for 30 minutes. The sections were dehydrated in ascending series of alcohol and cleared with 95% ethyl alcohol, absolute ethyl alcohol, and xylene, using 2 changes each, 5 minutes

each, mounted using resinous medium (Leica mountant), and allowed to dry overnight. Images at different magnifications were acquired using a microscope (Olympus 1x 80, Germany).

3.6.2.3.3 Alcian blue staining

For detecting the presence of proteoglycans, the sections were stained with alcian blue which stains acid mucosubstances. The deparaffinized slides were rehydrated to distilled water and stained with Wiegert's hematoxylin for 10 minutes as mentioned in the above section and washed. The washed slides were stained with alcian blue for 30 minutes. The staining solution was prepared by dissolving 1g alcian blue, 8GX (Himedia) in a 3% acetic acid (Merck) solution. The stained sections were washed in running tap water. The sections were dehydrated and cleared in xylene, mounted and images were taken as mentioned in the above section.

3.6.2.3.4 Trichrome staining:

Masson's trichrome staining is performed to identify an increase in collagenous connective tissue fibers or to differentiate between collagen and smooth muscle fibers. For this, tissue sections were deparaffinized, and rehydrated with distilled water. Sections were mordanted in Bouins fluid fixative consisting of saturated picric acid, formaldehyde, and glacial acetic acid for 1 hour at 56 °C. Once cooled, the washed sections are stained in Wiegert's hematoxylin for 10 minutes, rinsed, stained with trichrome stain for 20 minutes, and finally in 0.5% acetic acid for 2 minutes. The sections were dehydrated and cleared in xylene, mounted and imaged.

3.7 Statistical analysis

All qualitative and quantitative experiments were carried out in at least triplicates (n=3). All quantitative data are represented as mean \pm SD (Standard deviation). Statistical significance was calculated using a two-tailed t-test to determine differences among individual groups and a one-way analysis of variance (ANOVA) test. $P \leq 0.05$ was considered to be statistically significant for all experiments. $P < 0.05$ (*); $P < 0.01$ (**); $P < 0.001$ (***)

CHAPTER 4

4 RESULTS

This chapter presents the results obtained from *in vitro* and *in vivo* experiments defined in chapter 3, substantiated with adequate and relevant figures, tables, and graphs. The major illustrations comprise the results of fabrication methodology, physicochemical and mechanical characterization of three biphasic scaffolds and its cytocompatibility studies detailed in the first part. The isolation, culture, and characterization of adipose-derived MSCs and *in-vitro* production of ECM in 2D culture is illustrated in second part. The differentiation potential of MSCs seeded biphasic scaffolds to chondrogenic and osteogenic lineage are demonstrated as 3rd part. Furthermore, the comparative study results of the three systems were analyzed, and the best one was chosen for implantation in rat osteochondral defects. The ability of implanted osteochondral constructs to regenerate was demonstrated as 4th part of this chapter.

4.1 Development of biphasic scaffolds (BPS) mimicking osteochondral architecture

4.1.1 System A - BPS fabricated via combinatorial approach

4.1.1.1 Fabrication of biphasic scaffold

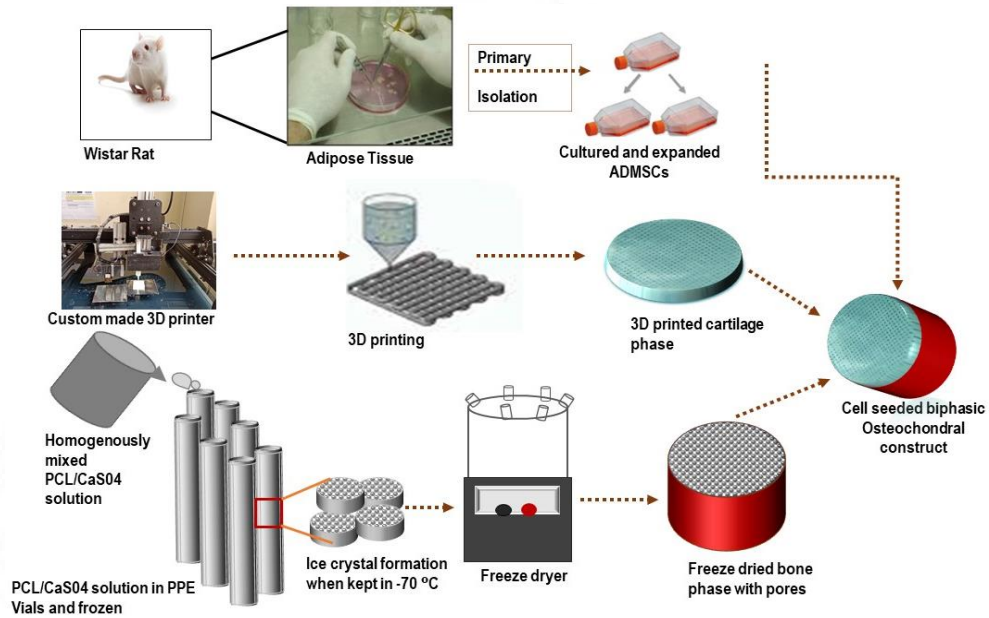
The study scaffolds with the hierarchical structure were successfully fabricated with our customized single-head 3D printer. Since different techniques were implied in fabricating the cartilage and bone phases, the fabrication of the biphasic scaffold was achieved in three steps. The schematic representation of the workflow is given in Scheme 4.1. In the first step, fabrication of PCL/Gelatin (P/G) based cartilage phase via 3D printing was done based on parameters optimized to get the gradient layer with different infill densities to get optimum porosity and thickness and were summarized in Table 6. Also, different concentrations of PCL/Gelatin solution were tried and finally, the ratio of 79:21 was found to be best suited and selected for developing gradient cartilage phase. The blueprint design and 3D printing process are shown in figure 4.1.1 (a)-(c). The extent of expansion of the ink during the plotting is

influenced by the needle diameter. Needle diameters ranging from 0.15 mm (30 gauge) to 0.51 mm (21 gauge) were tried to determine the optimal needle for 3D printing. The 23-gauge needle (0.33mm diameter) was the smallest needle size, which worked well with PCL: Gelatin (79:21) ink. This needle allowed the gradual extrusion of the ink and allowed the smooth flow of gelatin along with PCL, and prevented the accumulation of gelatin inside the syringe (Figure 4.1.1(c)).

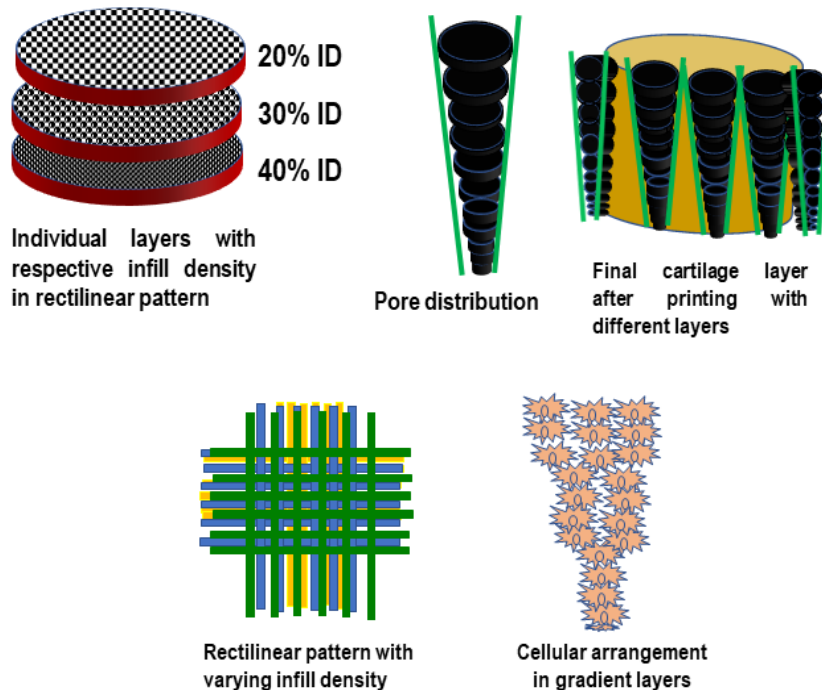
To mimic the microarchitectural pattern of hyaline cartilage and appreciate the influence of pore size of the scaffolds on the proliferation and differentiation of cells, the optimal filling spacing was investigated by changing the filling space and a gradient scaffold with different infill density (40%, 30%, and 20 %) from bottom to top respectively was thus fabricated. Based on our observations, 20% infill density was selected as the top layer to support easy cell seeding and 40% infill density at the bottom to prevent cell leakage. After assessing different patterns, we found that the rectilinear pattern is best suited for making the scaffolds with different infill densities (Figure 4.1.1 (d) and (e)). The schematic representation of pore distribution is given in Scheme 4.2. Two groups of cubical scaffolds (PCL, PCL/Gelatin) of the same dimensions, 50 (L)X 50 (B) X 2 (H) mm were constructed through 3D printing. A 0.8 cm diameter punch is used to get cylindrical scaffolds of dimension 8 (D) X 2 (H) mm for further studies. The control PCL scaffold is shown in figure 4.1.1 (f).

Secondly, fabrication of the bone phase was done by the freeze-drying process using a PCL/Calcium sulfate solution (95:5). Figure 4.1.1 (g) shows the macroscopic features of the PCL/CaSO₄ composite scaffold produced through the freeze-drying technique. Usage of homogenizer reduced the agglomeration and helped the CaSO₄ to get homogeneously dispersed, which was evident from the absence of large voids and crusts in the longitudinal section of the scaffolds (figure 4.1.1(g)). The macroscopic features of the 3D-printed cartilage and bone phase are given in figures 4.1.1(d)–(e) and (g).

In the final step, biphasic scaffolds of 8mm diameter x 5mm height were fabricated by combining the bone and chondral phase using a medical-grade sealant - Tisseel (height of chondral layer: 2mm and height of bone layer: 3mm) (figure (4.1.2 (a) & (b)))



Scheme 4.1: Fabrication of the biphasic scaffold – schematic representation of the workflow.



Scheme 4.2: Schematic representation of the gradient pores and cell alignment in the cartilage phase

Table 6: Printing parameters of BPS: System A

Parameters	Values	
	Cartilage Phase	Control
Concentration of printing solution	79:21 (PCL: Gelatin)	100:0 (PCL)
Flow rate (ml/hr)	100	108
Feed rate (ml/hr)	171	186
XYZ coordinates (l=50 mm: X=50 mm, Y=30 mm and l=10 mm: Z= 3 mm)	1, 1, 0.3	1, 1, 0.3
Nozzle temperature (°C)	25	25
Platform temp (°C)	25	25
Print speed (mm/s)	10	10
Layer height (mm)	0.15	0.1
First layer height	0.15	0.1
Infill density (%)	20, 30, 40	25, 30, 40
Probe type	23 Gauge needle (0.33 mm inner diameter)	22 Gauge needle (0.413 mm inner diameter)
Print layer (Number of layers)	35	35
Print pattern	Rectilinear	Rectilinear
Filling distance between adjacent pores in the topmost layer (Strut width) (mm)	0.372 ± 0.05	0.5 ± 0.07
Scaffold thickness (mm)	2	2

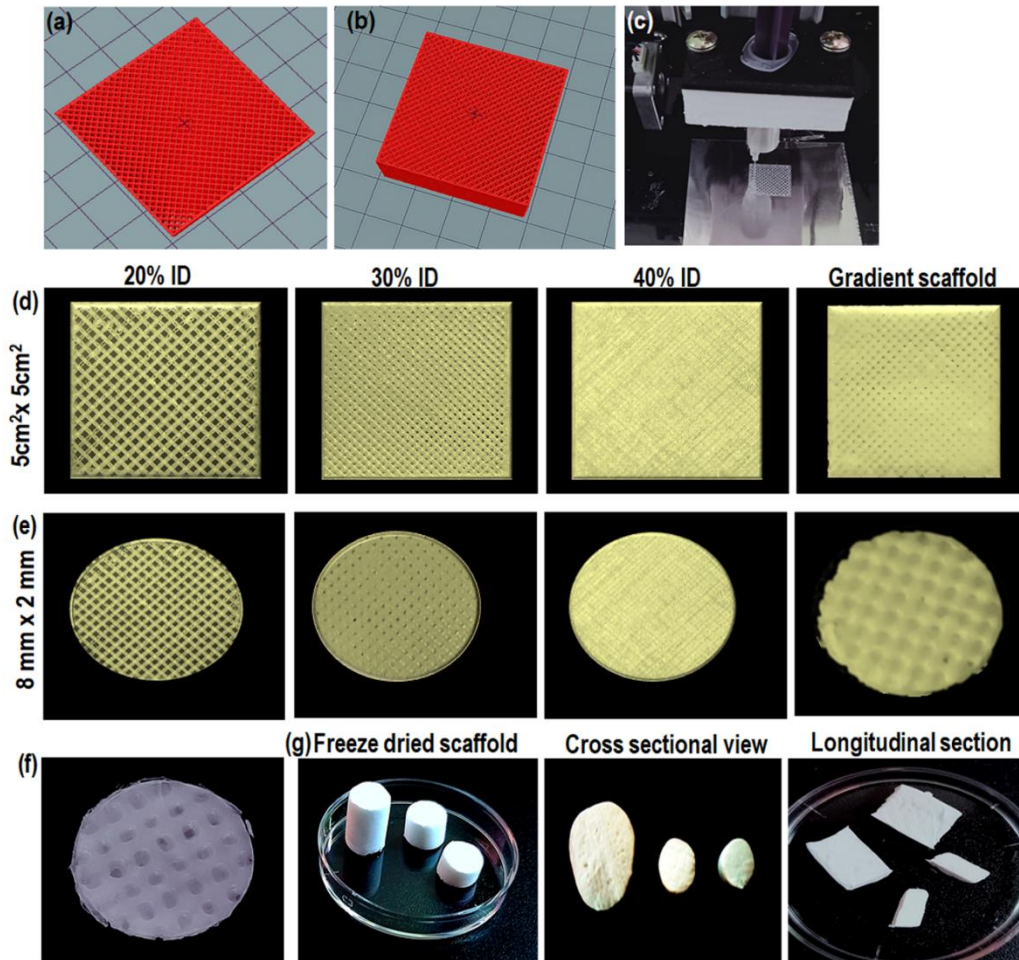


Figure 4.1.1: Fabrication of biphasic scaffold via combinatorial approach. Blueprint design and macroscopic features of the 3D-printed cartilage phase and freeze-dried bone phase. (a) & (b) shows blueprint design created using 123 design software, exported in STL format and G-code fed into the 3D printer. (c) represents the 3D printing process, (d) & (e) represent the morphological features of 3D printed layers with increasing fill densities (from left to right) and the gradient PCL/Gelatin scaffold as seen through a 5X magnifying lens, (f) represents the gradient PCL alone scaffolds and (g) representative images showing bone phase with different diameters and height and the longitudinal section showing absence of voids.

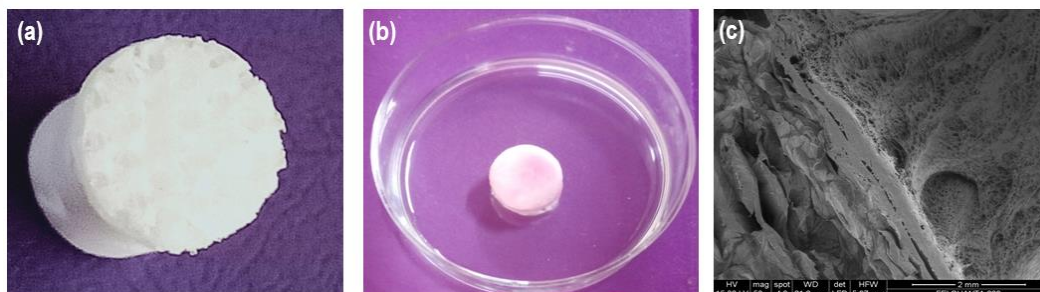


Figure 4.1.2: Biphasic scaffold. (a) & (b) represents the image of BPS viewed from the upper cartilage phase and lower bone phase respectively, and (c) represents SEM images of the cross-sectional view of biphasic scaffolds showing effective integration after 1 week of incubation in culture media.

4.1.1.2 Characterization of biphasic scaffold

4.1.1.2.1 Analysis of morphological features

SEM images of cartilage and bone phase are shown in Figure 4.1.3. The 3D printed PCL/Gelatin (P/G) scaffolds had uniform pores and struts that were distributed in an ordered pattern throughout the scaffolds. A textural difference between smooth and rough surfaces was observed on the PCL alone and P/G scaffolds respectively attributed to the presence of Gelatin in the scaffolds. SEM images showed an interconnected and continuous strand with pores of diameter 400 μm on the top layer that could aid in promoting cell growth. The optimized 3D printing conditions are required to achieve uniform pores and strands and rapid layer-by-layer construction of scaffolds, which prevents the construct from collapsing. As shown in figures 4.1.3 (c) & (d), the strands are parallel aligned in the horizontal and perpendicular planes, and the filling distance between adjacent pores in the topmost layer (Strut width) is 370 μm with a layer height of 150 μm respectively.

The SEM micrographs of the freeze-dried PCL-alone scaffold (figure 4.1.3 (e) & (f)) and PCL/ CaSO_4 (figure (g)- (h)) revealed the highly porous nature of the scaffold sample. The scaffolds produced through optimized parameters had uniform pore size distribution. Both the scaffolds have highly interconnected pores, with pore sizes ranging from 30 μm to a few hundred μm in size. The pore sizes and features of the PCL/ CaSO_4 scaffold were not significantly different from that of the PCL alone scaffold. Also, the addition of CaSO_4 imparted surface roughness which would provide adhesion sites for the seeded cells. The distribution of pores of cartilage and bone phases is shown in Table 7. The two layers adhered together without fail and were stable throughout the culture period. Figure 4.1.2 (c) shows the effective integration of the chondrogenic and osteogenic phases of the biphasic scaffold.

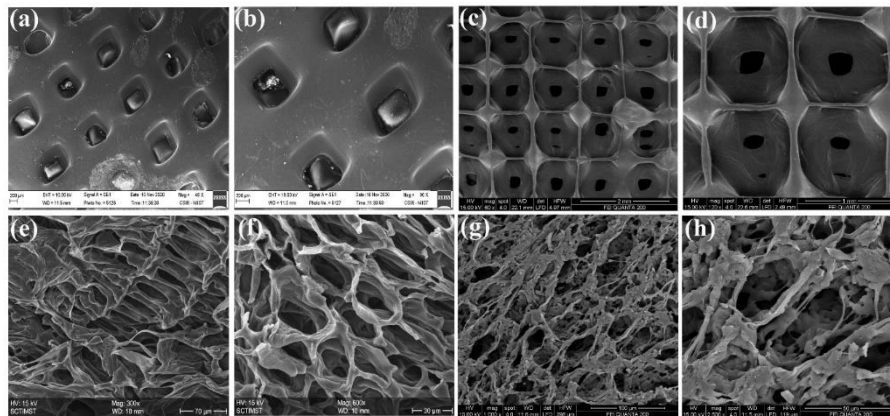


Figure 4.1.3: Analysis of morphological features. Scanning Electron micrographic (SEM) images of the scaffolds. Figure 2(a), (b), and (c) & (d) represent the SEM micrographs of PCL and PCL/ Gelatin scaffolds at low and high magnifications.

Table 7: The distribution of pores in cartilage and bone phases

Cartilage Phase (PCL/Gelatin)		Bone Phase (PCL/CaSO ₄)	
Pores	Diameter in μm	Pores	Diameter in μm
20 % ID	402 ± 20	1	50.0
30 % ID	151 ± 12	2	37.7
40 % ID	25 ± 5	3	48.7

4.1.1.2.2 Analysis of wettability features

Water contact angle images are shown in Figure 4.1.4. Compared to the PCL alone scaffolds, both the PCL/Gelatin (P/G) and PCL/CaSO₄ scaffolds showed decreased water contact angle suggesting improved hydrophilicity (figure 4.1.4 (a)-(c)). The water angle P/G composites decreased significantly, and surface hydrophilicity increased upon blending with gelatin. The P/G scaffold showed a contact angle of 62.5°, whereas the PCL-alone scaffold exhibited a contact angle of 128°. The Freeze-dried PCL/CaSO₄ scaffolds showed hydrophilicity (110°).

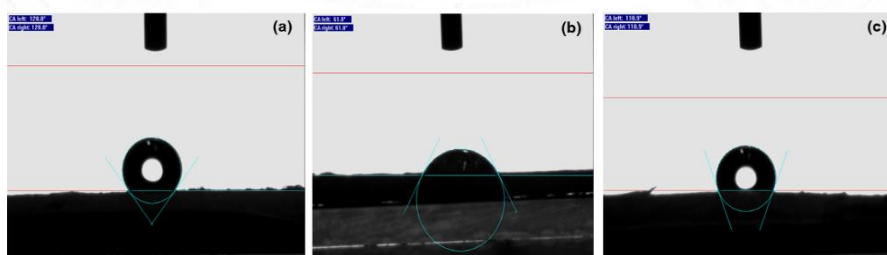


Figure 4.1.4: Analysis of wettability by contact angle measurements of scaffolds. (a), (b) & (c) represents contact angle and droplet profile after 5 sec on PCL alone ($128 \pm 3^\circ$), 3D printed PCL/Gelatin ($61 \pm 4^\circ$), and PCL/CaSO₄ ($110 \pm 2^\circ$) scaffolds respectively.

4.1.1.2.3 Analysis of chemical features

ATR-FTIR analysis was carried out for analysis of surface groups on the fabricated scaffolds and to see if there were any structural changes to the chemistry of the PCL during the fabrication of the scaffolds. The transmittance spectra at various wavelengths, which correspond to the various carbon compounds found in PCL, were examined. Figure 4.1.5 (a) & (b) shows the FTIR spectra of PCL, gelatin, and 79:21 3D printed PCL/Gelatin scaffolds. In the infrared spectra, characteristic peaks for PCL were observed for P/G scaffolds. These include $\sim 2942 \text{ cm}^{-1}$ (CH₂ stretching), $\sim 2866 \text{ cm}^{-1}$ (CH₂ stretching), $\sim 1729 \text{ cm}^{-1}$ (carbonyl stretching), $\sim 1291 \text{ cm}^{-1}$ (C–C stretching) and $\sim 1237 \text{ cm}^{-1}$ and $\sim 1165 \text{ cm}^{-1}$ (COC stretching). Common bands of Gelatin appeared in the FTIR spectra of gelatin-containing scaffolds, including bands of amide I (stretching vibrations of C=O bond of CONH₂) and amide II (bending of N-H bonds and stretching of C-N bonds) at 1650 cm^{-1} and 1540 cm^{-1} , respectively, confirming the presence of gelatin molecules in the scaffolds. The increase in the intensity of the vibration band at 1750 cm^{-1} in gelatin-containing scaffolds is due to the increase in the number of carbonyl groups in the scaffolds due to gelatin. Also, in the PCL/Gelatin scaffold, characteristic peaks of both PCL and Gelatin are identified with a slight shift in the peak which is attributed to physical interaction between the two through hydrogen bonding. In the FTIR spectra of PCL/CaSO₄ (figure 4.1.5 (c) & (d)), specific bands of both PCL and CaSO₄ are seen and characteristic bands of sulfate groups appeared at 640 cm^{-1} confirming the presence of CaSO₄ in the scaffolds.

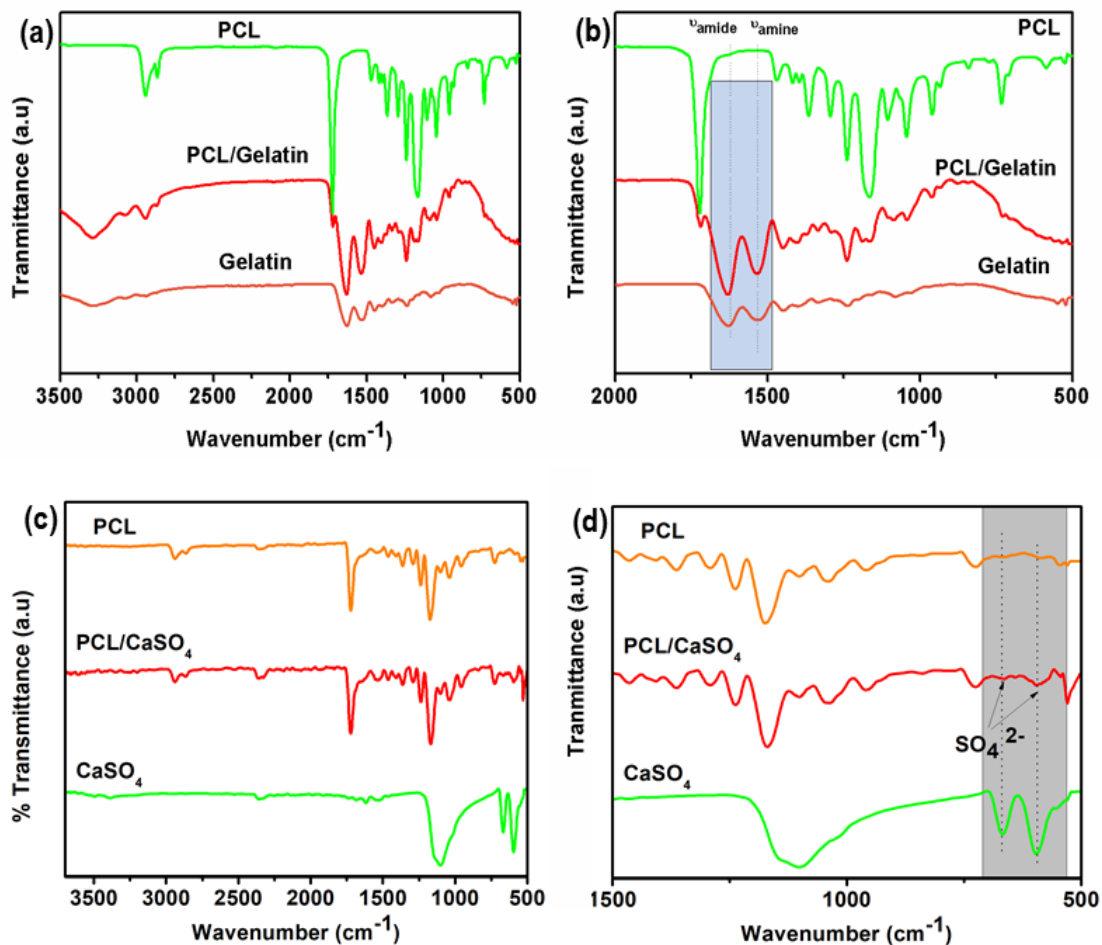


Figure 4.1.5: Analysis of chemical features. FTIR analysis of (a) & (b) 3D printed cartilage (PCL/Gelatin) and (c) & (d) bone (PCL/CaSO₄) phases.

4.1.1.2.4 Analysis of thermal features

The compositional analysis and the thermal stability of the blend in comparison with the components PCL and gelatin were studied using thermogravimetric analysis by heating the samples to 800 °C at a heating rate of 10 °C/min. The resulting thermogram is shown in figure 4.1.6 (a). PCL and gelatin are characterized by different types of thermograms. PCL is thermally stable up to 400 °C and follows a single decomposition pattern as indicated by the single peak in the DTG. At the same time, gelatin degradation starts from 100 °C resulting from the loss of adsorbed water molecules due to the hydrophilic nature of the gelatin which is followed by degradation between 200 to 400 °C and 400-800 °C due to protein degradation and decomposition of gelatin network respectively. The three-stage decomposition pattern of

the gelatin is confirmed by the DTG curve. The degradation of both PCL and gelatin is visible in the thermogram of the blend with a shift in the T_{max} (temperature with maximum degradation rate) towards the higher value of PCL concerning gelatin. This indicates the interaction between the PCL and gelatin. Moreover, the TGA and the DTG analysis confirm the thermal stability of the blend at the processing temperature (3D printing) which is mandatory for the effective mixing of the components without degradation or decomposition.

The thermogram of the scaffolds that mimic the bone phase in comparison with its component materials PCL and $CaSO_4$ are also depicted in figure 4.1.6 (b). The calcium sulfate used for the present work is in the form of dihydrate (gypsum) which exhibits a maximum degradation at $\sim 100^\circ C$ attributed to the removal of adsorbed water. During further heating to $800^\circ C$, the water of crystallization is driven off followed by the formation of anhydrate of $CaSO_4$ ($\sim 85\%$) which is stable up to the programmed temperature range. The thermogram of the PCL/ $CaSO_4$ blend is analogous to that of the PCL which is the main constituent, however with a slight enhancement in the maximum degradation temperature (T_{max}) from $401^\circ C$ to $408^\circ C$. Since the percentage of $CaSO_4$ present in the blend is 5 %, the small degradation at $\sim 100^\circ C$ for the blend is due to the adsorbed water on $CaSO_4$, which slightly reduces the onset temperature of degradation. On the other hand, the presence of $CaSO_4$ anhydrate which formed after $350^\circ C$ enhances the T_{max} of the blend.

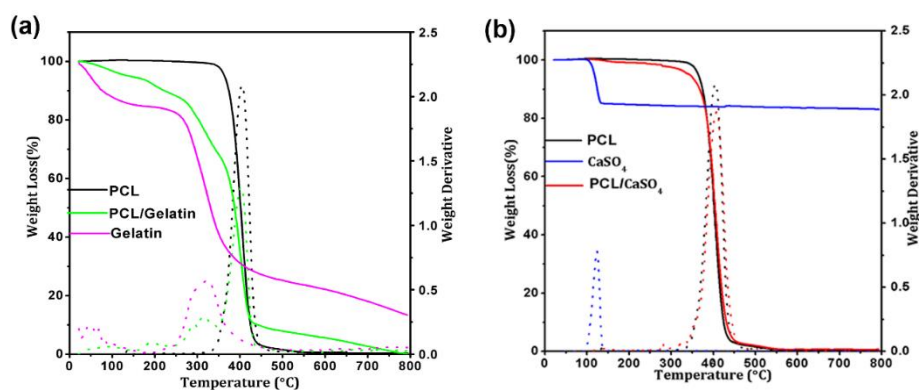


Figure 4.1.6: Analysis of thermal features by thermogravimetric analysis (TGA/DTG). (a) & (b) represents the TGA graph of cartilage (P/G) and bone phase (PCL/ $CaSO_4$) respectively.

4.1.1.2.5 Analysis of mechanical features

The compressive mechanical properties of four groups of cylindrical samples (3D printed PCL, 3D printed PCL/Gelatin, freeze-dried PCL, freeze-dried PCL/CaSO₄), of dimension 16 mm X 8 mm (height X diameter) were determined using an Instron tester (Instron 5848, USA).

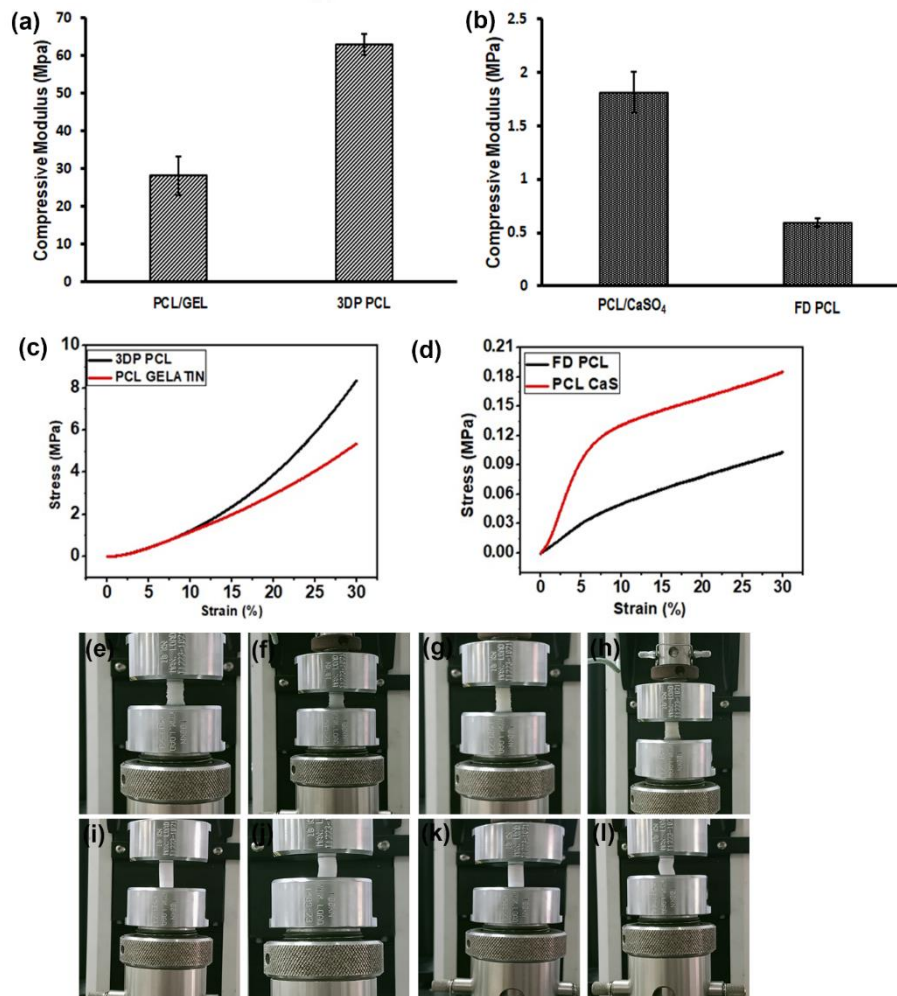


Figure 4.1.7: Analysis of mechanical features. (a) and (b) represents the compressive modulus and (c) and (d) represent the compressive stress-strain curve of cartilage and bone phase of the 3D printed scaffolds respectively when the scaffolds are compressed to 3mm. (e)-(l) represents the photomicrographs of scaffolds before and after compressive tests; (e) & (f) 3D printed PCL, (g) & (h) 3D printed PCL/Gelatin, (i) & (j) freeze-dried PCL/CaSO₄ and (k) & (l) freeze-dried PCL alone scaffolds.

The compressive modulus of articular cartilage is 1.36–39.2 MPa and subchondral bone are 1.4–9800 MPa (Yang et al., 2001). The fabricated cartilage scaffold showed greater compressive modulus when subjected to compressive loads. The compressive modulus at

maximum load when it is compressed to 3mm for the cartilage phase (3D printed PCL/gelatin) and its control (3D printed PCL alone) and bone phase (freeze-dried PCL/CaSO₄) and its control (freeze-dried PCL alone), is 28.2 ± 5 MPa, 62.90 ± 2.6 MPa, 1.8 ± 0.19 and 0.59 ± 0.04 respectively (figure 4.1.7 (a)-(b)). The stress-strain curve is represented in figures 4.1.7 (c)& (d). Images of mechanical testing for four groups of scaffolds are shown in figure 4.1.7 (e)-(l).

4.1.1.2.6 Analysis of degradation features

The influence of incorporating bioactive factor (CaSO₄) in the bone layer and blending Gelatin with PCL for the chondral layer on the degradation pattern of PCL-based scaffolds were analyzed qualitatively by SEM and quantitatively by weight changes. The results of *in vitro* degradation assessment of cartilage and bone phase at day 28 and day 90 are presented in Figure 4.1.8 (a)-(h) and PCL/Gelatin scaffolds showed a moderate degradation rate (<20%) by 28 days. However, by 90 days a significant mass loss ($\leq 50\%$) with appreciable changes in the morphology of the upper layers of the scaffold were observed. The SEM images of the cartilage (figure 4.1.8 (a)-(d)) phase showed degradation of the topmost layers and the prominence of intermediate and bottom layers. Also, the strut dimension was completely lost with the net-like appearance in the lower layers. These net-like strands were in the phagocyte size/length range. For the bone phase, upon quantitative estimation, negligible degradation was observed for freeze-dried PCL and PCL/CaSO₄ scaffolds upon immersion in PBS for 4 weeks (figure 4.1.8 (i)). However, from 28 days onwards a slower and steady degradation pattern was observed with 5% mass loss by 40 days was observed. Approximately 20% of the scaffold got degraded after 3 months of immersion in PBS. The SEM images revealed the appearance of micropores on the walls of the pores which will facilitate further degradation through the uptake of water (figure 4.1.8 (e)-(h)). In the control scaffolds, PCL also had a similar degradation pattern but the weight loss ratio was lower when compared to PCL/CaSO₄.

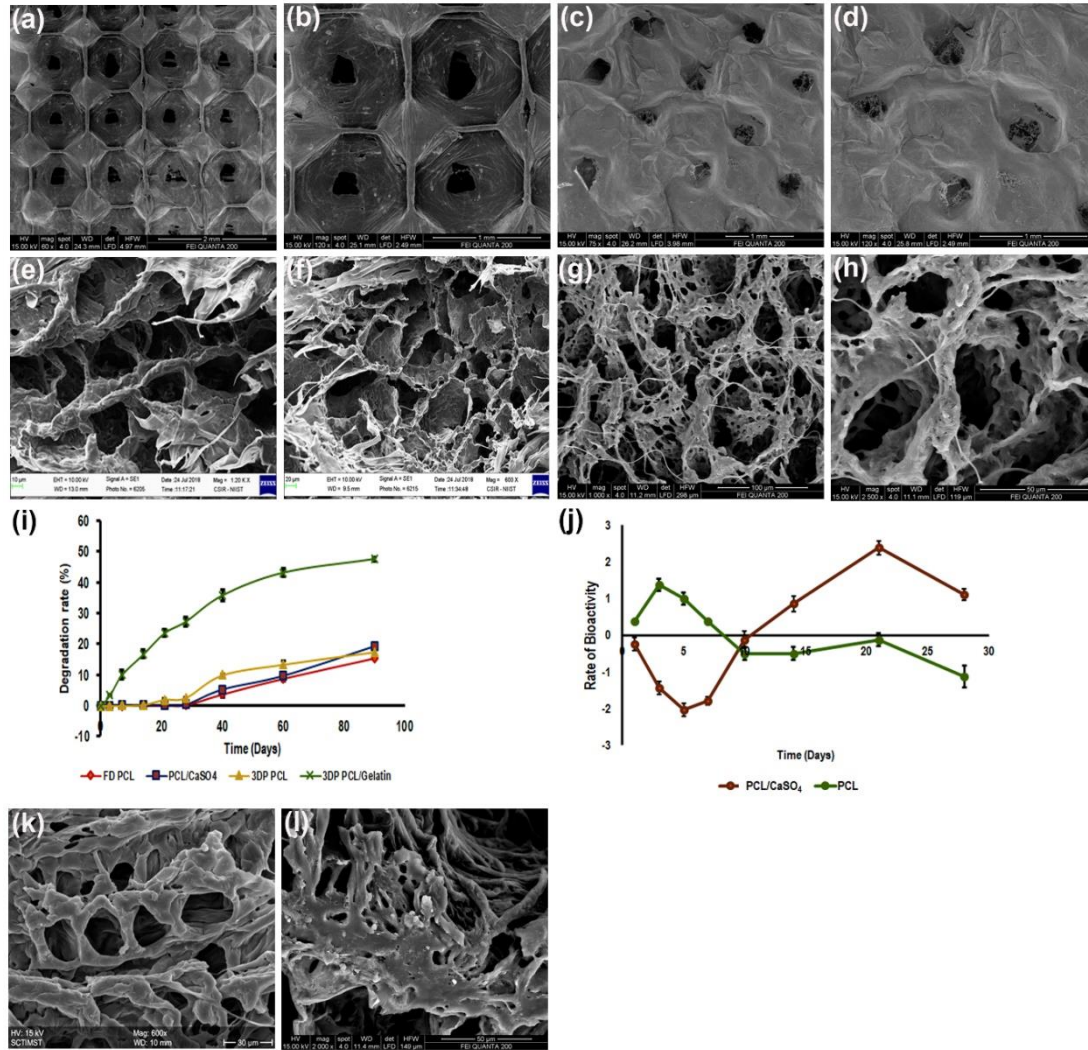


Figure 4.1.8: *In vitro* degradation of the scaffolds and *in vitro* bioactivity study of the bone phase. Representative SEM images of PCL/Gelatin after 28 (a)-(b) and 90 (c)-(d) days of incubation in PBS. (e)-(f) and (g)-(h) are the respective images of PCL/CaSO scaffolds after 28 and 90 days of incubation in PBS. (i) the graphical representation of weight change (degradation rate (%)) after three months of incubation in PBS. (j) represents the quantitative estimation of *in vitro* bioactivity of scaffolds (PCL and PCL/CaSO₄ scaffolds) in SBF (n = 3) for the time duration of 28 days. (k) & (l) represents the SEM images of *in vitro* bioactivity of PCL alone and PCL/CaSO₄ respectively, after 28 days.

4.1.1.2.7 Assessment of *in vitro* bioactivity

The apatite mineralization ability of the bone phase of BPS (PCL/CaSO₄) was evaluated and the results indicate a simultaneous process of precipitation and dissolution (figure 4.1.8 (j)). The test scaffolds upon incubation in SBF showed an initial weight loss on days 1, 3, 5, and 7 suggestive of dissolution of ions into the solution followed by weight gain on days 10, 14, and 21, indicating the process of precipitation of ions suggesting a weight gain. On the other side,

PCL alone scaffolds showed less appreciable weight gain throughout the study period. SEM analysis of the osteogenic phase of the BPS showed mineralization of the surface by day 28 (figure 4.1.8 (l)) when compared to its respective control (k). Thus, *in vitro* bioactivity studies confirmed the ability of the bone phase to undergo biomineralization.

4.1.1.2.8 Assessment of *in vitro* cytocompatibility

a. Cell Viability by Live dead assay.

The *in vitro* biological properties of the developed biphasic scaffolds were characterized by cell viability assay to confirm that the degradation products of components of scaffolds are non-toxic. The Live-Dead Assay performed using L929 cells revealed that (figure 4.1.9), both the cartilage (P/G) and bone phase (PCL/CaSO₄) demonstrated good cell viability at 7 days of *in vitro* culture (figure 4.2.9 (a)-(c)) and are favorable for cell survival and retention.

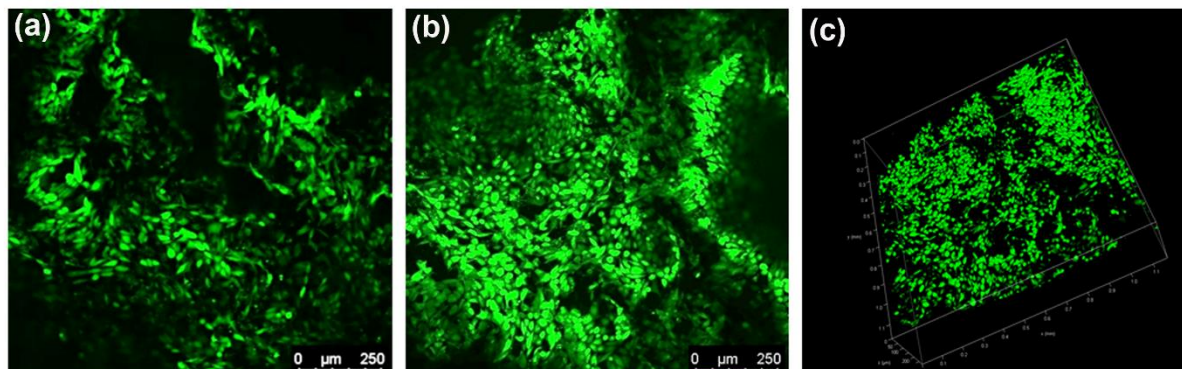


Figure 4.1.9: *In vitro* cytocompatibility assessment. Confocal microscopic images of the viability of L929 cells on Day 7 on the (a) 3D printed PCL/Gelatin cartilage phase, (b) freeze-dried PCL/CaSO₄ bone phase, and (c) biphasic scaffolds (BPS): maximum projection (a) & (b), volume viewer (c).

b. Cell Viability by MTT assay

Figure 4.1.10 presents the *in vitro* cytotoxicity test on cartilage and bone phase respective to control using L929 at incubation periods of 1, 2, and 3 days, using MTT assay and confirmed that the scaffolds demonstrated no pernicious effects on the viability of cells. No significant difference was observed between the experimental groups and the negative control group (figure 4.1.10 (a) & (b)) of immersion. Meanwhile, the addition of 5% DMSO, denoted as the positive control group, showed significant inhibition of the growth of cells. It is evident from

the results that the operating conditions of 3D printing and processing the scaffolds during lyophilization doesn't affect the viability and are thus highly cytocompatible.

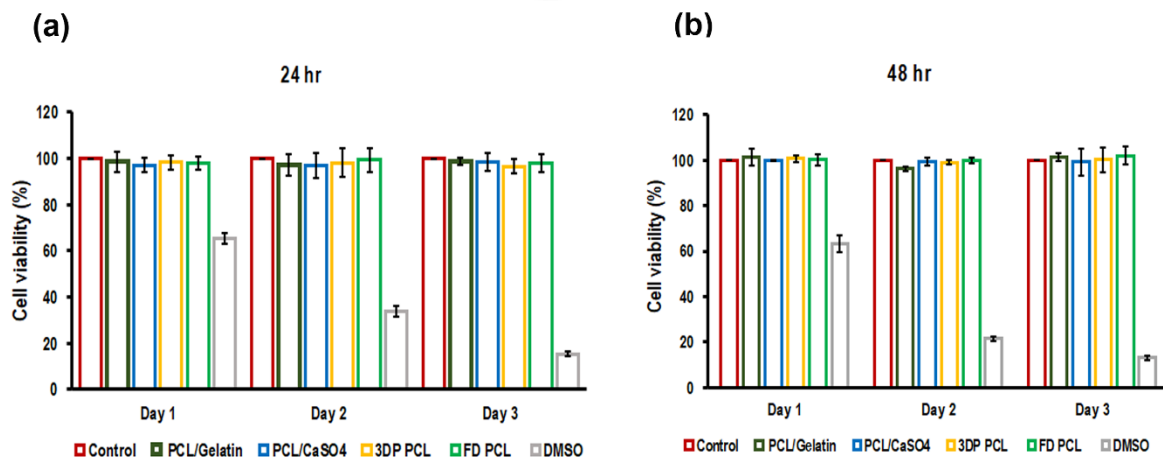


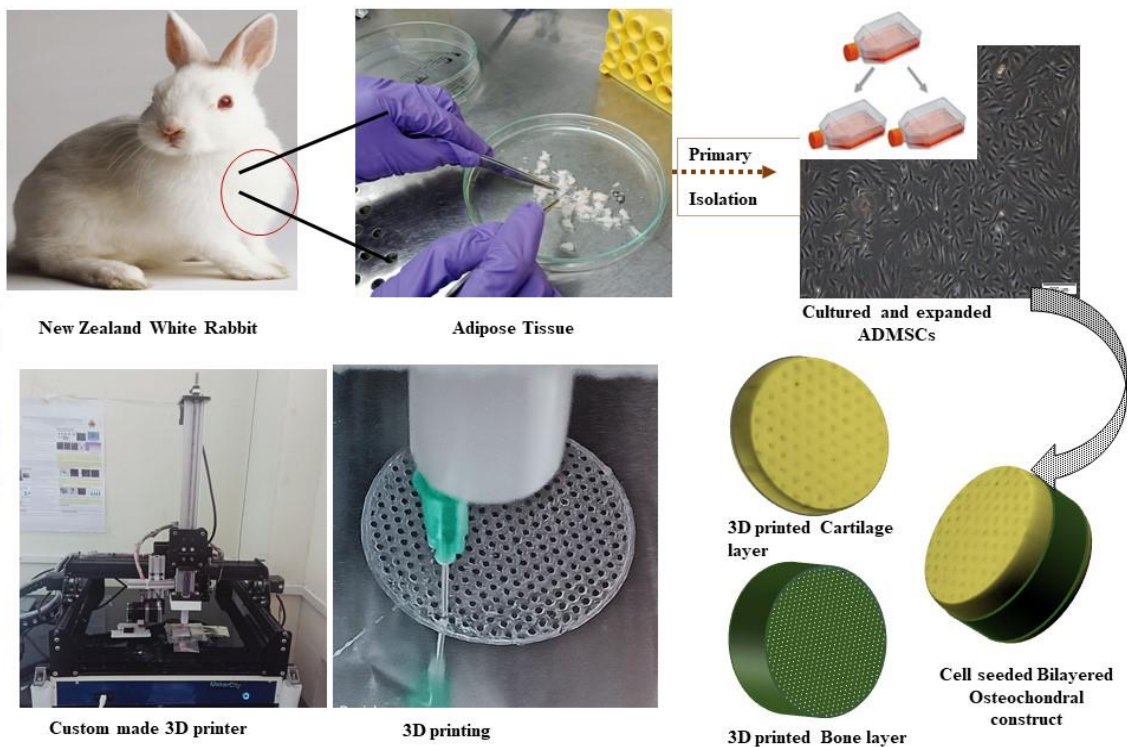
Figure 4.1.10: *In vitro* Cytocompatibility assessment of scaffolds on L929 cells by MTT assay showing the viable number of cells at 24 hr (a) and 48 hr (b).

4.1.2 System B – BPS fabricated via 3D printing and dissolution adhesion technology

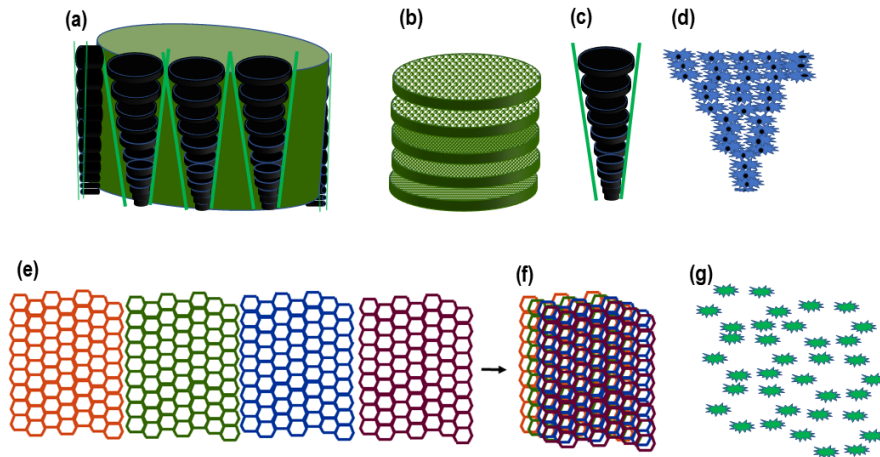
4.1.2.1 Fabrication of biphasic scaffolds (BPS) by 3D printing:

The BPS was developed in three steps, beginning with the printing of the cartilage phase, followed by the fabrication of the bone phase, and finally, the two phases were adhered together to form the biphasic osteochondral construct. Scheme 4.3 depicts a schematic representation of the workflow. The optimized printing conditions for 3D scaffolds are provided, including solution concentration and various parameters such as printer speed, layer height, flow rate, drawing pattern, and nozzle diameter (Table 8). For that, different concentrations of PCL/PLGA solutions with incorporated factors were tried, and finally PCL: PLGA: Factors (CS in cartilage phase and β TCP in bone phase) in the ratios 65:30:5 and 62.5: 31.25: 6.25 were found to be suitable for printing gradient layers with optimal porosity and thickness. The hierarchical architectural pattern of native tissues was replicated by printing layers with varying infill density based on a model created with 123 design software (Figure 4.2.1(a) & (b)). The first layer was printed with 50% infill density, and the remaining overlapping layers from bottom to top were printed with 40%, 30%, and 25% for the cartilage layer, whereas for bone

20% and 50 % form the top and bottom layer respectively, for directing osteochondrogenesis. The schematic representation of pore distribution is given in Scheme 4.4. Based on our studies, the specific infill density at the top was chosen to facilitate easy cell seeding, while the density at the bottom was chosen to prevent cell leakage during seeding. Different drawing patterns were tested, and the cubical pattern appears to be best suited for cartilage phase scaffolds (figure 4.2.1(d) & (f)), while the honeycomb pattern appears to be best suited for bone scaffolds ((figure 4.2.1(e) & (g)), and thus these patterns were chosen for developing respective scaffolds. Three groups of cylindrical scaffolds (PCL/PLGA, PCL/PLGA/CS, PCL/PLGA/ β TCP) of the same dimensions, 30 (D) X 2 (H) mm were constructed through 3D printing. A 1 cm diameter punch is used to cut the scaffolds of dimensions 10 (D) X 2 (H) mm (cartilage phase) and 3 mm(H) (bone phase) for further studies. The macroscopic features of the 3D-printed cartilage and bone phase are given in figure 4.2.1(d)– 1(g).



Scheme 4.3: Fabrication of the bi-layered scaffold – schematic representation of the workflow.



Scheme 4.4: Schematic representation of the gradient pores and cell alignment in the cartilage phase. The pore distribution is represented in (a), gradient layers with varying infill density in (b), gradient pores in (c), and the cell arrangement pattern in the gradient pores are shown in (d). (e), (f) and (g) represent individual layers, gradient layers in honeycomb patterns, and the cellular pattern in designed pores respectively.

Table 8: Printing parameters

	Cartilage Phase	Bone Phase	Control
Concentration of printing solution	65:30:5	62.5: 31.25: 6.25	65:35
(Print Thick) (mm)	0.26	0.26	0.26
Nozzle temperature ($^{\circ}$ C)	25	25	25
Platform temp ($^{\circ}$ C)	25	25	25
Print Speed (mm/s)	10	8	10
Layer height (mm)	0.1	0.1	0.1
First layer height	0.2	0.2	0.2
Infill density (%)	25, 30, 40, 50	20, 30, 40, 50	25, 30, 40, 50
Probe type	23 Gauge needle (0.33 mm inner diameter)	23 Gauge needle (0.33 mm inner diameter)	23 Gauge needle (0.33 mm inner diameter)
Print layer	35	33	35
Print pattern	Cubical	Honeycomb	Cubical
Filling distance between adjacent pores in the topmost layer (Strut width) (mm)	1	0.7	1
Scaffold thickness (mm)	2	3	2

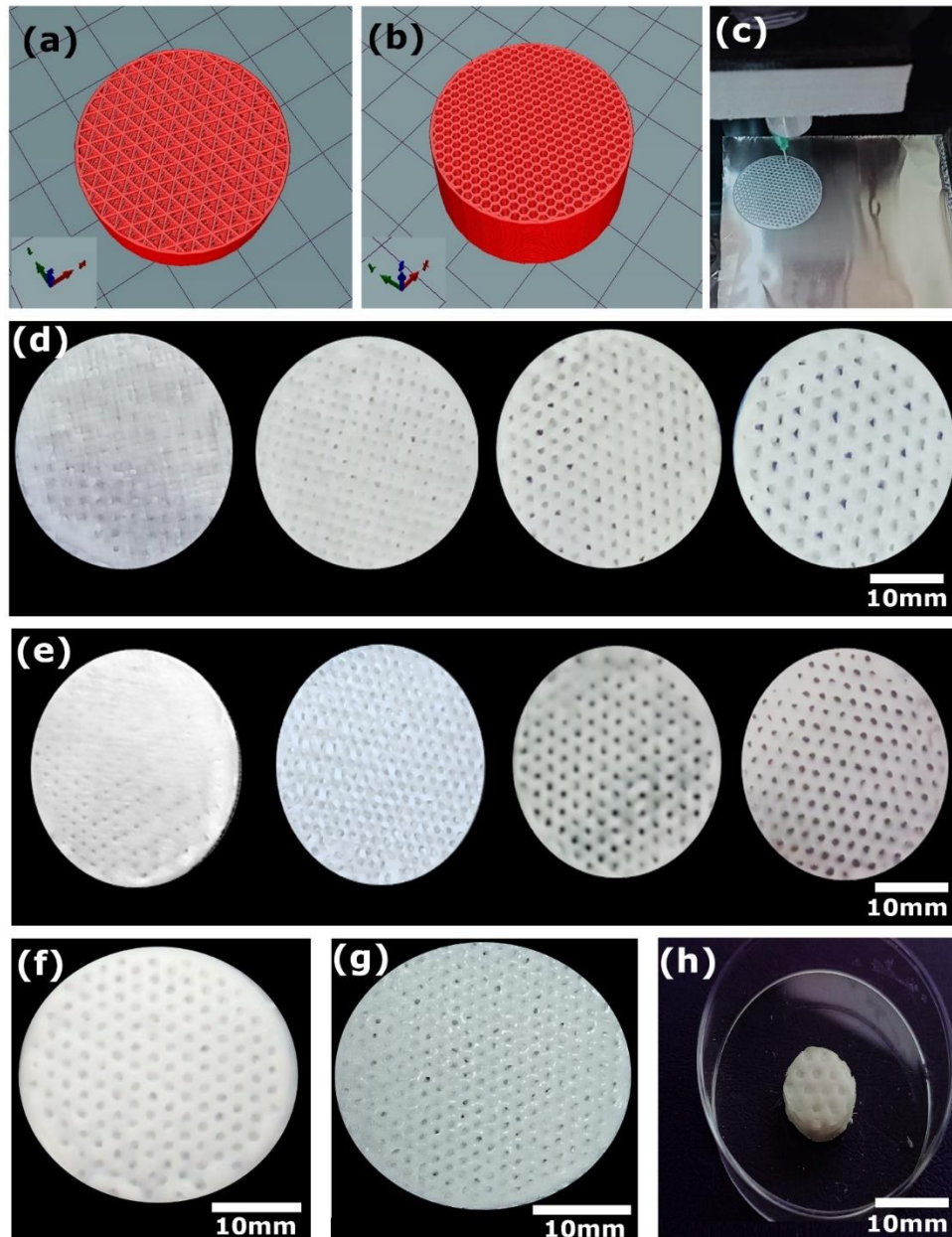


Figure 4.2.1: BPS fabricated via 3D printing and dissolution adhesion technology. (a) & (b) show the 3D model created for the upper cartilage and lower bone phase by using the 123-design software, converted into an STL file, and further sliced using Repetier Host. The scale of the model in (a) and (b) created through 123 design in XYZ coordinates is 1, 1, 0.5 (1=30.00 mm: X=30mm, Y=30mm, and 1=10mm: Z=0.5 mm); (c) shows a single layer of scaffold printed by the 3D printer (Maker City), (d) & (e) represents the macroscopic view of 3D printed individual layers for cartilage and bone scaffold respectively with decreasing infill densities (from left to right), (f) & (g) represent the macroscopic view of gradient cartilage and bone phase respectively with varying infill densities and (h) represents the photograph of the PCL/PLGA based biphasic scaffold (BPS) with bio factors incorporated of dimension 10mm (D) X 5mm (H) (top view).

Finally, the osteochondral constructs were made by the solvent-mediated amalgamation of the chondral phase (PCL/PLGA/CS) and bone phase (PCL/PLGA/ β TCP) and represented

as biphasic scaffolds (BPS) (figure 4.2.1(h)). The thickness of the top and bottom phases in the osteochondral construct is 2 and 3 mm, respectively. The two phases adhered together unfaillingly and were stable throughout the culture period.

4.1.2.2 Characterization of individual scaffolds and biphasic scaffolds:

4.1.2.2.1 Analysis of morphological features

The morphological and microstructural features of the scaffold were assessed by SEM analysis and the 3D printed porous structure featured a homogeneous and controlled structure. SEM images of three groups of (PCL/PLGA, PCL/PLGA/CS, PCL/PLGA/ β TCP) scaffolds at different magnifications are depicted in Figure 4.2.2. The scaffolds showed open, well-controlled, and interconnected porous structures. The surface of the PCL/PLGA scaffold was smooth and dense (figures 4.2.2 (a)–(d)), whereas the PCL/PLGA/CS and PCL/PLGA/ β TCP surface were rough owing to the presence of CS and β TCP particles (figure 4.2.2 (e)–(l)). In particular, the PCL/PLGA/CS and PCL/PLGA/ β TCP layers showed a cubic and honeycomb pattern respectively. SEM images revealed three-dimensionally intersecting pores with precise alignment of the struts separating the pores and the thickness of these struts is approximately 0.8-1 mm (figures 4.2.2 (a), (e), and (i)). A total of 35 (upper) and 33 (lower) layers are thus printed to get the designed thickness. The continuous filaments were deposited layer-by-layer and interconnected pores with a size of about 700 and 800 μ m at the topmost layer for cartilage and bone phases respectively. The pore sizes gradually reduced towards the bottom to form a narrow column of less than 20 μ m at the bottom (50% infill density) (figure 4.2.2 (m)). Higher magnification images indicated tightly integrated individual layers with a seamless interface between the cartilage and lower bone zone, (figure 4.2.2 (n)) which would prevent the cells from the bone phase from infiltrating the cartilage phase. The structural continuity at the interface of each phase is of great importance to improve the mechanical strength of the

scaffold showing the effective integration of the chondrogenic and osteogenic phases of the biphasic scaffold.

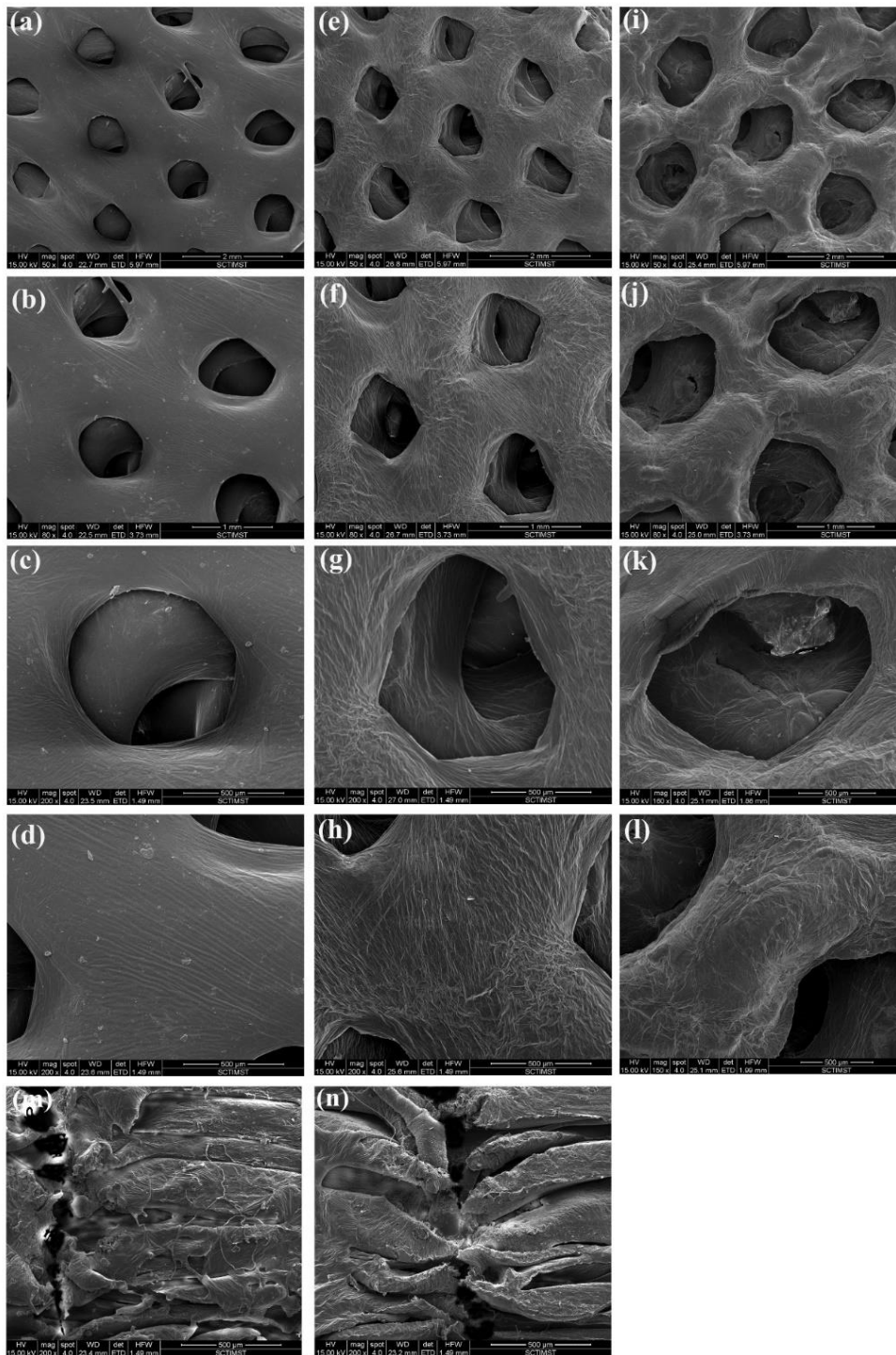


Figure 4.2.2: Analysis of morphological features by SEM of the scaffolds. (a) – (d), (e) – (h), and (i)- (l) represents the SEM micrographs of PCL/ PLGA scaffolds, PCL/PLGA/CS-based cartilage phase, and PCL /PLGA/βTCP based bone phase respectively at low and high magnifications. The SEM image showing gradient pores of the cartilage phase is depicted in (m) and (n) shows the structural continuity at the interface between the two phases.

4.1.2.2.2 Analysis of chemical features

ATR-FTIR analysis was carried out for analysis of surface groups on the fabricated scaffolds. Figure 4.2.3 (a) & (b) shows the FTIR spectra of PCL/PLGA/CS 3D printed scaffolds. In the infrared spectra, characteristic peaks for PCL and PLGA were observed for PCL/PLGA/CS scaffolds. These include $\sim 2941.9\text{ cm}^{-1}$ (asymmetric CH_2 stretching), $\sim 2864.5\text{ cm}^{-1}$ (symmetric CH_2 stretching), $\sim 1722.6\text{ cm}^{-1}$ (carbonyl stretching), $\sim 1290.6\text{ cm}^{-1}$ (C–C stretching) and $\sim 1237.9\text{ cm}^{-1}$ and $\sim 1164\text{ cm}^{-1}$ (asymmetric COC stretching). Common bands of chondroitin sulfate appeared at $\sim 830\text{ cm}^{-1}$ and 580 cm^{-1} which corresponds to the sulfate groups, confirming the presence of CS in the hybrid scaffolds. In the FTIR spectra of PCL/PLGA/ β TCP (figure 4.3.3 (c) & (d)), specific bands of PCL, PLGA, and β TCP were seen, and characteristic bands of phosphate groups appeared at 1025 cm^{-1} and 607 cm^{-1} confirming the presence of β TCP in hybrid bone scaffolds.

4.1.2.2.3 Analysis of thermal features

From the TGA/DTG results, the composition of the blend for the bone and cartilage phase can be determined (figure 4.2.3 (e) & (f)). PCL/PLGA blend is stable up to 280.79°C and shows a two-stage decomposition confirming the presence of two components. CS incorporated cartilage phase shows a three-stage decomposition relating to the presence of three components in the blend and is stable up to 226.98°C , followed by weight loss of 22.82 % and 87.1% at 361.72°C and 439.47°C respectively. However, the β TCP incorporated layer is stable up to 279.30°C , and as the thermal decomposition temperature of β TCP is above 1450°C , the DTG graph shows the thermal decomposition of PCL and PLGA only. From DTG, the thermal stability of the PCL component in all the three blends shows a similar trend whereas the PLGA exhibits variation. Hence upon blending with CS and β TCP, the thermal stability of the PCL/PLGA blend is slightly modified. The temperature at 85% loss (T_{85}) shows a shift from 340°C to 350°C confirming the increase in thermal stability. Notably, the decomposition

residue of CS enhanced the thermal stability of the PCL/PLGA blend and showed a higher percentage of char residue after the heating process. DSC thermogram of cartilage and bone phase showed an endotherm at 62°C and 60°C respectively, corresponding to the melting of PCL (figure 4.2.3 (g)). The β TCP in the bone phase reduces the melting temperature (T_m) of PCL, thereby lowering the processing temperature for PCL melt. A broad endothermic peak curve was also observed at 190°C for the cartilage phase, and it could be assigned to the melting of PLGA. In the case of the bone phase, the corresponding peak intensity is less indicating a different crystal size or shape of the PLGA due to the presence of β TCP.

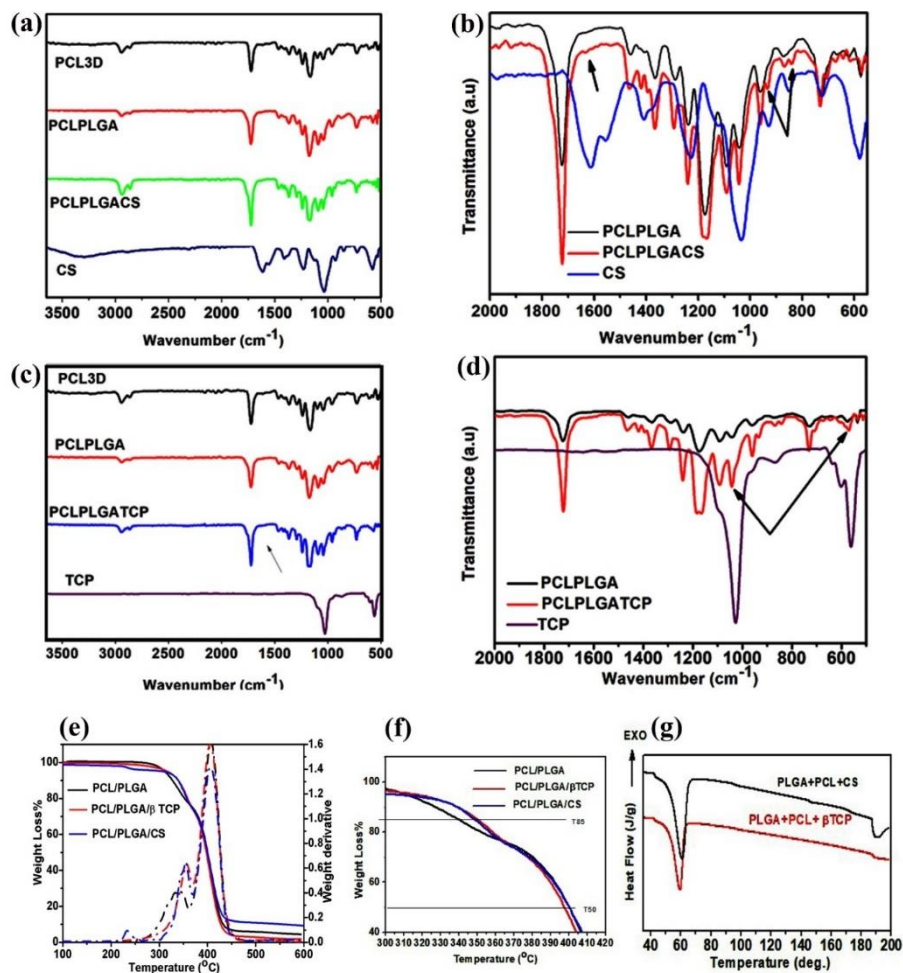


Figure 4.2.3: Analysis of chemical and thermal features. FTIR analysis of (a) & (b) 3D printed cartilage (PCL/PLGA/CS) and (c) & (d) bone (PCL/PLGA/ β TCP) phase (e) & (f) represents the TGA graph where the weight percentage of resulting mass change of each component of hybrid scaffolds upon the increase in temperature is measured and (g) represents the DSC graph in which heat flow into or out of the sample is measured as a function of temperature.

4.1.2.2.4 Analysis of wettability features

Water contact angle images are illustrated in Figure 4.2.4. The water angle of the composites decreased, and the surface hydrophilicity increased with the addition of PLGA and bioactive factors. The average values of the contact angles of PCL/PLGA ($93.3\pm 3.60^\circ$), PCL/PLGA/CS ($81.3\pm 1.9^\circ$), and PCL/PLGA/ β TCP ($87.2\pm 2.8^\circ$) and were significantly lower when compared to PCL alone ($115\pm 2.2^\circ$) (figure 4.3.4 (a)-(d)).

4.1.2.2.5 Analysis of mechanical features

The fabricated cartilage scaffold showed greater compressive modulus when subjected to compressive loads. The compressive modulus at maximum load when it is compressed to 4 mm for control (PCL/PLGA), cartilage (PCL/PLGA/CS), and Bone layers (PCL/PLGA/ β TCP is 16.21 ± 1.2 MPa, 30.20 ± 1.3 MPa and 25.13 ± 1.1 respectively (figure 4.2.4 (e)). The stress-strain curve is represented in figure 4.2.4 (f). The photomicrographs of mechanical testing for three groups of scaffolds are shown in figure 4.2.4 (g)-(l).

4.1.2.2.6 Analysis of degradation features

The results of *in vitro* degradation assessment are presented in Figure 4.2.5. Upon quantitative estimation, only 2% of the scaffolds (both PCL/PLGA and BPS with bio factors) have degraded upon immersion in PBS for 3 weeks (figure 4.2.5(c)). However, from 28 days onwards a higher degradation rate was observed in BPS scaffolds when compared to PCL/PLGA. Approximately 35% of BPS scaffold got degraded after 3 months of immersion in PBS. Though the initial degradation pattern of the control scaffolds PCL/PLGA was similar to BLS, they showed a slower and steady weight loss ratio for up to 3 months. The SEM images of cartilage (figure 4.2.5 (a) and bone surface (figure 4.2.5 (b)) show degradation of the topmost layers and the prominence of intermediate and bottom layers with diminished pores were seen. The images in the inserts show the surface morphology of scaffolds without immersing in PBS.

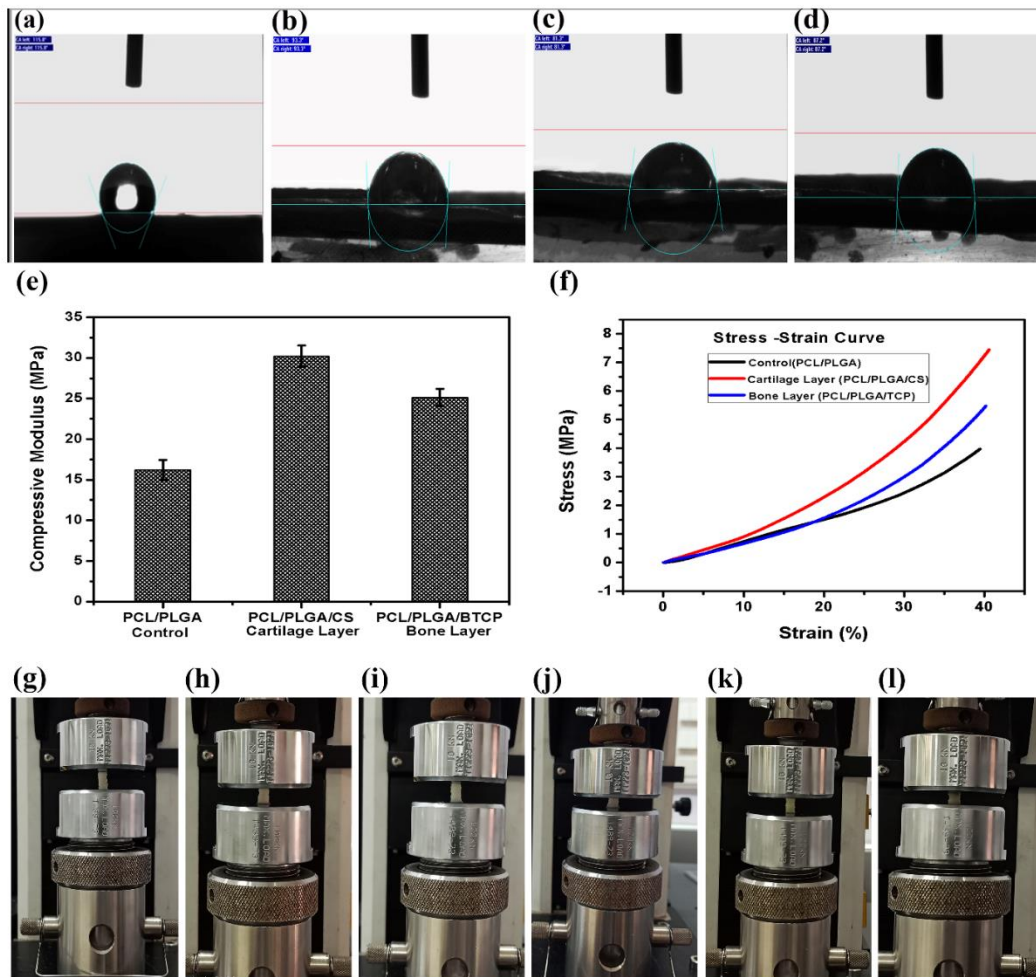


Figure 4.2.4: Analysis of wettability and mechanical features. (a), (b) (c) & (d) represents contact angle and droplet profile after 5 sec on 3D printed PCL alone ($115\pm 2.2^\circ$), PCL/PLGA ($93.3\pm 3.60^\circ$), PCL/PLGA/CS ($81.3\pm 1.9^\circ$) and PCL/PLGA/βTCP ($87.2\pm 2.8^\circ$) respectively. (e) and (f) represents the compressive modulus and compressive stress-strain curve for the 3D printed scaffolds when the scaffolds are compressed to 4mm. (g)-(l) represents the photomicrographs of scaffolds before and after compressive tests (g) & (h) PCL/PLGA, (i) & (j) PCL/PLGA/CS, (k) & (l) PCL/PLGA/βTCP scaffolds.

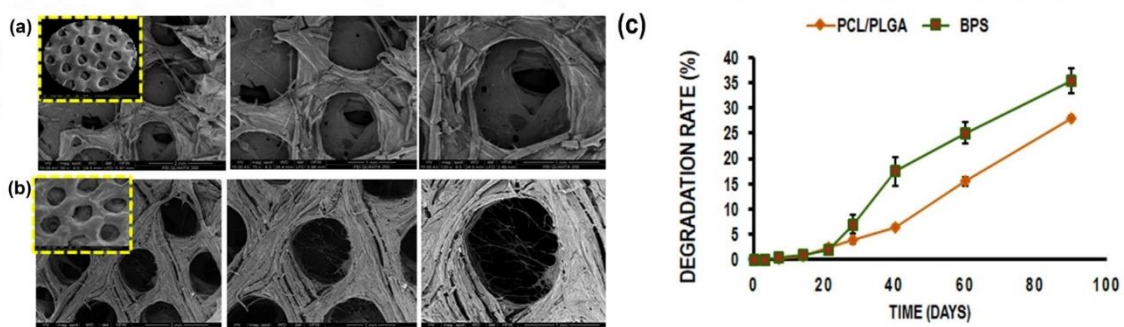


Figure 4.2.5: Analysis of *in vitro* degradation of developed scaffolds. The representative SEM images of the degradation pattern of the cartilage phase of BPS (a) and bone phase of BPS (b), after 3 months are shown. The inserts are representative images of scaffolds without immersion in PBS. The quantitative estimation of *in vitro* degradation rate of scaffolds (biphasic and PCL/PLGA scaffolds) in PBS ($n = 3$) for the time duration of 90 days is represented in (c).

4.1.2.2.7 Assessment of *in vitro* bioactivity

The bioactivity assessment of β TCP incorporated scaffolds was performed and the PCL/PLGA/ β TCP scaffolds upon incubation in SBF showed initial weight loss on days 1 and 3 followed by a net weight gain on days 7, 14, 28, and 40. On the other side, the PCL/PLGA scaffolds showed progressive weight loss up to 21 days followed by marginal weight gain on days 28 and 40 (figure 4.2.6 (a)). SEM analysis of the osteogenic phase of the BPS showed mineralization of the surface by day 28 (figure 4.2.6 (b) & (c)). Thus, the bioactivity assessment of β TCP incorporated scaffolds indicates a simultaneous process of precipitation and dissolution and confirmed the biomineralization ability of the bone phase.

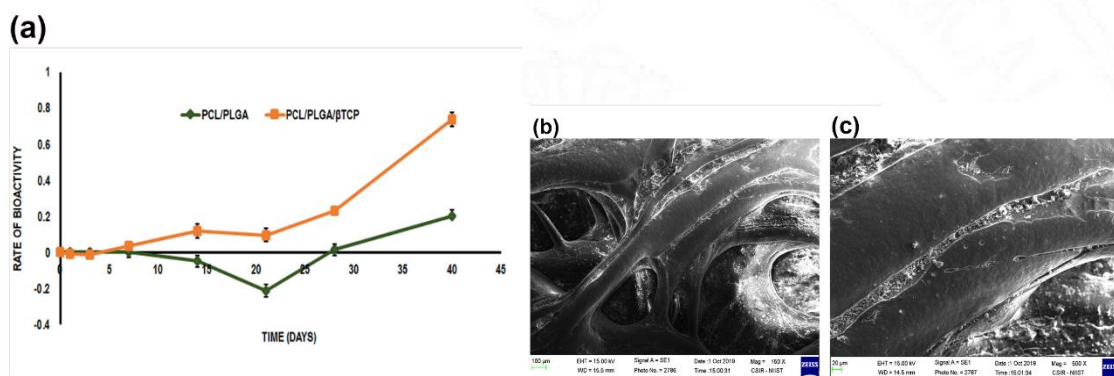


Figure 4.2.6: Assessment of *in vitro* bioactivity. The quantitative estimation of *in vitro* bioactivity of scaffolds (PCL/PLGA and PCL/PLGA/ β TCP scaffolds) in SBF ($n = 3$) for the time duration of 40 days is represented in (a). The SEM images of *in vitro* bioactivity of bone phase ((b) & (c)), after 28 days are also shown.

4.1.2.2.8 Assessment of *in vitro* cytocompatibility

a. Cell Viability by Live dead assay

Cellular activity assessment via Live/Dead assay using L929 cells revealed that the 3D printed scaffolds (i.e., PCL/PLGA/CS, PCL/PLGA/ β TCP, BPS) have a greater number of living cells with few dead cells (figure 4.2.7 (a), (b) & (c)) after 3 days of culture in the complete growth medium, with no alterations on the morphology of cells.

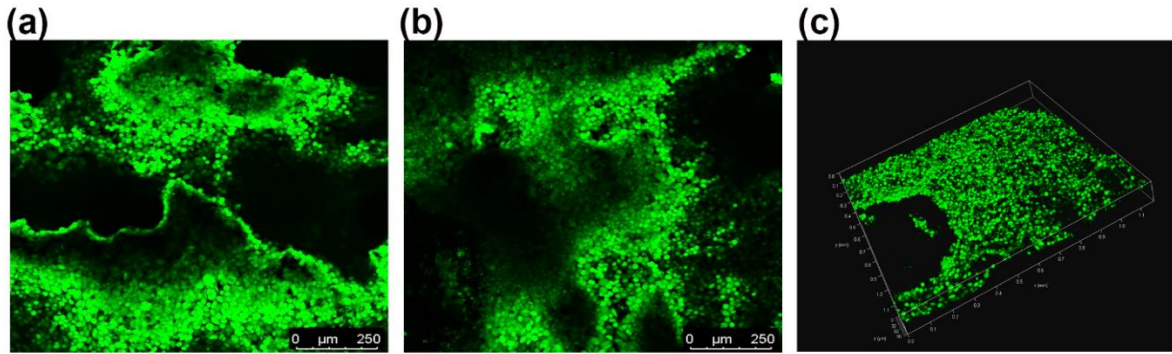


Figure 4.2.7: Assessment of *in vitro* cytocompatibility assessment, (a), (b) & (c) shows confocal microscopic images of the viability of L929 cells on the cartilage phase, bone phase, and biphasic scaffolds (BPS) respectively on 3rd day.

b. Cell Viability by MTT assay

Moreover, the *in vitro* cytotoxicity test at 24 hours and 48 hours, using the MTT assay confirmed that the scaffolds had no detrimental effects on the viability of cells (figure 4.2.8 (a) & (b)). No differences between the experimental groups and the control groups were observed. Further, cells cultured on scaffolds containing CS and β TCP showed higher metabolic activity than those cultured on monolayer or bare PCL/PLGA scaffolds. It is evident from the results that there is no residual solvent, (1, 4 Dioxan) on the 3D printed scaffolds, suggesting that the excess solvent was entirely removed by air drying overnight in a fume hood. This indicates that the materials tested (i.e., PCL/PLGA, PCL/PLGA/CS, PCL/PLGA/ β TCP composites) were non-cytotoxic and able to support attachment, proliferation, and viability of ADMSCs.

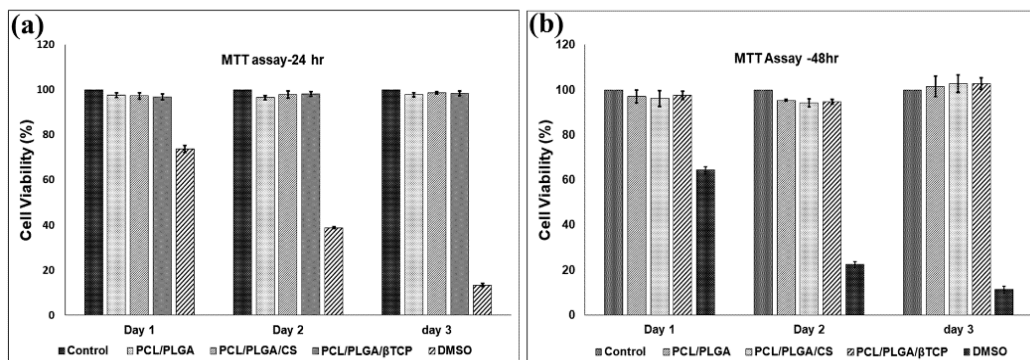


Figure 4.2.8: Analysis of cytotoxicity. MTT assay performed between the control group and the test groups after the periods of 24 hours (a) & 48 hours (b).

4.1.3 System C – BPS fabricated via 3D printing

In this study, we have incorporated biofactors into PCL/PVP printing solution and further complexed with PAA to prevent z-axis collapse and to fabricate diverse but closely integrated phases with designed dimensions mimicking respective niches of osteochondral tissues. The collaborative contribution of complexation in creating structures or channels within porous scaffolds as well as the effect of the presence of biofactors are studied in this system.

4.1.3.1 Fabrication of biphasic scaffolds (BPS) by 3D printing:

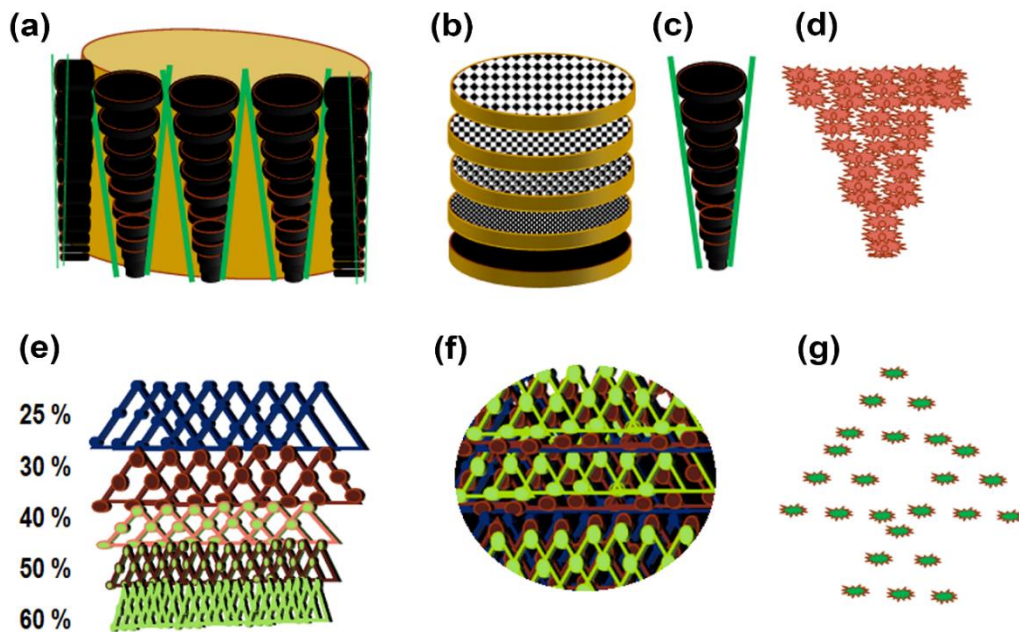
The biphasic osteochondral constructs were fabricated by a two-step process comprising an oriented 3D printed (3DP) PCL/PVP/CS/PAA (3DPPPCS)-derived cartilage phase and a 3DP porous PCL/PVP/ β TCP/PAA (3DPPPT) bone phase with pores arranged in a specific pattern using our room-temperature- 3DP machine (Maker City, India), based on optimized parameters (Table 9). The schematic representation of the workflow is given in Scheme 4.5. Firstly, the bone phase was fabricated where the layers are printed from an adequately blended solution of PCL/PVP/ β TCP/PAA in optimized concentration 72:25:3 spurted out layer by layer, with varying infill density (ID) in a star pattern as a close-packed array separated by a strut width of 0.3 mm and a wall thickness of 0.2mm (layer height) with a well-ordered porous structure by a computer-driven nozzle to form a homogenous cubic porous scaffold. The topmost layer is printed with 25% ID, followed by increasing the ID; to 30, 40, 50, and 60 % for subsequent bottom layers, and a total of 30 layers are printed with the final scaffold thickness of 3mm (figure 4.3.1(d)). Subsequently, the seamless cartilage phase was fabricated from a solution of PCL/PVP/CS/PAA (72:24:4) on the top of the bone scaffold which was upturned with the face having 60% infill density using the optimized 3DP protocol to form the compact composite BPS. The cartilage phase is printed in a cubical pattern with a strut width (filling distance between adjacent pores in the topmost layer) of 0.5mm and a wall thickness (layer height) of 0.2mm with varying infill density (ID) from top to bottom with the total scaffold thickness of

3mm. The hierarchical architectural pattern of native tissues is reproduced by printing the layers with different infill densities where the topmost layer is printed with 25% ID, followed by increasing the ID; 30, 40, 50, and 60 % for subsequent bottom layers in the room-temperature production chamber (figure 4.3.1 (c)). The schematic representation of pore distribution is given in Scheme 4.6. Finally, the BPS was cut into a cylindrical shape with a diameter of 10 mm and a total height of 6 mm (the upper cartilage phase was 3.0 mm, and the porous bone phase was 3.0 mm each) (figure 4.3.1 (e)). The thickness of the top and bottom phases is 3.0 and 3.0 mm, respectively; which are very close to the designed thickness. Also, the individual phases are found to be seamlessly integrated, which is of great importance to improve the mechanical strength of the scaffold and prevent cells from infiltrating the cartilage phase.

Table 9: Printing parameters

	Cartilage Phase PCL/PVP/PAA/CS	Bone Phase PCL/PVP/PAA/ β TCP	Control PCL/PVP/PAA
Concentration of printing solution	72:24:4	72: 25 :3	75:25
Feed rate	182	170	150
Flow rate	100	106	100
Nozzle temperature ($^{\circ}$ C)	25	25	25
Platform temp ($^{\circ}$ C)	25	25	25
Print speed (mm/s)	10	10	10
Layer height (mm)	0.2	0.18	0.1
First layer height	0.2	0.18	0.1
Infill density (%)	25, 30, 40, 50,60	25, 30, 40, 50, 60	25, 30, 40, 50,60

Probe type	22 Gauge needle (0.413 mm inner diameter)	22 Gauge needle (0.413 mm inner diameter)	22 Gauge needle (0.413 mm inner diameter)
Print layer	30	30	30
Print pattern	Cubical	Star	Cubical
Filling distance between adjacent pores in the topmost layer (Strut width) (mm)	0.5	0.3	0.6
Scaffold thickness (mm)	3	3	3



Scheme 4.5: Schematic representation of the gradient pores and cell alignment in the cartilage and bone phase. The pore distribution in cartilage phase is represented in (a), gradient layers with varying infill density in (b), gradient pores in (c), and the cell arrangement pattern in the gradient pores are shown in (d). (e), (f) and (g) represent the individual layers of bone phase, gradient layers in star patterns, and the cellular arrangement pattern in designed pores respectively.

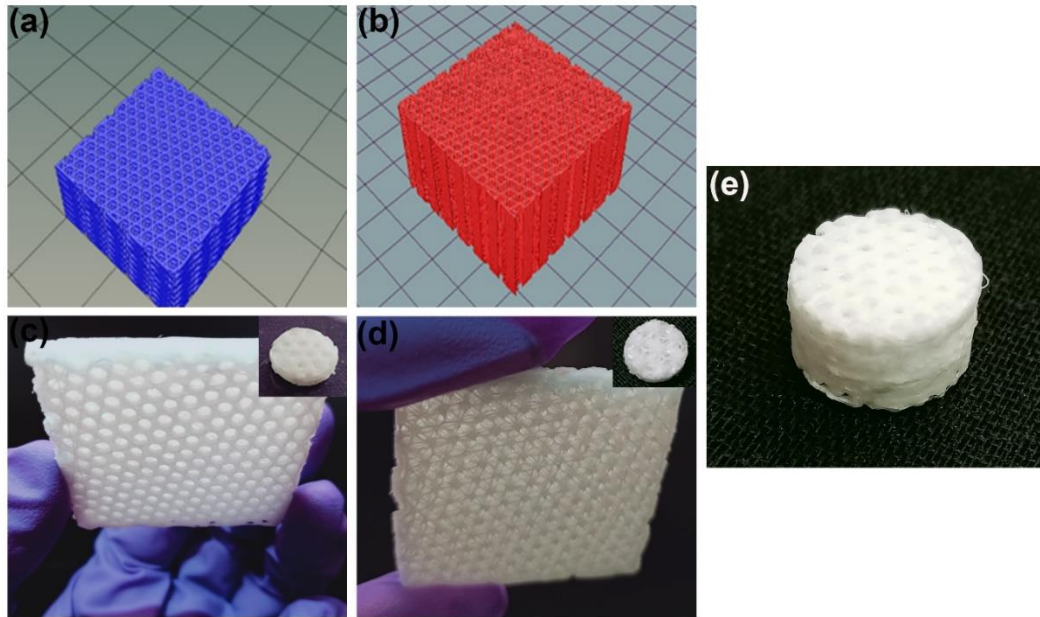


Figure 4.3.1: BPS fabricated via 3D printing. (a) & (b) show the 3D model created for the upper cartilage and lower bone phase by using the 123-design software, converted into an STL file, and further sliced using Repetier Host. The scale of the model in (a) and (b) created through 123 designs in XYZ coordinates is 1, 1, 0.3 (1=50.00 mm: X=50mm, Y=50mm and 1=10mm: Z= 3mm); (c) & (d) represent the macroscopic view of gradient cartilage and bone phase respectively with varying infill densities printed using the 3D printer (Maker City), and (e) represents the photograph of the PCL/PVP/PAA based biphasic scaffold (BPS) with respective bio factors incorporated of dimension 10mm (D) X 6mm (H) (top view).

4.1.3.2 Characterization of scaffolds:

4.1.3.2.1 Analysis of morphological features

The SEM images of different phases of biphasic scaffolds are shown in Figure.4.3.2. The high magnification SEM images of the cartilage phase (figure 4.3.2(d) –(f)) showed interconnected spherical pores with a size of about $320 \pm 6 \mu\text{m}$ on the top layer and $15 \pm 2 \mu\text{m}$ on the bottom layer, which favors effective cell seeding, and further proliferation. Also, the reduced pore diameter would prevent the leakage of differentiated cells to the lower phase. However, the SEM image of the lower bone phase (figure 4.3.2(g) –(i)) shows an interconnected microtubule-like structure of each layer in a star pattern since the continuous filaments were deposited layer-by-layer and could aid the cellular arrangement much similar to bone tissue. The upper and lower layer has a pore diameter of $491 \pm 8 \mu\text{m}$ and $13 \pm 2 \mu\text{m}$ respectively. The optimized 3D printing conditions and interpolymer complexation are needed to achieve rapid

construction of filaments uniformly and to prevent the construct from collapsing. The microscopic images of control scaffolds (PCL/PVP/PAA) are shown in figure 4.3.2 (a)-(c).

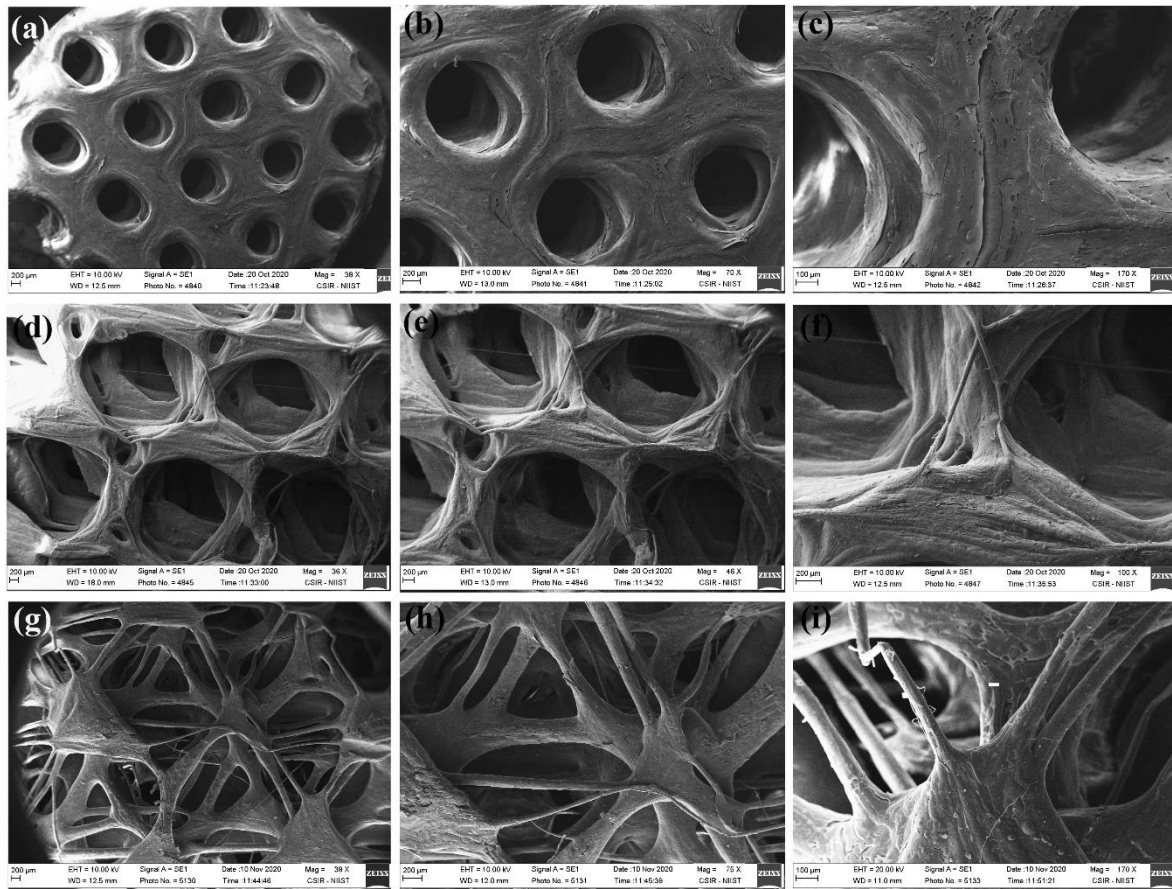


Figure 4.3.2: Analysis of morphological features. (a)- (c), (d)-(e) and (g)-(i) represents SEM images of PCL/PVP/PAA, PCL/PVP/CS/PAA and PCL/PVP/BTCP/PAA respectively at low and high magnifications.

Table 10: The distribution of pores in cartilage and bone phases

Cartilage Phase		Bone phase	
Pores	Diameter	Pores	Diameter
Layer 1-25 %	320 ± 6	Layer 1-25 %	491 ± 8
Layer 2- 30 %	231 ± 3	Layer 2- 30 %	301 ± 10
Layer 3 40 %	125 ± 5	Layer 3 40 %	52 ± 5
Layer 4-50 %	42 ± 3	Layer 4-50 %	35 ± 3
Layer 5- 60%	15 ± 2	Layer 5- 60 %	13 ± 2

4.1.3.2.2 Analysis of chemical features

ATR-FTIR analysis was carried out for analysis of surface groups on the fabricated scaffolds. Figure 4.3.3 (a), (b) and (c) shows the FTIR spectra of PCL/PVP/CS/PAA 3D printed scaffolds. In the infrared spectra, characteristics peaks for PCL, PVP, and CS were observed for PCL/PVP/CS/PAA scaffolds. These include $\sim 2941.9\text{ cm}^{-1}$ (CH_2 stretching), $\sim 2864.5\text{ cm}^{-1}$ (CH_2 stretching), $\sim 1722.6\text{ cm}^{-1}$ (stretching), $\sim 1290.6\text{ cm}^{-1}$ ($\text{C}-\text{C}$ stretching) and $\sim 1237.9\text{ cm}^{-1}$ and $\sim 1164\text{ cm}^{-1}$ (COC stretching). Common bands of chondroitin sulfate appeared at $\sim 830\text{ cm}^{-1}$ and 580 cm^{-1} which corresponds to the sulfate groups, confirming the presence of CS in the hybrid scaffolds. In the FTIR spectra of PCL/PVP/ β TCP/PAA (figure 4.3.3 (d), (e) & (f)), specific bands of PCL, PVP and β TCP were seen, and characteristic bands of phosphate groups appeared at 1025 cm^{-1} and 607 cm^{-1} confirming the presence of β TCP in hybrid bone scaffolds. Similarly, the abstraction of the hydrogen from the solvent (methanol) causes the acidification of the nitrogen in the pyrrolidone group of PVP and the so-formed quaternary ammonium salt ($-\text{NH}^+$) interacts with the negatively charged carboxyl group of the PAA. The complex formation between PVP and PAA is confirmed by the shifting of the peak from 1286 cm^{-1} to 1292 cm^{-1} which is attributed to the $\nu(\text{C}-\text{N})$ bending vibration of the pyrrolidone ring structure of the PVP. Moreover, there is a shift towards the lower wavenumber for the carbonyl stretching frequency of PAA in the PCL/PVP/PAA blend, which again affirms the polycomplex formation between PVP and PAA.

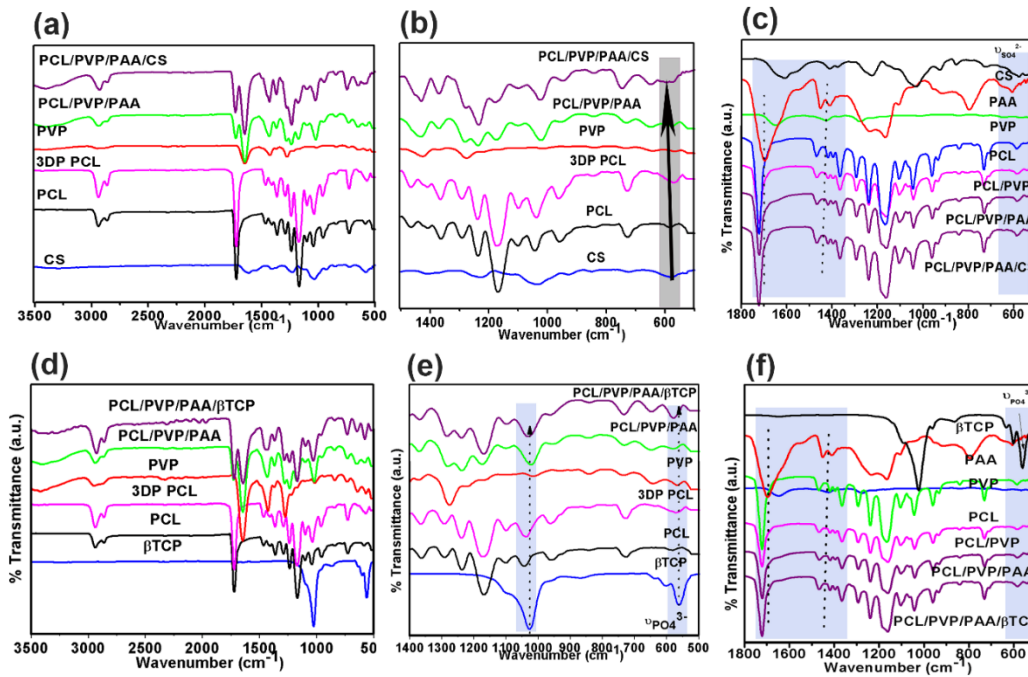


Figure 4.3.3: Analysis of chemical features. FTIR analysis of (a), (b)& (c) 3D printed cartilage (PCL/PVP/CS/PAA) and (d), (e) & (f) Bone (PCL/PVP/βTCP/PAA) phase.

4.1.3.2.3 Analysis of thermal features

TGA and DTG curves were shown in Figures 4.3.4 (a)-(c) respectively. The onset decomposition temperatures of the PCL scaffold are around 339°C (as shown in previous sections), which is in agreement with the earlier studies (Liu et al., 2013). The onset decomposition temperature of PCL/PVP, PCL/PVP/PAA, PCL/PVP/CS/PAA or PCL/PVP/TCP/PAA scaffolds are greater than that of PCL scaffold (between 350 and 450°C), indicating the improvement in the thermal stability due to the interaction between the different components in the blend. PCL 3D scaffolds exhibited single-stage decomposition with T_{max} at 400°C with a residue of 0.325% after the completion of the temperature program (800°C), whereas a two or more-step decomposition process could be observed in all other the scaffolds (PCL/PVP, PCL/PVP/PAA, PCL/PVP/CS/PAA, and PCL/PVP/βTCP/PAA) suggesting multicomponent system. The first decomposition step for PVP occurs between 50 and 100°C , attributed to residual water loss, and the second decomposition at 300 - 450°C is due to the breakdown of the polymer chain. The incorporation of PVP into PCL improves the thermal

stability of PCL and the thermogram resembles that of PCL, suggesting the good intermixing between PCL and PVP. Meanwhile, for PCL/PVP/PAA scaffolds the initial water loss is observed at $\sim 100^{\circ}\text{C}$ with a T_{max} of 404°C . TGA curves of PCL/PVP/CS/PAA scaffolds follow the same characteristics as that of pure PCL scaffolds, suggesting that the thermal properties were not significantly altered with blending PVP/CS or TCP and complexation with PAA. The increased percentage of the inorganic residue ($\sim 8\%$) after the completion of the TGA analysis indicates the presence of chondroitin sulfate in the cartilage phase (PCL/PVP/PAA/CS) which gave extra stability. At the same time, the incorporation of βTCP in the bone phase improved the T_{max} further to 411°C , with high inorganic residue % as the βTCP is stable in the range of the temperature program. Thus, the thermal stability of the blend at operating temperature conditions (3D printing process) was confirmed. Since PCL is a widely used biomaterial and used for in vivo experiments already, blend scaffolds are also inferred to be safer as the properties are very similar to PCL scaffolds.

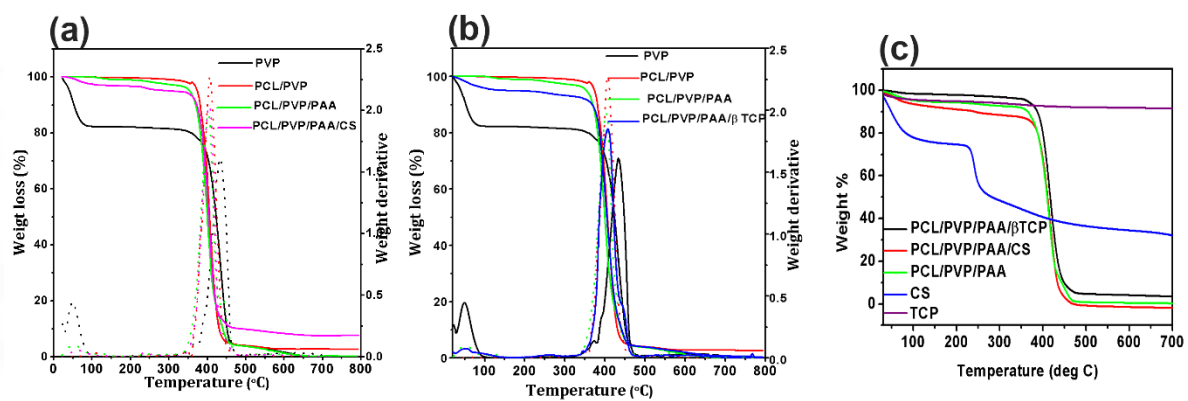


Figure 4.3.4: Analysis of thermal features. (a), (b) & (c) represents the TGA graph where the weight percentage of resulting mass change of each component of hybrid scaffolds upon the increase in temperature has measured as a function of temperature.

4.1.3.2.4 Analysis of wettability features

Water contact angle images are illustrated in Figure 4.3.5. The water angle of the composites decreased, and the surface hydrophilicity increased with the addition of PVP and bioactive factors. The average values of the contact angles of PCL/PVP/PAA ($92 \pm 3^{\circ}$),

PCL/PVP/CS/PAA ($84\pm 4^\circ$), and PCL/PVP/ β TCP/PAA ($89\pm 3^\circ$) were appreciably lower when compared to PCL alone ($125\pm 3^\circ$) (figure 4.3.5 (a)-(d)).

4.1.3.2.5 Analysis of mechanical features

The fabricated cartilage scaffold showed greater compressive modulus when subjected to compressive loads. The compressive modulus at maximum load when it is compressed to 4mm for control (PCL/PVP/PAA), cartilage (PCL/PVP/CS/PAA), and Bone phases (PCL/PVP/ β TCP/PAA) are 14.5 ± 1.6 MPa, 27.9 ± 2.0 MPa and 22.9 ± 1.3 respectively (figure 4.3.5 (e)). The stress-strain curve is represented in figure 4.3.5 (f). The photomicrographs of mechanical testing for three groups of scaffolds are shown in figure 4.3.5 (g)-(l).

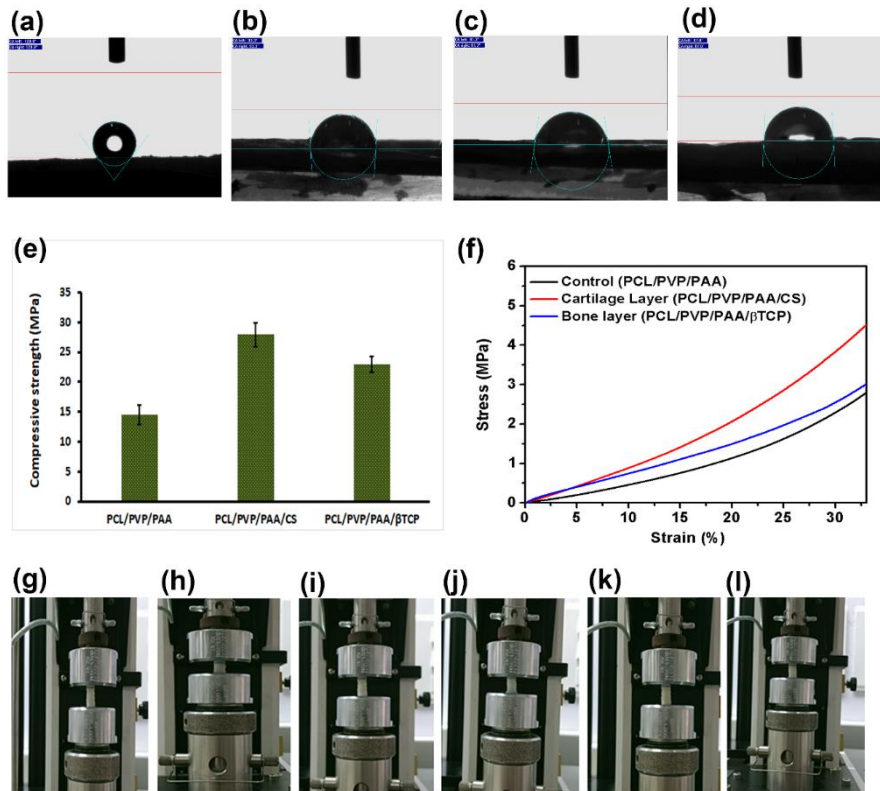


Figure 4.3.5: Analysis of wettability and mechanical features. (a), (b) (c) & (d) represents contact angle and droplet profile after 5 sec on 3D printed PCL alone ($125\pm 3^\circ$), PCL/PVP/PAA ($92 \pm 3^\circ$), PCL/PVP/CS/PAA ($84\pm 4^\circ$) and PCL/PVP/ β TCP/PAA ($89\pm 3^\circ$) respectively. (e) and (f) represents the compressive modulus and compressive stress-strain curve for the 3D printed scaffolds when the scaffolds are compressed to 4mm. (g)-(l) represents the photomicrographs

of scaffolds before and after compressive tests (g) & (h) PCL/PVP/PAA, (i) & (j) PCL/PVP/CS/PAA, (k) & (l) PCL/PVP/ β TCP/PAA scaffolds.

4.1.3.2.6 Analysis of degradation features

The *invitro* degradation studies of the developed scaffolds were assessed in terms of morphological change and mass loss percentage and the results are presented in Figure 4.3.6. Upon quantitative estimation, the composite scaffolds; PCL/PVP/CS/PAA and PCL/PVP/ β TCP/PAA developed after interpolymer complexation with PAA, approximately 16 and 14 wt % respectively has degraded when immersed in PBS for 4 weeks (figure 4.3.6 (d)). The interpolymer complexation with polyelectrolyte reduces the percentage of weight loss while in the scaffolds without complexation, the degradation rate is almost 35% and 30 % for cartilage and bone phases respectively by 28 days (figure 4.3.6 (c)). Further, the scaffolds with biomoeities showed a greater degradation rate (with or without PAA) attributed to the leaching of those incorporated factors with time. PAA binds to PVP via repetitive hydrogen bonds across the polymer backbone. The SEM images of cartilage (figure 4.3.6 (a)) and bone surface (figure 4.3.6 (b)) illustrate the morphological changes of the printed scaffolds after 28 days of incubation in PBS and showed a rugged surface morphology with the number of ultra-fine pores on the surface. To conclude, the degradation of the topmost layers and the prominence of intermediate and bottom layers were observed. Moreover, the structural integrity of both phases was appreciable during the study period. Present findings demonstrate that 3D printed PCL blended with water-soluble PVP provides important insights for further studies.

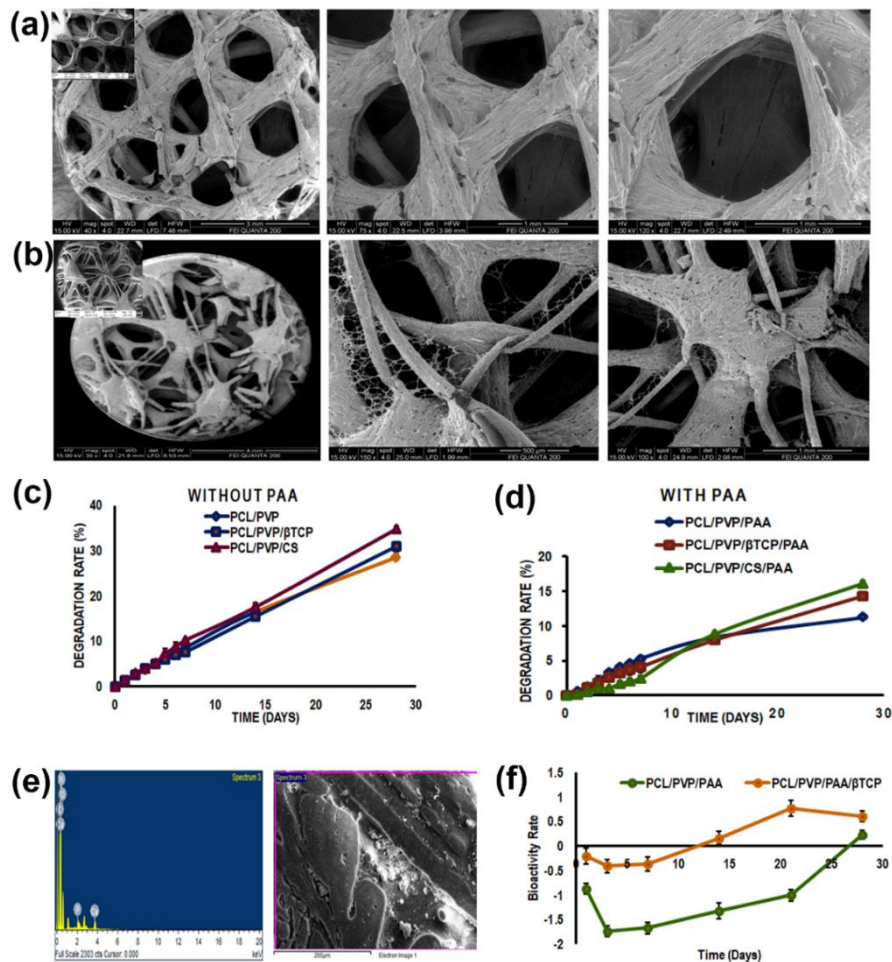
4.1.3.2.7 Assessment of *in vitro* bioactivity

The apatite mineralization ability of the bone phase of BPS was assessed by *invitro* bioactivity assessment of β TCP incorporated scaffolds and the results indicate a simultaneous process of precipitation and dissolution. The PCL/PVP/ β TCP/PAA scaffolds upon incubation in SBF showed an initial weight loss on days 1, 3, and 7 suggestive of initial dissolution of ions into

the solution followed by weight gain on days 14 and 21, indicating the process of precipitation of ions suggesting a weight gain (figure 4.3.6 (f)). On the other side, the PCL/PVP/PAA scaffolds also showed mild mineralization ability where there is a progressive weight loss up to 21 days followed by marginal weight gain. SEM and EDS analysis of the osteogenic phase of the BPS showed mineralization of the surface by day 28 (figure 4.3.6 (e)).

4.1.3.2.8 Assessment of Chondroitin sulfate (CS) leach out study:

The study suggests a burst release of CS in the initial hours for the scaffolds without interpolymer complexation with PAA. The immediate burst release is prevented upon complexation and the release peaked by the 14th day though a fall in the release was observed on day 7 (figure 4.3.6 (g)). The leaching out of CS as time advances favors the degradation as well by creating micropores.



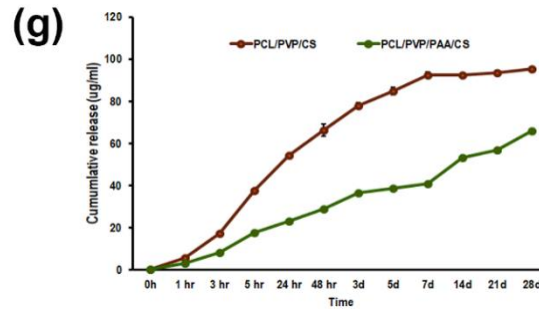


Figure 4.3.6: *In vitro* degradation of developed scaffolds, chondroitin sulfate leach out study for cartilage phase, and *in vitro* bioactivity of bone phase. (a) & (b) represents the SEM images of the degradation pattern of the cartilage and bone phase of BPS after 28 days. (c) & (d) shows the quantitative estimation of *in vitro* degradation rate of scaffolds without and with complexation using PAA, in PBS (n = 3) for 28 days. (e) represents SEM and EDS analysis of the bone phase of the BPS after 28 days of incubation in SBF, (f) shows the rate of bioactivity of the bone phase for 28 days and (g) represents the CS leach out study from the cartilage phase for 28 days by DMMB assay.

4.1.3.2.9 Assessment of *in vitro* cytocompatibility

a. Cell Viability by Live dead and MTT assay

Figure 4.3.7 presents the *in vitro* cytotoxicity test on cartilage and bone phase respective to the control at 24 hours and 48 hours, using the MTT assay and confirmed that the scaffolds had no unfavorable effects on the viability of cells (figure 4.3.7 (a) & (b)).

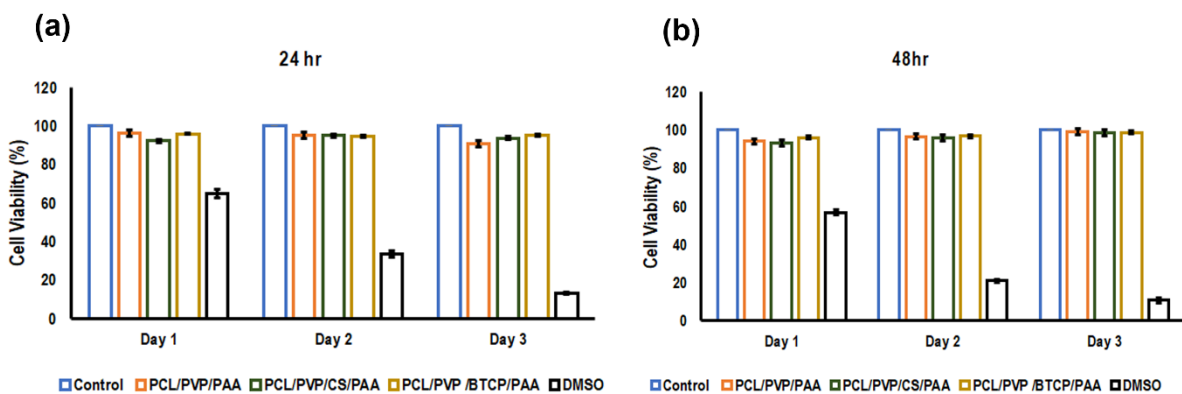


Figure 4.3.7: Assessment of cytocompatibility. MTT assay performed between the control group and the test groups after the periods of 24 hours (a) & 48 hours (b).

The experimental groups and the control groups showed no significant differences between them. Further, cells cultured on scaffolds containing CS and βTCP showed higher metabolic activity than monolayer or bare PCL/PVP/PAA scaffolds. It is evident from the results that

there is no residual solvent, (chloroform and methanol) on the 3D printed scaffolds, suggesting that the excess solvent was entirely removed by air drying overnight in a fume hood. This indicates that the materials tested (i.e., PCL/PVP/PAA, PCL/PVP/CS/PAA and PCL/PVP/ β TCP/PAA) composites) were non-cytotoxic and able to support attachment, proliferation, and viability of ADMSCs.

4.2 Isolation and characterization of MSCs

4.2.1 *Rat adipose-derived MSCs*

4.2.1.1 Isolation of rat MSCs

Isolation of the rat ADMSCs from the retroperitoneal fat pad of Wistar rats was done according to the standardized protocol of our laboratory (Aloysious N, Nair PD et.al). The cells were digested with collagenase II and centrifuged to separate the oil, remaining fat lobules and adipocytes, and MSCs were collected (figure 4.4.1(a)). The isolated cells showed plastic adherence with spindle-shaped morphology (figure 4.4.1(b)) after initial 24 hours in a culture that proliferated to confluency in 5-7 days.

4.2.1.2 Characterization of rat MSCs:

The isolated MSCs were characterized for their stem cell properties by analysis of standard surface antigens for MSCs (by flow cytometry and immunostaining) and trilineage differentiation, approved by the International Society for Cellular Therapy.

Morphology: FITC-Phalloidin staining of actin filaments of isolated MSCs (figure 4.4.1(c)) showed characteristic spindle-shaped morphology of the cells when attached to tissue culture-treated surface. Also staining of vimentin antigen, the intermediate filament protein of MSCs that maintains cellular integrity and stable cytoskeletal interactions showed positive staining (figure 4.4.1(d))

Surface marker analysis: Flow Cytometric analysis demonstrated that more than 80% of the cells in the culture expressed the established surface antigens CD90 (85%), CD73 (89%),

and CD105 (81%). The expression of approved negative markers for MSCs - CD34 and CD45 was less than 2%, which fulfilled the minimum criteria for cell surface antigens for MSCs (figure 4.4.2). In addition, immunofluorescence staining also showed positive staining for MSC surface antigens CD 90, CD73, and CD105 (figure 4.4.1 (e), (f) &(g)) and negative for CD 45 and CD 34 (figure 4.4.1(h)). Thus, the mesenchymal nature of the cells was confirmed.

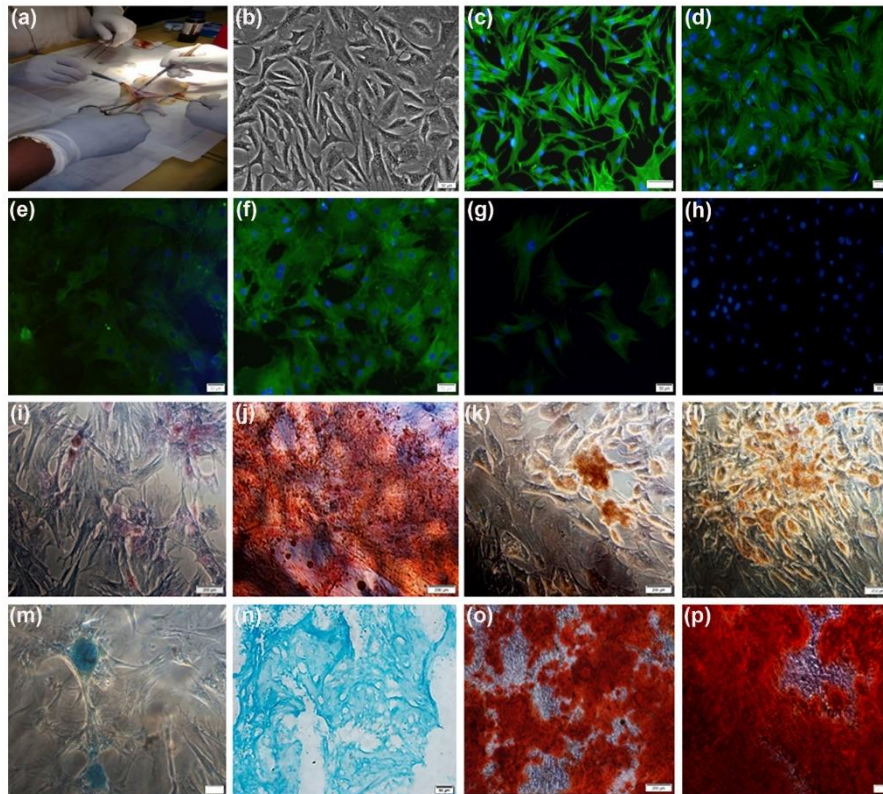


Figure 4.4.1: Isolation and characterization of rat MSCs. Representative images of (a) isolation of rat ADMSCs (b) rat ADMSCs at passage 3, (c) Phalloidin staining of actin filaments, (d) immunofluorescence staining for Vimentin, and (e), (f), (g) represents surface markers of MSCs - CD90, CD73 respectively and CD105, (h) CD34/CD45. (i) & (j), (k) & (l), (m) & (n) & (o) & (p) show trilineage differentiation assay for the assessment of rat ADMSCs cultured in respective induction media for 14 and 28 days and were stained with safranin o staining, Oil-red O staining, Alcian blue, and Alizarin red staining respectively.

Multilineage differentiation of MSC: The multilineage differentiation potential of MSCs was analyzed by trilineage differentiation assay on days 14 and 28. The isolated MSCs differentiated to chondrogenic, adipogenic, and osteogenic lineage upon induction with respective differentiation mediums. The chondrogenesis potential was confirmed by detecting the presence of proteoglycan, sulfated glycosaminoglycans, and aggrecan which stained bright

orange and dark blue respectively upon staining using the safranin -O stain and copper-containing dye, Alcian Blue, thus confirming chondrogenic lineage (figure 4.4.1(i), (j) and (m), (n)). Oil-o-red staining revealed the presence of red-colored triglycerides (oil droplets) confirming adipogenic lineage (figure 4.4.1(k)&(l)). The cells differentiated into osteogenic lineage showed the presence of red calcium deposits confirming the osteogenic differentiation (figure 4.4.1(o)&(p)). The positivity in MSC markers and trilineage differentiation proves the stemness of isolated ADMSCs.

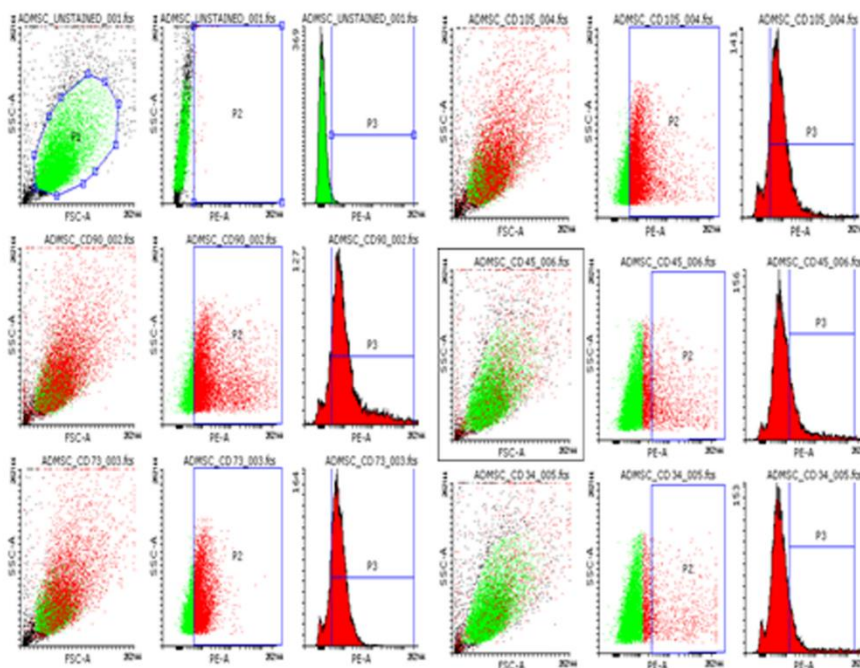


Figure 4.4.2: Flow cytometric analysis of surface markers of MSCs. The percentage of CD marker expression was analyzed and demonstrated that more than 80% of the cells expressed the surface antigens CD90 (85%), CD73 (89%), and CD105 (81%).

4.2.2 Rabbit adipose-derived MSCs

The cells isolated from rabbit adipose tissue were plastic adherent with spindle-shaped morphology (figure 4.4.3 (a)). The fluorescence microscopic images of the cytoskeleton arrangement of the stem cells where F-actin was stained with FITC conjugated phalloidin after 3 days of 2D culture is given in (figures 4.4.3 (b)). The MSCs adopted a well-spread morphology and showed extensive cell-cell interaction. Analysis of standard surface antigens

for MSCs approved by the International Society for Cellular Therapy, using Flow Cytometric analysis demonstrated that more than 80% of the cells expressed the surface antigens CD90 (82%), CD73 (92%), and CD105 (85%). The expression of approved negative markers for MSCs - CD34 and CD45 was less than 2%, which fulfilled the minimum criteria for cell surface antigens for MSCs (figure 4.4.4). In addition, immunofluorescence staining also showed good staining for MSC surface antigens CD105, CD90, and CD73 (figure 4.4.3 (d), (e) and (f)) and positive staining for Vimentin antigen (figures 4.4.3(c)). The multilineage differentiation assays showed the isolated MSCs could undergo chondrogenesis, adipogenesis, and osteogenesis when cultured in respective differentiation medium, which is confirmed by alcian blue, oil-o-red, and alizarin red staining respectively (Figure 4.4.3 – (g), (h) and (i)). Cells in passage 3 were used for further *in vitro* cytocompatibility and differentiation studies.

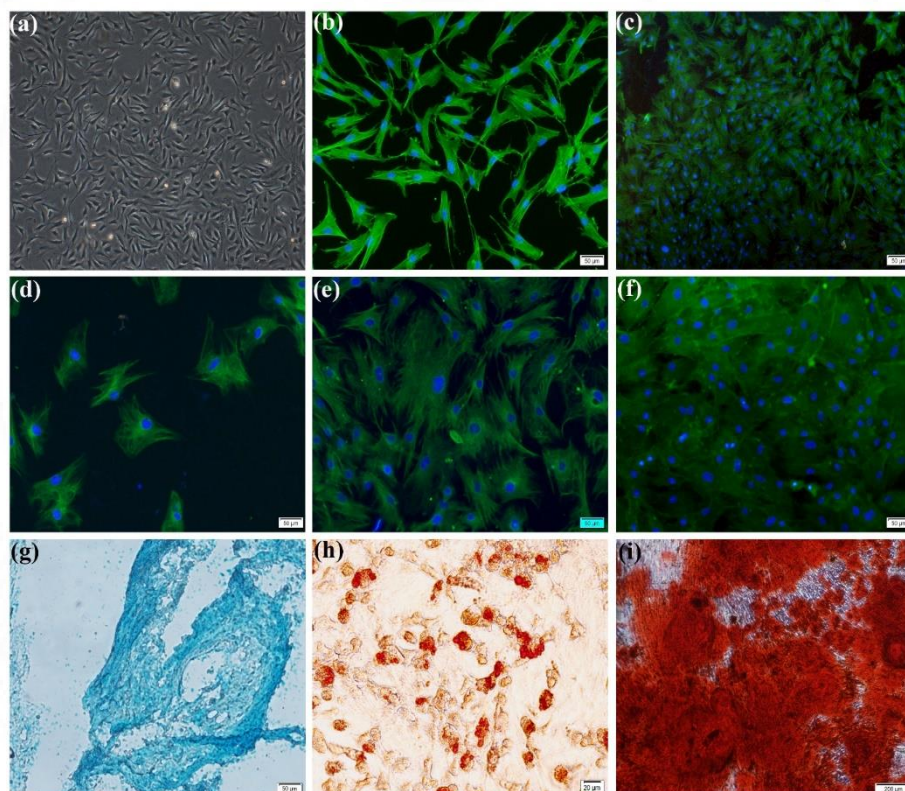


Figure 4.4.3: Isolation and characterization of rabbit MSCs. Representative images of (a) Rabbit ADMSCs at passage 3, (b) Phalloidin staining of actin filaments, (c) Immunofluorescence staining for Vimentin, and (d), (e), (f) represents surface markers of MSCs - CD90, CD73, and CD105, respectively. (g), (h), (i) show trilineage differentiation

assay for the assessment of rabbit ADMSCs cultured in respective induction media for 28 days and were stained with Alcian blue, Oil-red O staining, and Alizarin red staining respectively.

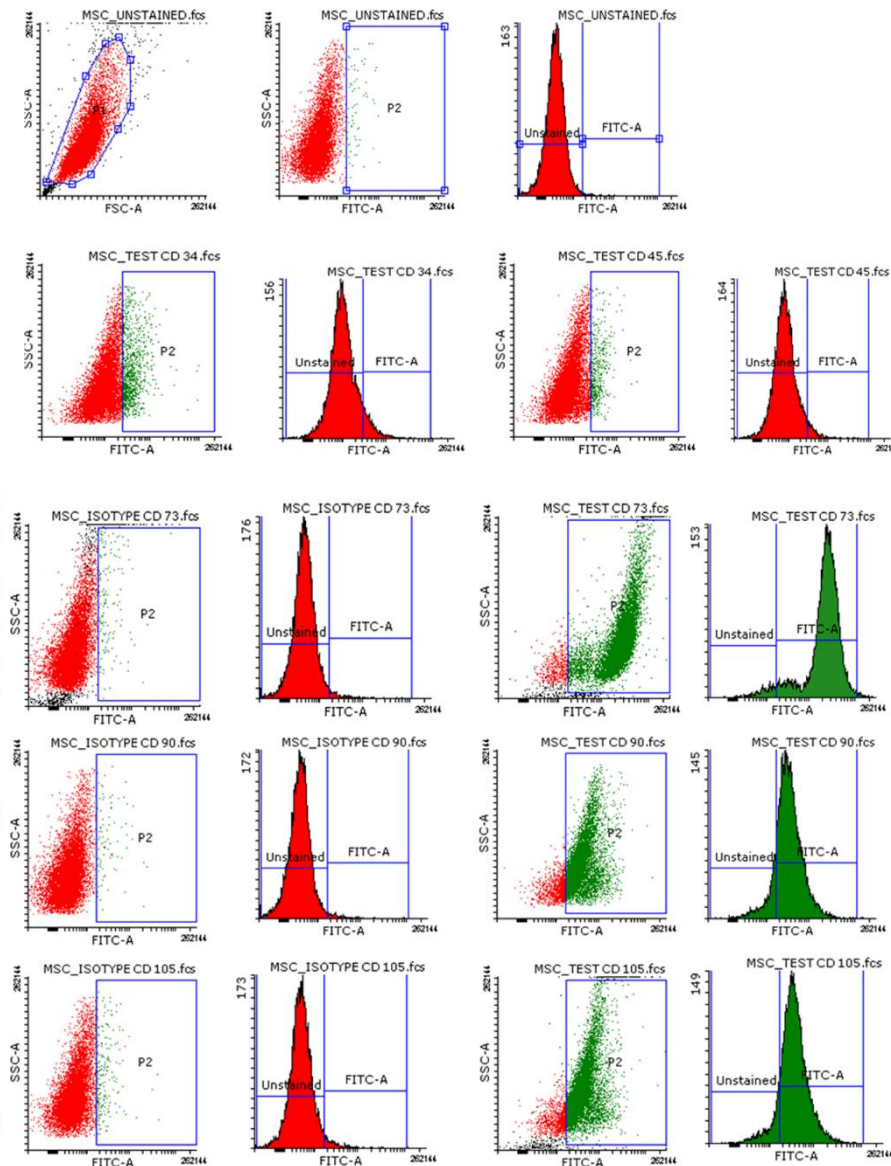


Figure 4.4.4: Flow cytometric analysis of surface markers of MSCs. The percentage of CD marker expression was analyzed and demonstrated that more than 80% of the cells expressed the surface antigens CD90 (82%), CD73 (92%), and CD105 (85%).

4.3 *In Vitro* culture of MSCs and evaluation of production of ECM

4.3.1 *Evaluation of chondrogenesis in 2D culture and production of ECM*

The rat ADMSCs cultured in tissue culture wells plate were induced to form pellets using chondrogenic induction medium (CIM) (figure 4.4.5 (a)). The sGAG content from the pellet was quantified by dimethyl methylene blue (DMMB) assay to assess the chondrogenic ECM

production. The concentration of sGAG from the pellet was estimated as $421 \pm 12.8 \mu\text{g}/\text{pellet}$. Further, the chondrogenic differentiation of MSC in 3D pellet culture that resulted in the formation of cartilage with its specific extracellular matrix was assessed by alcian blue staining for proteoglycan, aggrecan which stained dark blue (figure 4.4.5 (b)). The cryosections were further immunostained for cartilage-specific markers, aggrecan, and collagen 2 and showed positive signals around the cells (figure 4.4.5 (c)-(d)). For determining the *in vitro* chondrogenesis, RT PCR analysis was further performed to confirm the expression of marker genes; ACAN, COL2a1, HAS 2, and SOX9. When compared to day 3, the relative mRNA fold change for each gene was observed and found to be ~150-fold for COL 2A1, ~235- fold change for ACAN, ~4-fold change for HAS 2, and no significant fold change for SOX 9 (figure 4.4.5 (e)-(h)) on day 28. Thus, staining and sGAG estimation confirmed the production of ECM *in vitro* and RT PCR analysis confirmed the expression of marker genes for Chondrogenesis.

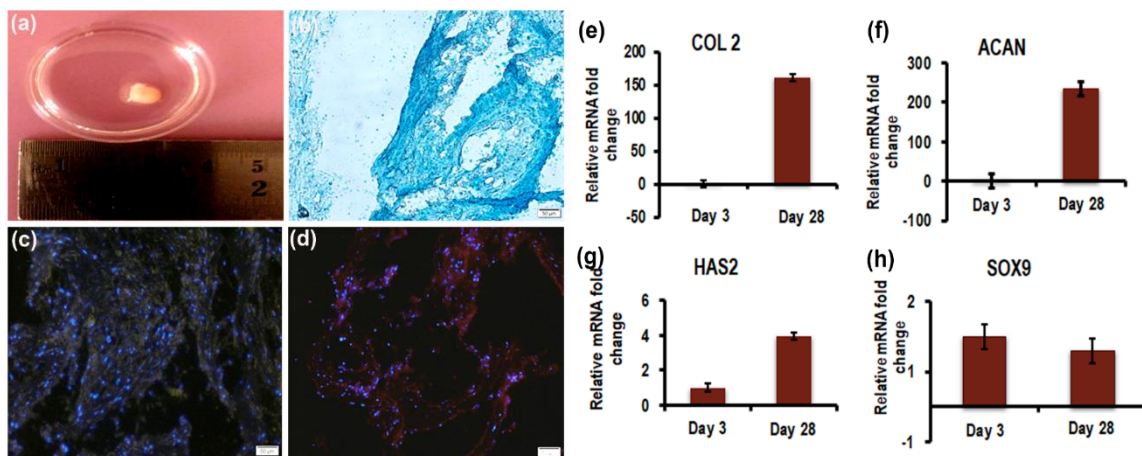


Figure 4.4.5: 3D pellet culture of MSCs and evaluation of chondrogenesis. (a) represents the gross appearance of the pellet formed after 14-days of culture in the chondrogenic induction medium (b) Alcian blue staining of cryosectioned pellets for proteoglycans and fluorescence images of immunostaining done for (c) aggrecan (d) collagen 2 and showed positive signals around the cells. (e)-(h) represents the relative mRNA fold change of COL2, ACAN, HAS2 and SOX 9 respectively after 28 days.

4.3.2 Evaluation of osteogenesis in 2D culture and production of ECM.

The osteogenic differentiation of ADMSCs on 2D culture and production of ECM after 28 days were assessed by Alizarin red staining and Calcium estimation, further confirmed by analyzing

osteogenic specific genes expression. The amount of calcium quantified was $\sim 15 \mu\text{g/ml}$. The alizarin red staining was done to qualitatively analyze the osteogenesis and detected intense red stains which confirmed the presence of calcium deposits (figure 4.4.6 (a)). When compared to day 3, the relative mRNA fold change for each gene was observed and found to be ~ 32 -fold for Bone sialoprotein (BSP), ~ 17 - fold change for Osterix, ~ 2 -fold change for Osteocalcin (BGLAP) (figure 4.4.6 (b)) on day 28. The ability for osteogenesis was thus confirmed.

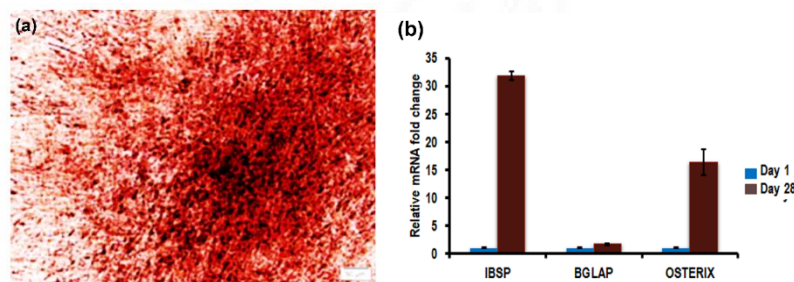


Figure 4.4.6: Evaluation of osteogenesis and production of ECM in vitro. (a) represents the alizarin red staining of differentiated MSCs in 2D culture after 28 days where the calcium deposits, stained intense red. (b) represents the relative mRNA fold change for Bone sialoprotein (BSP), Osterix, and Osteocalcin (BGLAP) on day 28.

4.4 *In vitro* differentiation potential of MSCs on the biphasic scaffold (BPS)

4.4.1 System A- BPS fabricated via Combinatorial approach

4.4.1.1 *In Vitro* cytocompatibility with rat ADMSCs

The Live-Dead Assay revealed that (figure 4.5.1), ADMSCs were viable on 3D printed PCL/Gelatin (figure 4.5.1 (a)-(c)) and freeze-dried PCL/CaSO₄ (figure 4.5.1 (g)-(i)) after 7 days of culture with a significantly higher number of living cells and fewer dead cells on hybrid scaffolds when compared to its respective control (figure 4.5.1 (d)-(f) & (j)-(l)) and thus these hybrid scaffolds are favorable for cell survival and retention. In addition, the ADMSCs were also found to be uniformly spread and grown well on the test scaffolds (figure 4.5.1 (b) & (h)). However, the control scaffolds also showed the viability of cells, yet in a different distributing pattern. ADMSCs displayed less spindle morphology on 3D printed PCL strands and only a limited amount of ADMSCs attached to the PCL alone scaffolds which are related to the

hydrophobicity of PCL that is not supporting cell adhesion and retention. Meanwhile, cells in hybrid scaffolds are evenly distributed not only in the pores but also spreading on the surfaces of scaffolds. After 28 days of culture in the growth medium, ADMSCs showed good viability in both the cartilage and bone phase with the neglectable number of dead cells (figure 4.5.1(m), (n) & (o), (p)). These observations suggested excellent biocompatibility of hybrid scaffold compared to hydrophobic PCL alone, which is due to the highly hydrated environment provided by the hybrid scaffolds. Therefore, the hybrid scaffolds displayed biomimetic matrices for cell survival and further expansion.

4.4.1.2 Cell adhesion/Attachment and morphology:

Adhesion rates of MSCs in the upper layer and lower were estimated quantitatively after 4, 8, 12, and 24 h (figure 4.5.2(a)) and found to have an increasing pattern with incubation time on all scaffolds. On comparing the adhesion rates in the different scaffold types, we found appreciable differences at the two-time points; 4 and 12 hr. Initially, the adhesion rate was minimal for freeze-dried scaffolds due to hydrophobicity even after a 4 hr of pre-wetting with culture medium. After 12 h, the adhesion rate on PCL/Gelatin and PCL/CaSO₄ scaffolds reached greater than 60 %, indicating minimal variations due to scaffold material. After 24h, the cell adhesion rate could reach 95.5 and 88.85 % for the upper and lower phases respectively. This adequately proved that both the phase provides a good microenvironment for cell adhesion and its spreading and thus acted as excellent cell affable assemble.

The multiphoton confocal images of the cytoskeleton arrangement of the stem cells (F-actin in green and cell nuclei in blue) cultured in both phases and BPS on day 3 are given in figures 4.5.3(a), (b) & (c). After 7days of incubation, MSCs on the PCL/Gelatin and PCL/CaSO₄ scaffold formed stress fiber in the cytoplasm and adopted a spread morphology and extensive cell-cell interaction (figure 4.5.3(a) & (b)). MSCs were orientated in different directions on the 3D scaffolds, with notably more intense cytoskeleton staining in cells on the

blend scaffold. In the cartilage phase, F-actin filaments were aligned with the printed struts that formed the scaffolds. Thus, assessment of the cell adhesion and spreading pattern/morphology of MSCs on the cartilage and bone phases using cytoskeletal staining against F-Actin indicated that both the phases are equally supporting ADMSCs attachment and infiltration into scaffold.

4.4.1.3 Cell proliferation studies:

Further, the proliferation of ADMSCs cultured on 3D printed cartilage phase and freeze-dried bone phase of BPS, its respective control, and 2D culture was quantified at different time points (1, 3, 5, 7, and 14) by PicoGreen assay and is shown in Fig.4.5.2(b). The DNA content ascended linearly from Day 1 to Day 14 in all 3D scaffold systems, indicating an increase in the number of cells in the scaffolds with time when compared to the number of cells initially embedded inside the scaffolds (0.1×10^6). Furthermore, on day 14, a significant difference was observed between the test groups. For PCL/Gelatin system, the DNA content was found to increase with incubation time. 3D printed gelatin-based cartilage phase showed a significant difference in DNA content on the 14th day, which represents its superiority when compared to other groups to support cell proliferation. These observations suggested a hydrated environment provided by the hybrid scaffolds and design pattern with varying infill density including micropore sizes favored faster proliferation that is advantageous for further construct development. The PCL/CaSO₄ scaffolds showed higher DNA content than that of the PCL alone scaffolds which indicated that cell proliferation on the PCL/CaSO₄ scaffolds was superior to PCL scaffolds. Also, the percentage of cell loss was estimated from DNA content. The amount of DNA in picograms in rat cells is 6.5. Hence out of 1×10^5 cells seeded (650000 pg DNA), the percentage loss of cells after cell seeding is greatest for PCL alone scaffolds irrespective of fabrication methodology due to its extreme hydrophobicity. However, PCL/Gelatin showed significant ability to retain the seeded cells. Hence, Live Dead, MTT assay, and proliferation assay reveals the cytocompatibility of the materials tested (i.e., PCL,

PCL/CaSO₄, 3D printed PCL, and PCL/Gelatin blend) and the BPS consisting of PCL/Gelatin as cartilage phase and PCL/CaSO₄ as bone phase can be used for further experiments.

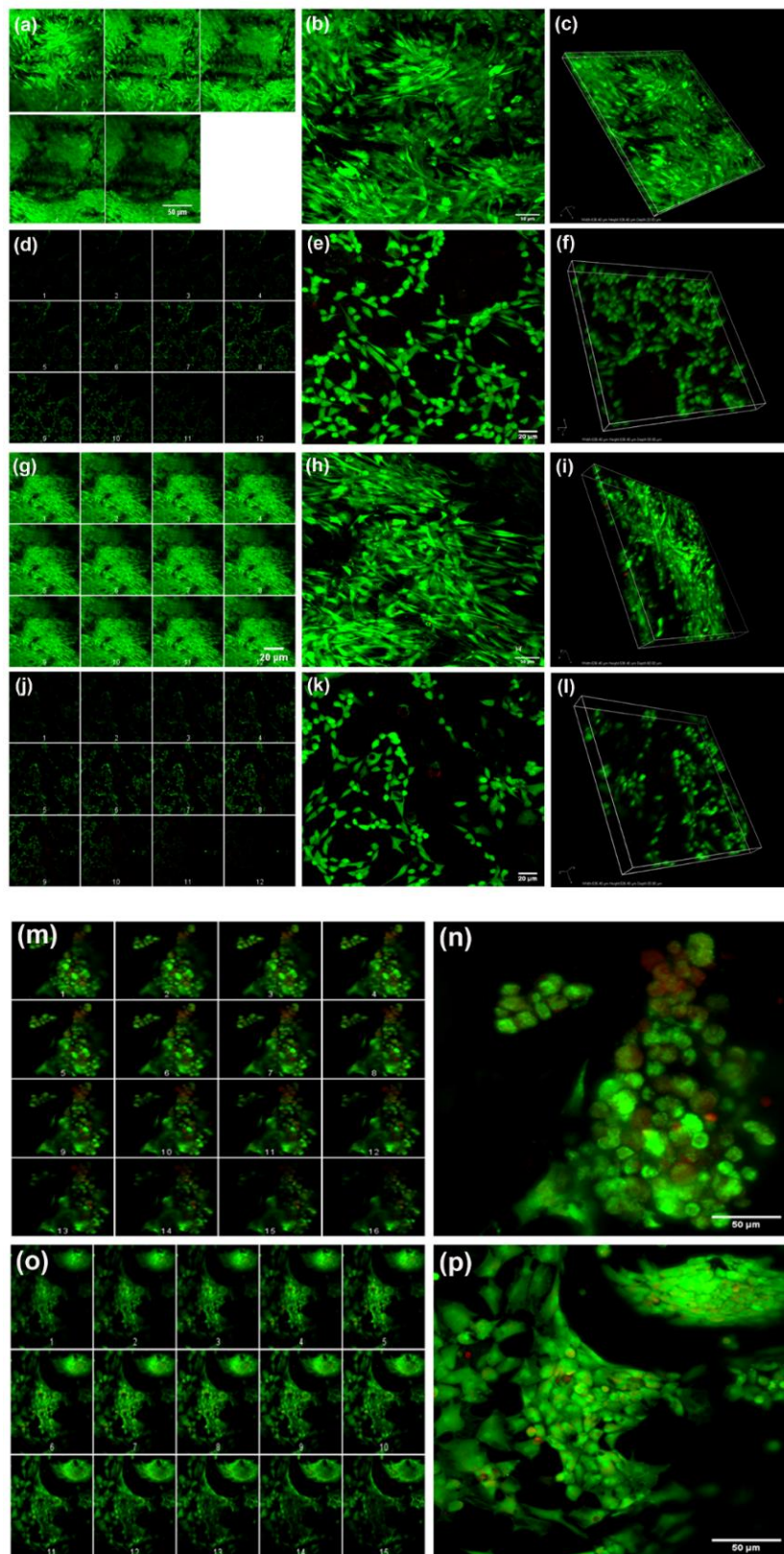


Figure 4.5.1: *In vitro* cytocompatibility assessment. Confocal microscopic images of the viability of MSCs at Day 7 on the PCL/Gelatin cartilage phase (a)-(c), 3D printed PCL (d)-(f), freeze-dried PCL/CaSO₄ bone phase (g)-(i) and freeze-dried PCL (j)-(l). (m), (n), (o) & (p) show confocal microscopic images of Live/Dead stained MSCs on cartilage phase and bone layer respectively, on the 28th day: montage view (a, d, g, j,m,o), maximum projection (b, e, h, k,n,p), volume viewer (c, f, i, l).

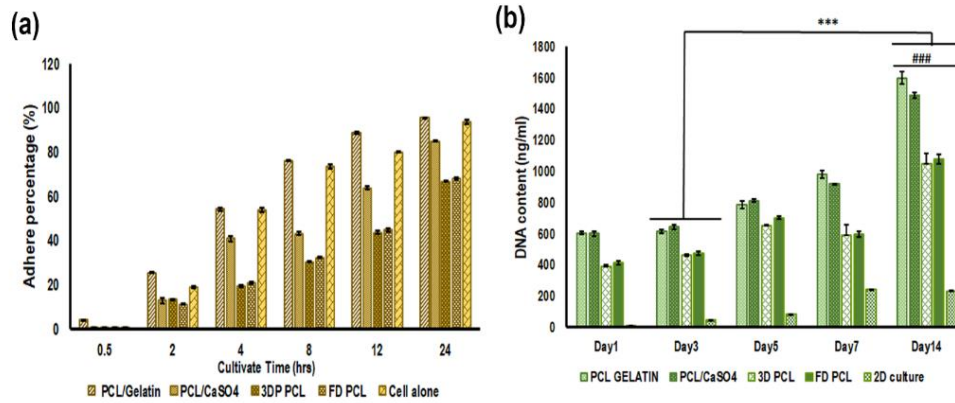


Figure 4.5.2: Cell adhesion and proliferation study of scaffolds using MSCs. (a) & (b) are representative graphs of cell adhesion rate for different scaffolds, at different culture time points and cell proliferation assay using pico green assay to determine the metabolic activity at different periods. (***: $p < 0.001$, *: $p < 0.05$, ns: $p > 0.05$).

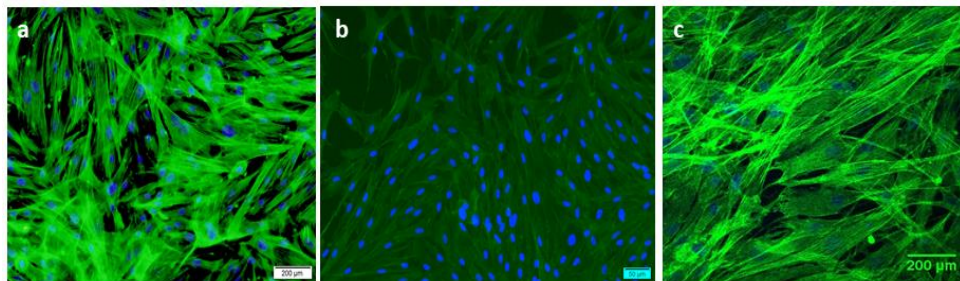


Figure 4.5.3: Study on cell morphology. Confocal images of F-Actin immunostained rat adipose-derived mesenchymal stem cells (ADMSCs) cultured on cartilage phase (a), bone phase (b), and biphasic scaffolds (c), respectively on day 3. Actin cytoskeleton arrangement is shown in green by fluorescent staining with Alexa fluor phalloidin and nuclei are depicted in blue by DAPI staining.

4.4.1.4 Differentiation of rat ADMSCs on 3D scaffolds into cartilage and bone lineages

The ADMSCs could differentiate into specific lineage upon induction, and hence these multipotent ADMSCs are often used for studies related to osteochondral defects regeneration.

4.4.1.4.1 Evaluation of chondrogenesis

a. Sulfated glycosaminoglycan (sGAG) Quantification:

The study was further extended to the estimation of *invitro* chondrogenesis for investigating the effect of 3D printing cartilage phase with specific design by quantification of sGAG secretion by the MSCs differentiated chondrocytes. The determination of sGAG content by DMMB assay is the appropriate method for the estimation of cartilage ECM formation and hence activity and functional state of MSCs that are differentiated into chondrocytes can be assessed. Figure 4.5.4 (a) depicts the content of sGAG secreted by cultured cells in a chondrogenic medium after 7, 14, 21, and 28 days. The results showed that the sGAG content increased gradually as culture time advances from 7 to 28 days of incubation. The PCL/Gelatin scaffolds showed significantly higher levels of sGAG content as compared to the PCL alone scaffold and the monolayer cultures ($P < 0.05$). Upon assessing the total DNA content in all groups, the PCL/Gelatin scaffolds have higher levels of DNA and sGAG/DNA content as compared to 3D-printed PCL alone scaffold and monolayer cultures. Notably, the sGAG content of PCL alone scaffolds was greater than 2D monolayer cultures. Overall, the scaffolds with optimum design exhibited a very significant promoting effect.

b. Collagen estimation

Upon collagen estimation (figure 4.5.4 (b)) by Sircol collagen assay, the collagen content increased progressively as the culture period advanced. On day 28, the PCL/Gelatin composite scaffolds have significantly greater collagen content when compared to bare PCL scaffolds and 2D cell control ($p < 0.05$) as well as significantly greater content than on day 14 ($p < 0.01$). These results suggest that collagen production is time and design dependant.

4.4.1.4.2 Evaluation of the osteogenesis

a. Assessment of ALP activity:

Assessment of the levels of ALP enzymatic activity (defined as the amount of by-product – PNP- produced as the result of enzymatic activity) on culture days 7, 14, 21, and 28 showed a

gradual increase in the ALP levels up to day 14 (figure 4.5.4 (c)). However, after peaking on day 14, we found a small, but insignificant decrease in ALP levels on day 21 suggesting ALP as an early marker. The PCL/CaSO₄ scaffolds showed higher levels of ALP activity at all time points, whereas the control groups, PCL alone and ADMSCs cultured in an osteogenic medium showed significantly lesser amounts of ALP on days 14 and 21.

b. Calcium estimation

Matrix mineralization is a late marker for fully differentiated osteoblasts. Hence, we assessed the levels of calcium deposits on the scaffolds by the OCPC method. The results showed that ADMSCs cultured on 3D scaffolds in an osteogenic medium differentiated and mineralized the matrix with higher calcium content in 28-day cultured scaffold when compared to those cultured for 14 days (figure 4.5.4(d)) and is thus an indication of later stage osteogenesis.

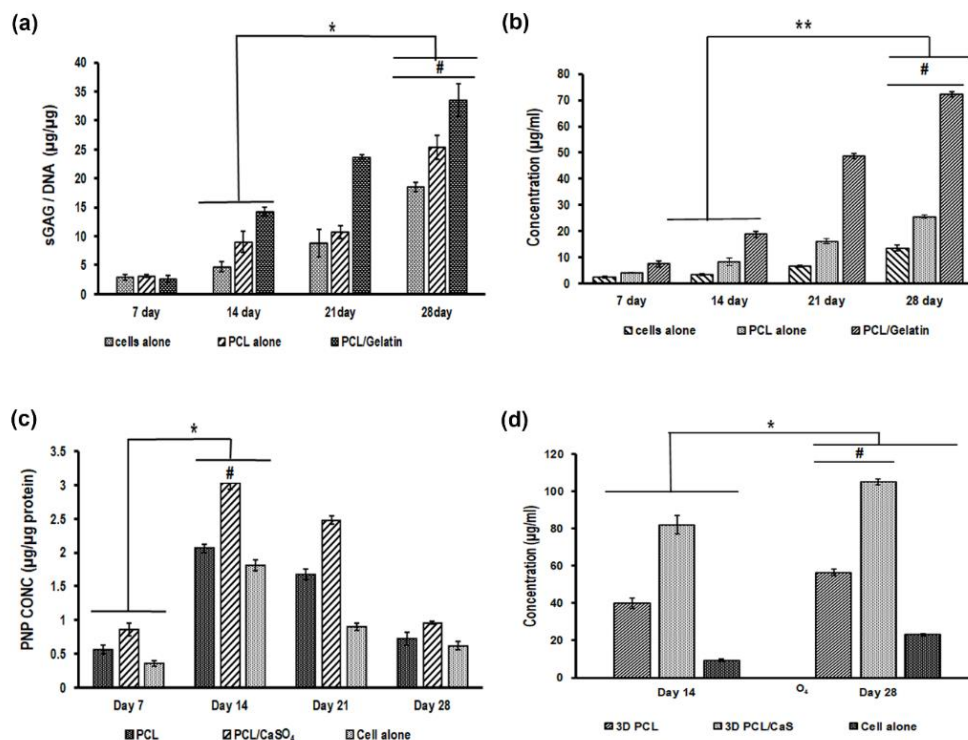


Figure 4.5.4: Biochemical assessment of chondrogenic and osteogenic differentiation of ADMSCs. Graphs (a), (b), (c) and (d) shows the quantitative information on the sulphated Glycosaminoglycan content sGAG/DNA ($\mu\text{g}/\mu\text{g}$), the total collagen content, quantitative estimation for the osteogenic differentiation marker Alkaline phosphatase (ALP) on bone phase and the extent of mineralization defined as the total Calcium content ($\mu\text{g}/\text{mL}$) on different scaffolds respectively. p < 0.05, ** represents p < 0.01, *** represents p < 0.005, and **** represents p < 0.0001).

However, the calcium content also showed noticeable differences among the scaffolds with higher calcium content in the PCL/CaSO₄ scaffolds when compared to the pristine PCL scaffolds. It was obvious that the addition of CaSO₄ particles enhanced the osteogenic properties of scaffolds, and PCL/CaSO₄ scaffolds were more favourable to the expression of alkaline phosphatase and matrix mineralization, which was important for osteogenesis.

4.4.1.4.3 Immunostaining for cartilage and Bone markers

The images of immunofluorescence staining of the cell-scaffold constructs were shown in figure 4.5.5 & figure 4.5.6. Immunofluorescence staining of cartilage-specific markers (Aggrecan, Collagen type II (COL 2)) revealed robustly expressed positive signal around differentiated MSCs on 3D-printed PCL/Gelatin scaffold (figures 4.5.5 (a)-(c) & (d)-(f)) when compared to PCL alone 3D scaffold (figure 4.5.5 (g)-(i) & (j) & (l)) after 28 days of *invitro* cell culture in chondrogenic medium.

The bone-specific markers (Osteonectin / SPARC (OSN), ALP, Osteocalcin (OCN)) showed diffuse and intense positive signal from the cells cultured on the bone phase (PCL/CaSO₄) of BLS (figure 4.5.6(a)-(c),(g)-(i) & (m)-(o) as compared to weak signal intensity on its respective controls (figures 4.5.6 (d)-(f), (j)-(l) & (p)- (r) on the 28th day.

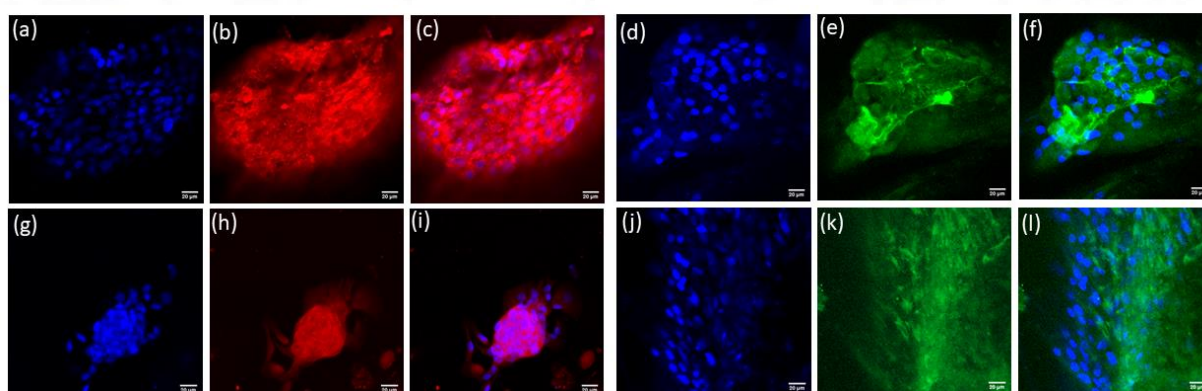


Figure 4.5.5: Immunofluorescence confocal microscopic images of cartilage markers. Aggrecan in cartilage phase of BPS (PCL/Gelatin) (a)-(c) and in control scaffold (PCL) (d)-(f); Type II Collagen expression in a cartilage phase of BPS (g)-(i) and control scaffolds (j)-(l).

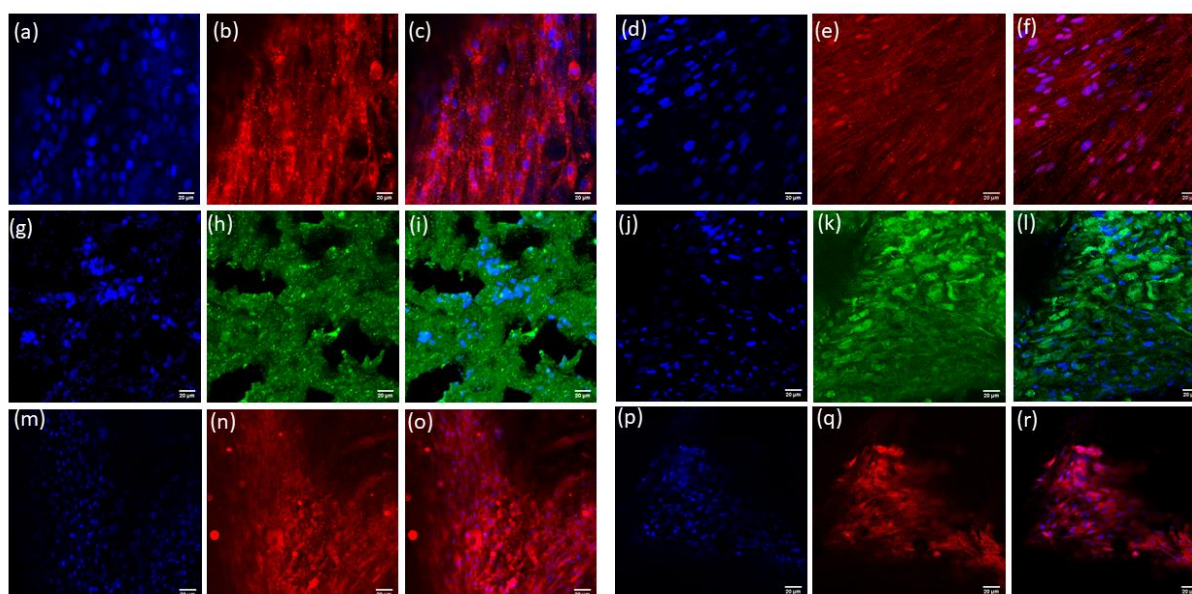
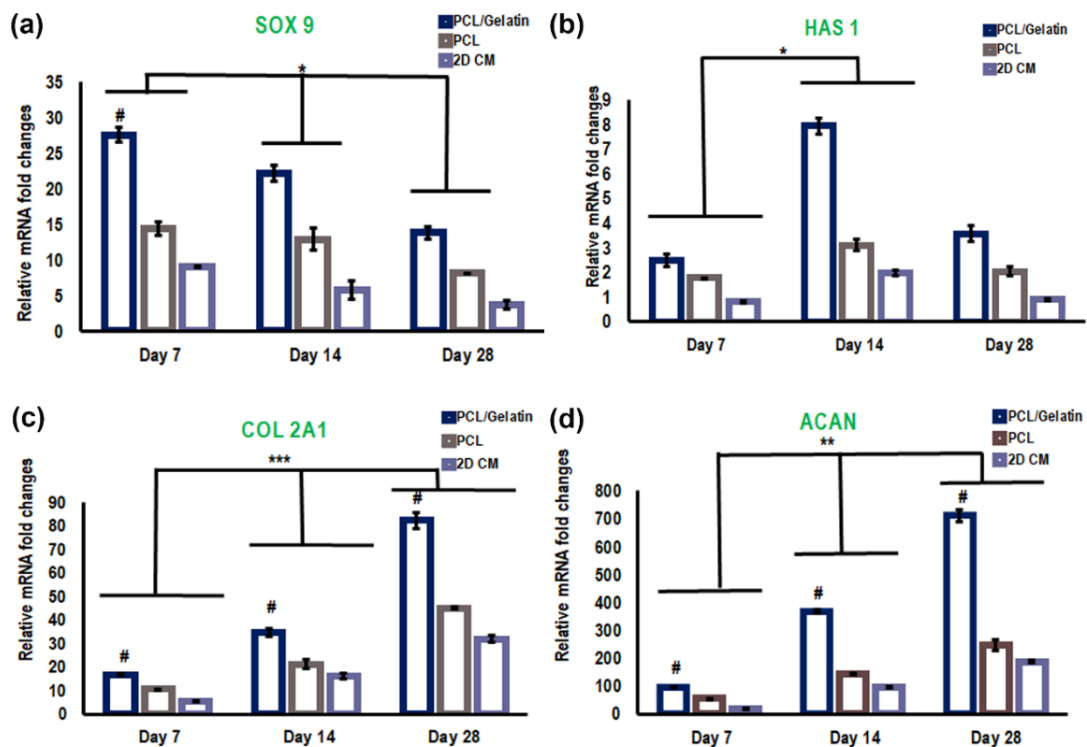


Figure 4.5.6: Immunofluorescence confocal microscopic images of osteogenesis markers. Alkaline Phosphatase (ALP) expression (a)-(c), osteocalcin expression (g)-(i), Osteonectin/ Sparc (OSN) expression (m)-(n) in bone phase of BPS (PCL/CaSO₄) and in control scaffold (PCL/PLGA) (g); (h), and (d)-(f), (j)-(l), (p)-(r) represents the ALP, osteocalcin and Osteonectin/ Sparc (OSN) in control scaffolds after 28 days.

4.4.1.4.4 Gene expression analysis qRT-PCR:

The gene expression of relevant chondrogenic and hypertrophic markers was analyzed for MSCs cultured in the cartilage phase of BPS in a chondrogenic medium (figure 4.5.7) on days 3, 7, 14, and 28. SOX 9 is one of the essential transcription factors for chondrocyte differentiation (Hardingham et al., 2006, p. 9). From the results, it was observed that SOX 9 increased and peaked at day 7 and then decreased on days 14 and 28 (figure 4.5.7 (a)). The SOX 9 expression in PCL/Gelatin and PCL groups peaked at day 7 before other chondrocyte markers (HAS1, COL 2). And the level of SOX9 was markedly higher in the blend (27 and 13-fold) than that in PCL alone group (14 and 8-fold) by day 7 and day 28 respectively. However, expression of HAS 1 peaked on Day 14 when compared to day 7 and then decreased on day 28 (figure 4.5.7(b)). Also, an increased expression of HAS 1 in the blend (7-fold) was noticed when compared to pure PCL scaffolds (3-fold) and 2D culture (1.9-fold) by Day 14. Accordingly, expressions of late markers COL2 and ACAN of all groups were significantly

upregulated on day 28 compared to that on days 7 and 14. PCL/Gelatin constructs expressed remarkably greater levels of COL 2 and, ACAN compared to pure PCL scaffolds and 2D culture at 28 days (figure 4.5.7 (c) & (d)) and almost a 16 (day 7), 34 (day 14), and 82-fold (day 28) increase in collagen type II and about a 95 (day 7), 368 (day 14), and 711-fold (day 28) increase in aggrecan gene expression could be observed in the PCL/Gelatin based cartilage layer when compared to Day 3. This is consistent with the mechanism that SOX9 and HAS 1 regulated the expression of COL 2, ACAN at an early stage. However, the expression of a hypertrophic marker, COL10 was less expressed in the blend on days 7 and 28 (figure 4.5.7 (e)). The 2D culture of MSCs without a 3D scaffold showed greater expression of COL10 and its differentiation towards hypertrophy.



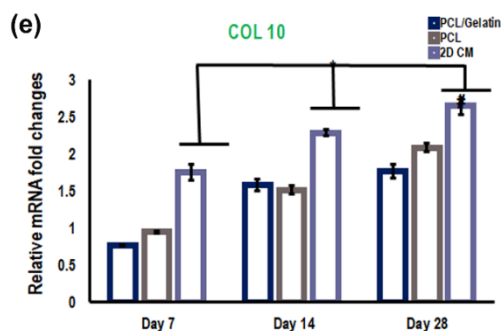


Figure 4.5.7: Assessment of expression of the chondrogenesis-specific genes. (a) SRY-Box Transcription Factor 9 (SOX 9), (b) Hyaluronan Synthase 1 (HAS1), (c) Collagen type 2 A1 (COL 2A1) (d) Aggrecan (ACAN) and (e) Collagen type 10 (COL 10) within the scaffolds. Results are expressed as mean \pm SD. (n = 3, *, # P < 0.05, **, ## P < 0.01; # represents significance compared to 2D culture at the same time points).

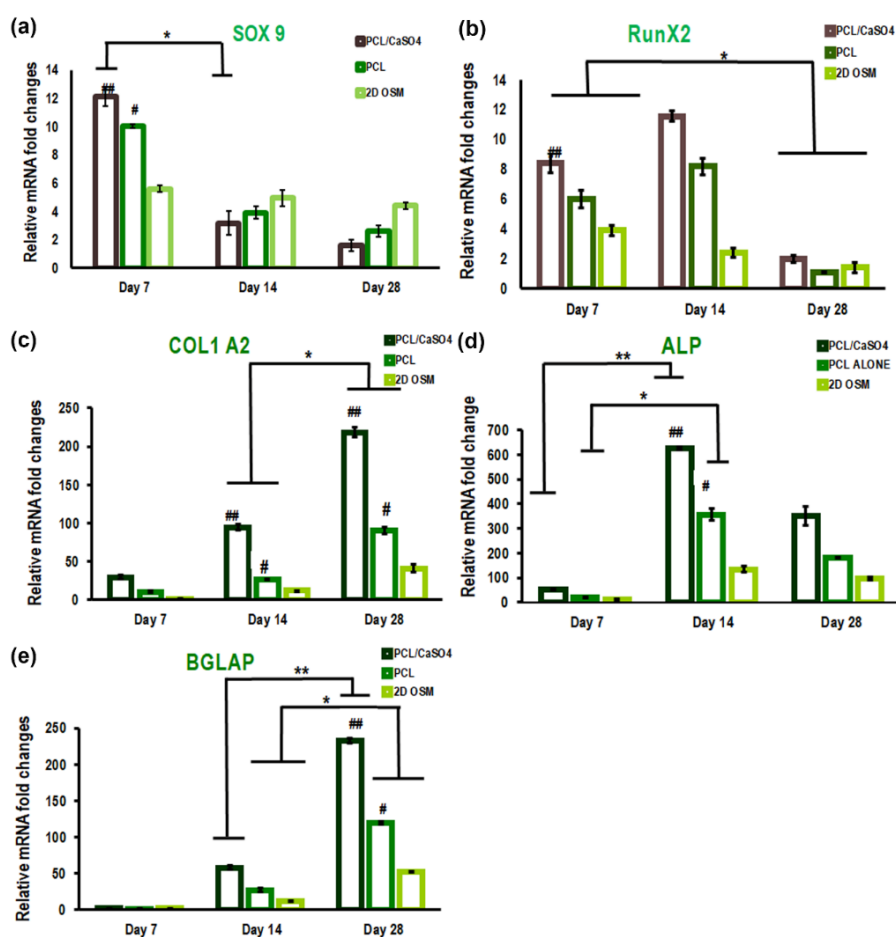


Figure 4.5.8. Assessment of expression of the osteogenesis-specific genes. (a) SRY-Box Transcription Factor 9 (SOX 9), (b) Runt-related transcription factor (RUNX2), (c) collagen type I (COL1), (d) alkaline phosphatase (ALP), and (e) bone gamma-carboxyglutamic acid-containing protein (BGLAP) /osteocalcin (OCN) within the scaffolds. Results are expressed as mean \pm SD. (n = 3, *, #P < 0.05, **, ##P < 0.01; #represents significance compared to 2D culture at the same time points).

Bone-specific gene expressions were also examined during *in vitro* osteogenic induction of MSC-seeded scaffolds evaluated on days 7, 14, and 28 as shown in figure 4.5.8. The osteogenic differentiation marker genes were found different between the study periods. The downregulation of SOX 9 expression on day 28 (1-fold), when compared to day 14 (5 -fold) on 3D scaffolds, was observed, hence osteo-chondroprogenitor cells differentiate toward osteogenic phenotypes (figure 4.5.8 (a)). RUNX2 is one of the osteogenesis-specific transcription factors. The SOX 9 expression was thus counter-checked with the RUNX2 expression which peaked at day 14 followed by a decrease in levels on day 21 (figure 4.5.8(b)).

PCL/CaSO₄ constructs expressed remarkably higher levels of RUNX2 (11-fold change) than that in the PCL group (8-fold) and 2D culture (2.2-fold) at day 14, suggesting initiation of bone formation. However, SOX 9 is more expressed in 2D culture on day 28 suggesting that SOX9 decreases Runx2 binding to its target sequences and drastically inhibits Runx2. Expressions of late markers COL1, and BGLAP of all groups were significantly upregulated on day 28 compared to that on day 14 whereas ALP was higher on day 14 (figure 4.5.8. (c,d,e)). Accordingly, PCL/ CaSO₄ constructs expressed remarkably greater levels of ALP, OCN, and COL1 compared to pure PCL scaffolds. However, the ALP expression was higher on day 14 (626-fold change) and reduced to 349-fold on day 28 indicating it as an early osteogenic marker. This is consistent with the mechanism that ALP regulated the expression of BGLAP, COL1 at an early stage. The late osteogenic markers BGLAP (232-fold change) and COL1 A2 (218-fold change) also showed greater expression on day 28 when compared to day 14. Thus, calcium sulfate-based scaffolds potentially provide a niche for MSCs in osteochondral tissue engineering based on their natural pre-osteogenic properties.

4.4.2 System B - BPS fabricated via 3D printing and dissolution adhesion technology

4.4.2.1 *In Vitro* cytocompatibility evaluation with rabbit MSCs

ADMSCs cultured on the biphasic scaffold consisting of PCL/PLGA/CS as cartilage phase and PCL/PLGA/ β TCP as bone phase were active even after 28 days of culture in medium, indicating the scaffolds are cytocompatible. Thus, *in vitro* cytocompatibility assay using ADMSCs confirms the suitability of the biphasic hybrid scaffold for cell adhesion, survival, and proliferation (figure 4.6.1 (a)).

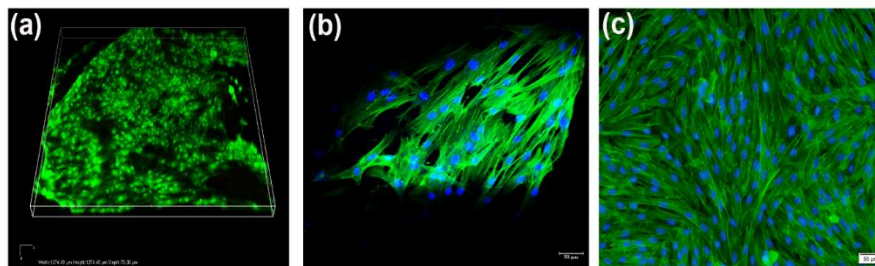


Figure 4.6.1: *In vitro* cytocompatibility assessment of BPS using MSCs. (a) represents the viability of MSCs on the developed bi-phasic scaffolds by Live Dead staining at day 28, whereas (b) & (c) are representative confocal images of MSCs on bone phase and fluorescence microscopic images on cartilage phase showing its spreading pattern and actin filament organization at 3 days of incubation.

4.4.2.2 Cell attachment and proliferation

The 3D printed osteochondral scaffolds showed excellent cell-attachment affable properties over the culture periods, as shown in figure 4.6.1. The cell adhesion and spreading pattern of MSCs on the bone (figure 4.6.1(b)) and cartilage phase (figure 4.6.1(c)) of BPS using cytoskeletal staining (phalloidin) against F-actin revealed a good spread morphology and well-organized actin filaments after 3 days of incubation in complete medium. The cells spread better and had begun to bridge across the scaffold's 3D printed filaments within 3 days.

This finding was also consistent with the results of the proliferation assay in which cell metabolic activity was evaluated by MTT assay using ADMSCs. The results demonstrated that all cell-scaffold constructs showed an active proliferation during 7 days of *in vitro* culture (figure 4.6.2(a)). There was no statistically significant difference in cell proliferation in the

initial time points among the scaffolds. However, ADMSCs proliferation showed a significant increase on composite scaffolds compared to the control scaffold after seven days ($p < 0.05$).

4.4.2.3 Differentiation of rabbit MSCs on 3D scaffolds into cartilage and bone lineages

4.4.2.3.1 Evaluation of chondrogenesis

The results of the biochemical analysis revealed that among the two constructs (PCL/PLGA, PCL/PLGA/CS) and the monolayer culture, the sGAG deposition significantly increased when a combination scaffold was used than the other one without CS indicating its chondrogenesis enhancing potential (figure 4.6.2(b), $p < 0.001$). The results showed a significantly higher amount of sGAG content in PCL/PLGA/CS scaffolds on day 28 when compared to PCL/PLGA scaffolds ($p < 0.001$). Also, the sGAG content of PCL alone scaffolds was remarkably greater than 2D monolayer cultures (cells alone). The results of collagen estimation demonstrated significantly elevated collagen production in the CS-incorporated scaffolds on day 28 when compared to bare PCL/PLGA scaffold (figure 4.6.2(c), $p < 0.001$).

4.4.2.3.2 Evaluation of osteogenesis

Alkaline phosphatase (ALP) is an important biochemical assay for osteogenesis wherein the osteogenic ability of seeded ADMSCs in various 3D printed scaffolds up to 28 days was evaluated. We compared the ALP activity of MSCs among the two constructs (PCL/PLGA and PCL/PLGA/ β TCP) and the monolayer culture, cultured in an Osteogenic medium (OS) (figure 4.6.2(d)). A gradual increase in the ALP levels was found in the constructs cultured under osteogenesis-inducing conditions and there is a significant difference in ALP activity among the scaffolds. The ALP activity of cells in the β TCP incorporated bone phase was significantly higher than that in PCL/PLGA scaffolds at 7 and 14 days ($p < 0.05$). There was a decrease in ALP activity by 28 days in all scaffolds as well as in monolayer cultures.

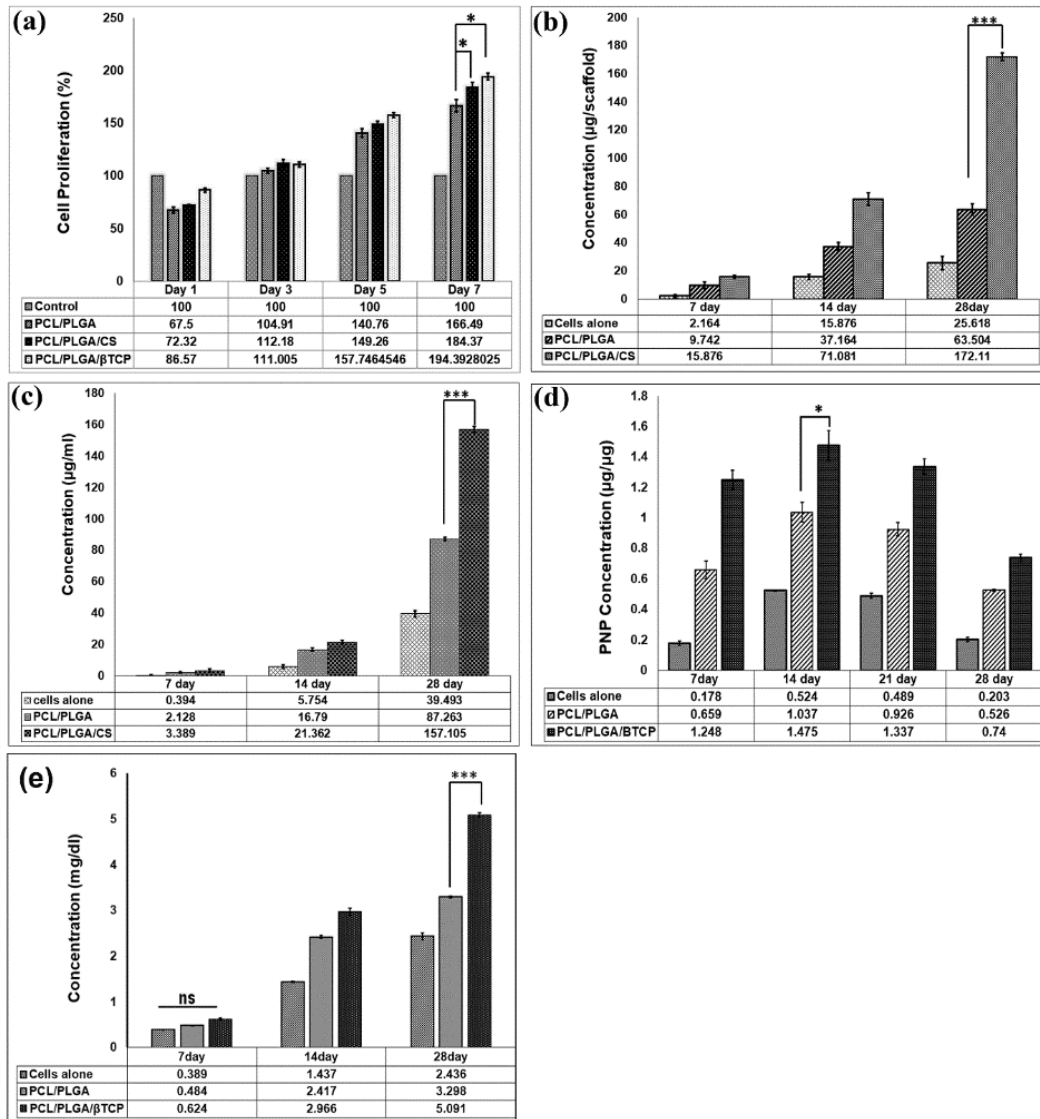


Figure 4.6.2: *In vitro* proliferation and differentiation studies. (a) represents cell proliferation assay using MTT protocol, (b) represents an estimation of total sGAG content after 28 days of culture, (c) represents total collagen content after 28 days, (d) shows ALP activity in different scaffolds on different time points, (e) representative graph of calcium estimation after 28 days of culture (***: $p < 0.001$, *: $p < 0.05$, ns: $p > 0.05$).

Matrix mineralization is a late marker for fully differentiated osteoblasts. Upon calcium estimation, our results showed that ADMSCs cultured on 3D scaffolds in an osteogenic medium showed mineralization of the matrix, indicated by the gradual increase in calcium content from day 14 to day 28 (figure 4.6.2 (e)). Notably, β TCP incorporated PCL/PLGA scaffolds showed significantly higher calcium content as compared to the PCL/PLGA alone scaffolds at day 28 ($p < 0.001$).

4.4.2.3.3 Immunostaining for cartilage and bone markers

Immunohistochemical analysis of cartilage specific markers (Aggrecan, Collagen type II (COL 2) (figures 4.6.3 (a to d)) and bone specific markers (Osteonectin / SPARC (OSN), ALP, Osteocalcin (OCN) (figures 4.6.3 (e- j)) showed robust expression of these markers by the cells cultured on cartilage phase with bioactive factors (PCL/PLGA/CS) (figures 4.6.3 (a) & (c)) and bone phase with bioactive factor (PCL/PLGA/ β TCP) (figure 4.6.3(e) , (g) & (i)) of BPS by day 28 when compared to its respective controls (figures 4.6.3.(b), (d) & (f), (h) & (j)).

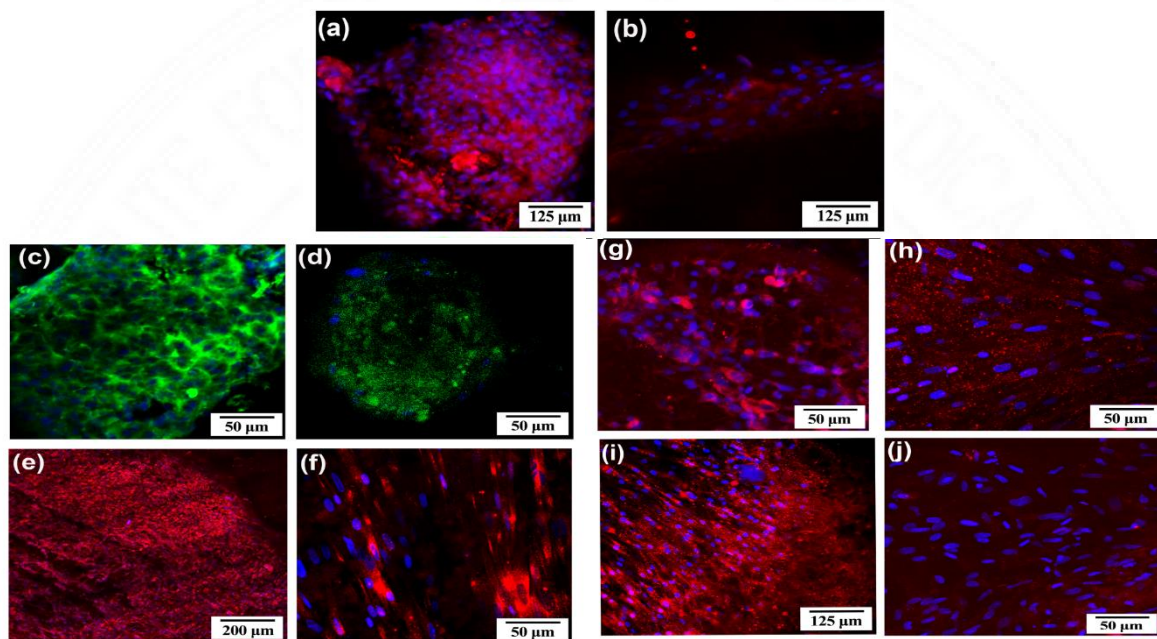
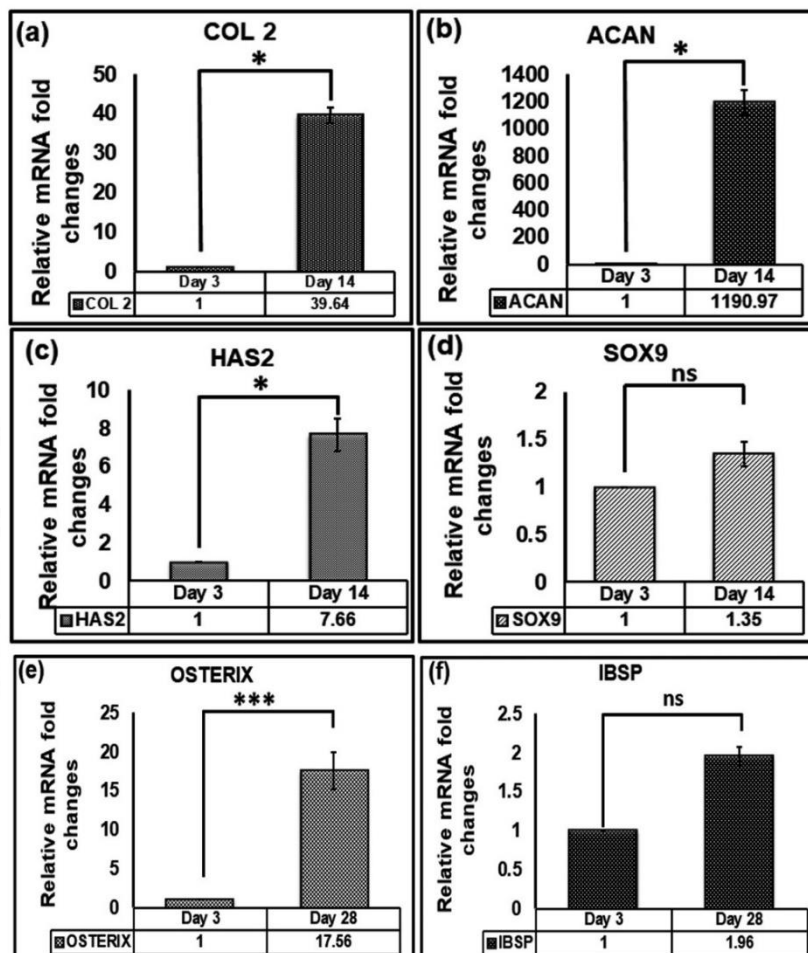


Figure 4.6.3: Immunohistochemical analysis for specific markers of chondrogenesis and osteogenesis. (a) – (j) represents the immunofluorescence confocal microscopic images showing the expression of important cartilage and bone markers. Aggrecan in cartilage phase of BPS (PCL/PLGA/CS) (a) and control scaffold (PCL/PLGA) (b); Type II Collagen expression in cartilage phase of BPS (c) and control scaffold (d). Well-known bone markers were also evaluated, viz. Osteocalcin expression in the bone phase of BPS (PCL/PLGA/ β TCP) (e) and control scaffold (PCL/PLGA) (f); Osteonectin/ Sparc (OSN) expression in the bone phase of BPS (g), and control (h); Alkaline Phosphatase (ALP) expression in the bone layer of BPS (i) and in control (j), after 28 days.

4.4.2.3.4 Gene expression analysis using qRT-PCR

The qRT PCR-based assessment of mRNA transcript levels of chondrocyte-specific genes, Collagen 2 (COL 2), Aggrecan (ACAN), Hyaluronan Synthase 2 (HAS2), and SOX 9 and osteogenic specific genes (Bone sialoprotein (BSP), Osteocalcin (BGLAP), Osterix was

performed. The results showed significant upregulation of chondrocyte/bone marker gene expression (Figure 4.6.4). The marker genes for chondrogenesis were evaluated on day 14 and an almost a 40-fold increase in collagen type II (figure 4.6.4(a), p-value < 0.05), and about a 1200-fold increase in aggrecan gene expression (figure 4.6.4(b), p-value < 0.05) could be observed in the cartilage phase of the biphasic scaffold when compared to Day 3. Also, an increased expression of the other cartilage-specific markers, HAS 2 (7.66-fold) (figure 4.6.4(c), p-value < 0.05) and SOX9 (1.35-fold) (figure 4.6.4 (d), p-value >0.05, non-significant(ns)) was noticed by Day 14. Meanwhile, the marker genes for osteogenesis were evaluated and there is a 17.56-fold increase in the expression of Osterix mRNA levels (figure 4.6.4(e), p-value < 0.001) on day 28 compared to that on day 3. Bone sialoprotein (IBSP, ~2-fold increase), (figure 4.6.4(f), p-value >0.05, ns), Osteocalcin (BGLAP, 1.27-fold increase), (figure 4.6.4(g), p-value > 0.05, ns) expression were also found to be upregulated at Day 28.



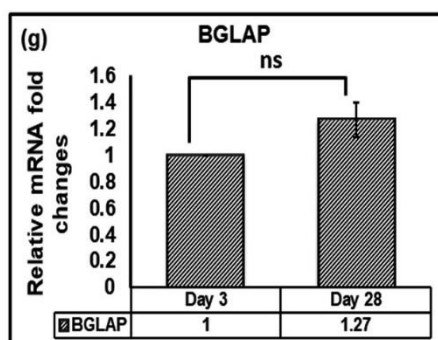


Figure 4.6.4: Assessment of marker genes for chondrogenesis (a) Collagen 2 (COL 2), (b) Aggrecan (ACAN), (c) Hyaluronan Synthase 2 (HAS2) (d) SOX 9 and Osteogenesis (e) Osterix, (f) Bone sialoprotein (IBSP) and (g) Osteocalcin (BGLAP).

4.4.3 System C - BPS fabricated via 3D printing

In vitro cell culture on scaffolds:

The ADMSCs could differentiate into specific lineage upon induction, and hence these multipotent ADMSCs are often used for studies related to osteochondral defects regeneration.

4.4.3.1 *In Vitro* cytocompatibility evaluation of the 3D printed scaffolds with rat

ADMSCs: Cell Viability by Live dead assay

In this study, the biocompatibility of different phases of biphasic scaffolds was assessed by *in vitro* culture of ADMSCs on the 3D printed scaffolds (i.e., PCL/PVP/PAA, PCL/PVP/CS/PAA, and PCL/PVP/ β TCP/PAA). The viability assessment via the live/dead staining of ADMSCs on scaffolds after 7 days of culture is shown in Figure. 4.7.1 and it was apparent that rat ADMSCs survived well in test and control scaffolds (figure 4.7.1 (a)- (i)) and exhibited a uniform distribution with a polygonal and spindly appearance. Also, when compared to the control, the test scaffolds; cartilage phase (figure 4.7.1(d)-(f)) and bone phase (figure 4.7.1(g)-(i)) with biomimetics showed favorable adhesion with the greater number of living cells with few dead cells after 7 days of culture in the complete growth medium, with no alterations on the morphology of cells. However, the control scaffolds also showed the viability of cells, yet in a different distributing pattern.

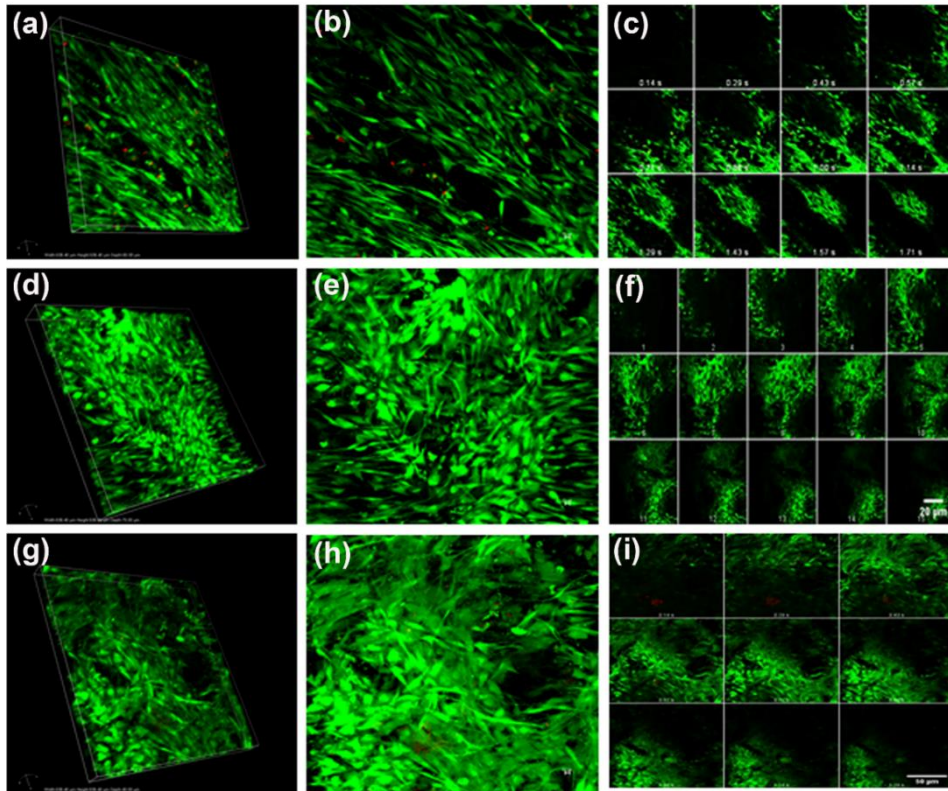


Figure 4.7.1: In vitro cytocompatibility assessment on day 7. Confocal microscopic images of viability of MSCs at Day 7 on the 3D printed PCL/PVP/PAA (a)-(c), PCL/PVP/CS/PAA cartilage phase (d)-(f), PCL/PVP/ β TCP/PAA bone phase (g)-(i): volume viewer (a,d,g), maximum projection, merged and stacked images (b, e, h,), montage view (c, f, i)

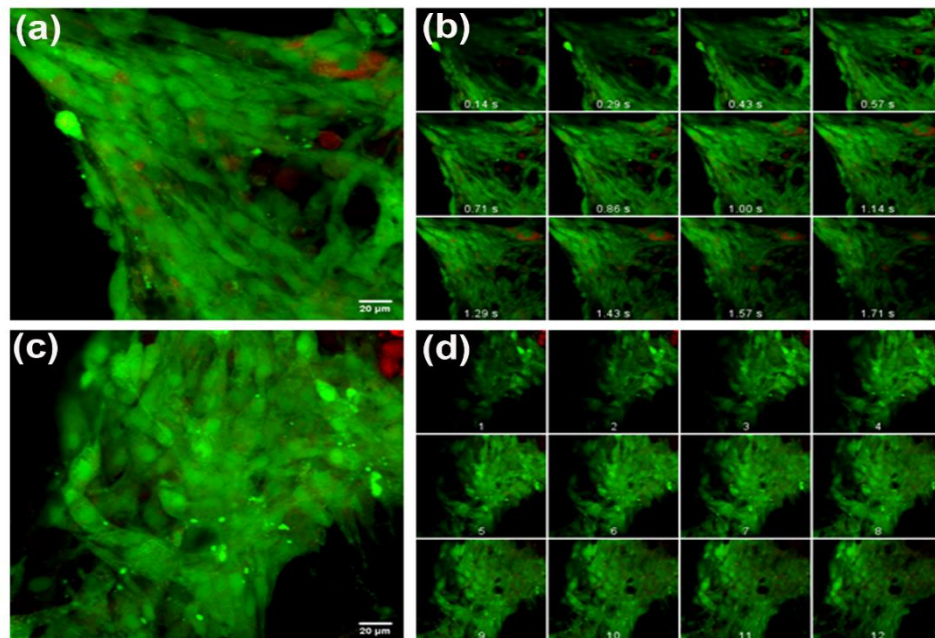


Figure 4.7.2: In vitro cytocompatibility assessment at day 28. Confocal microscopic images of viability of MSCs at Day 28 on the 3D printed PCL/PVP/ β TCP/PAA bone phase (a) & (b), and PCL/PVP/CS/PAA cartilage phase (c) & (d): maximum projection, merged and stacked images ((a) & (c)) and montage view ((b) & (d)).

Meanwhile, cells in hybrid scaffolds are evenly distributed not only in the pores but also spreading on the surfaces of scaffolds. ADMSCS were active and viable on the biphasic scaffold even after 28 days of culture in the differentiation medium, with a negligible number of dead cells (figure 4.7.2 (a)-(d)), indicating the scaffolds are cytocompatible. Besides, ADMSCs gradually formed clusters on the surface of the cartilage phase after 28 days, which is a primitive sign of chondrogenesis of ADMSCs.

4.4.3.2 Cell proliferation studies:

Further, to quantify the total DNA content on the cell-seeded construct (PCL/PVP/CS/PAA, PCL/PVP/TCP/PAA, PCL/PVP/PAA) and 2D culture, a PicoGreen assay was performed and cell proliferation is illustrated in the Figure. 4.7.3(b). ADMSCs proliferated well and continuously on all scaffolds during the 14-day culture and there was a significant difference in DNA content among the tested groups on 14-day when compared to day 3. Also, in the 14th-day samples, the DNA content was significantly higher in the scaffolds with biomoeities when compared control and had increased about 3-fold at 14 days, which was in line with growth trend, suggesting cells proliferated faster. The confocal images of cells proliferated on both the phases on day 14 are illustrated in figures 4.7.3 (c) & (d). The cartilage phase has a cubical pattern with gradient pores, and the cells are aligned and proliferated in the designed pattern, which is a conical arrangement of cells from the top (broad) to the bottom (narrow). However, in bone phase, cells proliferated in concentric circles in designed star pattern.

4.4.3.3 Cell morphology:

Figure 4.7.3 (e) - (f) illustrates the confocal microscopic images of the morphology of the cells (attachment and spreading) in the scaffolds cultured in the growth medium for 3 days studied by staining against F-actin using FITC-conjugated phalloidin. ADMSCs adhered and spread on the pores of the scaffold as early as day 3 by forming a thick layer of cells covering the surface of the scaffold. The images revealed cells with good spread morphology and well-

organized actin filaments. Both the layers provide a good microenvironment for cell adhesion and its spreading and thus acted as excellent cell-friendly assemble.

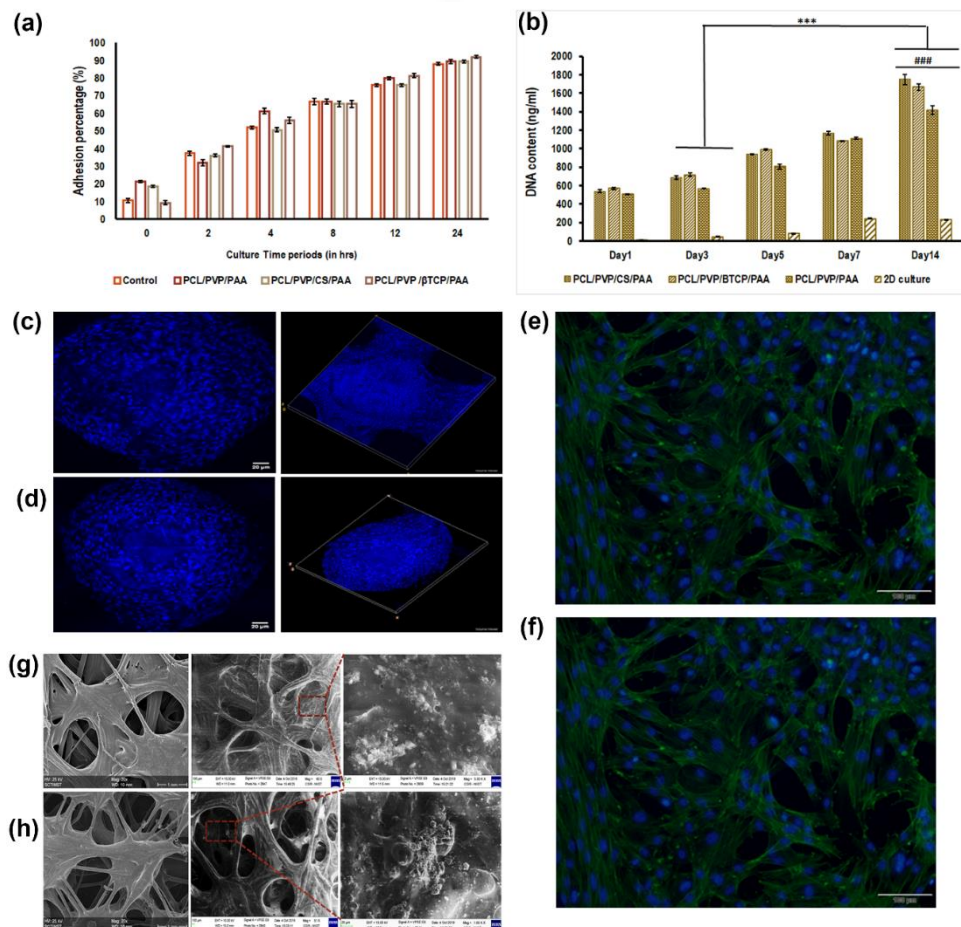


Figure 4.7.3: Cell adhesion, proliferation and morphology. The cell adhesion rate at different culture periods (a), (b) represents cell proliferation using Pico green assay to determine the DNA content with time, (c) & (d) represents confocal images of cells stained with DAPI at day 14 to study the proliferation pattern qualitatively on cartilage and bone phases (e) & (f) are representative confocal images of MSCs on cartilage phase (PCL/PVP/CS/PAA) and bone phase (PCL/PVP/βTCP/PAA) respectively showing its spreading pattern and actin filament organization by staining against F-actin using FITC-conjugated phalloidin on 3rd day, (g) and (h) represents the SEM image showing the cells cultured in respective differentiation medium after 28 days.

The effect of scaffold structure on cell morphology was studied by the osteochondrogenic culture of respective phases for 28 days. Figure 4.7.3 (g)-(h) illustrates SEM micrographs of the morphology of attached ADMSCs seeded on the 3D printed scaffolds (i.e., PCL/PVP/CS/PAA and PCL/PVP/βTCP/PAA) after 28 days of culture in respective differentiation medium. The majority of cells exhibited their phenotypic morphology on

cartilage and bone phases. The spindle-shaped MSCs upon differentiation aggregated and exhibited clustered cells with rounded morphology. However, cell spreading was enhanced on biomimetic scaffolds rather than control scaffolds; PCL/PVP/PAA. It was observed that cells spread but filled in pores and the differentiated cells aligned and distributed on the struts and pores of the tested scaffolds. However, few pores were closed with secreted ECM when compared to the scaffolds without cells.

4.4.3.4 Differentiation of rat ADMSCs on 3D scaffolds into cartilage and bone lineages

4.4.3.4.1 Evaluation of chondrogenesis

The efficacy of the 3D printed cartilage phase to augment differentiation of the seeded MSCs to chondrogenic lineage and production of hyaline cartilage-specific extracellular matrix is assessed by quantification of sGAG via DMMB assay and DNA content by nanodrop method. Figure 4.7.4 (a) represents the content of sGAG secreted by cultured cells in the chondrogenic medium after 7, 14 and 28 days. The results showed that the sGAG content increased gradually throughout the study period and among the two constructs (PCL/PVP/PAA, PCL/PVP/CS/PAA) and the monolayer culture, the sGAG deposition was significantly higher by day 28 when the combination scaffold was used than the other one without CS, indicating its chondrogenesis enhancing potential ($p \leq 0.001$). Also, there was no statistically significant difference between the sGAG/DNA in the PCL/PVP/PAA and PCL/PVP/CS/PAA group on day 14 suggesting both the scaffolds favored chondrogenesis and produced comparable sGAG. Upon assessing the total DNA content, the only minimal difference was observed and PCL/PVP/PAA/CS scaffolds have slightly higher compared to the other one without CS suggesting similar proliferation activity and sGAG production. However, by day 28, the sGAG significantly increased in PCL/PVP/PAA/CS scaffolds with a similar amount of DNA in PCL/PVP/PAA suggesting though the proliferation of cells ceased, the production of sGAG is

more. Thus, the availability or effect of incorporated biofactor which is either released or retained enhanced chondrogenesis and production of ECM by day 28 suggesting effect of CS.

The results of collagen estimation are illustrated in figure 4.7.4(b) and the collagen content increased during the culture period. When compared to day 14, a significantly higher amount of collagen was quantified ($P < 0.001$) in the PCL/PVP/CS/PAA than in the other groups on Day 28 ($P < 0.001$, suggesting the MSCs differentiated towards chondrogenic lineage and produced cartilage-specific ECM. Thus, the collagen production was more effective in the PCL/PVP/CS/PAA group, at an early stage (4 weeks).

4.4.3.4.2 Evaluation of osteogenesis

To evaluate the osteogenic ability of seeded ADMSCs in fabricated 3DP scaffolds, we compared and evaluated the ALP activity of MSCs in 3 groups of constructs, PCL/PVP/ β TCP/PAA, PCL/PVP/PAA, and 2D culture (cell alone) (figure 4.7.4.(c)) cultured in osteogenic medium (OS) up to 28 days. ALP activities of ADMSCs in PCL/PVP/ β TCP/PAA were significantly higher ($p < 0.05$) than that in PCL/PVP/PAA and 2D culture group at 14 days, and gets reduced by 28 days in all the three groups. These results suggested ALP activity as an early marker for osteogenesis and β TCP incorporated PCL-based scaffolds showed enhanced osteogenesis of ADMSCs as early as 7 and 14 days, compared to other groups. However, no greater difference in ALP activity was observed between with and without β TCP incorporated scaffolds on day 7. The enhanced ALP activity in the β TCP incorporated scaffolds in the later periods (day 14) suggests the availability of β TCP for enhanced differentiation.

Matrix mineralization is a late marker for fully differentiated osteoblasts. To demonstrate the extent of matrix calcification, calcium content was quantified and our results showed ADMSCs cultured on 3D scaffolds in an osteogenic medium showed mineralization of the matrix, exhibited a prominent increased and gradual increase in calcium content from day 14 to day 28 (figure 4.7.4(d)). Notably, β TCP incorporated PCL/PVP/ β TCP/PAA scaffolds

showed significantly higher Ca content as compared to the PCL/PVP/ PAA alone scaffolds on days 14 and 28 ($p < 0.001$). Control cultures showed increase in Ca content over time.

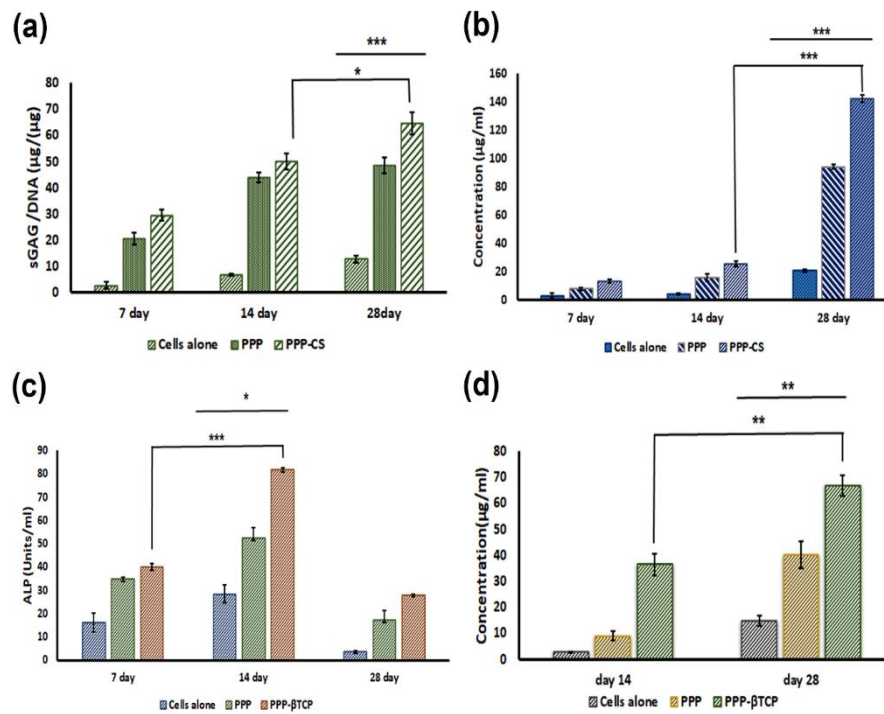


Figure 4.7.4: Evaluation of differentiation of rat ADMSCs on 3D scaffolds into cartilage and bone lineages on respective phases by biochemical analysis. (a) represents estimation of total sulfated glycosaminoglycan (sGAG) content after 28 days of culture, (b) represents total collagen content after 28 days of culture, (c) shows ALP activity in different scaffolds on different time points, (d) representative graph of calcium estimation after 28 days of culture of MSCs on the developed bone phase in osteogenic differentiation media (***: $p < 0.001$, **: $p < 0.01$, *: $p < 0.05$, ns: $p > 0.05$).

4.4.3.4.3 Immunostaining for cartilage and bone markers

Immunofluorescence images of the cell-scaffold constructs were shown in figure 4.7.5. Immunohistochemical analysis of cartilage-specific markers; aggrecan and collagen type II (COL 2) were detected as diffuse and robust positive extracellular signals around differentiated MSCs after 28 days of *invitro* cellular culture on cartilage phase with bioactive factors (PCL/PVP/CS/PAA) (figures 4.7.5(a)-(f)) in chondrogenic medium. The bone-specific markers; osteonectin / SPARC (OSN), osteocalcin (OCN), and ALP showed robust and positive expression of these markers by the cells cultured in the bone phase with bioactive factor (PCL/PVP/βTCP/PAA) (figure 4.7.5(g) - (o)) of BLS by day 28 in osteogenic medium.

However, in some areas of the scaffold, weak signal of ALP and uneven distribution of the expression of osteocalcin was observed.

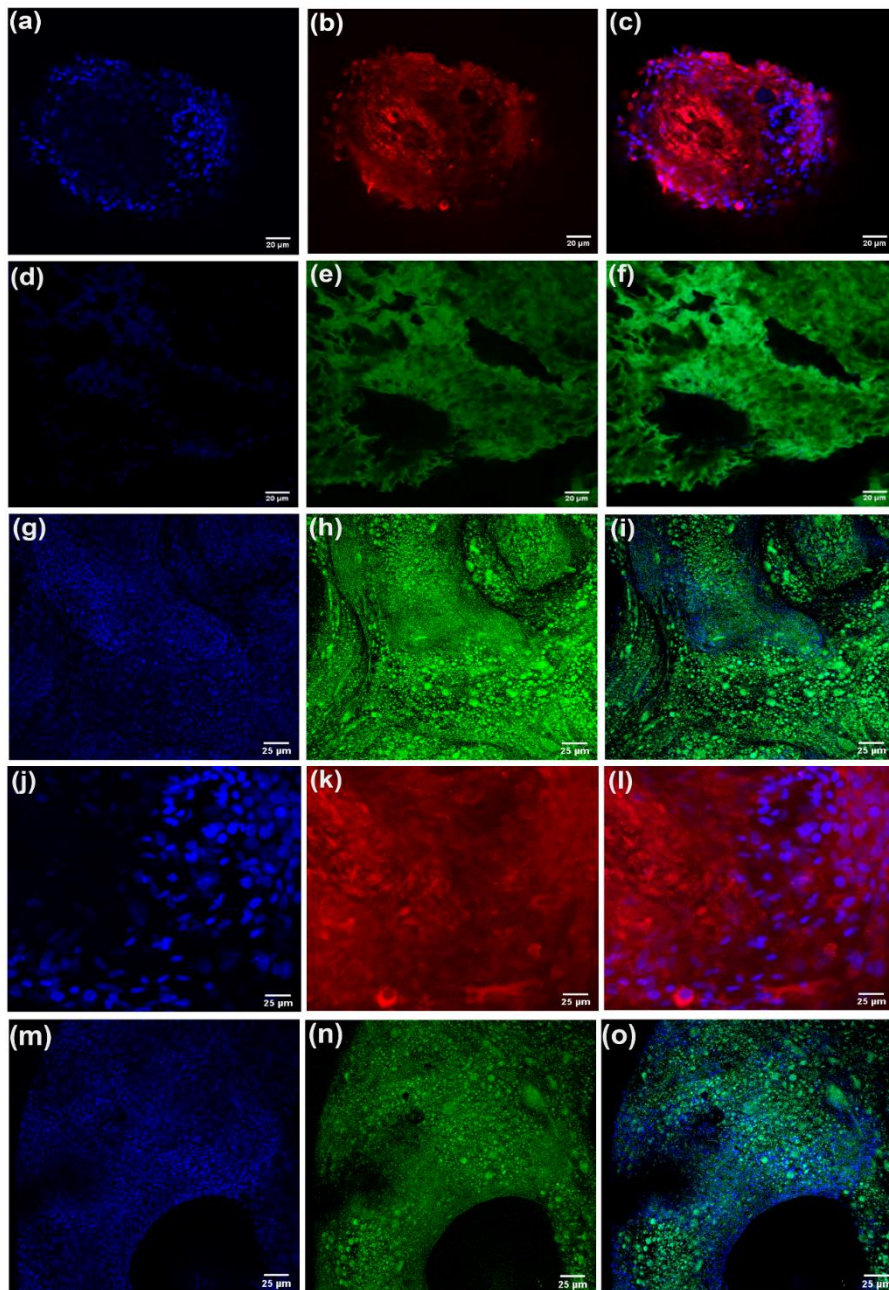


Figure 4.7.5: Immunohistochemical analysis for specific markers of chondrogenesis and osteogenesis. Immunofluorescence confocal microscopic images showing the expression of important cartilage markers; aggrecan (a)-(c) and type II collagen (d)-(f) in cartilage phase of BLS (PCL/PVP/CS/PAA) (b) Well-known bone markers were also evaluated, viz. osteonectin/ Sparc (OSN) (g)-(i), osteocalcin (j)-(l) and alkaline phosphatase (ALP) expression in the bone phase of BLS (PCL/PVP/ β TCP/PAA) after 28 days.

4.4.3.4.4 Gene expression analysis using qRT-PCR

The marker genes for chondrogenesis (figure (4.7.6(a)-(e)), was evaluated on day 3, 14, and 28 and an almost a 60 (day 14) and 105-fold (day 28) increase in collagen type II and about a 725 (day 14) and 1210-fold (day 28) increase in aggrecan gene expression could be observed in the cartilage phase with CS (PCL/PVPCS/PAA) when compared to Day 3. Also, an increased expression of the other cartilage-specific markers, HAS 1 (10-fold and 2-fold) and SOX9 (5 and 2-fold) was noticed on Day 14 and Day 28 respectively. However, the expression of the hypertrophic marker, COL10 was less expressed in CS incorporated layer at both the time points. The 2D culture of MSCs without a 3D scaffold showed greater expression of COL10 and its differentiation towards hypertrophy.

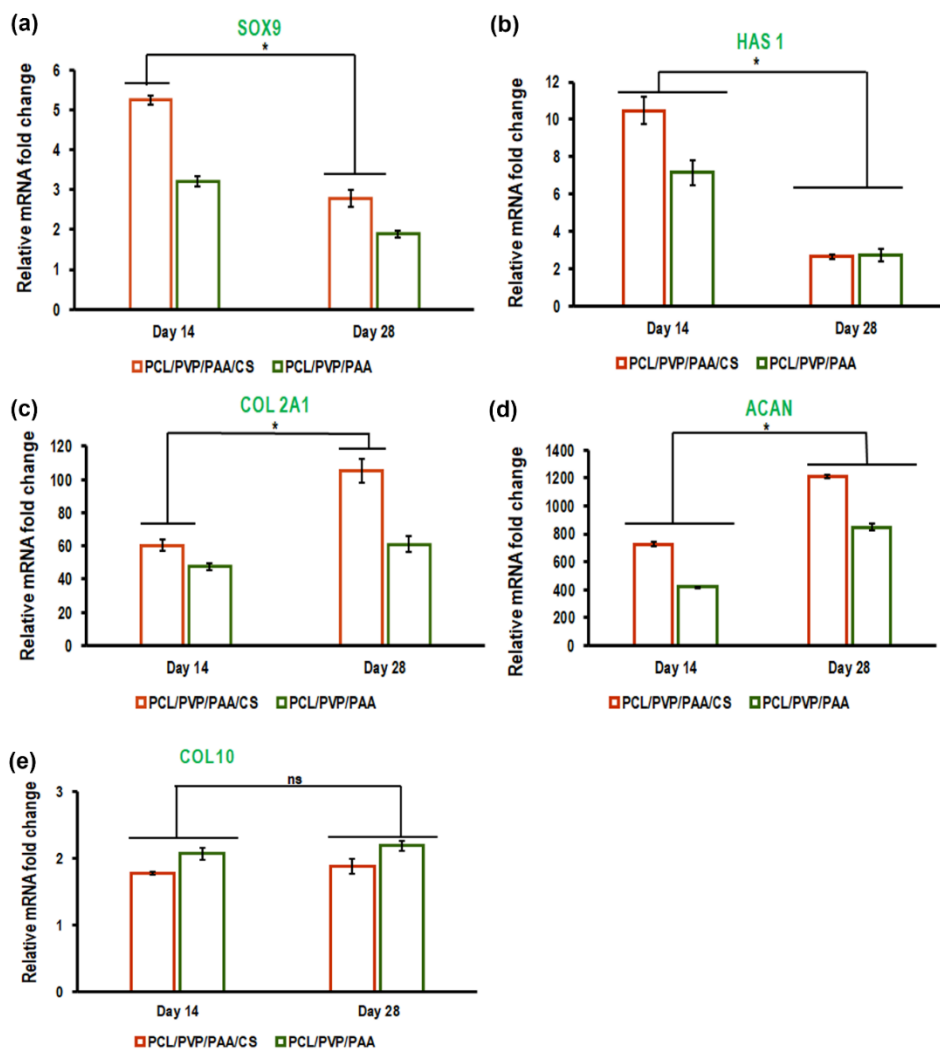


Figure 4.7.6: Assessment of marker genes for chondrogenesis. (a) SRY-Box Transcription Factor 9SOX 9, (b) Hyaluronan Synthase 1 (HAS1), (c) Collagen 2 A1 (COL 2A1) (d) Aggrecan (ACAN) and (e) Collagen 10 (COL 10). Results are expressed as mean \pm SD. (n = 3, *, # P < 0.05, **, ### P < 0.01; # represents significance compared to 2D culture at the same time points).

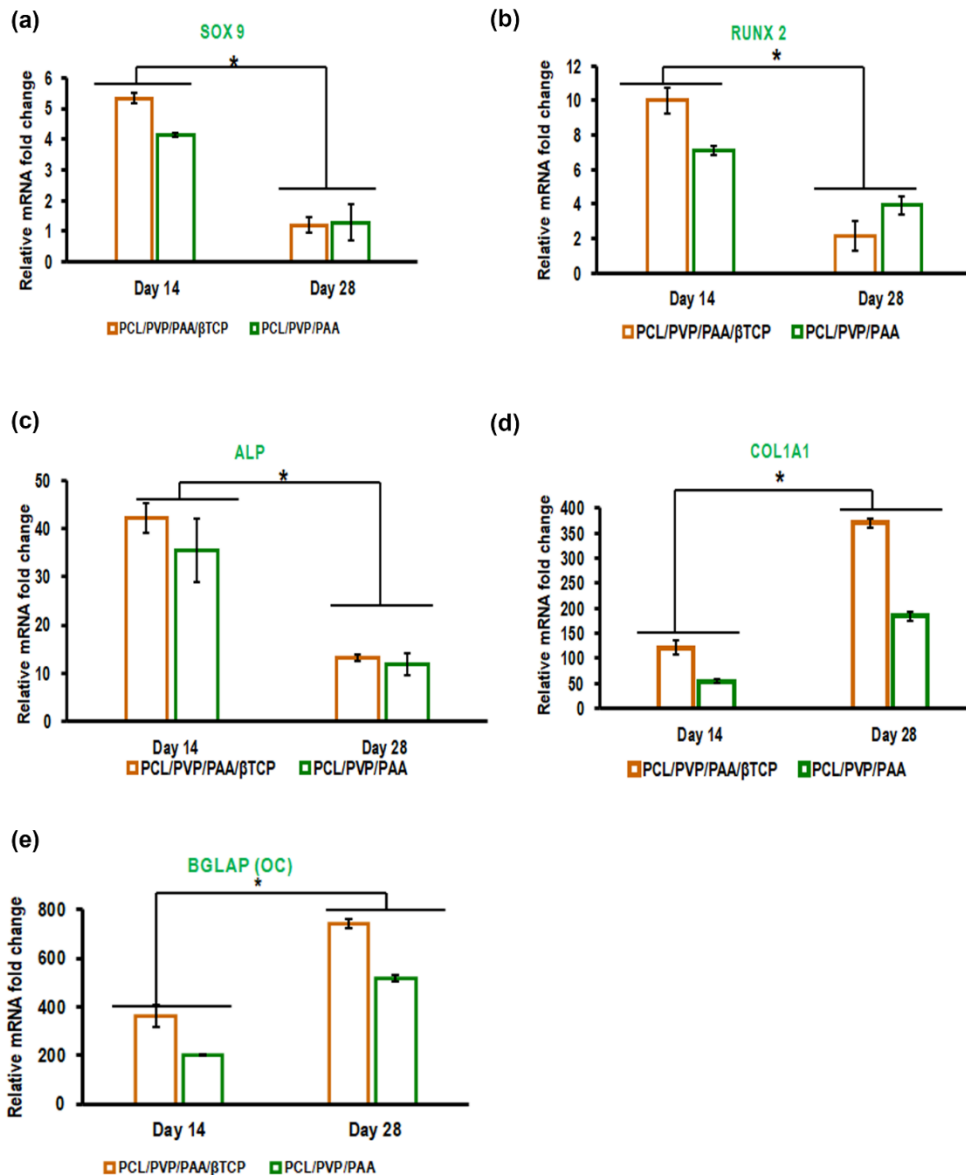


Figure 4.7.7: Assessment of expression of the osteogenesis-specific genes. (a) SRY-Box Transcription Factor 9 (SOX 9), (b) Runt-related transcription factor (RUNX2), (c) alkaline phosphatase (ALP), (d) collagen type I (COL1), (e) bone gamma-carboxyglutamic acid-containing protein (BGLAP)/osteocalcin (OCN) within the scaffolds. Results are expressed as mean \pm SD. (n = 3, *, #P < 0.05, **, ###P < 0.01; #represents significance compared to 2D culture at the same time points).

The marker genes for osteogenesis (figure 4.7.7 (a)-(e)), was evaluated on day 3, 14, and 28 and there is downregulation of SOX 9 expression on Day 28 (1-fold) when compared

to day 14 (5 -fold) on 3D scaffolds (PCL/PVP/ β TCP/PAA and PCL/PVP/PAA). The SOX 9 expression was counterchecked with the RUNX2 expression and there is a 10- fold increase in the Beta TCP incorporated layer on Day 28 compared to other time points and other groups. The ALP expression was higher on day 14 (42-fold change) and reduced to 13 on Day 28, indicating it was an early osteogenic marker. The late osteogenic markers, BGLAP (741-fold change) and COL1 A2 (370-fold change) also showed greater expression on Day 28.

4.5 Tissue engineering an osteochondral construct and its in vivo evaluation

4.5.1 Comparative study

The progress of any tissue-engineered scaffold intended for reconstruction defects is the equity between mechanical properties and functionality where pore design and structure determine the cell intrusion, proliferation, and differentiation. The scaffolds should allow for the in-growth of neo-tissue while providing a provisional physical supporting environment for MSCs to differentiate *in vivo*. Thus, to expand the application of the developed BPS in OCTE, these three biphasic scaffolds fabricated with different design patterns were compared and the best one is selected to get implanted into the osteochondral defects created in the rat knee joint to evaluate its ability to generate osteochondral tissues with or without MSCs. Hence, a comparative study was done among the three different BPS systems developed with respect to mechanical, proliferation ability, and bio functionality studies.

4.5.1.1 Mechanical studies

To investigate the structural integrity of different developed BPS, their mechanical properties were determined by a compression testing device and the results were compared. The results suggest comparable compression strength between systems B and C for both cartilage and bone phases (figure 4.8.1 (a) & (b)). In the bone phase of System, A; PCL/CaSO₄ displayed the weakest compressive strength compared to the bone phases of other systems (figure 4.8.1 (b)). The compressive strength possessed by PCL/PLGA/ β TCP and PCL/PVP/ β TCP/PAA scaffolds

are about 25 and 22 MPa (similar to cancellous bone tissue) and is much higher than PCL/CaSO₄ and other scaffolds made of PLGA or PCL alone. No significant difference in compression modulus was found between system B and system C for cartilage and bone phases ($P > 0.1$). As a result, the chosen biomaterial composites and design pattern with specific pore alignment mimicking native OC tissues determined the mechanical properties.

4.5.1.2 Proliferation studies

Cell proliferation studies among the different scaffold systems and 2D culture were quantified using the PicoGreen dsDNA assay. Concerning cartilage and bone phases as the culture time advances, the proliferation of cells varied among the three systems. As shown in Figure. 4.8.1(c) & (d), all cell-scaffold constructs showed an active proliferation during 14 days of *in vitro* culture indicated by the increase in the number of cells in the scaffolds with time when compared to the number of cells initially embedded inside the scaffolds (0.1×10^6). Through the analysis and comparisons, the DNA content was greater in system C at all time points and hence higher proliferation ability by the system. Though system 3 showed lesser DNA content on Day 1 when compared to other systems, enhanced DNA content was quantified upon Day 7 and significantly higher proliferation on day 14 when compared to day 5 suggesting cell proliferation promoting ability. Even its corresponding control without biofactors also showed enhanced proliferation (explained in previous sections). However previous studies showed biofactors incorporated scaffolds direct differentiation of MSCs to respective lineage upon induction and production of ECM when compared to its control. Thus, biofactors promote differentiation and ECM secretion and don't play a vital role in the proliferation of MSCs. However, system 2 showed a significant ability to retain the seeded cells.

4.5.1.3 Functional estimation

Some materials have appropriate mechanical properties and proliferation ability but lack differentiation potential. Hence to study the functional ability of seeded MSCs on the scaffold and the production of respective ECM, chondrogenesis was assessed by quantifying sGAG

content using DMMB assay and osteogenesis by estimating ALP activity. The result showed that the cartilage phase (PCL/PVP/CS/PAA) of system C showed greater sGAG content when compared to systems A and B at 28 days (figure 4.8.1 (e)), suggesting the composition and design pattern favored and exhibited better chondrogenesis of seeded MSCs.

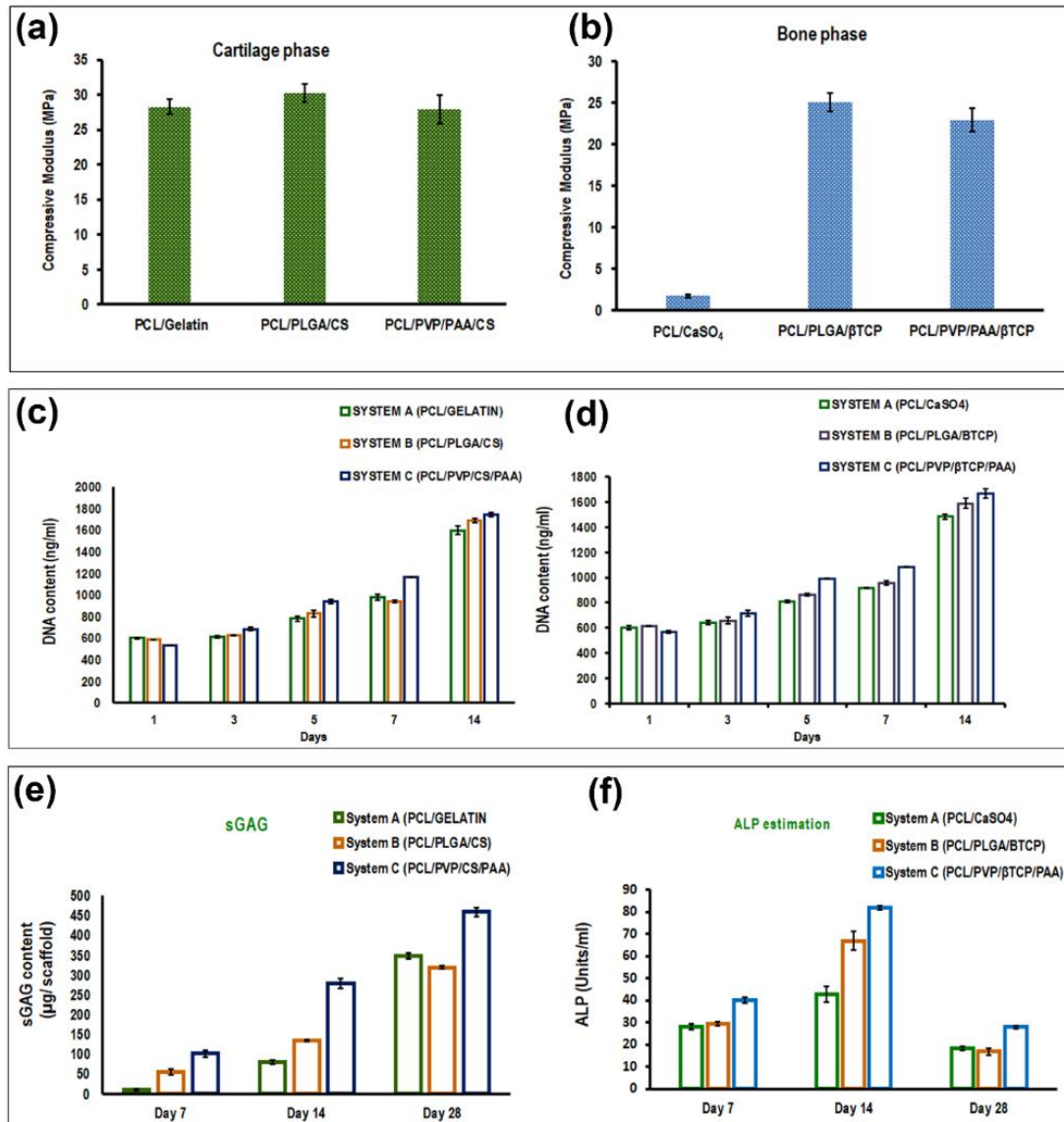


Figure 4.8.1: Comparative study among the three BPS fabricated. (a) and (b) represents the compressive modulus for the cartilage and bone phase respectively when the scaffolds are compressed to 4mm. (c) &(d) represents cell proliferation for the cartilage and bone phase respectively using Pico green assay to determine the DNA content with time, (e) represents the estimation of total sulfated glycosaminoglycan (sGAG) content after 28 days of culture of MSCs on the developed cartilage phase of biphasic systems developed in chondrogenic differentiation media, (f) shows ALP activity after 28 days of culture of MSCs on the developed bone phases of different BPS in osteogenic media at different time points.

Upon ALP estimation, the results suggested enhanced osteogenesis of ADMSCs as early as 7 days by all systems, and the levels were maintained until 14 days. Among the bone phases of three systems, system C (PCL/PVP/ β TCP/PAA) showed significantly higher ALP activity than those in systems A and B on day 14 (figure 4.8.1 (f)). However, the ALP activities among the three groups were not significantly different at 7 days ($p > 0.05$). When compared to day 3, system C showed enhanced DNA content on days 7 and 14. The greater proliferation was seen in its corresponding control without biofactors suggesting the design pattern favored the proliferation of MSCs. However, differentiation was promoted by the bio factors incorporated phases of system C BPS. Because the scaffolds PCL/PVP/CS/PAA and PCL/PVP/ β TCP/PAA exhibited higher cell proliferation and osteo-chondrogenic ability, the BPS consisting of the above phases were selected for implantation into the medial femoral condyle defects of Wistar rats for 4 and 12 weeks.

4.5.2 In vivo repair of osteochondral defect

Osteochondral defects of sizes 1.5 mm in diameter and 1.5 mm in depth were created successfully through both the chondral and the subchondral bone layer of the medial femoral condyle in the right and left knee joint of Wistar rats. The biphasic matrices (either with or without cells) were press-fitted into the defect and the defects in the sham group were left with no inserts. The surgical procedure is represented in figure 4.8.2. All animals exhibited normal movement postoperatively, and no infection was observed after 4 and 12 weeks.

4.5.2.1 Gross morphological analysis

Upon sacrifice of animals on termination day, the joints were opened and photographed. The gross appearance of knee and repair tissue with different treatments after 4 and 12 weeks was evaluated with naked eyes by the investigators unaware of the treatment group and is shown in figure 4.5.4. There were no visible changes on the surface of the knee in any of the sites. At 4 weeks post-transplantation, macroscopic observation showed no abnormal findings that

suggested the absence of rejection or infection, such as severe inflammation or extensive fibrosis in 9 rats (18 defects). In groups 1(BPS) and 2 (BPS+cells), the defects were filled with neo-formed tissues which were predominantly whitish to translucent, and a smooth (heterogenous) intact surface with significant depressions and irregularity was observed. A clear demarcation was observed between the neotissue and the native articular cartilage surface. In contrast, defects in sham group (group 3) increased in size from 1.5 to 1.8 mm in diameter.



Figure 4.8.2: Surgical procedure of osteochondral defect creation and scaffold implantation in the medial femoral condyle of an anesthetized Wistar rat. (a)-(e) represents images of lateral parapatellar longitudinal incision, the tibia pushed to displaced laterally and exposure of the medial femoral condyle (f) image of defect creation using a contra-angled micro motor handpiece with RA 245 carbide bur, (g) full-thickness critical size defect of size 1.5 mm×1 mm after saline irrigation (h) represents fully inserted osteochondral biphasic implant into the defect and (i) closure of articular capsule and skin bound with sutures.

In group 1, the articular surfaces of the defect site in experimental knees were relatively smoother than in group 2 and had coloration closer to that of surrounding normal cartilage than to that of groups 2 and 3. Furthermore, border areas of defects were less distinct and depressions were less obvious in Group 1 than in groups 2 & 3 (figure 4.8.4 (a)- (c)) at 4 weeks post implantation. In the gross appearance scoring shown in figure 4.8.3 (a), the experimental knees with BLS had higher scores compared to group 2 (BLS+CELLS) and Group 3 (SHAM) control knees, (**P<0.0001, * P <0.05).

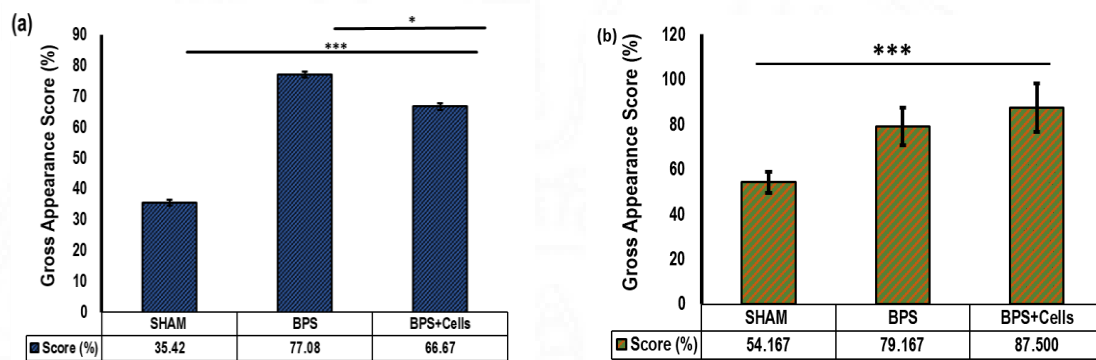


Figure 4.8.3: Gross appearance scores of knees in three different groups at 1 and 3 months. (a) & (b) represents the graphical representation of gross appearance score after 1- and 3-months study respectively where the experimental knee in group 1 was transplanted with BPS, group 2 with BPS+Cells, and group 3 ‘control knee’ is designated as SHAM with no constructs. (n = 6/group, ***P≤ 0.001, *P <0.05).

At 12 weeks post-implantation, gross examination of the BPS+Cells showed that they were completely filled with glossy and translucent, firm, and smooth cartilage-like tissues. The repaired tissue integrated imperceptibly with the surrounding native tissue (figure 4.8.4 (f)) when compared with the BPS ((figure 4.8.4 (e)) and control joints (figure 4.8.4 (d)). The margin of the defects was well delineated in BPS scaffolds implanted defects. However, depression of repaired tissues in the defect area was often present in control knees without constructs. According to the ICRS scores, the average scores of both the BPS and BPS+cells groups were significantly higher than that of the sham group at 4- and 12-weeks post-implantation, ((figure 4.8.3 (a) & (b)P < 0.001)). Although the BPS + cells group had a slightly higher score, it was

not significantly different from that of the BPS group in the 12-week duration of this study (figure 4.8.3 (b). There was no evidence of infiltration of inflammatory cells, lysis, or formation of cysts in the subchondral bone of BPS or BPS+ cells joints. This outcome confirmed that the tested scaffolds were biocompatible.

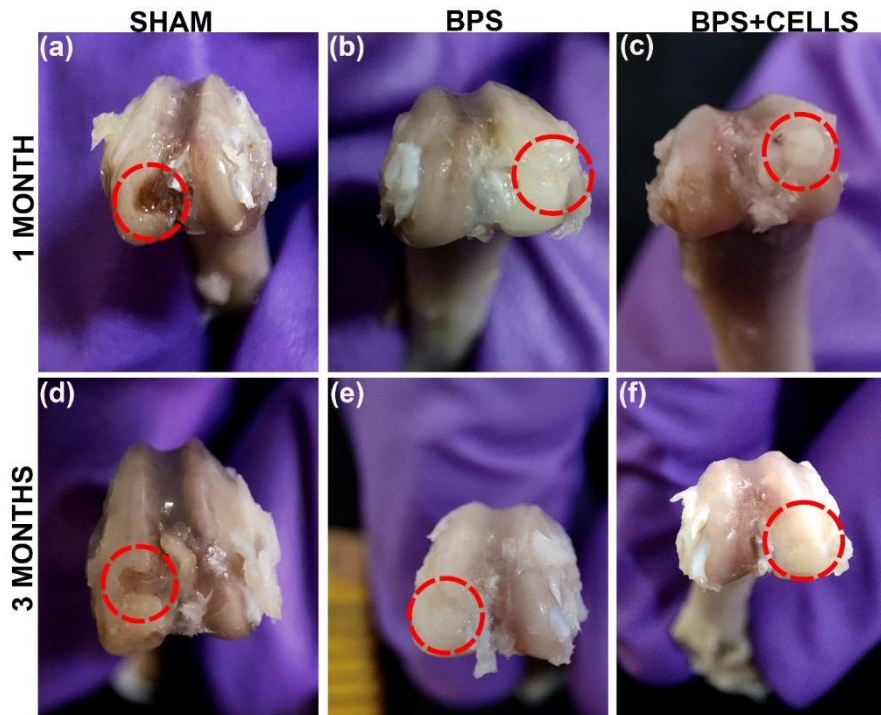


Figure 4.8.3: Representative gross images of knee joints from each experimental group. (a)-(c) and (d)- (e) represents photographs of the gross appearance of repair tissue at osteochondral defects in rat knees after 1 and 3 months of implantation. At 4 weeks postoperatively, tissue defects in BPS transplanted knees were repaired to almost the normal level, and border regions between repair and normal tissue were less distinct than those in BPS+Cells and control knees (Sham). At 12 weeks, the surface area of repair tissue in the BPS+Cells is more consistent and congruous with normal surrounding articular cartilage than in the BPS and control defects.

4.5.2.2 Histological examination of the retrieved construct and regenerated osteochondral tissue from rat knee joint

The tissues from implanted knee joints at one and three months were retrieved, and decalcified and extent of regeneration was assessed by various histological staining methods. Histological sections of the regenerative tissues at 4 and 12 weeks after surgery were examined by H and E staining, Safranin -O-staining, Trichrome staining, and Alcian blue staining for all different groups of implantations in osteochondral defects at both the time points (1month and 3 months.

4.5.2.2.1 H&E staining

The H&E-stained images of osteochondral sections at 1 and 3 months are represented in Figures 4.8.5 and 4.8.6. At 4 and 12 weeks postoperatively, H&E staining revealed cartilage defects in the blank scaffold group. In contrast, cartilage defect areas in the BPS and BPS + cells groups were mostly covered with new cartilage; the thickness of new tissue was similar to that of surrounding normal cartilage layer. In the SHAM group, the typical columnar arrangement of cells has been disrupted and is evident from the image that the lack of treatment has caused a scattered pattern. At 4 weeks, BPS and BPS+Cells showed a slight level of columnar arrangement of chondrocytes similar to native cartilage. By 12 weeks, a moderate to the normal level of a columnar arrangement was observed in the BPS+Cells group. Overall, the columnar alignment of cells can be graded as follows: BPS+cells> BPS>SHAM. The chondrocyte concentration and ECM deposition were enhanced, while negligible number of inflammatory cells by 12 weeks, compared with 4 weeks postoperatively.

4.5.2.2.2 Trichrome staining

Trichrome staining was done for all different groups of implantations in rat osteochondral defects at both time points. Figures 4.8.5 and 4.8.6 show histological examination of regenerated osteochondral tissue using Trichrome staining after 1 and 3 months of implantation. The interstitial collagen stained green, cartilage and mucin stained green-blue, cytoplasm and muscle fibers stained pink-red whereas dark brown to black shows cell nuclei. In Masson's trichrome, experimental knees with cells (n=6) were superior in the predominant tissue, structural characteristics, and freedom from degenerative changes in adjacent cartilage compared to control knees after 3 months of implantation. In the group BPS+cells, a smooth and intact surface with hyaline articular cartilage with good column alignment of chondrocytes was observed which is similar to the morphology of native cartilage. In the deep portion of the repair tissue, a vigorous repair process can be observed. However, though articular contours

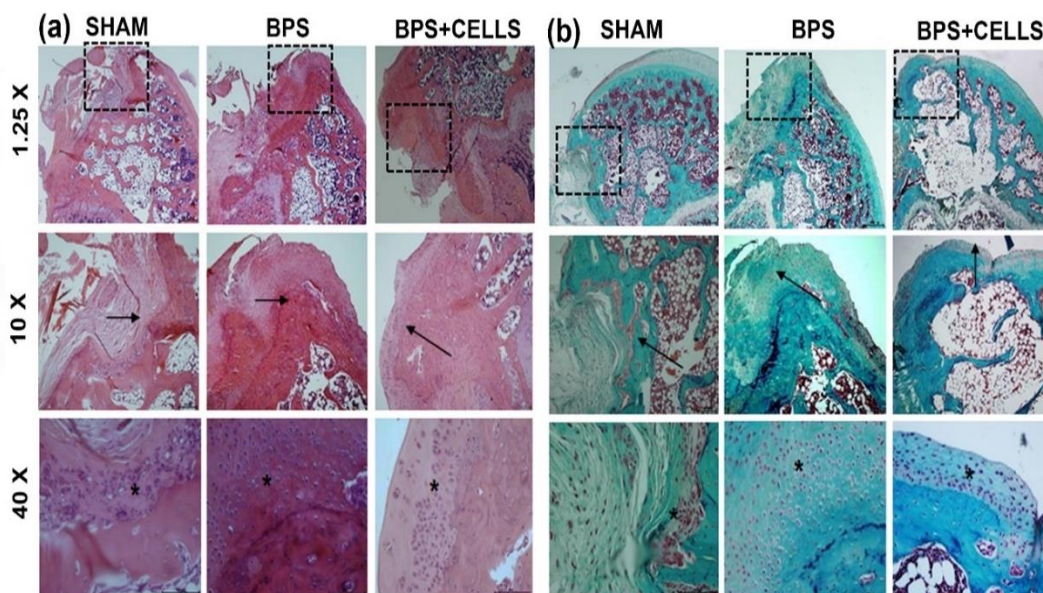
were restored, a nonsignificant gap and reduced positive staining were noted in the border area stretching to subchondral bone. In group 3 (sham) experimental knees, overall articular contours were not restored and the histological repair process appeared more irregular and immature than in groups 1 and 2. The sham knees showed meager staining and moderate hypocellularity and decreased cell number in the defect area. Inflammatory responses, such as cysts, were not observed in any images.

4.5.2.2.3 Safranin-O staining

The quality of regenerated cartilage tissue in the defects can be assessed by Safranin O staining. The thin and disintegrated fibrocartilage formed as repaired tissue in the defect area of the SHAM group showed complete absence or inappreciable Safranin O staining at both the time points. The defects implanted with biphasic scaffolds (BPS) and BPS+cells regenerated with thick neocartilage accompanied by mild Safranin O staining (figures 4.8.5) after 1-month of implantation. However, after 3 months of study, the defects implanted with BPS and BPS+cells the neocartilage were stained profoundly (darkest orange) with Safranin O, demonstrating the formation of high-quality hyaline cartilage in the defects suggesting enhanced glucosamine polysaccharide content in the cartilage ECM (figure 4.8.6). The regenerated tissue in both types of scaffold groups had a smooth surface and integrated well with adjacent OC tissue. The unique columnar arrangement of chondrocytes was observed in both the implanted groups at 3 months. However, the density of chondrocytes is higher suggesting active proliferation of cells in BPS groups. In the group BPS+Cells, a smooth and intact surface with hyaline articular cartilage with good column alignment of chondrocytes was observed which is similar to the morphology of native cartilage. In the deep portion of the repair tissue, a vigorous repair process can be observed. In both types of scaffold groups, the subchondral bone thickness and trabecular bone volume underneath the regenerated cartilage were higher compared to controls.

4.5.2.2.4 Alcian blue staining

Alcian Blue staining was done to assess the quality and deposition of aggrecans, the largest found proteoglycans in the ECM of cartilage, in the implanted groups: BPS and BPS+cells and is represented in the figures 4.8.5 and 4.8.6. Staining was done for all groups at both time points. Cell nuclei were stained brown (Weigert's hematoxylin) and surrounding proteoglycans, acid mucosubstances, and acetic mucins were stained blue. Compared to defect control (sham), BPS and BPS +cells showed increased production of proteoglycans and were comparable with normal tissue in terms of aggrecan deposition by 3 months (figure 4.8.6). But greatest proteoglycan deposition was found in the BPS +cells group and a moderate amount in the BLS group. Thus, the addition of aggrecan further improved the quality of regenerated tissue, with visibly lined chondrocytes surrounded by proteoglycans in the BPS+cells group. In this study, the successful repair of rat osteochondral defects by implantation of BPS+Cells scaffolds provides a promising way for human osteochondral defect treatment.



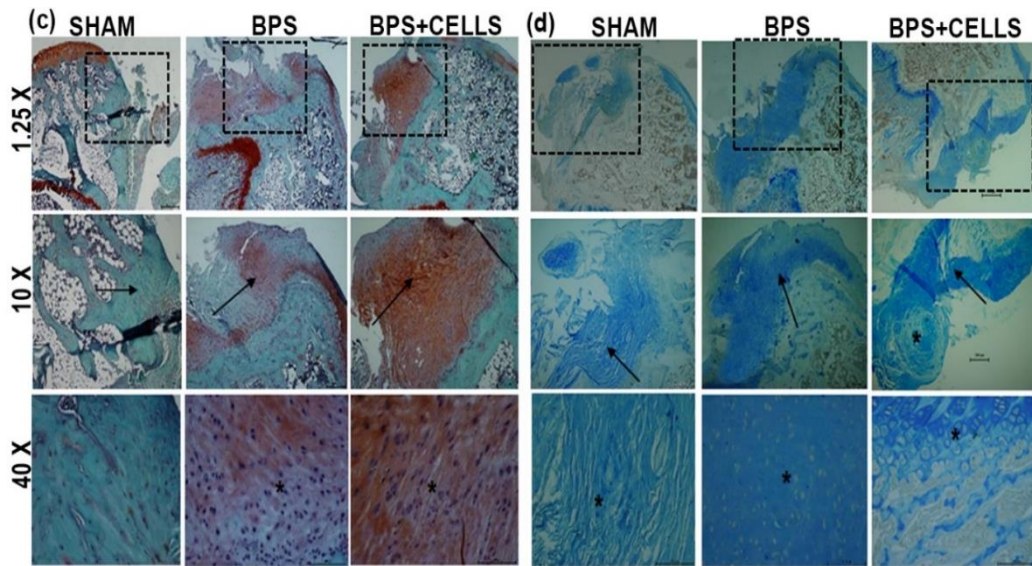


Figure 4.8.5: Histological examination of regenerated osteochondral tissue. (a) H & E, (b) trichrome, (c) Safranin-O, and (d) Alcian blue Staining in test (BPS and BPS+cells) groups and control groups after 1 month of implantation.

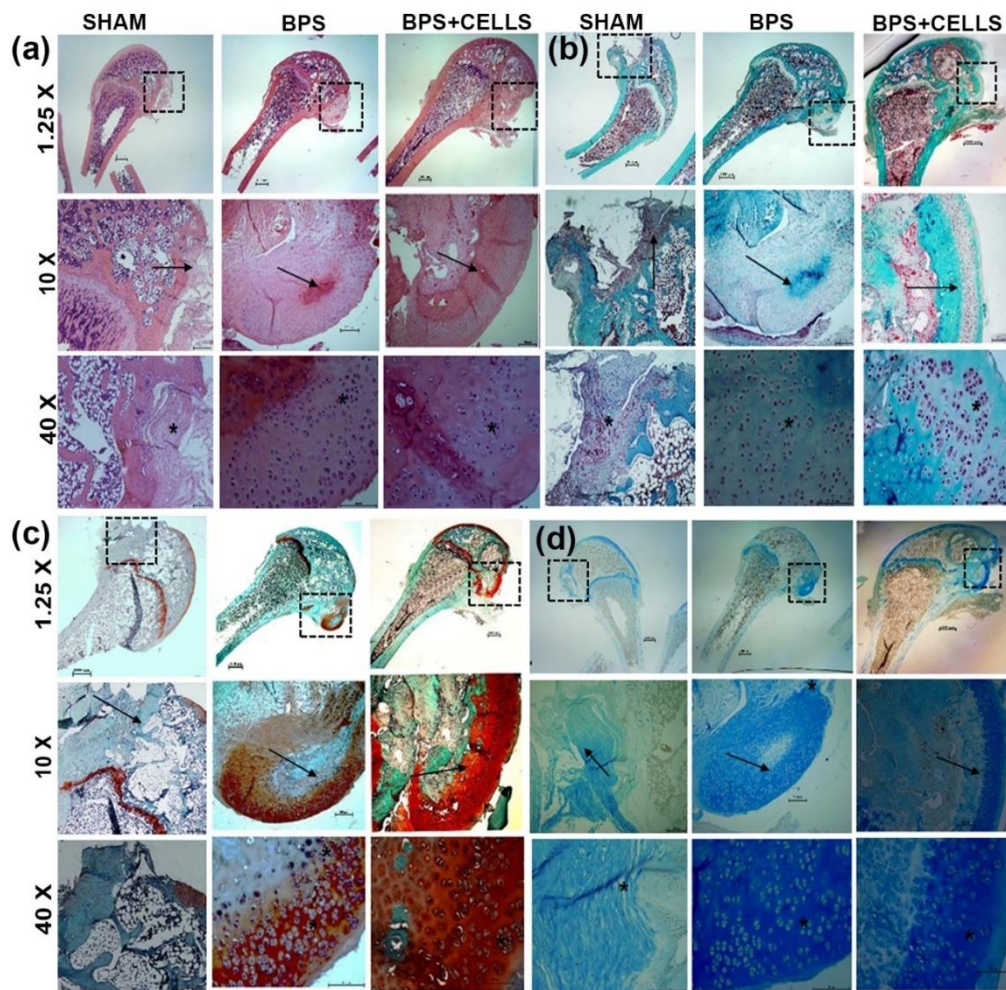


Figure 4.8.6: Histological examination of regenerated osteochondral tissue using (a) H & E, (b) trichrome, (c) Safranin-O, and (d) Alcian blue Staining in test (BPS and BPS+ cells) groups and control groups after 3 months of implantation.

CHAPTER 5

5 DISCUSSION

This chapter provides a detailed discussion of the results presented in Chapter 4 in terms of current knowledge in the field and published literature. In addition, the study hypothesis is taken into account, and the results are discussed in light of the defined objectives to evaluate the study outcome. The study's main goal was to design and develop cell-based biphasic osteochondral scaffolds that would mimic the hierarchical organization of native tissue and its regenerative potential in critical-size osteochondral defects. The feasibility of biphasic scaffolds for enhanced osteochondral regeneration was demonstrated in this promising study. The findings are thoroughly discussed in the sections.

5.1 Development of biphasic scaffolds (BPS) mimicking osteochondral architecture

5.1.1 System A- BPS fabricated via Combinatorial approach

Towards regenerating osteochondral defects by mirroring complex native tissue structures exhibiting anisotropic properties, using potential customized tissue-engineered implants, a dual-zonal scaffold material-cell combination was proposed. Among the three major components in Tissue Engineering and Regenerative medicine (TERM), the scaffold (3D polymeric matrix) plays a pivotal role by interacting with the cells and reinvigorating appropriate signals at the tissue, cellular, and molecular scales (Nooeaid et al., 2012). Ideally, the composition, design, mechanical behavior, and degradation pattern of the biological substitute (scaffold) persuade the other components of TERM; cells, and growth factors for recreating the microstructural features of desired tissue, thus repairing/replacing damaged tissue or organ (Li et al., 2018). Firstly, the components of the scaffolds with desired characteristics such as biocompatibility, biodegradability, and similar degradation rate to the rate of native tissue regeneration are selected. Also, emulating the morphological structure and chemical composition of the extracellular matrix (ECM), for superior cellular adherence, its

proliferation, differentiation and proper tissue growth (Galperin et al., 2013). Thus, the combination of biomaterials would be desirable to tailor a scaffold with the desired characteristics. Polycaprolactone (PCL), a synthetic polymer, with good mechanical properties showed poor cell adhesion and a slow biodegradation rate (Cakmak et al., 2020). Meanwhile, gelatin is a biocompatible, biodegradable, natural polymer derived from collagen by hydrolysis, and a major component of native ECM. Gelatin has excellent cell adhesion, proliferation, and differentiation properties, but it shows low mechanical strength and a high degradation rate, which is not suitable for tissue engineering applications (Binulal et al., 2014). For scaffold implantation in a load-bearing osteochondral defect, the scaffold should possess adequate mechanical strength to withstand the mechanical requirement (Li et al., 2015). To incorporate the beneficial properties of PCL and gelatin, the PCL/gelatin composite scaffold showed good mechanical properties as well as good cell adhesion and proliferation (Gautam et al., 2013). Hence in system A, gelatin was blended with PCL and the cartilage phase was fabricated by 3D printing. By blending the natural polymer with synthetic as shown in this work, the advantages of gelatin are preserved, while the mechanical performance is warranted by the PCL component, which entitles this hybrid scaffold to be competent for potential OCTE scaffold application. On the other hand, among the bioceramics used for bone tissue engineering, calcium sulfate (CS) possesses many of the characteristics of an ideal material for the desired purpose and is also an excellent agent as an osteoconductive, osteoinductive, and osteogenic material (Qi et al., 2017). Thus, the porous 3D bone phase based on PCL and calcium sulfate were fabricated using the freeze-drying technique followed by its characterization. The scaffolds properties were evaluated for potential use as the bone phase for osteochondral tissue engineering

Secondly, the design of the scaffold is considered. Among the different factors tried during the fabrication of the biphasic scaffolds, the criteria of selectivity were dependent on

certain key factors for obtaining relatively homogeneous three-dimensional scaffolds of different sizes with comparable biomechanical properties and the ease of handling. Hence the new generation scaffolds rely on advanced fabrication methodologies for accurately reproducing intricate ECM mimicking 3D structures based on CAD models. Thus, it enables production of customizable scaffolds with tuned porosities based on need (Vyas et al., 2020).

In this study, we tested the potential of a combinatorial approach in fabricating biphasic osteochondral scaffolds. The solution-based 3D printing of biocompatible polymers was adopted for fabricating the cartilage phase with preferred dimensions. The 3D-printed PCL/Gelatin layers were used for mimicking the zonal cellular arrangement of native hyaline cartilage whereas the lower freeze-dried PCL/CaSO₄ layer acted as an osteoinductive layer for directing the simultaneous differentiation ADMSCs into chondrocytes and osteoblast-like cells *in vitro*. Here, 3D printing of a blended solution of PCL and gelatin in optimized concentration was found to be an efficient technique to fabricate 3D scaffolds with the appropriate resolution with design reproducibility, albeit at the expense of printing speed (8 mm/s) and time. An essential parameter, the dimension of the pore size greatly affects the quality and quantity of new tissue. The pore size should be large enough to efficiently transport nutrients and remove waste, but it should be smaller for better mechanical performance (Chen and Kawazoe, 2018). Hence the balance between the two determines the cell migration, mass transport and further quality of new tissue formed. The infill density demonstrates the percentage of infill that defines the pores in a solid printed layer and the pore size is decreased upon increasing the infill rate. The novelty of the aforementioned scaffold is that the cartilage phase is printed with varying infill density to achieve a layered architecture from top to bottom with open and interconnected pores, which not only will help in the patterned arrangement of the ADMSCs during seeding but also will enhance the initial cell attachment, migration, and mass transport. This was achieved by printing at infill densities of 20, 30, and 40 % from top to bottom.

The surface morphology was analyzed via SEM imaging and the images revealed pores of dimensions 25 (bottom layers) to 400 μm (top layers). The pore size, an indispensable parameter for scaffold, affects the characteristics and quantity of new tissue formed. The smaller pore sizes ($<100 \mu\text{m}$) affect cell migration and mass transport and can cause the formation of endochondral cartilage (Karageorgiou and Kaplan, 2005). Much larger pore sizes can result in superfluous void space and compromise the mechanical properties of the scaffold (Yu et al., 2008). Pore size is determined by the infill density and as shown in Figure 4.2.1, the pore size decreased with the filling ratio, and Figure 4.2.2 shows SEM images and pore size distribution of the 3D printed cartilage layer. The varying infill density from top to bottom provides a gradient structure and facilitates a reduced percentage of cell loss. Also, tapering pore dimensions favor the alignment of cells more like a native cartilage organization. The much-diminished pores in the bottom layer impart a hypoxic environment, thus promoting a calcified layer above the bone layer. Meanwhile, the precise design aids in the molecular cross-talks between the two layers having disparate properties. Another prime factor that can influence cellular performance is the surface characteristics of the developed scaffolds. The SEM images also revealed the surface roughness of the scaffold upon blending and distinct differences when compared to its respective control, bearing a smooth surface.

FTIR spectra of PCL/gelatin scaffolds revealed characteristic peaks of the amide groups indicating the presence of gelatin molecules in the blend. Generally, the hydrophilic/hydrophobic characteristic of scaffold is important in tissue culture and can influence the initial cell adhesion and migration via adhesion molecules to a higher extent (Ehtesabi and Massah, 2021). Thus, the presence of gelatin in PCL scaffolds can improve the hydrophobicity of PCL, apparent from the contact angle measurement where there is a shift of contact angle from 128 degrees in PCL to 62 degrees in 79:21 PCL/gelatin scaffold. This could

be attributed to the amine and carboxylic functional groups in gelatin structure whereas such functional groups are not present in PCL structure.

During physiological loading, the force is dissipated through the articular cartilages and subchondral bone and allows frictionless movements without causing failure. Hence, the mechanical properties of biphasic scaffolds must match the surrounding tissue and is essential for articular cartilage and subchondral bone regeneration. The instantaneous compressive Young's modulus of articular cartilage is 1.36–39.2 MPa and the ultimate compressive strength is 7–23 MPa (Elder and Athanasiou, 2009; Pan et al., 2015). The solid components of the ECM support shear stress, whereas the incompressible interstitial water is responsible for withstanding compressive loading. The compressive modulus of subchondral bone is 1.4–9800 MPa (Yang et al., 2001). The compressive strength of human cancellous bone is 0.8–11 MPa and cortical bone is 12–140 MPa. Whereas mid-range values of compressive modulus of cancellous bone are 90–400MP which varies considerably across different locations and patients (Martens et al., 1983). We tested the mechanical properties of the three kinds of scaffolds (control, cartilage and bone phases showed better than those without biofactors (control), The mechanical studies demonstrated that porous cartilage and bone phases showed appreciable results comparable to the native tissues, possibly because of the specific pore design incorporated into 3D printed scaffolds. The sufficient biomechanical capacity exhibited by the scaffolds is required to support respective tissue regeneration. Therefore, once implanted into the joint, these scaffolds can provide a powerful mechanical structure that bears loads encountered in the OCD region.

Synchronization of tissue regeneration and rate of biodegradation of the scaffold is very important for proper tissue integration and for attaining optimum healing. Gelatin is well known to improve the biodegradability of PCL-based scaffolds within the tissue regeneration time frame (Binulal et al., 2014). In consent with this, the degradation rate was significantly

higher for scaffolds with gelatin content as compared to PCL alone scaffolds. This could be because the addition of gelatin can increase the hydrophilicity, loosen the pore structures, and enhance the ability of the scaffold to absorb more degradation fluid. Previous studies have shown that blending bioactive proteins into synthetic PCL can reduce the gap in biodegradation and biocompatibility properties of PCL. The major factor determining the success of the regeneration of tissues is the long-term survival of anchorage-dependent cells in the scaffolds during the regeneration time frame. So, Gelatin alone scaffolds can disintegrate faster and affects the structural integrity of the scaffolds, which is necessary for the cells to proliferate, differentiate and produce ECM to their surroundings. The faster degradation of gelatin by matrix metalloproteinases (Lu et al., 2011) disrupts the architecture of the scaffold and can be harmful to cell survival. However, PCL degrades by hydrolysis, and blending with Gelatin can have a balanced degradation rate, thus maintaining the structural integrity of the scaffolds (Gautam et al., 2014).

Concerning the bone layer, scaffolds intended for bone regeneration should be osteoconductive, degradable, and bioactive, and also should have a complex three-dimensional (3D) interconnected porous network and strong mechanical loading properties. Hence, calcium sulfate, a highly biocompatible and biodegradable material, and much more economic synthetic bone-like grafts are blended with PCL and freeze-dried to get 3D scaffolds. SEM images of the bone phase suggest that the freeze-dried scaffolds have optimal pore size distribution to increase bone formation by way of cell migration, vascularization, and nutrient diffusion. The FTIR spectra confirmed the presence of osteoconductive material (CaSO_4) in the PCL-based freeze-dried bone zone. The incorporation of CaSO_4 does not significantly improve the hydrophilicity, which is evident from the results of contact angle measurement of PCL/ CaSO_4 scaffolds. However, it provided an interfacial bond between the implanted materials and their surrounding tissues. Many studies have shown that CaSO_4 also aids in cell adhesion, its

proliferation, and the differentiation of mesenchymal stem cells (Fernandes et al., 2021; Huang et al., 2021). With regards to biodegradation which is critical when synthesizing a new material: the degradation rate must help hasten and ease the process of tissue regeneration. The PCL/CaSO₄ scaffolds showed negligible degradation initially upon immersion in PBS for 4 weeks, the degradation rate increased gradually after day 28 and the scaffold showed more than 20% degradation by 90 days, indicating its suitability for bone tissue engineering. The appearance of micropores on the walls of the pores will facilitate further degradation through the uptake of water and would enhance tissue regeneration *in vivo*. Consequently, the biomineralization ability of the bone phase containing osteoconductive material- calcium sulfate was studied by immersion in SBF and confirmed the formation of Ca-P nucleation and further apatite crystal formation on the surface of the scaffold. Analysis of surface morphologies confirmed the apparent presence of the hydroxyapatite layer when compared to the control.

5.1.2 System B - BPS fabricated via 3D printing and dissolution adhesion technology

The adhesive force between the cartilage and bone phases adhered using fibrin glue as in system A of the previous section or sewing silk thread is very weak and the layers can separate easily. Hence, we conceived the dissolution-adhesion technology to intricately link the two phases effectively. The solution-based 3D printing materials with biomaterials are thus developed in this section. The printing ink contains the dispersion of cartilage ECM mimicking chondroitin sulfate (CS) and osteogenesis favoring β TCP along with the biocompatible polymers. Scaffolds are designed to have oriented pores in a tapering fashion to recreate the microarchitecture of hyaline cartilage. While the bone part is designed to have pores to mimic its counterparts for enhancing osteogenesis.

The incorporation of key elements into the tissue-engineered construct can be obtained through additive manufacturing technologies like 3D printing, in which a wide range of design

iterations are possible. Though numerous studies on 3D printing for creating TEC, none reached the clinical level primarily due to the lesser availability of biomaterials used for 3D printing and their toxic additives produced during processing (Wasti and Adhikari, 2020; Wu et al., 2017). The present work is thus dedicated to the development of a new scalable and reproducible 3D printed biomaterial-based biphasic system with defined micro-architectures, using a mix of PCL/PLGA for osteochondrogenesis. The novelty of the aforementioned scaffold is that cartilage phases are printed with a layered architecture having different infill densities to have open and interconnected pores. To mimic the hierarchical pattern of directional cartilage, the layer just above the bone part is made with more infill density (the pore size is reduced) without adding an additional layer to depict the calcified layer. This diminished pore size is expected to create an environment, so that the cells may turn to deposit hypercalcified cartilage. The developed scaffolds more closely mimic natural joint structure when compared to conventional scaffolds. The physiological calcified joint layer is thinner, and the extracellular chondrocyte matrix in this layer is calcified as in bone tissues (Tatari, 2007).

Here, we fabricated a porous 3D scaffold using the 3D plotting technique (solution printing) from PCL/PLGA in which PCL was employed as the elementary component of scaffolds (S. Wang et al., 2020; Yao et al., 2015) because of its favorable characteristics in 3D printing, appreciable mechanical strength, and biocompatibility. However, the pristine PCL being hydrophobic and slowly degradable (Tokiwa et al., 2009), we choose PLGA as the versatile component of the scaffold to tune the properties of PCL without compromising its advantages (Peng et al., 2018; Won et al., 2016). The morphology and distribution of the cells, bioactive components, and collagen fibers in the articular cartilage and subchondral bone exhibits greater variance (Zhang et al., 2009). Hence, chondroitin sulfate is incorporated in the upper cartilage phase and β TCP in the lower bone zone for recapitulating the respective niche.

SEM images showed oriented pores with regular array patterns. Also, the presence of biofactors in the scaffolds can incorporate micro-roughness on the scaffold surface and plays an important role in cell attachment, proliferation, and phenotype expression (Chang and Wang, 2011). In high magnification, SEM images of struts showed a smooth surface for PCL/PLGA whereas a rough surface for the factors incorporated ones. Besides the chemical nature of scaffolds, the precise designability of structure with internal pores that mimics the native tissues is important for scaffolds, so that scaffolds could guide and promote cellular migration, its adherence, proliferation, and a better regeneration (Chen et al., 2018). The pore sizes (i.e, the percentage of filling space) showed a decreasing size pattern concerning the increasing filling ratio. This is a greater interest in terms of cell seeding its further expansion and survival along with greater nutrient transport and waste removal. Besides these factors, the small dimension pores produced due to greater filling space will favor the molecular crosstalk between upper and lower layers through permitting diffusion of molecules and hence better functionality can be achieved. Moreover, this tapering pore pattern could aid in the cell alignment perpendicularly in the cartilage layer of the biphasic scaffold, which in turn can mimic the cellular arrangement in native hyaline cartilage. Moreover, MSCs being comparatively larger cells ($\sim 30\mu\text{m}$ to $60\mu\text{m}$ in size) (Ge et al., 2014), these aligned tapering pores with $\sim 20\mu\text{m}$ pore size at the bottom could also help in preventing the migration of MSCs between the osteogenic and chondrogenic layers. However, these pores will allow nutrition transport throughout the interface.

We conceived the dissolution-adhesion technology to intricately link the 2 layers effectively. SEM images of the interface ensure the effectiveness of the connections and found that the 2 layers have adhered tightly without any gaps. One of the major challenges to clinical relevance is the scalability of scaffolds to macroscale in terms of their thickness. The scaffolds developed in this study have the feasibility to create thicker ones without compromising the microstructural features and hence can overcome the current difficulties facing today.

The degradation studies show an initial slower degradation among the scaffolds and could be attributed to the material composition, PCL and PLGA. Notably, the rate of degradation ratio of the BPS scaffolds was higher than that of scaffolds without bioactive factors. After a few days, the incorporated bio factors i.e., CS and β TCP may undergo dissolution and lead to the appearance of micropores which facilitates easy entry of water molecules that accelerates the degradation process. But the slowly degrading PCL (Seyednejad et al., 2012) can maintain the scaffold strength *in vivo*, which could meet the need for gradual reconstruction of new tissue within the regeneration time frame. Since the rate of degradation of hybrid BPS scaffolds matches the time required for new tissue formation *in vivo* (Yh et al., 2007), we presume that this scaffold can enhance tissue regeneration *in vivo*.

The bioactivity studies showed a net weight gain on the β TCP incorporated scaffolds when compared to the control group, indicating deposition of minerals on the scaffold. The initial weight loss may be due to the dissolution of ions from the scaffold. Preferably, these simulate the native environment and could enhance the process of osteogenesis. The marginal weight gain exhibited by PCL/PLGA scaffolds suggests poor bioactivity. The incorporation of osteoconductive materials such as β TCP can exercise greater influence on osteoconductive, osteoinductive properties, and bioresorbability (Eliaz and Metoki, 2017). β TCP is known for its fast degradation rate when compared to other bioceramics including hydroxyapatite (HA). The presence of β TCP provides mechanical strength, improved hydrophilicity, chemical stability, release of Ca and phosphate ion products *in vitro* and *in vivo*, and a strong interfacial (bone–calcium phosphate) bond between the implanted materials and their surrounding calcified tissues (S et al., 2013).

5.1.3 System C - BPS fabricated via 3D printing

The hierarchical microarchitectural pattern of the heterogeneous tissues, the articular cartilage, and subchondral bone constituting the osteochondral region necessitates the requirement of a

stratified scaffold to recreate the different lineage-specific biological properties and support its effective regeneration. Thus, attention was paid more to designing and developing a gradient composite scaffold (varying pore diameters) mimicking the zonal organization in normal cartilage and specific ECM pattern in bone. Among the wide array of fabrication techniques employed, 3D printing is a promising technique to fabricate the complex scalable three-dimensional (3D) osteochondral substitute via a layer-by-layer deposition process with precise, controllable, and reproducible morphological properties concerning pore structure to enhance the functionality of the differentiated cells (Daly et al., 2017).

A variety of polymers and their composites have been successfully 3D printed to produce a 3D-porous architecture for use in regenerative medicine and tissue repair (Do et al., 2015; Wu and Hsu, 2015). Herein we described the development of chondroitin sulfate and β TCP incorporated inks for cartilage and bone phase respectively and evaluated their suitability for 3D printing of osteochondral-like tissues. The biomimetic biphasic scaffold (BPS) was designed to have closely integrated layers, mimicking the hierarchical construction and composition of native osteochondral tissues as described in previous sections. The porous 3D scaffolds were fabricated using the 3D printing technique (solution printing) from PCL/PVP/CS and PCL/PVP/ β TCP in which an FDA-approved aliphatic semi-crystalline polyester, poly(ϵ -caprolactone) (PCL) was employed as the basic component of scaffolds. PCL, owing to its favorable characteristics in 3D printing, desirable properties of tunability, chemical diversity, excellent mechanical properties, low anti-immune response, and phenotype maintenance, is widely used for repairing cartilage defects as well as ossified and spongy bone tissue regeneration (Ngo et al., 2018). However, PCL is often composited with other polymers to overcome its hydrophobicity which impedes its use in medical applications that require rapid absorption rates. Blending techniques involving hydrophilic polymers can improve the diffusion of water to the proximities of PCL chains and accelerate their hydrolytic cleavage to

enhance microarchitecture with controlled porosity (Jia et al., 2011). In this section, polyvinylpyrrolidone (PVP) was chosen as the polymer to blend with PCL because of its ideal properties such as biocompatibility, remarkable solubility in polar as well as most organic solvents, and potential to interact with both hydrophobic and hydrophilic materials (Kim et al., 2013). The anisotropic properties and respective niches are recapitulated by incorporating chondroitin sulfate in the upper cartilage layer and β TCP in the lower bone zone. However, the solution-based 3D printing of biocompatible polymers with preferred dimensions is incredibly challenging as there is a Z-axis collapse of each printed layer upon drying. Achieving the desired height is always tricky and the parameters which had a direct influence to produce good quality scaffolds depend on the polymer molecular weight, solution concentration, type of solvent, layer height dimension, feed rate, flow rate, and nozzle size. Here, interpolymer complexation is done to improve the printing and prevent the z-axis collapse of printed layers.

This work documents the possibility of blending PCL with PVP and biofactors, followed by complexation with PAA in fabricating the gradient scaffolds with interconnected pores and gradient pore geometry or channels along the longitudinal direction, which was the main objective of this section. Also, achieving control over scaffold degradation, enhanced cell viability, attachment, and spreading and ameliorating the cellular response and functionality of the scaffolds were the other objectives investigated.

The 3D printing parameters were optimized to enable the production of reproducible scaffolds with regularly spaced aligned polymer filaments in the x, y and z directions with high yield. The physicochemical, morphological, and mechanical properties of these biphasic scaffolds were characterized, and the degradation pattern and bioactivity studies were also done. ADMSCs were cultured on the respective phases of BPS to undergo induced osteochondrogenic differentiation. The osteo-chondrogenic potential was assessed at the cellular and molecular levels. This precise control of scaffold design allowed a direct

comparison of the cellular and ECM production responses to the scaffold structure. The expression of osteogenic and chondrogenic gene-markers was studied to evaluate the differentiation of ADMSCs on the 3D scaffolds using a real-time quantitative polymerase chain reaction (RT-PCR) assay.

The articular cartilage is an avascular tissue with low oxygen tension in chondrocytes (ranging from 2 to 7% O₂) (Portron et al., 2013). Besides, related studies indicated that low oxygen tension could enhance the chondrogenic differentiation of mesenchymal stem cells (MSCs) (Markway et al., 2010). Subchondral bone, on the other hand, is a highly vascularized tissue with high oxygen content (Buckwalter and Mankin, 1998b). We fabricated a BPS consisting of PCL/PVP/CS/PAA which acted as the cartilage phase of the hierarchical scaffold and PCL/PVP/BTCP/PAA as the bone phase with a well-ordered macroporous structure using room-temperature 3DP technology. To mimic the native OC tissue, a gradient scaffold was designed where the bottom layers of the cartilage phase with small pores form a pivotal physical barrier between the cartilage and subchondral bone regions. Calcified cartilage marks the physiological barrier between cartilage and subchondral bone, which allows only the molecules lower than 500 Da that moves unidirectionally from subchondral bone to cartilage (Arkill and Winlove, 2008). The specific design allows a low oxygen tension and avascular microenvironment in the upper cartilage phase to induce chondrogenic differentiation of endogenous MSCs at the defect site. Many studies based on 3D printed scaffolds for articular cartilage regeneration adopted simple patterns and did not intend to mimic the zonal architecture of articular cartilage (Longley et al., 2018; O'Shea and Miao, 2008).

It is well known that the pore geometry of the scaffold is crucial for cell survival, ingrowth and proliferation (Loh and Choong, 2013). The 3DP technology used in this study allowed the fabrication of complicated designs with high precision and accuracy with closely integrated distinct layers and well-controlled pore sizes within the wide range of 15–320 μm

for the cartilage phase and 15 to 500 μm for the bone phase. Previous studies in tissue engineering revealed that the sectioned scaffold with a pore size of 100 to 400 μm was found appropriate for the chondrogenic differentiation of adipose stem cells (Liang et al., 2018; Oh et al., 2010). Whereas the scaffolds representing subchondral bone, the pore size of 300–800 μm are considered beneficial for bone ingrowth (Murphy and O'Brien, 2010) and 300–500 μm for enhancing vascularization and bone formation. But smaller pore sizes less than 100 μm adversely affect cell migration and mass transport and may encourage endochondral cartilage formation before osteogenesis happens (Karageorgiou and Kaplan, 2005). But larger pores compromise the mechanical properties of the scaffold. It was also reported that the chondrogenic markers and ECM deposition increase gradually as the pore size decreases in the gradient scaffold (Luca et al., 2016). The scaffolds of strut width 0.5 (cartilage phase) and 0.3 mm (bone phase) were fabricated by specific infill density with cubical and star infill patterns respectively. SEM micrographs demonstrated that the interconnected pore channels were not occluded and no surface damage was apparent which would aid in promoting cell seeding, its attachment, and proliferation in a tapered fashion similar to native hyaline cartilage.

Also, the diminished pore diameter at the bottom layers of the cartilage phase would prevent the leakage of differentiated cells to the lower phase. The lower bone phase exhibited a different design pattern to favor the cell attachment and proliferation much similar to the osteocytes embedded in the bone matrix. The printing solution was deposited layer-by-layer in a star pattern and SEM images of bone phase revealed an interconnected microtubule-like structure with channels resembling net like bags. Further, the topological features of the scaffold analyzed using SEM revealed surface micro-roughness due to incorporated biofactors in both the phases which could influence the cell behaviors properties of the scaffolds, in terms of attachment, spreading, proliferation, and phenotype expression significantly. The optimized 3D printing conditions and interpolymer complexation are needed to achieve rapid construction

of filaments uniformly and to prevent the construct from collapsing. Moreover, the feasibility to produce thicker scaffolds in the preferred dimension with microstructural details as designed will overcome the limitations of poor scalability and further clinical applications.

The scaffolds intended for tissue engineering purpose need to degrade with time as neo tissue regenerate and replace the 3D matrices mimicking the native tissue; this enriches the quality and quantity of regenerated tissue (Tamaddon et al., 2018). PCL was blended with the water-soluble poly(N-vinyl-2-pyrrolidone) to develop scaffolds with tunable surface topography and controllable degradation rates. The incorporated PVP phase can easily be extracted by immersing them in a cell culture medium or PBS if not complexed. Thus, to control the degradation rates within the desired time frame and to enhance the printability without Z-axis collapse, an interpolymer complexation was done using PAA which binds to a PVP via repetitive hydrogen bonds across the polymer backbone. This was confirmed by FTIR analysis, where the quaternary ammonium salt ($-NH^+$) formed upon acidification of the nitrogen in the pyrrolidone group of PVP interacts with the negatively charged carboxyl group of the PAA causing appreciable shifting of the characteristic peaks of PVP and PAA as described in the results section. However, without interpolymer complexation, the degradation rates were much higher and beyond the regeneration time frame.

The interpolymer complexation reduces the percentage of weight loss while in the scaffolds without complexation, the degradation rate is higher by 28 days. The extraction of the PVP phase from the main polymer PCL backbone exhibiting nano/microporosity on the surface leads to striking results, where these pores facilitated not only biodegradation rates, but also improved cell attachment and spreading on the blend and complexed scaffolds. The degree of crystallinity controls the hydrolysis rate, which determines scaffold degradability. Further, the leaching of incorporated biomolecules from the scaffolds with time enhanced the degradation rate (with or without PAA) by favoring the entry of more water molecules into the backbone

of the polymer chain and accelerating the degradation process. The rugged surface morphology observed on the printed scaffolds after 28 days of immersion in PBS in SEM images can be attributed to the nano/microporosity developed on the surface due to extraction of PVP and leaching out of biofactors. However, integrity of both cartilage and bone phases is maintained in the original dimension till the end, although they were immensely eroded due to dissolution and extraction of the hydrophilic PVP part from the 3D printed strands as early as 28 days of PBS immersion with the appearance of micropores. Thus, the successful tuning of biodegradation rate was accomplished. The rapid degradation of PVP in composite scaffolds and leaching out of incorporated biofactors enables new tissue formation, while the remaining PCL is expected to provide additional mechanical support. The lower biodegradation of PCL alone scaffolds will hinder regeneration of desired tissue and thus, blending with PVP and interpolymer complexation favored the scaffold for the envisioned purpose.

The scaffold should be robust enough to sustain the mechanical requirements of implantation in a load-bearing osteochondral defect. Within joints, articular cartilage facilitates a smooth motion by absorbing impacts and subchondral bone enhances the load-bearing capacity by alleviating the majority of load on the joints. Physiologically, cartilage attenuates 1–3% and subchondral bone reduces 30% of the loads through joints (Madry et al., 2010). Serious damages to these tissues alter the mechanical and biochemical balance within the OC unit. Hence, OC scaffold is exposed to complicated dynamic biomechanical environment within the joints that includes changes in stresses, strains and fluid pressure. Hence, the mechanical properties of biphasic scaffolds must match the surrounding tissue (to withstand physiological loading without causing fatigue or failure. The compressive Young's modulus of articular cartilage is 1.36–39.2 MPa and the compressive modulus of subchondral bone is 1.4–9800 MPa (Yang et al., 2001). Both cartilage and bone phases showed better mechanical properties than those without biofactors (control), attributed to the zonal organization of the

cartilage phase and oriented directional structure of the bone phase. Also, the addition of an appropriate proportion of PCL/PVP could provide sufficient biomechanical strength to both the phases of BPS. However, the incorporation of CS into the cartilage phase resulted in increased compressive modulus.

The ability of the biomaterials to form an apatite layer on its surface in the presence of physiological fluid is very important as it contributes to the proliferation and differentiation of cells and further osteoblastic activity (Eliaz and Metoki, 2017). Further, the *in vivo* bone bioactivity can also be predicted from the results. The results of *in-vitro* bioactivity assessment showed that PCL/PVP/PAA scaffolds have very less apatite mineralization where only marginal weight gain was observed suggesting its poor bioactivity. However, there is an initial weight loss followed by a net weight gain on the β TCP incorporated scaffolds when compared to the control group, suggesting the simultaneous process of dissolution of ions from the scaffold and precipitation of minerals on the scaffold. Thus, the apatite layers on the β TCP incorporated PCL/PVP/PAA scaffolds were markedly increased. The mechanism of apatite mineralization is through the release of Ca and phosphate ions from β TCP that induces the formation of Ca–P nucleation and further apatite crystal formation on the surface of the scaffold. Preferably, these simulate the native environment and could enhance the process of osteogenesis (Turnbull et al., 2018).

The surface morphologies of PCL/PVP/ β TCP/PAA scaffolds were characterized to evaluate apatite formation after 28 days of immersion in SBF and noticeable differences in the bone phase could be observed on the surface compared to the relatively smooth surface before SBF immersion. Besides, EDS analysis of PCL/PVP/ β TCP/PAA scaffolds indicated apparent characteristic peaks of Ca and P elements on EDS spectra after SBF immersion. The obtained Ca/P ratios is 1.602, which is close to 1.67 of hydroxyapatite (Singh et al., 2007)-. Thus, the incorporation of osteoconductive materials such as β TCP, can exercise greater influence on

osteoconductive, osteoinductive properties, and bioresorbability and provides mechanical strength, improved hydrophilicity, chemical stability, and strong interfacial (bone–calcium phosphate) bond between the implanted materials and their surrounding calcified tissues.

The interpolymer complexation prevented the initial burst release of CS due to the strong hydrogen bonding interaction between PAA and PVP where CS gets entrapped in between the insoluble complexes. The greater release of the CS in the initial hours from the PCL/PVP/CS/PAA could be due to the release of noncovalently bound hydrophilic CS present on the scaffold surface. Furthermore, polymer chains were swollen in an aqueous medium that aided in the sustained release of CS from the scaffolds. However, leaching out of CS in the initial hours was rapid and greater from PCL/PVP/CS because CS was not chemically trapped within the PCL/PVP printed structures. Besides, the micropores created during leaching out of CS as time advances favor the degradation. These are beneficial for enhanced chondrogenesis compared to the scaffolds without CS by favoring the attached cells to further proliferate through micropores and the modulatory effects of entrapped or released CS on the MSCs to promote the cells to differentiate towards chondrogenic lineage and enhancing the synthesis of hyaline matrix components.

The design and composition of the scaffold influence cell viability, attachment, and proliferation (Tamaddon et al., 2018). The initial step in assessing the scaffold's ability for cellular acceptance or behavior is through the cytocompatibility studies of both the phases of BPS. The results of *in vitro* assessments by MTT assay confirmed that they exhibited good cytocompatibility with rat ADMSCs, which could be ascribed to the composition and specific design of these constructs.

5.2 Isolation and characterization of Mesenchymal stem cells (MSCs)

5.2.1 Mesenchymal stem cells (MSCs) from rat and rabbit adipose tissues

Researchers in the field of tissue engineering technologies have access to plethora of stem cells with varying potencies and choosing the right stem cell is vital for obtaining promising results in regenerative medicine. The stroma of adipose tissue contains MSCs and its use in numerous exogenous cell-based tissue engineering are extensively acknowledged owing to its potential to differentiate into different cell types and known therapeutic applications. The MSCs with spindle-shaped morphology are successfully isolated from rat and rabbit adipose tissue using an enzymatic protocol. Conferring to the Mesenchymal and Tissue Stem Cell Committee of the International Society for Cellular Therapy, isolated MSCs need to satisfy three minimal criteria: (1) the cells display anchorage-dependence / plastic adherence, (2) multilineage differentiation potential, and (3) express mesenchymal cell surface markers but lack hematopoietic and endothelial surface markers (Dominici et al., 2006). The cytoskeleton of the cell plays major roles in maintaining its shape, cell division, migration, adhesion, and responds to various external mechanical stimuli and further signaling cascades (Stossel, 1993).

Out of three components (actin filaments, intermediate filaments, and microtubules) of cytoskeleton, F-actin forms the backbone, which clusters to form actin filaments (Yourek et al., 2007). Vimentin intermediate filaments are involved in many cellular processes including modulating MSC characteristics and behavior, its contribution to the deformability of MSCs, cell spreading response, ability of MSCs to interact with various microenvironments, and resisting fluid shear stress related cell area changes (Sharma, 2017). Thus, FITC-Phalloidin staining of actin filaments and vimentin antigen staining of plastic-adhering, widely replicating clonogenic somatic cells showed characteristic spindle-shaped morphology, confirming the key criteria of anchorage dependence MSCs. Besides, to diminish the ambiguity in the identification of MSCs, the stem cell properties were further confirmed by analyzing the

specific surface antigen set through flow cytometry. The expression profile of approved positive markers for MSCs (more than 80% of the cells) and lack of expression of CD34 and CD45 (less than 2%) were in consistent with the previous studies reported (Odabas et al., 2014). In addition, the immunophenotype feature of adipose tissue MSCs described here through immunofluorescence staining (positive staining for MSC surface antigens CD105, CD90, and CD73 and negative for hematopoietic marker CD 45 and CD 34) is in concert with those previous reports (Jung et al., 2012). The trilineage mesoderm namely chondrogenic, adipogenic, and osteogenic differentiation *invitro* confirmed the multilineage potential of the isolated MSCs upon induction with respective differentiation mediums. Thus, the results of microscopic examination, immunophenotyping, and trilineage differentiation assays indicate that the isolated cells in the present study are MSCs and met the ISCT criteria.

5.3 *In Vitro* 2Dculture of MSCs and evaluation of production of ECM

The ECM of articular cartilage predominantly consists of type II collagen and aggrecan, where collagen microfibrils, fibrils and fibers are intertwined with proteoglycan aggregate (F. H. Chen et al., 2006). Aggrecan, a glycosylated protein monomer containing negatively charged glycosaminoglycans (GAGs) (hyaluronic acid, chondroitin sulfate, keratan sulfate and dermatan Sulfate) chains covalently bonded to a protein core and interacts with hyaluronan chains *via* link proteins to form larger proteoglycan aggregates. The sulphated GAGs in the aggrecan can attract cations in water and offer the articular cartilage with osmotic properties (Gautieri et al., 2011). The 3D pellet culture of MSC in chondrogenic differentiation medium resulted in the formation of cartilage with its specific extracellular matrix assessed by quantification of sGAG and alcian blue staining for proteoglycan. The cartilage-specific markers (aggrecan, and collagen 2) showed positive signals around the cells in immunostained sections of the pellet confirming the *in vitro* chondrogenesis. RT PCR analysis further confirmed the expression of marker genes for chondrogenesis; ACAN, COL2a1, HAS 2, and

SOX9 where SOX 9 and HAS 2 are early expression markers that regulate the expression of downstream late marker genes of cartilage-specific extracellular matrix (Hardingham et al., 2006). Thus, results confirmed the production of ECM by the differentiated cells.

Also, the osteogenic differentiation potential of ADMSCs on 2D culture and production of ECM was assessed by Alizarin red staining and Calcium estimation, further confirmed by analyzing the expression of osteogenic specific genes, Bone sialoprotein (BSP), Osterix, and Osteocalcin (BGLAP) on day 28. Osteogenesis is a multi-step regulated process of differentiation of mesenchymal cells into osteoblast and osteocytes. An osteoblast-specific transcription factor, osterix activates a series of genes during differentiation of preosteoblasts into mature bone cells (Sinha and Zhou, 2013). The presence of enzyme alkaline phosphatase (ALP) indicates the commitment of stem cells to the osteoblastic phenotype while the osteocalcin (OC) protein produced by osteoblasts is a sign of osteoblastic transformation (Ma et al., 2019). The ability for osteogenesis and production of ECM was thus confirmed. It is remarkable that, the isolated MSCs were a homogeneous population that makes effectual proliferation and differentiation for further studies.

5.4 Invitro differentiation potential of MSCs on the biphasic scaffold (BPS)

5.4.1 System A- BPS fabricated via Combinatorial approach

The results of cell viability studies using ADMSCs confirmed that cells were alive after 28 days of culture suggesting the cell-friendly behavior of our developed scaffolds. Enhanced cell adhesion and growth of ADMSCs on these test scaffolds suggested that the operating conditions of 3D printing and processing the scaffolds are highly cytocompatible. Interestingly, gelatin on the blend scaffolds promoted enhanced cell adhesion when compared to bare PCL alone scaffolds. Cell adhesion necessitates the presence of a suitable proteinaceous substrate to which cell adhesion receptors, such as integrins, can bind and form cell-anchoring points. The bioactive molecules can be whole protein molecules such as ECM proteins or short peptide

sequences (cell-binding domains) isolated from ECM proteins and bound to integrin receptors on cell membranes. Here, gelatin is a collagen-derived protein that acts as a bioactive molecule. The ability of these proteins to promote many integrin binding sites for cell adhesion and differentiation is well studied (Hwang et al., 2016). Following initial adhesion, cells secrete ECM into their environment, such as collagen, fibronectin, and vitronectin, which influence cell behavior. These proteins will adsorb to the surface of the material and provide a temporary matrix for cell adhesion (Huang et al., 2017). Here, gelatin in PCL/Gelatin blend thus supports and stimulates ADMSC adhesion, growth, and proliferation of cells during *in vitro* studies. Thus, composite scaffolds could better mimic natural ECM and provide good cell affinity when compared to PCL alone scaffolds. This implies that the gelatin incorporated scaffold has the potential to recruit undifferentiated cells from the local environment to attach and enhance their growth when implanted into defects. The PCL /CaSO₄ scaffolds also showed good cell adhesion and proliferation ability due to the ability to release calcium ions and possibly surface-mediated Ca ion exchange has an effect on cell behavior. Local changes in extracellular Ca ions may regulate cell activity and have an impact on cell proliferation and differentiation. Extracellular Ca ions have been reported to be a major promoting factor in transmitting messages that affect cell behavior, having a significant effect on the regulation of osteoblast proliferation and differentiation (Jeong et al., 2019).

The architecture and surface topography of the scaffolds supports appropriate cell attachment and proliferation (Chang and Wang, 2011). The PCL/gelatin-derived oriented scaffolds with aligned pores and struts promoted ADMSC adhesion, migration, and proliferation where the cells exhibited spindle-shaped morphology with well-organized actin filaments. The consistent array patterns encourage MSC infiltration through the microchannels created by varying infill density and proliferate within the core of the cartilage phase due to surplus cell-to-cell contacts. However, in the control scaffolds comprising 3D printed PCL

alone, the cells exhibited limited adhesion and penetration into the core of the scaffold, which is attributed to the hydrophobicity of PCL that is not supporting cell adhesion and retention. ADMSCs displayed less spindle morphology due to a lack of adhesion sites and cell-to-cell contact in the control scaffolds. Concerning the bone phase, both freeze-dried PCL/CaSO₄ and PCL alone scaffolds showed good viability of cells, yet in a different distributing pattern in the later ones where only a limited amount of ADMSCs was attached to the PCL alone scaffolds.

The effect of oriented structures and pores on stem cell proliferation and differentiation has been extensively studied for efficient tissue engineering (Chen et al., 2015). A scaffold intended for OCTE should be functionally active in addition to its cell-friendly properties, for which they need to be fabricated with designed composition and aligned structure to mimic the structure of ECM. In such circumstances, the fabricated scaffold can force the stem cells to produce and secrete the necessary components of ECM of the desired tissue (Chan and Leong, 2008). The *in vitro* chondrogenesis ability of 3D printed PCL/ Gelatin scaffolds were studied and showed enhanced chondrogenic differentiation, which was evident from abundant sGAG levels and total collagen content on 3D printed scaffolds. The synthesis of sGAG, an important component of cartilage ECM marks the initiation of a chondrocyte phenotype of the seeded cells and allows the functional evaluation of the cellular performance. Thus, the higher levels of sGAG content of PCL/Gelatin scaffolds can be attributed to the induction of rapid cell proliferation and a highly favorable environment for chondrogenesis, compared to the other two groups. Notably, the sGAG content of PCL alone scaffolds was greater than 2D monolayer cultures, implying the dependence of ADMSCs functional response to scaffold architecture developed by 3D printing, which favored efficient nutrient diffusion.

The significantly higher levels of collagen content in PCL/gelatin composite scaffolds compared to bare PCL scaffolds and 2D cell control point toward the higher compatibility and differentiation ability of PCL/Gelatin scaffolds for chondrogenesis. The behaviour of cultured

cells is greatly influenced by the surface topography of the scaffolds which include the shape, morphology as well as the orientation of stem cells through the guidance and arrangement of cytoskeletal filaments inside the cytosol. The change in surface topographies leads to the specific alignment of intracellular filaments which influence the signaling pathways and activate lineage-specific genes, thereby enhancing the expression of lineage-specific markers (Miyoshi and Adachi, 2014). These specific markers can be detected by immunofluorescent staining and robust positive signals from PCL/gelatin scaffolds confirmed the extracellular deposition of COL 2 and aggrecan at the protein level as evident from immunostaining.

The tendency of MSC-derived chondrocytes to undergo phenotypic transformations to hypertrophic chondrocytes could deteriorate the quality of hyaline cartilage in terms of biomechanical functionality (Somoza et al., 2014). No studies have shown that the hierarchical architectural pattern of 3D printed scaffolds can provide a favorable niche for the cells. Further, the presence of analogs of cartilage ECM like gelatin could help to recreate biological aspects of native cartilage within the scaffolds and also could overcome the pitfalls in PCL-based tissue engineering discussed in the introduction part. In the present study, we addressed both of these requirements of cartilage tissue engineering. The hierarchical architectural pattern of the native hyaline cartilage was mimicked by gradually increasing infill densities from top to bottom of the 3D printed scaffolds to create tapering pores, with a diameter of around 300 μ m size at the top whereas at the bottom the diameter of pores narrowed down to around 20 μ m. By doing this, can be able to spatially organize the seeded ADMSCs into a hyaline cartilage-like manner.

The gene expressions of SOX9, HAS1, collagen II, aggrecan, and collagen X were estimated to compare the chondrogenic capacity of the 3D printed PCL/gelatin-based cartilage phase. The differentiation of MSCs into chondrocytes is associated with the expression of cartilage-specific genes. These genes include the transcription factor SOX 9, a key regulator of chondrogenic differentiation, and chondrocyte phenotype and control the expression of the

cartilage extracellular matrix genes, such as COL 2, ACAN, and cartilage link protein, which all encode important cartilage ECM proteins (Hattori et al., 2010, p. 9). Collagen II is mainly produced by chondrocytes, aggrecan is largely distributed in the ECM, and SOX9 is the earliest marker for MSC differentiation into chondrocytes. Collagen X is commonly associated with chondrocyte hypertrophy. Hyaluronan (HA), a nonsulfated highly hydrated glycosaminoglycan, is considered a potential niche matrix for stem cells during embryogenesis, morphogenesis, migration, proliferation, and differentiation. The chondrocyte pericellular matrix in the cartilage is directly assembled and retained at the cell surface through HA and its receptors (Wilusz et al., 2014). The SOX 9 expression in PCL/Gelatin and PCL groups peaked at day 7 before other chondrocyte markers (HAS1, COL 2) and then decreased on days 14 and 28, suggesting SOX 9 as a key regulator of chondrogenic differentiation.

However, expression of HAS 1 peaked on Day 14 when compared to day 7 and then decreased on day 28, suggesting it acts as a potential niche matrix for stem cells due its function as a regulator of cellular behavior during differentiation. Accordingly, expressions of late markers COL2 and ACAN of all groups were significantly upregulated on day 28 suggesting SOX 9 and HAS1 control the expression of the downstream genes for cartilage extracellular matrix proteins, such as COL 2, ACAN. According to the results represented in the figure 4.4.12, greater upregulated expression of chondrogenic-specific genes of collagen II, aggrecan, HAS 1, and SOX9 were observed in PCL/gelatin scaffolds when compared to PCL alone and 2D culture, confirming the enhanced chondrogenesis potential of the blend group. However, the expression of a hypertrophic marker, COL10 was less expressed in the blend suggesting less tendency of differentiation towards hypertrophy.

Further, the incorporation of CaSO₄ can enhance the differentiation of MSCs to osteoblasts, suggesting that these components can be used as promising instructive scaffolds for OCTE (Fernandes et al., 2021). In consent with this notion, we found that incorporation of

CaSO₄ into the freeze-dried scaffolds enhanced the biochemical markers for bone regeneration. During the proliferation and differentiation of osteoprogenitors into osteoblasts and finally, a new bone formation is associated with a significant increase in expression of the Alkaline phosphatase enzyme. It was observed that the PCL/CaSO₄ composite freeze-dried scaffolds had an osteoinductive effect on the rat ADMSCs and showed enhanced ALP activity compared to control scaffolds by day 14. The availability of calcium for enhanced differentiation and greater osteogenesis as early as 14 days, is attributed to the osteogenesis ability of calcium sulfate. Also, greater calcium content by day 28 suggested osteoblast differentiation which is generally accompanied by ALP and OC secretion. CaSO₄ is an inducer of osteogenesis and promotes mineral deposition of the matrix (Huang et al., 2021). At the protein level, the extracellular deposition of ALP, osteocalcin, and osteonectin was visualized by immunofluorescent imaging across the scaffolds confirming the osteogenesis ability of PCL/CaSO₄ scaffolds.

During condensation of the skeletal analgen, MSC-derived osteochondroprogenitors express both transcription factors, Sox9 and Runx2. RUNX2 is an essential transcription factor, which determines the fate of mesenchymal stem cells towards the osteoblast lineage and influences osteoblast differentiation (Akiyama et al., 2005). But Sox9 has an inhibitory effect on osteoblast maturation by directly interacting with Runx2 and repressing its activity. Hence, osteo-chondroprogenitor cells differentiate toward osteogenic phenotypes when Sox9 expression is lower than Runx2 (Loebel et al., 2015). Calcium sulfate incorporated PCL scaffolds potentially provide a niche for MSCs based on their natural pre-osteogenic properties. The marker genes for osteogenesis was evaluated on day 7, 14, and 28 and the greater expression of Runx2 and the downregulation of SOX 9 expression on Day 14, when compared to day 7 on PCL/CaSO₄, suggests the onset of cartilage–bone transition and transactivation of osteoblast-specific enhancers through RUNX2 and further bone formation. RUNX2 is the

major regulator of downstream osteoblastic marker gene expression, including COL 1, and BGLAP (OCN) (Thiagarajan et al., 2017). The ALP expression was higher on day 14 followed by its downregulation in later periods indicating it is an early osteogenic marker that controls the downstream late marker genes. The late osteogenic markers (BGLAP and COL1 A2) also showed greater expression on Day 28 suggesting the PCL/CaSO₄ favors differentiation of MSCs into osteoblast-like cells and ECM production. The most abundant non-collagenous protein expressed in bone is osteocalcin, which is found specifically in cells of the osteoblast lineage, including mature osteoblasts (Florencio-Silva et al., 2015).

Thus, the mechanism of endochondral ossification is replicated where the formation of hypertrophic cartilage is a prerequisite step in bone development and the coordination of Runx2 and Sox9 is highly important for the process of cartilage and bone development. The complete absence of Sox9 from hypertrophic chondrocytes suggests that Sox9 downregulation is required to allow the onset of subsequent events for bone formation (Zhou et al., 2006). However, SOX 9 is more expressed in 2D culture on Day 28 suggesting that SOX9 decreases Runx2 binding to its target sequences and inhibits Runx2 either by preventing transactivation of osteoblast-specific enhancers and further bone formation.

We demonstrated the feasibility of developing biphasic scaffold using methods and biomaterials with a history of safe use in osteochondral scaffold fabrication. The BPS consists of ECM-mimicking, PCL/gelatin composite 3D printed scaffold with gradient pores as cartilage phase and CaSO₄ incorporated freeze-dried PCL as the bone phase. Their favorable chemical, mechanical, and biological properties were endowed to structurally and biochemically reproduce the respective 3D ECM microenvironment, which successfully enhanced cellular proliferation and differentiation throughout the scaffold and improved the efficacy of cell scaffolds for tissue regeneration. Thus, provides a novel solution to the current

challenges of osteochondral scaffolds. However, *in vivo* studies are necessary to establish its efficacy for the repair of large osteochondral defects.

5.4.2 System B - BPS fabricated via 3D printing and dissolution adhesion technology

The viability of ADMSCs after 28 days of culture confirmed that this blended polymer can support stem cell adhesion and proliferation. The confluent layer of attached cells with spread-out cell morphology depicts the excellent response of cells towards our 3D printed scaffolds with good surface area. This provides high ligand density for initial cell attachment and proliferation. Also, highly porous scaffolds enable better mass transport and are hence used for culturing cells. Homogenous cell distribution in a patterned way deep into the thicker construct and maintaining its viability during the culture period is the biggest challenge faced by the different groups of researchers. Densely distributed cells inside the porous scaffolds structure are necessary to regenerate artificial tissues. The biphasic scaffolds presented good cell viability throughout the culture period. At the end of the culture period, cells were seen to be uniformly distributed throughout the scaffolds and along the cross-sectional length of the scaffold.

Cell functionality in both the layers was assessed by measuring sGAG and collagen secretion of cells in cartilage mimicking scaffolds and ALP and Calcium estimation in the bone layer over time. The gradual increase in sGAG and collagen secretion throughout the culture period indicates that the cells were able to maintain their phenotypic stability and functionality while cultured in the fabricated 3D scaffold. Chondrogenic differentiation of ADMSCs was higher on the scaffolds with incorporated CS than those with bare scaffolds. Hence, it is clear that CS plays a vital role in the chondrogenic differentiation of ADMSCs. In addition, it was previously reported that chondroitin sulfate (CS) based scaffolds possess MSC immunosuppressive potential also (Corradetti et al., 2016).

As suggested earlier, β TCP is an inducer of osteogenesis and promotes mineral deposition of the matrix (Prabha et al., 2020). β TCP closely mimics bone tissues and many studies demonstrated that 3D printing scaffolds containing β TCP provide a microenvironment supporting cell adhesion, its proliferation, and differentiation of mesenchymal stem cells (Shim et al., 2013). In consent with the aforementioned studies, our PCL/PLGA/ β TCP layer showed enhanced ALP activity and mineralization when compared to its control. The seeded cells differentiated and mineralized the matrix as the culture time advanced. The increase in ALP amount production at day 14 indicates that ADMSCs growing on the developed scaffolds differentiate to the osteogenic lineage upon induction. Hence, β TCP incorporated PCL/PLGA scaffolds had an osteoinductive effect by showing enhanced osteogenesis of ADMSCs as early as 7 days, compared to control scaffolds.

The results of immunostaining confirm the instructive property of 3D printed scaffolds (PCL/PLGA/CS and PCL/PLGA/ β TCP) to direct ADMSCS to undergo chondrogenesis and osteogenesis respectively upon culturing in respective differentiation medium. However, a weaker expression of the above-mentioned markers in the control (PCL/PLGA) group substantiates the effect of incorporated factors in the two layers. Real-time PCR-based gene expression analysis further confirmed the results. A significantly increased expression of the specific genes associated with chondrogenesis (collagen II, SOX-9, HAS2, and Aggrecan) and osteogenesis (IBSP, BGLAP, and Osterix) was observed in respective scaffolds. Thus, we succeeded in fabricating biphasic composite scaffolds from two FDA-approved biomaterials and our results suggest that the incorporation of bioactive factors into scaffolds along with the implementation of advanced techniques like 3D printing could provide desired results in OCTE. Further *in vivo* studies are required.

5.4.3 System C - BPS fabricated via 3D printing

The success of a scaffold for the intended use depends on how effectively it provides a nurturing microenvironment for the seeded cells. Through highly organized design structures, the scaffolds can provide cell adhesive regions, mechanical stability, and structural guidance which influences the cell attachment, proliferation, and differentiation of MSCs into the desired lineage (Tamaddon et al., 2018). The results of *in vitro* assessments by Live/Dead staining confirmed that they exhibited good cytocompatibility with rat ADMSCs, which could be ascribed to the composition of these constructs.

According to confocal microscopy, a uniform cell distribution pattern of spindle-shaped ADMSCs with few dead cells was observed in all the test groups revealing high cell viability and confirming the absence of residual solvents which can cause potential cytotoxicity. Also, when compared to the control, the test scaffolds; cartilage phase, and bone phase with biomimetics showed good adhesion where the morphology of cells was maintained. Moreover, a typical morphological change from a fibroblast-like to a rounded chondrocyte-like shape or clusters occurred after MSCs upon chondrogenesis induction on the surface of the cartilage phase after 28 days, suggesting the MSCs differentiation to chondrocyte phenotypes. Hence along with the composition, the design pattern with specific pore dimensions is yet another crucial parameter favoring the initial attachment and viability of cells. The presence or absence of biofactors does not significantly affect the viability of cells which can be related to the fact that the scaffolds present more hydrophilicity, higher porosity, and specific surface area, that provide more attachment or adhesion sites for stem cells.

Also, this blended polymer can support stem cell proliferation, differentiation to desired lineages, and ECM production. The cell distribution deep into the thicker construct and maintaining its viability during the culture period is the biggest challenge faced by the different groups of researchers. The cell morphology studies by phalloidin staining of F-actin revealed

a confluent layer of well-attached cells with spread-out cell morphology depicting the excellent response of cells towards our 3D printed scaffolds with good surface area. The hierarchical structure of 3D-printed scaffolds is precisely controlled which offers anchoring sites to cell extensions, thus permitting them to spread and invade the biomaterial. Besides, leakage of cells from the large pore of the scaffolds is prevented through gradient scaffolds with varying pores. Thus, both phases fulfilling the design requirements could provide good microenvironments for cell growth.

The biphasic scaffolds presented good cell proliferation throughout the culture period. Though there was little difference in initial cell proliferation among the groups on day 1, a significant transformation took place over one week. From day 5 onwards, scaffolds with biofactors had a considerable amount of cell proliferation in comparison to scaffolds without biofactors. While the presence of biofactors significantly enhanced cell proliferation after 7 and 14 days, the type of biofactors did not cause a significant difference. These results support that biofactors incorporated composite scaffolds with specific design patterns that improved ADMSC proliferation. It can be reasoned that cells infiltrated the scaffold throughout the structures between 1 and 3 days, thereby allowing further cell proliferation after 5 to 14 days. This result can be related to the fact that scaffolds present more hydrophilicity, favorable design patterns with varying infill density including micropore sizes, and the presence of biofactors led to the greater amount of cell infiltration into the center of the scaffold.

Thus, the *in vitro* biological studies using ADMSCs confirms the suitability of the biphasic hybrid scaffold for cell adhesion, survival, and proliferation with no detrimental effects on the viability of cells.

Articular cartilage possesses a higher anisotropy and an internal zonal structure. (Di Luca et al., 2015). The scaffolds intended for OCTE should mimic the structure of osteochondral tissue and need to be functionally active besides being a cell-friendly assemble.

Considering the abundance of CS as GAGs in cartilage ECM, it was added into the cartilage phase to obtain the scaffolds with a biomimetic environment. On account of the unique biological characteristics of stem cells, many reports have confirmed the great application prospect of stem cells in tissue engineering (Mahmoudifar and Doran, 2013). The enhanced sGAG content as culture time advanced, suggested the chondrogenic differentiation of ADMSCs. The incorporation of CS to the scaffolds resulted in increased accumulation of cartilage matrix molecules which is reflected in the results showing expectedly higher sGAG on the scaffolds with CS. Whereas chondrogenesis was less observed on the scaffolds without CS incorporation. This was likely a function of the longer period of CS leach out from the scaffold. The CS released or entrapped within the printed structures provides a favorable niche, within which cells showed preferential accumulation and have utilized the entrapped or released CS which resulted in higher hyaline cartilage-specific matrix synthesis. Hence, CS display a vital role in the chondrogenic differentiation of ADMSCs. The greater collagen content by day 28 confirms the chondrogenesis potential of PCL/PVP/CS/PAA group and production of cartilage ECM. The effect of incorporating CS is thus justified.

At the protein level, the extracellular deposition of COL 2 and aggrecan was visualized by immunofluorescent imaging across the scaffolds. Collagen Type II is the major component of extracellular matrix (ECM) in articular cartilage and together with aggrecan and other proteoglycans provide compressive properties to the tissue. The unique structure and composition of ECM regulate cellular functions such as adhesion, morphology, proliferation, and differentiation (Sophia Fox et al., 2009). The increased expression of COL 2 and aggrecan protein over time by MSCs-seeded scaffolds confirmed the function of CS in promoting the biosynthesis of cartilage-specific matrix molecules. The effect of composition and design of the scaffold has a greater influence on activating specific genes for directing stem cell differentiation to desired lineages. The shape, morphology and orientation of cultured stem

cells is influenced by the surface topography of the scaffolds which provide sufficient guidance and favours arrangement of cytoskeletal filaments. Also, the difference in cell responses to the various surface topographies can be related to the influence of specific arrangement and orientation of intracellular filaments on the signaling pathways of lineage-specific genes and enhance corresponding markers (Zamanlui et al., 2018).

Chondrogenic-specific gene expressions were also examined during *in vitro* chondrogenic induction of MSC-seeded scaffolds. SOX 9 regulates the chondrocyte phenotype and controls the expression of the downstream genes which encode cartilage-specific ECM proteins (Wang et al., 2016). The SOX-9 gene is expressed in resting and proliferating chondrocytes and co-expressed with Collagen Type 2 in the early phase. The combined expression of these genes is highly related to the production of cartilage ECM (Hardingham et al., 2006). From the results, it was observed that the expression of SOX 9 and HAS 1 peaked at day 14 (early phase) and then decreased on day 28, (late phase of chondrogenesis) when compared to other chondrocyte markers (COL 2, ACAN). The chondroitin sulfate (CS) based scaffolds showed enhanced SOX 9 and HAS1 expression which upregulated the downstream genes for ECM production, ie. COL 2 and ACAN. Accordingly, expressions of late markers COL2 and ACAN of all groups were significantly upregulated on day 28 compared to that on day 14 where blend with CS showed markedly higher expression over time. This is consistent with the mechanism that SOX9 and HAS 1 regulated the expression of COL 2, ACAN at an early stage. These observations could be correlated firstly with the CS leach-out profile. Comparatively, CS has been reported and verified widely to be a potent chondrogenic inducer of ADMSCs (Varghese et al., 2008). Thus, CS-based scaffold potentially provides a niche for MSCs to proliferate and differentiate based on its natural pre-chondrogenic properties and aids in assembling chondrocyte pericellular matrix. Thus, the 3D-printed biomimetic CS-based cartilage phase forms a viable substrate for the promotion of chondrogenesis. Secondly, the

effect of porous structure on the biological property and functionality of differentiated cells is observed. The cell network formation and tissue ingrowth depend on pore geometry. It was observed that cells choose a radius of curvature much larger than that of cells themselves (Zadpoor, 2015). The seeded cells exhibited curvature-driven migration, proliferation, and differentiation in cartilage phase printed with a cubical pattern. It was seen that high curvature leads to mechanical forces in cells and formation of actin stress fibers leading further tissue growth. (Rumpler et al., 2008)

Similarly, the bone phase of the OCTE scaffolds should be ideally instructive for MSCs differentiation towards osteogenic lineage (Kim et al., 2006). Previous studies reported the ability of β TCP incorporated 3D printed scaffolds in providing a microenvironment that supports cell adhesion, proliferation, and differentiation of MSCs related to their bone matrix resemblance (Ma et al., 2018). The quantitative estimation of ALP protein revealed a non-significant difference in ALP activity between with and without β TCP incorporated scaffolds on day 7 suggesting the influence of design pattern and net-like bags that favored the initial attachment, proliferation, and differentiation of ADMSCs to osteoblast-like cells irrespective of incorporating β TCP. The enhanced ALP activity in the PCL/PVP/PAA/ β TCP compared to control scaffolds by day 14 suggested the availability of the biological cues for enhanced differentiation and greater osteogenesis by 14 days, suggesting the osteogenesis ability of β TCP. Also, greater calcium content by day 28 suggested β TCP as an inducer of osteogenesis and promotes mineral deposition of the matrix.

β TCP is the most favorable form of bioceramic owing to its mechanical strength, chemical stability, good biocompatibility, osteoconductivity, and potential osteoinductivity. The release of Ca and phosphate ion products during the partial dissolution of β TCP renders bioactivity through the formation of apatite precipitate on the surface of the scaffold. The potential ability of released ions into the surrounding environment promotes the differentiation

of mesenchymal stem cells (MSCs) (Shim et al., 2017). In addition, hierarchical porous structures composed of ordered macropores (on the top layers) and micropores (bottom layers) obtained through gradient infill density with star infill pattern significantly promote their osteogenic activity and bioactivity through excellent apatite-mineralization ability. Also, micro-networks resembling a net bag formed while printing with specific star pattern led to higher cell density which promotes the intercellular contacts and paracrine signaling and further aids in differentiation of cells. Moreover, β TCP degradation produces nanoporosities to which the cells could adhere and proliferate better.

At the protein level, the extracellular deposition of ALP, osteonectin, and osteocalcin were visualized by immunofluorescent imaging across the scaffolds. The robust expression of these extracellular proteins in PCL/PVP/ β TCP/PAA confirmed the osteogenic differentiation of the ADMSCs in 3D scaffolds with the specific pattern. The weak signal of ALP, in some areas, suggested the decline in expression of ALP as culture time advances suggesting less expression of an early marker of osteogenesis. Also, the expression of osteocalcin showed uneven distribution and could be a result of partially differentiated MSCs.

The expressions for bone markers were also examined during *in vitro* osteogenic induction of MSC-seeded scaffolds. The downregulation of SOX marks the onset of cartilage–bone transition including cartilage resorption and formation of bone marrow. Runx2 is mainly associated with osteoblast differentiation and are found in pre-osteoblasts which gets up-regulated in immature osteoblasts, but ultimately down-regulated during osteoblast maturation (Carbonare et al., 2011). The coordination of Runx2 and SOX 9 is important for the process of cartilage and bone development and progenitor cells differentiate toward osteogenic phenotypes when SOX 9 expression is lower than Runx2. The complete absence of SOX 9 from hypertrophic chondrocytes suggests the onset of bone formation (Akiyama et al., 2005).

Thus, β TCP based scaffolds potentially provide a niche for MSCs on their natural pre-osteogenic properties. The marker genes for osteogenesis were evaluated and there is downregulation of SOX 9 expression on Day 28 when compared to day 14 on 3D scaffolds, hence progenitor cells differentiate toward osteogenic phenotypes. However, SOX 9 is more expressed in 2D culture on Day 28 (previous studies) suggesting that SOX 9 decreases Runx2 binding to its target sequences and prevents transactivation of osteoblast-specific enhancers and further bone formation. Alkaline phosphatase (ALP) in bone tissue is encoded by the tissue non-specific ALP (TNAP) gene and is regarded as a by-product of osteoblast activity. It is expressed early in the initial phases of bone development and is up-regulated during the active formation of new bone. Conversely, the expression of ALP decreases as bone tissue matures. Therefore, ALP is considered to be an early marker of osteogenic mineralization. The ALP expression was higher on day 14 and reduced on Day 28, indicating it as an early osteogenic marker. The COL 1 gene is associated with the synthesis and secretion of collagen type I, which is an essential organic component of the bone ECM. Meanwhile, the osteocalcin gene encodes an essential bone protein produced by osteoblasts known as BGLAP, which is associated with bone matrix mineralization. Thus, the late osteogenic markers (BGLAP and COL1 A2) also showed greater expression on Day 28. To conclude, the osteogenic differentiation appears to be more impacted by the presence of β TCP. The results suggested the availability of β TCP in later phase has a positive effect on the osteogenic differentiation of MSCs and plays a crucial role in bone formation and the production of the ECM. However, the result may differ when the hybrid scaffold is applied *in vivo* where mechanical load also plays a role in the regulation of cell differentiation.

In summary, biphasic scaffolds consisting of PCL/PVP/CS/PAA as cartilage phase and PCL/PVP/ β TCP/PAA as bone phase were fabricated by combining different components using the 3D printing method. The layers printed with cubic/star pattern in upper and lower phases

created channel structures by combining the pores of all layers, thus mimicking the hierarchical pattern of native tissue. The complexed tri-component scaffold with well organized and regularly patterned structure showed more promising characteristics during *in vitro* studies with ADMSCs, which can be ascribed to the synergistic effect of the bio factors as well as the specific design in the porous scaffolds. The new 3D printed BPS thus presents a promising prospect for future OCTE applications.

5.5 Tissue engineering an osteochondral construct and its *in vivo* evaluation.

Though there are numerous bioengineered materials and fabrication techniques explored in the tissue engineering field, especially in osteochondral tissue regeneration, the number of discoveries from the laboratory that reaches the clinical level is a handful due to the translational barrier (Tamaddon et al., 2020). For a technology that needs to be marketized in terms of tissue-engineered products, firstly the developed scaffold's effectiveness in *in vitro* system needs to be proved where the information about the safety, efficacy, and potential of developed substitutes for the repair of desired tissues are obtained. This is followed by *in vivo* animal studies which involve acquiring data regarding their safeness, regenerative capabilities and the immunological reactions, which in turn increases the probability to get approval from regulatory bodies for translation and final marketization (Hoemann et al., 2011).

The principles of the three R's; Reduction, Replacement and Refinement (W. M. S. Russell and R. L. Burch, 1960) were carefully considered while designing animal studies to reduce the number of animals to the minimum to achieve a valid result. The selection of suitable animal models that can mimic the disease condition or bear the critical size defects necessitates a thorough literature review. Even though many small and large animal models have been discussed in published literature, the rat can serve as an ideal *in vivo* model as it satisfies all the conditions for developing osteochondral defects to further evaluate the scaffold bio functionality. Though many *in vivo* studies were carried out widely in rabbit models (Filardo

et al., 2018; Liu et al., 2019; Paul et al., 2017), as per our literature review, we identified major lacunae involving higher metabolic activity and density of pluripotent stem cells near the defect site owing to greater rates of innate repair in rabbit articular cartilage models. Furthermore, the overall cell volume density in cartilage from the human medial femoral condyle is approximately 1.7 percent (1800 per mm³), compared to 12.2 per cent (7500 per mm³) in adult rabbit cartilage (Hunziker, 1999) which attributes to the poor levels of selfrepair in human cartilage. The load characteristics and cartilage thickness were different in the rabbit stifle joints compared to humans, making it difficult to investigate translation potential in this model (Moran et al., 2016). Also, the rabbit has different biomechanics where the gait pattern during hopping which is a wide landing of the hindlimb leads to increased force in the joint and subsequent bone mineral density. The bone mineral density for a rabbit at a depth of 3 mm was 0.65 g/cm³ compared to 0.36 g/cm³ in humans and the bone volume fraction was 58 ± 10 % in the rabbit MFC compared to 33 ± 13 % in humans (Chevrier et al., 2015). Hence due to the differing biomechanics and innate self-repair ability, there is difficult in comparing the results from rabbit studies to humans and thus rat species are selected as suitable animal models for our study.

The specific alignment, number, and size of cells support the integrity of ECM in each zone of hyaline cartilage, while the specific matrix protects the cells from harmful stimuli and stresses. (Sophia Fox et al., 2009). During the progression of OA, the integrity of homeostatic ECM is altered where there are significant changes in the composition and structure of ECM. Meanwhile, the proliferative chondrocytes undergo morphological variations which further changes the quantity and quality of the ECM. The columnar arrangement of chondrocytes is disrupted leading to fibrillation of the cartilage surface and the formation of microcracks (Akkiraju and Nohe, 2015). This structural deterioration disturbs the joint function is disturbed along with the destabilization of collagen network, and expression profile of matrix molecules.

The objective of the present study was to evaluate the ability of the developed biphasic scaffold (BPS) to repair osteochondral tissues in a rat osteochondral defect with or without MSCs. We hypothesized that BPS with a hierarchical pattern would lead to enhanced osteochondral repair. Among the three biphasic scaffolds fabricated with different design patterns, the best one is selected to evaluate its ability to regenerate osteochondral tissues. Hence, a comparative study was done among the three different BPS systems developed for mechanical, proliferation ability, and bio functionality studies. The compressive modulus obtained for systems B and C were comparable to the values typically reported for articular cartilage (1.36–39.2 MPa) and subchondral bone (1.4–9800 MPa). The factors that determine the compressive properties of scaffolds include the shape and size of the pores, complex internal architecture, pore interconnectivity and composition of the scaffold. The proliferation studies indicate the cell growth in channels with different geometries varies and system C showed higher proliferation ability suggesting the design pattern of scaffolds mitigates the proliferation of MSCs. The design with a maximum contact area at intersections, at the same time, maintaining the high porosity would be favorable for the cells to attach, migrate and proliferate better. Beyond scaffold's compatibility, degradability, and mechanical stability, tissue formation necessitates cell proliferation, migration, and differentiation while secreting ECM components. The functional ability of seeded MSCs on the three systems and the production of respective ECM were studied. The greater sGAG content in the cartilage phase (PCL/PVP/CS/PAA) of system C, when compared to systems A and B, can be attributed to the composition and design pattern of scaffold that favored enhanced chondrogenesis of seeded MSCs. The enzyme ALP is an indicator of osteogenesis, and greater ALP activity shown by the system C (PCL/PVP/ β TCP/PAA) compared to systems A and B on day 14, suggested the commitment of seeded stem cells to the osteoblastic phenotype and formation of bone minerals. These *in vitro* studies thus illustrate that the mixing of biofactors (CS/ β TCP) in PCL/PVP/PAA

is successful, and could be the reason of better osteo-chondrogenesis. Thus, suitable selection of material and design is very critical for interesting biological phenomenon where the synergistic effect of these scaffold related factors of system C demonstrated superior *invitro* performance through enhance cell proliferation and differentiation.

For investigating the *in vivo* performance in terms of biocompatibility and osteochondral regenerative potential, based on the desirable *invitro* evidence, we chose the System C, namely, BPS having PCL/PVP/CS/PAA as the cartilage phase and PCL/PVP/ β TCP/PAA as the bone layer, of dimensions 1.5mm (H) and 1.5 mm (D) for further implantation into the medial femoral condyle defects of Wistar rats for 4 and 12 weeks.

After opening the joints, no evidence of an immune response was seen either to the allogeneous cells or to the polymer-based BPS at both time points which is evident from the absence of joint inflammation and revealed good adhesions between the joint capsule, fat pad and joint compartment upon inspecting the joint. Besides, absence of degenerative changes or delamination of the phases of scaffold in the joints were observed.

The neo-formed tissues that filled the defect in BPS and BPS+ cells at one month were predominantly whitish to translucent, and the surface was smooth (heterogeneous) and intact, but with significant depressions and irregularity. The native articular cartilage is white, smooth, lustrous and is semi-transparent in appearance at fresh state. Articular cartilage facilitates the bone movement through transmitting the mechanical loads deep into the underlying subchondral bone plate. Hence, the articular surface plays an imperative role in load transfer across the joint and conditions leading to increased or altered load dispersal can further deteriorate the joint functionality (Roos, 2005). The irregularities on the surface can lead to interrupted dissipation of forces which alters the homeostasis of ECM and embedded chondrocytes where synthesis and remodeling of ECM are altered. At one month after implantation, the line of distinction observed between newly formed cartilage tissue and host

cartilage indicates a lack of integration of the scaffolds, which suggests more time is needed for the neotissue to integrate with the native tissue. Besides, Safranin O and alcian blue staining showed signs of proteoglycan synthesis in all the samples under groups 1 and 2. In contrast, defects in the sham group (group 3) increased in size from 1.5 to 1.8 mm in diameter.

At 12 weeks, enhanced levels of defect fill were observed in both BPS and BPS+Cells groups. The color of the regenerated cartilage was similar to that of the host tissue, especially at the periphery showing adequate integration. The surface of regenerated cartilage in BPS + cells is smooth and more homogenous. But BPS alone scaffolds featured small cracks and fissures indicating that the gross morphological appearance of the regenerated cartilage was superior for BPS+cells at 3 months. The histological staining of all samples from the scaffold implanted groups showed evidence of newly formed repair tissue that integrated with the surrounding tissue. In addition, we observed thicker hyaline-like cartilage formation with intense Safranin O and uniform Alcian blue staining in MSCs seeded BPS, suggesting GAGs presence and proteoglycan formation. Aggrecan, facilitates the cell-cell and cell-matrix interactions by stabilizing the cell-substratum interactions, resulting in a significantly enhanced healing process. Along with regenerated cartilage, the integrated subchondral bone without voids or cysts in the BPS+cells, revealed an enhanced osteochondral repair. The embedded cells within the regenerated cartilage were observed to reside within the lacunae in a columnar arrangement and showed a rounded morphology. Also, the presence of fibrocartilage, a common form of repair tissue composed primarily of collagen type I and low amounts of type II collagen and proteoglycans was less observed in these groups. No fibrous tissue or inflammatory infiltrates were detected in all examined cases. Besides, in the BPS group, the central region of the defect was unfilled when compared to the BPS+cells where a more homogenous response was observed.

The cartilage-bone interface must be analyzed to determine the overall success of the surgical procedure. The trichrome staining revealed a greater deposition of collagen in the regenerated area with a distribution of cells similar to native cartilage, further confirming the higher quality of the newly formed tissue in composition and structure. The importance of incorporating chondroitin sulfate is thus proved to improve the biological function of the implanted scaffold and for a more functional and durable new tissue compared to the fibrocartilage seen in the sham groups.

The prime reason for the failure of osteochondral substitutes in achieving the clinical satisfactory outcome is related to insufficient subchondral bone formation. The lack of appropriate biomechanical support due to inadequate subchondral thickness will affect the quality of neocartilage. As a result, fibrocartilage is often observed instead of hyaline type, which has inferior durability. Therefore, the main focus of the proposed osteochondral scaffold was to simultaneously enhance the regeneration of cartilage and subchondral bone, so that the subchondral integration can help to achieve a stable mechanical fixation of the scaffold and provide strong support for the overlying cartilage.

In the BPS+Cells group, at the 3rd month of implantation, the staining revealed good integration of the newly formed bone with the neighboring native bone, which contributed to the secure attachment of the implant within the defect, followed by replacing the scaffold material with the regenerated tissue. The quality of regenerated cartilage depends on the underlying subchondral bone and the presence of any voids or cysts in the subchondral bone will affect the biomechanical properties of the whole osteochondral region. During physiological loading, the external stresses exerted in normal cartilage induce hydrostatic pressure that helps in dissipating the load. The hydrostatic pressure is maintained as a function of the subchondral bone, thereby supporting the cartilage (Correia et al., 2012). This function may get interfered due to the presence of voids and can consequently lead to the initiation of

cartilage matrix destruction. The regenerated cartilage in the BPS+cells group was hyaline-like and superior whereas slightly inferior regeneration of cartilage in the BPS group may be due to the presence of a few voids in the subchondral bone that leads to increased levels of strain in the cartilage layer. These findings prove that a mechanically stable osteochondral scaffold directs the early bone repair and subsequently improving the quality of regenerated cartilage. Thus, β TCP incorporation improved the integration of scaffolds to the native bone and influence the longevity of the repair tissue.

Thus, newly formed cartilage of the BPS and BPS+cells were in many ways significantly higher quality repair tissue than the sham samples. The better surface regularity in BPS+cells at 3 months of implantation may be a result of the adequate amount of cartilage formation that integrated well with the surrounding tissue. Alternatively, the poor surface regularity in BPS could be a result of the lack of bone formation in the subchondral region, and thus lack of stability of the newly formed tissue. Furthermore, in some samples of BPS group, the new cartilage tissue had a slight concave structure with the center filled with fibrous tissue. This indentation may be further evidence of a lack of underlying structural support in these samples.

The integrity of the scaffold was maintained even at 12 weeks, attributed to the slow degradability of PCL component. Previous reported studies (Lam et al., 2009) and absence of inflammatory cell infiltrates and no foreign body reaction documented in our study confirmed that the degradation products of construct were not eliciting any adverse immunological rejection at the areas of defect site. Though PCL degrades slowly, the regeneration of tissues was appreciable as the the water-soluble PVP provides important insights for successful tuning of the biodegradation rate of PCL. PVP component of the constructs degrades via hydrolysis much faster and provided room for the cells to proliferate, differentiate and eventual tissue formation through ECM secretion. Moreover, fast degradation of PVP component could

expose more bioactive factors on the surface of a scaffold and the released biofactors may stimulate cells to trigger the delivery of endogenous growth factors to induce the differentiation of cells in the scaffolds.

In summary, we have designed and successfully fabricated a suitable spatial structure through 3D printing technique which mimics the stratified structure of natural osteochondral tissue to facilitate regeneration of large osteochondral defects. Previous *in vitro* studies have shown that system C promoted proliferation and differentiation of ADMSCs, with a high proliferation rate and expression of cartilage and bone-related genes in respective layers. The biphasic composite PCL-PVP-CS-PAA / PCL-PVP- β TCP-PAA scaffolds displayed satisfactory *in vivo* efficacy after being implanted into the medial femoral condyle of rat knee joints for 12 weeks. The closely integrated phases provided cues to the cells and facilitated the endogenous and exogenous MSCs to proliferate and differentiate. They conveniently acted as a template to guide hyaline cartilage and subchondral bone growth in respective phases to form regenerated neo-osteochondral tissues. The introduction of the exogenous cells led to better results when compared to BPS alone, and found to repair an osteochondral defect. The results of *in vivo* evaluation of biphasic scaffold encompassing a mineralized bony phase and a non-mineralized cartilage phase, performed in this rat model thus confirmed a good biocompatibility profile. Taken together, the *in vivo* evaluation thus confirmed the potentiality of biomimetic BPS as an advanced strategy for repairing OCD. Further studies in large animal models are needed to investigate and confirm if the promising findings documented in this study can further enhance the potential of this BPS for osteochondral regeneration.

CHAPTER 6

6 SUMMARY AND CONCLUSION

An osteochondral injury of the joint due to trauma, tumor, or other diseases leads to deep osteochondral defects and subsequent onset of osteoarthritis when left untreated, disturbing the articular cartilage and the underlying subchondral bone. There have been numerous repair/regeneration strategies projected as solutions for osteochondral defects. The current clinical treatment options are suboptimal and associated with donor-site morbidity, a tendency to form fibrocartilage, and further destruction of the joint. Among the widely acknowledged methods, the tissue regeneration approach uses biodegradable and bioactive materials which can recruit the endogenous cells, whereas the tissue engineering approach utilizes osteochondral 3D porous scaffolds and exogenous cells to engineer tissues. Advancements in tissue engineering (TE) strategies provided promising methods to treat osteochondral defects through the implantation of engineered cartilage-bone composite tissues. These tissue engineering strategies demonstrated favorable and satisfactory durable regeneration of tissue when used for small osteochondral defects. But numerous approaches so far tested, could not provide solutions for large critical size defects (>8 mm) due to the inability to capture the zonal nature of the native joint and biomechanical complexity of osteochondral tissues. Hence, osteochondral TE constructs/ implants that replace the full osteochondral unit are required for synchronized regeneration of both articular cartilage and the underlying subchondral bone.

Accordingly, developing clinically satisfactory osteochondral scaffolds using materials that are nearer to the translation phase was our target. The current study on “Design and development of cell-based osteochondral constructs” was based on the hypothesis that

biomaterials-based biphasic scaffolds which replicate osteochondral structure could favor differentiation of MSCs to corresponding lineages.

Scaffolds play a vital role in engineering tissue and provide an environment for increasing the viability of cells and promoting the synthesis of the neo-ECM. In our study, the exogenous cells used for OCTE were ADMSCs. Adipose tissue is a potential source for mesenchymal stem cells (MSC) capable of forming specific tissues like bone, cartilage, or muscle. A healthy population of spindle-shaped cells expressing positive surface markers specific for MSCs was successfully isolated from rat and rabbit adipose tissue. The isolated cells satisfied the minimal criteria to define MSCs upon functional characterization by multi-lineage differentiation assay. Upon induction, ADMSCs differentiated into chondrocytes and bone-forming cells and produced extracellular matrix in 2D culture *in vitro*. Collectively, our data indicate that viable ADMSCs could be obtained consistently and can be used for further studies.

The choice of an appropriate scaffold is critical for the quality of engineered cartilage. Three novel biphasic osteochondral scaffolds named system A, B, and C, recapitulating the graded structure and functionality of the unit has been successfully developed through methodical optimization of various processing parameters. In the current study, both the phases of all systems except the bone phase of system A were developed by the bottom-up strategy to get patterned constructs with specific structures. In system A, 3D printed PCL/Gelatin with gradient pores in a rectilinear pattern forms the cartilage phase, and freeze-dried PCL/CaSO₄ with non-uniform pores as the bone phase. In System B, chondroitin sulfate (CS) incorporated 3D printed PCL/PLGA constitutes the cartilage phase which had oriented pores printed in a cubical pattern in a tapering fashion to recreate the zonal variations of hyaline cartilage. However, the bone part consists of β TCP along with PCL and PLGA and 3D printed in a honeycomb pattern to simulate the native tissue for enhancing osteogenesis. In System C,

PCL/PVP/CS and PCL/PVP/ β TCP were taken as the ink for 3D printing cartilage and bone phase in cubical and star patterns respectively. The interpolymer complexation using PAA improved the printing process and prevented the z-axis collapse of the printed layer. By carefully characterizing the physical, mechanical, degradation, bioactivity, and biological properties of the three systems developed, it was found that some crucial parameters in scaffolds dictate the fate of ADMSCs for chondrogenic and osteogenic induction in respective phases which includes chemical composition, pore morphology and alignment, compressive strength, hydrophilicity, and cell confluency.

The study concerning the fabrication of system A improvised a solution-based 3D printing technique to create tapering pores on the chondromimetic layer, with wide pores at the top and narrow pore sizes at the bottom. Each of these tapering cavities could help in the initial arrangement of ADMSCs in a hyaline cartilage-like manner, where the ADMSCs can undergo differentiation into chondrocytes and secrete ECM in a pattern similar to that of the hyaline cartilage. For the lower subchondral bone part of the biphasic scaffold, we used the freeze-dried PCL/CaSO₄ scaffolding method, which could enhance cartilage-bone interfacial properties. Both the phases provided a good microenvironment for cell adhesion and its spreading and thus acted as excellent cell affable assemble. The gradual increase in sGAG and collagen secretion throughout the culture period indicates that the cells were able to maintain their functionality. The presence of CaSO₄ an inducer of osteogenesis promoted mineral deposition of the matrix and showed enhanced ALP activity and mineralization. Immunostaining and gene expression analysis further confirmed the differentiation potential of biphasic scaffolds. The approach provided evidence that these scaffolds are customizable according to the need and both the layers can act as scaffolds for the regeneration of respective tissues wherein the differentiated cells showed stable phenotype during the study period.

In system B, solution-based 3D printing of biomaterials with bioactive ingredients was employed for fabricating biphasic scaffolds because conventional 3D printing involves the use of heat or crosslinkers that reduce the bioactivity of the ingredients. The printing ink contains the dispersion of Cartilage ECM mimicking chondroitin sulfate (CS) and osteogenesis favoring β TCP along with the biocompatible polymers. The design incorporating oriented pores and struts in a regular array pattern favors the precise alignment of cells. The best-suited pattern is cubical and honeycomb for cartilage and bone layer respectively. The fabricated scaffolds offered a better degradation rate, bioactivity, and cytocompatibility as compared to the bare scaffolds. These scaffolds conveniently supported the differentiation of MSCs towards both osteo and chondral lineages and produced ECM in the presence of bioactive ingredients.

The osteochondrogenic differentiation-inducing potential of the third system C was tested *in vitro*, using rat adipose-derived mesenchymal stem cells (ADMSCs) after characterizing the critical properties such as chemical, physical, mechanical, degradation and biological ones. The scaffold design of the cartilage phase has a hierarchical organization with great precision and control over the zonal organization of layered hyaline cartilage. The star pattern of the bone phase favored the specific alignment of cells and simulated its native tissue. 3D printed BPS were highly cytocompatible, with excellent cell adhesion properties and cellular morphology, and directed the differentiation of a single stem cell population into two cell lineages (simultaneous differentiation of rat ADMSCs into chondrocytes and osteoblasts). These scaffolds enhanced the production of ECM and induced robust expression of marker genes that is specific for respective cartilage and bone layers. The 3D printed OCTE scaffold hence can simulate the native osteochondral unit and could be a potential futuristic biomimetic scaffold for osteochondral defects.

Both the phases of all systems successfully stimulated the attachment, growth, proliferation, and differentiation of adipose-derived mesenchymal stem cells (MSCs). We also

showed these scaffolds are customizable according to the need and both the phases act as a scaffold for their respective tissues wherein the differentiated cells maintained their phenotype and the cells were able to maintain their functionality. The presence of bioactive ingredients in systems B and C showed enhanced chondrogenic and osteogenic differentiation of MSCs in respective layers and produced a matrix for osteochondral repair.

System C showed greater functionality and comparable mechanical properties and was found to be appropriate for *in vivo* studies and hence selected for further implantation in Rat osteochondral defects. The *in vivo* evaluation of the developed scaffold in the medial femoral condyle confirmed the potentiality to address the unmet clinical need for the repair of large osteochondral defects. The promising results include a lack of adverse effects, and stable mechanical fixation directing improved bone ingrowth which provided sturdy support to the overlying cartilage, leading to enhanced cartilage fill of hyaline-like nature. Thus, this study would contribute useful information on the use of 3D printed-based biphasic scaffolds which provides the clinicians with a feasible treatment option for critical-size defects without a full joint replacement.

Limitation of the study:

The biphasic scaffold was developed with the aim of taking it closer to the translation stage in the clinic which necessitates *in vivo* studies in a clinically relevant animal model to evaluate its performance in terms of osteochondral tissue regeneration. However, the study was performed on a small-size animal model (rat) to specifically analyze the ability of cell-based biphasic scaffolds and evaluated their contribution to the complete results in terms of osteochondral regeneration. The osteochondral regenerative potential of this biphasic scaffold can be concluded only after conducting a pilot study on a large animal model.

FUTURE DIRECTIONS

Through decades there is considerable progress in the field of biomaterials for restoring the heterogeneities in anatomical, biological, physicochemical and mechanical properties of osteochondral tissues. However, developing continuously gradient osteochondral scaffolds having closely integrated layers, and mimicking the stratified structure of natural osteochondral tissue is still a challenging goal. Hence, fabricating 3D printed biphasic scaffolds loaded with a small molecular organic compound that plays a constructive role in promoting the repair of damaged tissues for enhanced osteochondrogenesis and tuning its sustained release forms one of the future goals. Also, further studies in large animal models are needed to investigate if the favorable findings documented in our study supporting the use of the biphasic scaffold can be confirmed. Thus, enhancing the potential of this BPS as a translation-ready technology with improved efficacy for the treatment of large osteochondral defects becomes another major goal to be completed in near future.

REFERENCES

- Adkisson, H.D., Martin, J.A., Amendola, R.L., Milliman, C., Mauch, K.A., Katwal, A.B., Seyedin, M., Amendola, A., Streeter, P.R., Buckwalter, J.A., 2010. The potential of human allogeneic juvenile chondrocytes for restoration of articular cartilage. *Am J Sports Med* 38, 1324–1333.
- Akbarzadeh, R., Yousefi, A.-M., 2014. Effects of processing parameters in thermally induced phase separation technique on porous architecture of scaffolds for bone tissue engineering. *J Biomed Mater Res B Appl Biomater* 102, 1304–1315.
- Akiyama, H., Kim, J.-E., Nakashima, K., Balmes, G., Iwai, N., Deng, J.M., Zhang, Z., Martin, J.F., Behringer, R.R., Nakamura, T., de Crombrughe, B., 2005. Osteo-chondroprogenitor cells are derived from Sox9 expressing precursors. *Proc Natl Acad Sci U S A* 102, 14665–14670.
- Aloysious, N., Nair, P.D., 2013. Enhanced Survival and Function of Islet-Like Clusters Differentiated from Adipose Stem Cells on a Three-Dimensional Natural Polymeric Scaffold: An In Vitro Study. *Tissue Engineering Part A* 20, 1508–1522.
- Aprato, A., Risitano, S., Sabatini, L., Giachino, M., Agati, G., Massè, A., 2016. Cementless total knee arthroplasty. *Ann Transl Med* 4, 129.
- Arkill, K.P., Winlove, C.P., 2008. Solute transport in the deep and calcified zones of articular cartilage. *Osteoarthritis Cartilage* 16, 708–714.
- Baghaban Eslaminejad, M., Bagheri, F., Zandi, M., Nejati, E., Zomorodian, E., Mivehchi, H., 2010. Comparison of proliferation and osteoblast differentiation of marrow-derived mesenchymal stem cells on nano- and micro-hydroxyapatite contained composite scaffolds. *Iranian Journal of Biotechnology* 8, 234–242.
- Balakrishnan, B., Joshi, N., Jayakrishnan, A., Banerjee, R., 2014. Self-crosslinked oxidized alginate/gelatin hydrogel as injectable, adhesive biomimetic scaffolds for cartilage regeneration. *Acta Biomater* 10, 3650–3663.
- Balamurugan, A., Rebelo, A., Kannan, S., Ferreira, J. m. f., Michel, J., Balossier, G., Rajeswari, S., 2007. Characterization and in vivo evaluation of sol–gel derived hydroxyapatite coatings on Ti6Al4V substrates. *Journal of Biomedical Materials Research Part B: Applied Biomaterials* 81B, 441–447.
- Bekkers, J.E.J., Bartels, L.W., Vincken, K.L., Dhert, W.J.A., Creemers, L.B., Saris, D.B.F., 2013. Articular Cartilage Evaluation After TruFit Plug Implantation Analyzed by Delayed Gadolinium-Enhanced MRI of Cartilage (dGEMRIC). *AM J SPORT MED* 41, 1290–1295.
- Bessa, P.C., Casal, M., Reis, R.L., 2008. Bone morphogenetic proteins in tissue engineering: the road from the laboratory to the clinic, part I (basic concepts). *Journal of Tissue Engineering and Regenerative Medicine* 2, 1–13.
- Bhosale, A.M., Richardson, J.B., 2008. Articular cartilage: structure, injuries and review of management. *British Medical Bulletin* 87, 77–95.
- Binulal, N.S., Natarajan, A., Menon, D., Bhaskaran, V.K., Mony, U., Nair, S.V., 2014. PCL–gelatin composite nanofibers electrospun using diluted acetic acid–ethyl acetate solvent system for stem cell-based bone tissue engineering. *Journal of Biomaterials Science, Polymer Edition* 25, 325–340.
- Blaney Davidson, E.N., Vitters, E.L., van Lent, P.L.E.M., van de Loo, F.A.J., van den Berg, W.B., van der Kraan, P.M., 2007. Elevated extracellular matrix production and degradation upon bone morphogenetic protein-2 (BMP-2) stimulation point toward a role for BMP-2 in cartilage repair and remodeling. *Arthritis Res Ther* 9, R102.
- Boland, T., Xu, T., Damon, B., Cui, X., 2006. Application of inkjet printing to tissue engineering. *Biotechnol J* 1, 910–917.
- Buckwalter, null, Mow, null, Ratcliffe, null, 1994. Restoration of Injured or Degenerated Articular Cartilage. *J Am Acad Orthop Surg* 2, 192–201.
- Buckwalter, J.A., Mankin, H.J., 1998a. Articular cartilage: tissue design and chondrocyte-matrix interactions. *Instr Course Lect* 47, 477–486.

- Buckwalter, J.A., Mankin, H.J., 1998b. Articular cartilage repair and transplantation. *Arthritis & Rheumatism* 41, 1331–1342.
- Bunnell, B.A., Flaat, M., Gagliardi, C., Patel, B., Ripoll, C., 2008. Adipose-derived Stem Cells: Isolation, Expansion and Differentiation. *Methods* 45, 115–120.
- Bunpetch, V., Zhang, X., Li, T., Lin, J., Maswikiti, E.P., Wu, Y., Cai, D., Li, J., Zhang, S., Wu, C., Ouyang, H., 2019. Silicate-based bioceramic scaffolds for dual-lineage regeneration of osteochondral defect. *Biomaterials* 192, 323–333.
- Cakmak, A.M., Unal, S., Sahin, A., Oktar, F.N., Sengor, M., Ekren, N., Gunduz, O., Kalaskar, D.M., 2020. 3D Printed Polycaprolactone/Gelatin/Bacterial Cellulose/Hydroxyapatite Composite Scaffold for Bone Tissue Engineering. *Polymers (Basel)* 12.
- Cao, T., Ho, K.-H., Teoh, S.-H., 2003. Scaffold design and in vitro study of osteochondral coculture in a three-dimensional porous polycaprolactone scaffold fabricated by fused deposition modeling. *Tissue Eng* 9 Suppl 1, S103–112.
- Carbonare, L., Giulio, I., Valenti, M., 2011. Transcription Factor Runx2 and its Application to Bone Tissue Engineering. *Stem cell reviews* 8, 891–7.
- Castaño, O., Eltohamy, M., Kim, H.-W., 2012. Electrospinning technology in tissue regeneration. *Methods Mol Biol* 811, 127–140.
- Chan, B.P., Leong, K.W., 2008. Scaffolding in tissue engineering: general approaches and tissue-specific considerations. *Eur Spine J* 17, 467–479.
- Chan, V., Zorlutuna, P., Jeong, J.H., Kong, H., Bashir, R., 2010. Three-dimensional photopatterning of hydrogels using stereolithography for long-term cell encapsulation. *Lab Chip* 10, 2062–2070.
- Chang, C.-H., Lin, F.-H., Lin, C.-C., Chou, C.-H., Liu, H.-C., 2004. Cartilage tissue engineering on the surface of a novel gelatin–calcium-phosphate biphasic scaffold in a double-chamber bioreactor. *Journal of Biomedical Materials Research Part B: Applied Biomaterials* 71B, 313–321.
- Chang, H.-I., Wang, Y., 2011. Cell Responses to Surface and Architecture of Tissue Engineering Scaffolds. *Regenerative Medicine and Tissue Engineering - Cells and Biomaterials*.
- Chen, F.H., Rousche, K.T., Tuan, R.S., 2006. Technology Insight: adult stem cells in cartilage regeneration and tissue engineering. *Nat Clin Pract Rheumatol* 2, 373–382.
- Chen, G., Kawazoe, N., 2018. Porous Scaffolds for Regeneration of Cartilage, Bone and Osteochondral Tissue. *Adv Exp Med Biol* 1058, 171–191.
- Chen, G., Tanaka, J., Tateishi, T., 2006. Osteochondral tissue engineering using a PLGA–collagen hybrid mesh.
- Chen, J., Yang, J., Wang, L., Zhang, X., Heng, B.C., Wang, D.-A., Ge, Z., 2021. Modified hyaluronic acid hydrogels with chemical groups that facilitate adhesion to host tissues enhance cartilage regeneration. *Bioact Mater* 6, 1689–1698.
- Chen, L., Deng, C., Li, J., Yao, Q., Chang, J., Wang, L., Wu, C., 2019. 3D printing of a lithium-calcium-silicate crystal bioscaffold with dual bioactivities for osteochondral interface reconstruction. *Biomaterials* 196, 138–150.
- Chen, P., Tao, J., Zhu, S., Cai, Y., Mao, Q., Yu, D., Dai, J., Ouyang, H., 2015. Radially oriented collagen scaffold with SDF-1 promotes osteochondral repair by facilitating cell homing. *Biomaterials* 39, 114–123.
- Chen, X., Fan, H., Deng, X., Wu, L., Yi, T., Gu, L., Zhou, C., Fan, Y., Zhang, X., 2018. Scaffold Structural Microenvironmental Cues to Guide Tissue Regeneration in Bone Tissue Applications. *Nanomaterials (Basel)* 8.
- Cheng, A., Schwartz, Z., Kahn, A., Li, X., Shao, Z., Sun, M., Ao, Y., Boyan, B.D., Chen, H., 2019. Advances in Porous Scaffold Design for Bone and Cartilage Tissue Engineering and Regeneration. *Tissue Eng Part B Rev* 25, 14–29.
- Chevrier, A., Kouao, A.S.M., Picard, G., Hurtig, M.B., Buschmann, M.D., 2015. Interspecies comparison of subchondral bone properties important for cartilage repair. *J Orthop Res* 33, 63–70.

- Chung, C.B., Frank, L.R., Resnick, D., 2001. Cartilage imaging techniques: current clinical applications and state of the art imaging. *Clin Orthop Relat Res* S370-8.
- Corradetti, B., Taraballi, F., Minardi, S., Van Eps, J., Cabrera, F., Francis, L.W., Gazze, S.A., Ferrari, M., Weiner, B.K., Tasciotti, E., 2016. Chondroitin Sulfate Immobilized on a Biomimetic Scaffold Modulates Inflammation While Driving Chondrogenesis. *Stem Cells Transl Med* 5, 670–682.
- Correia, C., Pereira, A.L., Duarte, A.R.C., Frias, A.M., Pedro, A.J., Oliveira, J.T., Sousa, R.A., Reis, R.L., 2012. Dynamic culturing of cartilage tissue: the significance of hydrostatic pressure. *Tissue Eng Part A* 18, 1979–1991.
- Critchley, S., Sheehy, E.J., Cunniffe, G., Diaz-Payno, P., Carroll, S.F., Jeon, O., Alsberg, E., Brama, P.A.J., Kelly, D.J., 2020. 3D printing of fibre-reinforced cartilaginous templates for the regeneration of osteochondral defects. *Acta Biomaterialia* 113, 130–143.
- Da, H., Jia, S.-J., Meng, G.-L., Cheng, J.-H., Zhou, W., Xiong, Z., Mu, Y.-J., Liu, J., 2013. The Impact of Compact Layer in Biphasic Scaffold on Osteochondral Tissue Engineering. *PLoS One* 8, e54838.
- Daly, A.C., Freeman, F.E., Gonzalez-Fernandez, T., Critchley, S.E., Nulty, J., Kelly, D.J., 2017. 3D Bioprinting for Cartilage and Osteochondral Tissue Engineering. *Adv Healthc Mater* 6.
- Darling, E., Athanasiou, K., 2003. Articular Cartilage Bioreactors and Bioprocesses. *Tissue engineering* 9, 9–26.
- Deng, C., Chang, J., Wu, C., 2019. Bioactive scaffolds for osteochondral regeneration. *Journal of Orthopaedic Translation* 17, 15–25.
- Deng, Z.H., Li, Y.S., Gao, X., Lei, G.H., Huard, J., 2018. Bone morphogenetic proteins for articular cartilage regeneration. *Osteoarthritis Cartilage* 26, 1153–1161.
- Di Luca, A., Van Blitterswijk, C., Moroni, L., 2015. The osteochondral interface as a gradient tissue: from development to the fabrication of gradient scaffolds for regenerative medicine. *Birth Defects Res C Embryo Today* 105, 34–52.
- Do, A.-V., Khorsand, B., Geary, S.M., Salem, A.K., 2015. 3D Printing of Scaffolds for Tissue Regeneration Applications. *Adv Healthc Mater* 4, 1742–1762.
- Dominici, M., Le Blanc, K., Mueller, I., Slaper-Cortenbach, I., Marini, F., Krause, D., Deans, R., Keating, A., Prockop, D., Horwitz, E., 2006. Minimal criteria for defining multipotent mesenchymal stromal cells. The International Society for Cellular Therapy position statement. *Cytotherapy* 8, 315–317.
- Du, Y., Guo, J.L., Wang, J., Mikos, A.G., Zhang, S., 2019. Hierarchically designed bone scaffolds: From internal cues to external stimuli. *Biomaterials* 218, 119334.
- Du, Y., Liu, H., Yang, Q., Wang, S., Wang, J., Ma, J., Noh, I., Mikos, A.G., Zhang, S., 2017. Selective laser sintering scaffold with hierarchical architecture and gradient composition for osteochondral repair in rabbits. *Biomaterials* 137, 37–48.
- Duan, P., Pan, Z., Cao, L., He, Y., Wang, H., Qu, Z., Dong, J., Ding, J., 2014. The effects of pore size in bilayered poly(lactide-co-glycolide) scaffolds on restoring osteochondral defects in rabbits. *J Biomed Mater Res A* 102, 180–192.
- Edwards, P.K., Ackland, T.R., Ebert, J.R., 2013. Accelerated weightbearing rehabilitation after matrix-induced autologous chondrocyte implantation in the tibiofemoral joint: early clinical and radiological outcomes. *Am J Sports Med* 41, 2314–2324.
- Ehtesabi, H., Massah, F., 2021. Improvement of hydrophilicity and cell attachment of polycaprolactone scaffolds using green synthesized carbon dots. *Materials Today Sustainability* 13, 100075.
- Elder, B.D., Athanasiou, K.A., 2009. Hydrostatic pressure in articular cartilage tissue engineering: from chondrocytes to tissue regeneration. *Tissue Eng Part B Rev* 15, 43–53.
- Eliaz, N., Metoki, N., 2017. Calcium Phosphate Bioceramics: A Review of Their History, Structure, Properties, Coating Technologies and Biomedical Applications. *Materials (Basel)* 10.
- Fereshteh, Z., 2018. Freeze-drying technologies for 3D scaffold engineering. In: *Functional 3D Tissue Engineering Scaffolds: Materials, Technologies, and Applications*. pp. 151–174.
- Fernandes, G., Abhyankar, V., O'dell, J., 2021. Calcium Sulfate as a Scaffold for Bone Tissue Engineering: A Descriptive Review. *Journal of Dentistry, Oral Disorders & Therapy* 9, 1–22.

- Filardo, G., Perdisa, F., Gelinsky, M., Despong, F., Fini, M., Marcacci, M., Parrilli, A.P., Roffi, A., Salamanna, F., Sartori, M., Schütz, K., Kon, E., 2018. Novel alginate biphasic scaffold for osteochondral regeneration: an in vivo evaluation in rabbit and sheep models. *J Mater Sci Mater Med* 29, 74.
- Florencio-Silva, R., Sasso, G.R. da S., Sasso-Cerri, E., Simões, M.J., Cerri, P.S., 2015. Biology of Bone Tissue: Structure, Function, and Factors That Influence Bone Cells. *Biomed Res Int* 2015, 421746.
- Florine, E.M., Miller, R.E., Porter, R.M., Evans, C.H., Kurz, B., Grodzinsky, A.J., 2013. Effects of Dexamethasone on Mesenchymal Stromal Cell Chondrogenesis and Aggrecanase Activity. *Cartilage* 4, 63–74.
- Frank, R.M., Lee, S., Levy, D., Poland, S., Smith, M., Scalise, N., Cvetanovich, G.L., Cole, B.J., 2017. Osteochondral Allograft Transplantation of the Knee: Analysis of Failures at 5 Years. *Am J Sports Med* 45, 864–874.
- Frassica, M.T., Grunlan, M.A., 2020. Perspectives on Synthetic Materials to Guide Tissue Regeneration for Osteochondral Defect Repair. *ACS Biomater. Sci. Eng.* 6, 4324–4336.
- Fu, J.-N., Wang, X., Yang, M., Chen, Y.-R., Zhang, J.-Y., Deng, R.-H., Zhang, Z.-N., Yu, J.-K., Yuan, F.-Z., 2022. Scaffold-Based Tissue Engineering Strategies for Osteochondral Repair. *Frontiers in Bioengineering and Biotechnology* 9.
- Furuya, M., Kikuta, J., Fujimori, S., Seno, S., Maeda, H., Shirazaki, M., Uenaka, M., Mizuno, H., Iwamoto, Y., Morimoto, A., Hashimoto, K., Ito, T., Isogai, Y., Kashii, M., Kaito, T., Ohba, S., Chung, U., Lichtler, A.C., Kikuchi, K., Matsuda, H., Yoshikawa, H., Ishii, M., 2018. Direct cell–cell contact between mature osteoblasts and osteoclasts dynamically controls their functions in vivo. *Nat Commun* 9, 300.
- Galperin, A., Oldinski, R.A., Florczyk, S.J., Bryers, J.D., Zhang, M., Ratner, B.D., 2013. Integrated Bi-Layered Scaffold for Osteochondral Tissue Engineering. *Adv Healthc Mater* 2, 872–883.
- Gao, F., Xu, Z., Liang, Q., Li, H., Peng, L., Wu, M., Zhao, X., Cui, X., Ruan, C., Liu, W., 2019. Osteochondral Regeneration with 3D-Printed Biodegradable High-Strength Supramolecular Polymer Reinforced-Gelatin Hydrogel Scaffolds. *Adv Sci (Weinh)* 6, 1900867.
- Gao, Y., Liu, S., Huang, J., Guo, W., Chen, J., Zhang, L., Zhao, B., Peng, J., Wang, A., Wang, Y., Xu, W., Lu, S., Yuan, M., Guo, Q., 2014. The ECM-Cell Interaction of Cartilage Extracellular Matrix on Chondrocytes. *BioMed Research International* 2014, e648459.
- Garg, T., Goyal, A.K., 2014. Biomaterial-based scaffolds--current status and future directions. *Expert Opin Drug Deliv* 11, 767–789.
- Gautam, S., Chou, C.-F., Dinda, A.K., Potdar, P.D., Mishra, N.C., 2014. Fabrication and characterization of PCL/gelatin/chitosan ternary nanofibrous composite scaffold for tissue engineering applications. *J Mater Sci* 49, 1076–1089.
- Gautam, S., Dinda, A.K., Mishra, N.C., 2013. Fabrication and characterization of PCL/gelatin composite nanofibrous scaffold for tissue engineering applications by electrospinning method. *Materials Science and Engineering: C* 33, 1228–1235.
- Gautieri, A., Vesentini, S., Redaelli, A., Buehler, M.J., 2011. Hierarchical Structure and Nanomechanics of Collagen Microfibrils from the Atomistic Scale Up. *Nano Lett.* 11, 757–766.
- Ge, J., Guo, L., Wang, S., Zhang, Y., Cai, T., Zhao, R.C.H., Wu, Y., 2014. The size of mesenchymal stem cells is a significant cause of vascular obstructions and stroke. *Stem Cell Rev Rep* 10, 295–303.
- Getgood, A., Henson, F., Skelton, C., Herrera, E., Brooks, R., Fortier, L.A., Rushton, N., 2012. The Augmentation of a Collagen/Glycosaminoglycan Biphasic Osteochondral Scaffold with Platelet-Rich Plasma and Concentrated Bone Marrow Aspirate for Osteochondral Defect Repair in Sheep: A Pilot Study. *Cartilage* 3, 351–363.
- Goebel, L., Orth, P., Cucchiari, M., Pape, D., Madry, H., 2017. Macroscopic cartilage repair scoring of defect fill, integration and total points correlate with corresponding items in histological scoring systems – a study in adult sheep. *Osteoarthritis and Cartilage* 25, 581–588.

- Goldring, M.B., 2012. Chondrogenesis, chondrocyte differentiation, and articular cartilage metabolism in health and osteoarthritis. *Ther Adv Musculoskelet Dis* 4, 269–285.
- Goldring, M.B., Marcu, K.B., 2009. Cartilage homeostasis in health and rheumatic diseases. *Arthritis Res Ther* 11, 224.
- Goldring, S.R., Goldring, M.B., 2016. Changes in the osteochondral unit during osteoarthritis: structure, function and cartilage-bone crosstalk. *Nat Rev Rheumatol* 12, 632–644.
- Guilak, F., Mow, V.C., 2000. The mechanical environment of the chondrocyte: a biphasic finite element model of cell-matrix interactions in articular cartilage. *J Biomech* 33, 1663–1673.
- Guo, F., Mao, Z., Chen, Y., Xie, Z., Lata, J.P., Li, P., Ren, L., Liu, J., Yang, J., Dao, M., Suresh, S., Huang, T.J., 2016. Three-dimensional manipulation of single cells using surface acoustic waves. *Proc Natl Acad Sci U S A* 113, 1522–1527.
- Guo, J., Li, C., Ling, S., Huang, W., Chen, Y., Kaplan, D.L., 2017. Multiscale design and synthesis of biomimetic gradient protein/biosilica composites for interfacial tissue engineering. *Biomaterials* 145, 44–55.
- Guo, X., Park, H., Young, S., Kretlow, J.D., van den Beucken, J.J., Baggett, L.S., Tabata, Y., Kasper, F.K., Mikos, A.G., Jansen, J.A., 2010. Repair of osteochondral defects with biodegradable hydrogel composites encapsulating marrow mesenchymal stem cells in a rabbit model. *Acta Biomater* 6, 39–47.
- Hangody, L., Füles, P., 2003. Autologous osteochondral mosaicplasty for the treatment of full-thickness defects of weight-bearing joints: ten years of experimental and clinical experience. *J Bone Joint Surg Am* 85-A Suppl 2, 25–32.
- Hardingham, T.E., Oldershaw, R.A., Tew, S.R., 2006. Cartilage, SOX9 and Notch signals in chondrogenesis. *J Anat* 209, 469–480.
- Harris, J.D., Siston, R.A., Brophy, R.H., Lattermann, C., Carey, J.L., Flanigan, D.C., 2011. Failures, reoperations, and complications after autologous chondrocyte implantation – a systematic review. *Osteoarthritis and Cartilage* 19, 779–791.
- Hattori, T., Müller, C., Gebhard, S., Bauer, E., Pausch, F., Schlund, B., Bösl, M.R., Hess, A., Surmann-Schmitt, C., von der Mark, H., de Crombrughe, B., von der Mark, K., 2010. SOX9 is a major negative regulator of cartilage vascularization, bone marrow formation and endochondral ossification. *Development* 137, 901–911.
- He, Q., Zhang, Jingwei, Liao, Y., Alakpa, E.V., Bunpetch, V., Zhang, Jiayan, Ouyang, H., 2020. Current advances in microsphere based cell culture and tissue engineering. *Biotechnol Adv* 39, 107459.
- Hoemann, C., Kandel, R., Roberts, S., Saris, D.B.F., Creemers, L., Mainil-Varlet, P., Méthot, S., Hollander, A.P., Buschmann, M.D., 2011. International Cartilage Repair Society (ICRS) Recommended Guidelines for Histological Endpoints for Cartilage Repair Studies in Animal Models and Clinical Trials. *Cartilage* 2, 153–172.
- Hong, H., Seo, Y.B., Kim, D.Y., Lee, J.S., Lee, Y.J., Lee, H., Ajiteru, O., Sultan, M.T., Lee, O.J., Kim, S.H., Park, C.H., 2020. Digital light processing 3D printed silk fibroin hydrogel for cartilage tissue engineering. *Biomaterials* 232, 119679.
- Howell, M., Liao, Q., Gee, C.W., 2021. Surgical Management of Osteochondral Defects of the Knee: An Educational Review. *Curr Rev Musculoskelet Med* 14, 60–66.
- Hu, K., Olsen, B.R., 2016. Osteoblast-derived VEGF regulates osteoblast differentiation and bone formation during bone repair. *J Clin Invest* 126, 509–526.
- Huang, K.-H., Wang, C.-Y., Chen, C.-Y., Hsu, T.-T., Lin, C.-P., 2021. Incorporation of Calcium Sulfate Dihydrate into a Mesoporous Calcium Silicate/Poly-ε-Caprolactone Scaffold to Regulate the Release of Bone Morphogenetic Protein-2 and Accelerate Bone Regeneration. *Biomedicines* 9.
- Huang, S.-H., Hsu, T.-T., Huang, T.-H., Lin, C.-Y., Shie, M.-Y., 2017. Fabrication and characterization of polycaprolactone and tricalcium phosphate composites for tissue engineering applications. *Journal of Dental Sciences* 12, 33–43.

- Hunziker, E.B., 1999. Biologic repair of articular cartilage. Defect models in experimental animals and matrix requirements. *Clin Orthop Relat Res* S135-146.
- Hutmacher, D., 2001. Scaffolds in Tissue Engineering Bone and Cartilage. *Biomaterials* 21, 2529–43.
- Hwang, P.T.J., Murdock, K., Alexander, G.C., Salaam, A.D., Ng, J.I., Lim, D.-J., Dean, D., Jun, H.-W., 2016. Poly(ϵ -caprolactone)/gelatin composite electrospun scaffolds with porous crater-like structures for tissue engineering. *J Biomed Mater Res A* 104, 1017–1029.
- Jeong, J., Kim, J.H., Shim, J.H., Hwang, N.S., Heo, C.Y., 2019. Bioactive calcium phosphate materials and applications in bone regeneration. *Biomaterials Research* 23, 4.
- Jia, Y., Zhu, X., Liu, Q., 2011. In Vitro Degradation of Electrospun Fiber Membranes of PCL/PVP Blends. *Advanced Materials Research* 332, 1330–1334.
- Jung, S., Panchalingam, K.M., Rosenberg, L., Behie, L.A., 2012. Ex Vivo Expansion of Human Mesenchymal Stem Cells in Defined Serum-Free Media. *Stem Cells International* 2012, e123030.
- Kamboj, N., Kazantseva, J., Rahmani, R., Rodríguez, M.A., Hussainova, I., 2020. Selective laser sintered bio-inspired silicon-wollastonite scaffolds for bone tissue engineering. *Materials Science and Engineering: C* 116, 111223.
- Karageorgiou, V., Kaplan, D., 2005. Porosity of 3D biomaterial scaffolds and osteogenesis. *Biomaterials* 26, 5474–5491.
- Keeney, M., Pandit, A., 2009. The osteochondral junction and its repair via bi-phasic tissue engineering scaffolds. *Tissue Eng Part B Rev* 15, 55–73.
- Keriquel, V., Oliveira, H., Rémy, M., Ziane, S., Delmond, S., Rousseau, B., Rey, S., Catros, S., Amédée, J., Guillemot, F., Fricain, J.-C., 2017. In situ printing of mesenchymal stromal cells, by laser-assisted bioprinting, for in vivo bone regeneration applications. *Sci Rep* 7, 1778.
- Kim, G.-M., Le, K.H.T., Giannitelli, S.M., Lee, Y.J., Rainer, A., Trombetta, M., 2013. Electrospinning of PCL/PVP blends for tissue engineering scaffolds. *J Mater Sci Mater Med* 24, 1425–1442.
- Kim, S.-S., Sun Park, M., Jeon, O., Yong Choi, C., Kim, B.-S., 2006. Poly(lactide-co-glycolide)/hydroxyapatite composite scaffolds for bone tissue engineering. *Biomaterials* 27, 1399–1409.
- Kim, Y.G., Choi, J., Kim, K., 2020. Mesenchymal Stem Cell-Derived Exosomes for Effective Cartilage Tissue Repair and Treatment of Osteoarthritis. *Biotechnol J* 15, e2000082.
- Ko, J.-Y., Kim, K.-I., Park, S., Im, G.-I., 2014. In vitro chondrogenesis and in vivo repair of osteochondral defect with human induced pluripotent stem cells. *Biomaterials* 35, 3571–3581.
- Kon, E., Delcogliano, M., Filardo, G., Busacca, M., Di Martino, A., Marcacci, M., 2011. Novel nano-composite multilayered biomaterial for osteochondral regeneration: a pilot clinical trial. *Am J Sports Med* 39, 1180–1190.
- Kon, E., Verdonk, P., Condello, V., Delcogliano, M., Dhollander, A., Filardo, G., Pignotti, E., Marcacci, M., 2009. Matrix-Assisted Autologous Chondrocyte Transplantation for the Repair of Cartilage Defects of the Knee: Systematic Clinical Data Review and Study Quality Analysis. *Am J Sports Med* 37, 156–166.
- Korpayev, S., Kaygusuz, G., Şen, M., Orhan, K., Oto, Ç., Karakeçili, A., 2020. Chitosan/collagen based biomimetic osteochondral tissue constructs: A growth factor-free approach. *Int J Biol Macromol* 156, 681–690.
- Kosik-Kozioł, A., Costantini, M., Mróz, A., Idaszek, J., Heljak, M., Jaroszewicz, J., Kijeńska, E., Szöke, K., Frerker, N., Barbetta, A., Brinchmann, J.E., Świążzkowski, W., 2019. 3D bioprinted hydrogel model incorporating β -tricalcium phosphate for calcified cartilage tissue engineering. *Biofabrication* 11, 035016.
- Kwon, H., Brown, W.E., Lee, C.A., Wang, D., Paschos, N., Hu, J.C., Athanasiou, K.A., 2019. Surgical and tissue engineering strategies for articular cartilage and meniscus repair. *Nat Rev Rheumatol* 15, 550–570.

- Lam, C., Hutmacher, D., Schantz, J.-T., Woodruff, M., Teoh, H., 2009. Evaluation of polycaprolactone scaffold degradation for 6 months in vitro and in vivo. *Journal of Biomedical Materials Research Part A* 90.
- Langer, R., Vacanti, J.P., 1993. Tissue engineering. *Science* 260, 920–926.
- Lee, B.-C., Kang, K.-S., 2020. Functional enhancement strategies for immunomodulation of mesenchymal stem cells and their therapeutic application. *Stem Cell Research & Therapy* 11, 397.
- Levingstone, T.J., Ramesh, A., Brady, R.T., Brama, P.A.J., Kearney, C., Gleeson, J.P., O'Brien, F.J., 2016. Cell-free multi-layered collagen-based scaffolds demonstrate layer specific regeneration of functional osteochondral tissue in caprine joints. *Biomaterials* 87, 69–81.
- Li, G., Yin, J., Gao, J., Cheng, T.S., Pavlos, N.J., Zhang, C., Zheng, M.H., 2013. Subchondral bone in osteoarthritis: insight into risk factors and microstructural changes. *Arthritis Res Ther* 15, 223.
- Li, H., Qian, J., Chen, J., Zhong, K., Chen, S., 2016. Osteochondral repair with synovial membrane-derived mesenchymal stem cells. *Molecular Medicine Reports* 13, 2071–2077.
- Li, X., Ding, J., Wang, J., Zhuang, X., Chen, X., 2015. Biomimetic biphasic scaffolds for osteochondral defect repair. *Regen Biomater* 2, 221–228.
- Li, X., Ding, J., Zhang, Z., Yang, M., Yu, J., Wang, J., Chang, F., Chen, X., 2016. Kartogenin-Incorporated Thermogel Supports Stem Cells for Significant Cartilage Regeneration. *ACS Appl Mater Interfaces* 8, 5148–5159.
- Li, Z., Jia, S., Xiong, Z., Long, Q., Yan, S., Hao, F., Liu, J., Yuan, Z., 2018. 3D-printed scaffolds with calcified layer for osteochondral tissue engineering. *Journal of Bioscience and Bioengineering* 126, 389–396.
- Liang, X., Duan, P., Gao, J., Guo, R., Qu, Z., Li, X., He, Y., Yao, H., Ding, J., 2018. Bilayered PLGA/PLGA-HAp Composite Scaffold for Osteochondral Tissue Engineering and Tissue Regeneration. *ACS Biomater. Sci. Eng.* 4, 3506–3521.
- Liu, J., Li, L., Suo, H., Yan, M., Yin, J., Fu, J., 2019. 3D printing of biomimetic multi-layered GelMA/nHA scaffold for osteochondral defect repair. *Materials & Design* 171, 107708.
- Liu, X., Wei, Y., Xuan, C., Liu, L., Lai, C., Chai, M., Zhang, Z., Wang, L., Shi, X., 2020. A Biomimetic Biphasic Osteochondral Scaffold with Layer-Specific Release of Stem Cell Differentiation Inducers for the Reconstruction of Osteochondral Defects. *Advanced Healthcare Materials* 9, 2000076.
- Loebel, C., Czekanska, E.M., Bruderer, M., Salzmann, G., Alini, M., Stoddart, M.J., 2015. In Vitro Osteogenic Potential of Human Mesenchymal Stem Cells Is Predicted by Runx2/Sox9 Ratio. *Tissue Eng Part A* 21, 115–123.
- Loeser, R.F., 2014. Integrins and chondrocyte–matrix interactions in articular cartilage. *Matrix Biology* 39, 11–16.
- Loeser, R.F., Goldring, S.R., Scanzello, C.R., Goldring, M.B., 2012. Osteoarthritis: A Disease of the Joint as an Organ. *Arthritis Rheum* 64, 1697–1707.
- Loh, Q.L., Choong, C., 2013. Three-Dimensional Scaffolds for Tissue Engineering Applications: Role of Porosity and Pore Size. *Tissue Engineering Part B: Reviews* 19, 485–502.
- Longley, R., Ferreira, A.M., Gentile, P., 2018. Recent Approaches to the Manufacturing of Biomimetic Multi-Phasic Scaffolds for Osteochondral Regeneration. *Int J Mol Sci* 19.
- Lopa, S., Madry, H., 2014. Bioinspired scaffolds for osteochondral regeneration. *Tissue Eng Part A* 20, 2052–2076.
- Lu, P., Takai, K., Weaver, V.M., Werb, Z., 2011. Extracellular Matrix Degradation and Remodeling in Development and Disease. *Cold Spring Harb Perspect Biol* 3, a005058.
- Luca, A.D., Szlajak, K., Lorenzo-Moldero, I., Ghebes, C.A., Lepedda, A., Swieszkowski, W., Blitterswijk, C.V., Moroni, L., 2016. Influencing chondrogenic differentiation of human mesenchymal stromal cells in scaffolds displaying a structural gradient in pore size. *ACTA BIOMATER* 36, 210–219.

- Lyons, T.J., McClure, S.F., Stoddart, R.W., McClure, J., 2006. The normal human chondro-osseous junctional region: evidence for contact of uncalcified cartilage with subchondral bone and marrow spaces. *BMC Musculoskeletal Disorders* 7, 52.
- M, J.C., Reardon, P.J.T., Konwarh, R., Knowles, J.C., Mandal, B.B., 2017. Mimicking Hierarchical Complexity of the Osteochondral Interface Using Electrospun Silk–Bioactive Glass Composites. *ACS Appl. Mater. Interfaces* 9, 8000–8013.
- Ma, H., Feng, C., Chang, J., Wu, C., 2018. 3D-printed bioceramic scaffolds: From bone tissue engineering to tumor therapy. *Acta Biomater* 79, 37–59.
- Ma, J., Lin, L., Zuo, Y., Zou, Q., Ren, X., Li, J., Li, Y., 2019. Modification of 3D printed PCL scaffolds by PVAc and HA to enhance cytocompatibility and osteogenesis. *RSC Adv.* 9, 5338–5346.
- Madry, H., van Dijk, C.N., Mueller-Gerbl, M., 2010. The basic science of the subchondral bone. *Knee Surg Sports Traumatol Arthrosc* 18, 419–433.
- Mahmoudifar, N., Doran, P.M., 2013. Osteogenic differentiation and osteochondral tissue engineering using human adipose-derived stem cells. *Biotechnol Prog* 29, 176–185.
- Malafaya, P.B., Pedro, A.J., Peterbauer, A., Gabriel, C., Redl, H., Reis, R.L., 2005. Chitosan particles agglomerated scaffolds for cartilage and osteochondral tissue engineering approaches with adipose tissue derived stem cells. *J Mater Sci: Mater Med* 16, 1077–1085.
- Maldonado, M., Nam, J., 2013. The Role of Changes in Extracellular Matrix of Cartilage in the Presence of Inflammation on the Pathology of Osteoarthritis. *Biomed Res Int* 2013, 284873.
- Mano, J.F., Reis, R.L., 2007. Osteochondral defects: present situation and tissue engineering approaches. *J Tissue Eng Regen Med* 1, 261–273.
- Marcacci, M., Kon, E., Zaffagnini, S., Reggiani, L.M., Neri, M.P., Iacono, F., 2007. Cell-Based Cartilage Repair Using the Hyalograft Transplant. In: Williams, R.J. (Ed.), *Cartilage Repair Strategies*. Humana Press, Totowa, NJ, pp. 207–218.
- Markway, B.D., Tan, G.-K., Brooke, G., Hudson, J.E., Cooper-White, J.J., Doran, M.R., 2010. Enhanced chondrogenic differentiation of human bone marrow-derived mesenchymal stem cells in low oxygen environment micropellet cultures. *Cell Transplant* 19, 29–42.
- Marmotti, A., Mattia, S., Castoldi, F., Barbero, A., Mangiavini, L., Bonasia, D.E., Bruzzone, M., Dettoni, F., Scurati, R., Peretti, G.M., 2017. Allogeneic Umbilical Cord-Derived Mesenchymal Stem Cells as a Potential Source for Cartilage and Bone Regeneration: An In Vitro Study. *Stem Cells Int* 2017, 1732094.
- Martel-Pelletier, J., Barr, A.J., Cicuttini, F.M., Conaghan, P.G., Cooper, C., Goldring, M.B., Goldring, S.R., Jones, G., Teichtahl, A.J., Pelletier, J.-P., 2016. Osteoarthritis. *Nat Rev Dis Primers* 2, 1–18.
- Martens, M., Van Audekercke, R., Delpont, P., De Meester, P., Mulier, J.C., 1983. The mechanical characteristics of cancellous bone at the upper femoral region. *J Biomech* 16, 971–983.
- Martin, R., Jakob, R.P., 2022. Review of K.H. Pridie (1959) on “A method of resurfacing osteoarthritic knee joints.” *Journal of ISAKOS* 7, 39–46.
- Matai, I., Kaur, G., Seyedsalehi, A., McClinton, A., Laurencin, C.T., 2020. Progress in 3D bioprinting technology for tissue/organ regenerative engineering. *Biomaterials* 226, 119536.
- Matta, C., Szűcs-Somogyi, C., Kon, E., Robinson, D., Neufeld, T., Altschuler, N., Berta, A., Hangody, L., Veréb, Z., Zákány, R., 2019. Osteogenic differentiation of human bone marrow-derived mesenchymal stem cells is enhanced by an aragonite scaffold. *Differentiation* 107, 24–34.
- Meghdadi, M., Pezeshki-Modaress, M., Irani, S., Atyabi, S.M., Zandi, M., 2019. Chondroitin sulfate immobilized PCL nanofibers enhance chondrogenic differentiation of mesenchymal stem cells. *Int J Biol Macromol* 136, 616–624.
- Mellor, L.F., Mohiti-Asli, M., Williams, J., Kannan, A., Dent, M.R., Guilak, F., Lobo, E.G., 2015. Extracellular Calcium Modulates Chondrogenic and Osteogenic Differentiation of Human Adipose-Derived Stem Cells: A Novel Approach for Osteochondral Tissue Engineering Using a Single Stem Cell Source. *Tissue Eng Part A* 21, 2323–2333.

- Meretoja, V.V., Dahlin, R.L., Wright, S., Kasper, F.K., Mikos, A.G., 2013. The effect of hypoxia on the chondrogenic differentiation of co-cultured articular chondrocytes and mesenchymal stem cells in scaffolds. *Biomaterials* 34, 4266–4273.
- Minas, T., Ogura, T., Bryant, T., 2016. Autologous Chondrocyte Implantation. *JBJS Essent Surg Tech* 6, e24.
- Miyoshi, H., Adachi, T., 2014. Topography Design Concept of a Tissue Engineering Scaffold for Controlling Cell Function and Fate Through Actin Cytoskeletal Modulation. *Tissue Eng Part B Rev* 20, 609–627.
- Moran, C.J., Ramesh, A., Brama, P.A.J., O’Byrne, J.M., O’Brien, F.J., Levingstone, T.J., 2016. The benefits and limitations of animal models for translational research in cartilage repair. *J Exp Orthop* 3, 1.
- Mow, V.C., Guo, X.E., 2002. Mechano-electrochemical properties of articular cartilage: their inhomogeneities and anisotropies. *Annu Rev Biomed Eng* 4, 175–209.
- Murphy, C.M., O’Brien, F.J., 2010. Understanding the effect of mean pore size on cell activity in collagen-glycosaminoglycan scaffolds. *Cell Adh Migr* 4, 377–381.
- Murphy, S.V., Atala, A., 2014. 3D bioprinting of tissues and organs. *Nature Biotechnology* 32, 773–785.
- Naahidi, S., Jafari, M., Logan, M., Wang, Y., Yuan, Y., Bae, H., Dixon, B., Chen, P., 2017. Biocompatibility of hydrogel-based scaffolds for tissue engineering applications. *Biotechnol Adv* 35, 530–544.
- Nehrer, S., Chiari, C., Domayer, S., Barkay, H., Yayon, A., 2008. Results of Chondrocyte Implantation with a Fibrin-Hyaluronan Matrix: A Preliminary Study. *Clin Orthop Relat Res* 466, 1849–1855.
- Ng, W.L., Lee, J.M., Yeong, W.Y., Naing, M.W., 2017. Microvalve-based bioprinting – process, bio-inks and applications. *Biomater. Sci.* 5, 632–647.
- Ngo, T.D., Kashani, A., Imbalzano, G., Nguyen, K.T.Q., Hui, D., 2018. Additive manufacturing (3D printing): A review of materials, methods, applications and challenges. *Composites Part B: Engineering* 143, 172–196.
- Ning, L., Chen, X., 2017. A brief review of extrusion-based tissue scaffold bio-printing. *Biotechnol J* 12.
- Nooeaid, P., Salih, V., Beier, J.P., Boccaccini, A.R., 2012. Osteochondral tissue engineering: scaffolds, stem cells and applications. *J Cell Mol Med* 16, 2247–2270.
- Nour-Eldeen, G., Abdel-Rasheed, M., EL-Rafei, A.M., Azmy, O., El-Bassyouni, G.T., 2020. Adipose tissue-derived mesenchymal stem cells and chitosan/poly (vinyl alcohol) nanofibrous scaffolds for cartilage tissue engineering. *Cell Regen* 9, 7.
- Nukavarapu, S.P., Dorcemus, D.L., 2013. Osteochondral tissue engineering: Current strategies and challenges. *Biotechnology Advances, Pearl (30th) Anniversary Edition: Nanotechnology & Regenerative Medicine* 31, 706–721.
- Odabas, S., Elçin, A.E., Elçin, Y.M., 2014. Isolation and characterization of mesenchymal stem cells. *Methods Mol Biol* 1109, 47–63.
- Oh, S.H., Kim, T.H., Im, G.I., Lee, J.H., 2010. Investigation of pore size effect on chondrogenic differentiation of adipose stem cells using a pore size gradient scaffold. *Biomacromolecules* 11, 1948–1955.
- Okamoto, M., John, B., 2013. Synthetic biopolymer nanocomposites for tissue engineering scaffolds. *Progress in Polymer Science, Progress in Bionanocomposites: from green plastics to biomedical applications* 38, 1487–1503.
- O’Shea, T.M., Miao, X., 2008. Bilayered scaffolds for osteochondral tissue engineering. *Tissue Eng Part B Rev* 14, 447–464.
- Oyane, A., Kim, H.-M., Furuya, T., Kokubo, T., Miyazaki, T., Nakamura, T., 2003. Preparation and assessment of revised simulated body fluids. *J Biomed Mater Res A* 65, 188–195.
- Pan, Z., Duan, P., Liu, X., Wang, H., Cao, L., He, Y., Dong, J., Ding, J., 2015. Effect of porosities of bilayered porous scaffolds on spontaneous osteochondral repair in cartilage tissue engineering. *Regen Biomater* 2, 9–19.
- Paul, K., Lee, B.Y., Abueva, C., Kim, B., Choi, H.J., Bae, S.H., Lee, B.T., 2017. In vivo evaluation of injectable calcium phosphate cement composed of Zn- and Si-incorporated β -tricalcium

- phosphate and monocalcium phosphate monohydrate for a critical sized defect of the rabbit femoral condyle. *J Biomed Mater Res B Appl Biomater* 105, 260–271.
- Pearle, A.D., Warren, R.F., Rodeo, S.A., 2005. Basic science of articular cartilage and osteoarthritis. *Clin Sports Med* 24, 1–12.
- Peng, C., Zheng, J., Chen, D., Zhang, X., Deng, L., Chen, Z., Wu, L., 2018. Response of hPDLSCs on 3D printed PCL/PLGA composite scaffolds in vitro. *Molecular Medicine Reports* 18, 1335–1344.
- Pereira, D.R., Reis, R.L., Oliveira, J.M., 2018. Layered Scaffolds for Osteochondral Tissue Engineering. *Adv Exp Med Biol* 1058, 193–218.
- Pina, S., Rebelo, R., Correlo, V.M., Oliveira, J.M., Reis, R.L., 2018. Bioceramics for Osteochondral Tissue Engineering and Regeneration. *Adv Exp Med Biol* 1058, 53–75.
- Portron, S., Merceron, C., Gauthier, O., Lesoeur, J., Sourice, S., Masson, M., Fellah, B.H., Geffroy, O., Lallemand, E., Weiss, P., Guicheux, J., Vinatier, C., 2013. Effects of In Vitro Low Oxygen Tension Preconditioning of Adipose Stromal Cells on Their In Vivo Chondrogenic Potential: Application in Cartilage Tissue Repair. *PLoS One* 8, e62368.
- Pouran, B., Arbabi, V., Bleys, R.L., René van Weeren, P., Zadpoor, A.A., Weinans, H., 2017. Solute transport at the interface of cartilage and subchondral bone plate: Effect of micro-architecture. *J Biomech* 52, 148–154.
- Prabha, R.D., Ding, M., Bollen, P., Ditzel, N., Varma, H.K., Nair, P.D., Kassem, M., 2020. Strontium ion reinforced bioceramic scaffold for load bearing bone regeneration. *Materials Science and Engineering: C* 109, 110427.
- Pulai, J.I., Chen, H., Im, H.-J., Kumar, S., Hanning, C., Hegde, P.S., Loeser, R.F., 2005. NF-kappa B mediates the stimulation of cytokine and chemokine expression by human articular chondrocytes in response to fibronectin fragments. *J Immunol* 174, 5781–5788.
- Qi, X., Pei, P., Zhu, M., Du, X., Xin, C., Zhao, S., Li, X., Zhu, Y., 2017. Three dimensional printing of calcium sulfate and mesoporous bioactive glass scaffolds for improving bone regeneration in vitro and in vivo. *Scientific reports*.
- Quinn, T.M., Hunziker, E.B., Häuselmann, H.-J., 2005. Variation of cell and matrix morphologies in articular cartilage among locations in the adult human knee. *Osteoarthritis Cartilage* 13, 672–678.
- Redman, S.N., Oldfield, S.F., Archer, C.W., 2005. Current strategies for articular cartilage repair. *Eur Cell Mater* 9, 23–32; discussion 23-32.
- Retting, K.N., Song, B., Yoon, B.S., Lyons, K.M., 2009. BMP canonical Smad signaling through Smad1 and Smad5 is required for endochondral bone formation. *Development* 136, 1093–1104.
- Reyes, R., Delgado, A., Solis, R., Sanchez, E., Hernandez, A., San Roman, J., Evora, C., 2014. Cartilage repair by local delivery of transforming growth factor- β 1 or bone morphogenetic protein-2 from a novel, segmented polyurethane/polylactic-co-glycolic bilayered scaffold. *J Biomed Mater Res A* 102, 1110–1120.
- Roos, E.M., 2005. Joint injury causes knee osteoarthritis in young adults. *Curr Opin Rheumatol* 17, 195–200.
- Rumpler, M., Woesz, A., Dunlop, J.W.C., van Dongen, J.T., Fratzl, P., 2008. The effect of geometry on three-dimensional tissue growth. *J R Soc Interface* 5, 1173–1180.
- S, T., Nm, D., A, B., S, B., 2013. 3D printed tricalcium phosphate scaffolds: Effect of SrO and MgO doping on in vivo osteogenesis in a rat distal femoral defect model. *Biomater Sci* 1, 1250–1259.
- Sanchez, C., Deberg, M.A., Bellahcène, A., Castronovo, V., Msika, P., Delcour, J.P., Crielaard, J.M., Henrotin, Y.E., 2008. Phenotypic characterization of osteoblasts from the sclerotic zones of osteoarthritic subchondral bone. *Arthritis Rheum* 58, 442–455.
- Sasaki, A., Mizuno, M., Ozeki, N., Katano, H., Otabe, K., Tsuji, K., Koga, H., Mochizuki, M., Sekiya, I., 2018. Canine mesenchymal stem cells from synovium have a higher chondrogenic potential than those from infrapatellar fat pad, adipose tissue, and bone marrow. *PLoS One* 13, e0202922.

- Saunders, R.E., Derby, B., 2014. Inkjet printing biomaterials for tissue engineering: bioprinting. *International Materials Reviews* 59, 430–448.
- Schneider, U., Rackwitz, L., Andereya, S., Siebenlist, S., Fensky, F., Reichert, J., Löer, I., Barthel, T., Rudert, M., Nöth, U., 2011. A prospective multicenter study on the outcome of type I collagen hydrogel-based autologous chondrocyte implantation (CaReS) for the repair of articular cartilage defects in the knee. *Am J Sports Med* 39, 2558–2565.
- Schubert, T., Anders, S., Neumann, E., Schölmerich, J., Hofstädter, F., Grifka, J., Müller-Ladner, U., Libera, J., Schedel, J., 2009. Long-term effects of chondrospheres on cartilage lesions in an autologous chondrocyte implantation model as investigated in the SCID mouse model. *Int J Mol Med* 23, 455–460.
- Schuette, H.B., Kraeutler, M.J., McCarty, E.C., 2017. Matrix-Assisted Autologous Chondrocyte Transplantation in the Knee: A Systematic Review of Mid- to Long-Term Clinical Outcomes. *Orthop J Sports Med* 5, 2325967117709250.
- Selmi, T. a. S., Verdonk, P., Chambat, P., Dubrana, F., Potel, J.-F., Barnouin, L., Neyret, P., 2008. Autologous chondrocyte implantation in a novel alginate-agarose hydrogel: outcome at two years. *J Bone Joint Surg Br* 90, 597–604.
- Seo, J.-P., Tanabe, T., Tsuzuki, N., Haneda, S., Yamada, K., Furuoka, H., Tabata, Y., Sasaki, N., 2013. Effects of bilayer gelatin/ β -tricalcium phosphate sponges loaded with mesenchymal stem cells, chondrocytes, bone morphogenetic protein-2, and platelet rich plasma on osteochondral defects of the talus in horses. *Res Vet Sci* 95, 1210–1216.
- Seyednejad, H., Gawlitta, D., Kuiper, R.V., de Bruin, A., van Nostrum, C.F., Vermonden, T., Dhert, W.J.A., Hennink, W.E., 2012. In vivo biocompatibility and biodegradation of 3D-printed porous scaffolds based on a hydroxyl-functionalized poly(ϵ -caprolactone). *Biomaterials* 33, 4309–4318.
- Sharma, A.R., Jagga, S., Lee, S.-S., Nam, J.-S., 2013. Interplay between cartilage and subchondral bone contributing to pathogenesis of osteoarthritis. *Int J Mol Sci* 14, 19805–19830.
- Sharma, B., Fermanian, S., Gibson, M., Unterman, S., Herzka, D.A., Cascio, B., Coburn, J., Hui, A.Y., Marcus, N., Gold, G.E., Elisseeff, J.H., 2013. Human cartilage repair with a photoreactive adhesive-hydrogel composite. *Sci Transl Med* 5, 167ra6.
- Sharma, P., 2017. The Influence of Vimentin Intermediate Filaments on Human Mesenchymal Stem Cell Response to Physical Stimuli.
- Shim, J.-H., Huh, J.-B., Park, J.Y., Jeon, Y.-C., Kang, S.S., Kim, J.Y., Rhie, J.-W., Cho, D.-W., 2013. Fabrication of blended polycaprolactone/poly(lactic-co-glycolic acid)/ β -tricalcium phosphate thin membrane using solid freeform fabrication technology for guided bone regeneration. *Tissue Eng Part A* 19, 317–328.
- Shim, J.-H., Won, J.-Y., Park, J.-H., Bae, J.-H., Ahn, G., Kim, C.-H., Lim, D.-H., Cho, D.-W., Yun, W.-S., Bae, E.-B., Jeong, C.-M., Huh, J.-B., 2017. Effects of 3D-Printed Polycaprolactone/ β -Tricalcium Phosphate Membranes on Guided Bone Regeneration. *Int J Mol Sci* 18, 899.
- Shoulders, M.D., Raines, R.T., 2009. Collagen structure and stability. *Annu Rev Biochem* 78, 929–958.
- Siddiqui, N., Asawa, S., Birru, B., Baadhe, R., Rao, S., 2018. PCL-Based Composite Scaffold Matrices for Tissue Engineering Applications. *Mol Biotechnol* 60, 506–532.
- Singh, R., Tan, C., Abd Shukor, M., Sopyan, I., Teng, W., 2007. The influence of Ca/P ratio on the properties of hydroxyapatite bioceramics. *Proc SPIE* 6423.
- Sinha, K.M., Zhou, X., 2013. Genetic and molecular control of Osterix in skeletal formation. *J Cell Biochem* 114, 975–984.
- Slattery, C., Kweon, C.Y., 2018. Classifications in Brief: Outerbridge Classification of Chondral Lesions. *Clinical Orthopaedics and Related Research*® 476, 2101–2104.
- Somoza, R.A., Welter, J.F., Correa, D., Caplan, A.I., 2014. Chondrogenic Differentiation of Mesenchymal Stem Cells: Challenges and Unfulfilled Expectations. *Tissue Eng Part B Rev* 20, 596–608.

- Sophia Fox, A.J., Bedi, A., Rodeo, S.A., 2009. The Basic Science of Articular Cartilage. *Sports Health* 1, 461–468.
- Steadman, J.R., Rodkey, W.G., Rodrigo, J.J., 2001. Microfracture: surgical technique and rehabilitation to treat chondral defects. *Clin Orthop Relat Res* S362–369.
- Steinhaus, M.E., Christ, A.B., Cross, M.B., 2017. Total Knee Arthroplasty for Knee Osteoarthritis: Support for a Foregone Conclusion? *HSS J* 13, 207–210.
- Stewart, H.L., Kawcak, C.E., 2018. The Importance of Subchondral Bone in the Pathophysiology of Osteoarthritis. *Frontiers in Veterinary Science* 5.
- Stossel, T.P., 1993. On the crawling of animal cells. *Science* 260, 1086–1094.
- Suh, J.K., Matthew, H.W., 2000. Application of chitosan-based polysaccharide biomaterials in cartilage tissue engineering: a review. *Biomaterials* 21, 2589–2598.
- Szepesi, Á., Matula, Z., Szigeti, A., Várady, G., Szalma, J., Szabó, G., Uher, F., Sarkadi, B., Német, K., 2016. In Vitro Characterization of Human Mesenchymal Stem Cells Isolated from Different Tissues with a Potential to Promote Complex Bone Regeneration. *Stem Cells International* 2016, e3595941.
- Tamaddon, M., Gilja, H., Wang, L., Oliveira, J., Sun, X., Tan, R., Liu, C., 2020. Osteochondral scaffolds for early treatment of cartilage defects in osteoarthritic joints: from bench to clinic 1.
- Tamaddon, M., Wang, L., Liu, Z., Liu, C., 2018. Osteochondral tissue repair in osteoarthritic joints: clinical challenges and opportunities in tissue engineering. *Bio-des. Manuf.* 1, 101–114.
- Tampieri, A., Sandri, M., Landi, E., Pressato, D., Francioli, S., Quarto, R., Martin, I., 2008. Design of graded biomimetic osteochondral composite scaffolds. *Biomaterials* 29, 3539–3546.
- Tatari, H., 2007. [The structure, physiology, and biomechanics of articular cartilage: injury and repair]. *Acta Orthop Traumatol Turc* 41 Suppl 2, 1–5.
- Thambyah, A., Broom, N., 2009. On new bone formation in the pre-osteoarthritic joint. *Osteoarthritis Cartilage* 17, 456–463.
- Thiagarajan, L., Abu-Awwad, H.A.-D.M., Dixon, J.E., 2017. Osteogenic Programming of Human Mesenchymal Stem Cells with Highly Efficient Intracellular Delivery of RUNX2. *Stem Cells Transl Med* 6, 2146–2159.
- Tokiwa, Y., Calabria, B.P., Ugwu, C.U., Aiba, S., 2009. Biodegradability of Plastics. *Int J Mol Sci* 10, 3722–3742.
- Travis, M.A., Sheppard, D., 2014. TGF- β activation and function in immunity. *Annu Rev Immunol* 32, 51–82.
- Truong, L.-H., Kuliwaba, J.S., Tsangari, H., Fazzalari, N.L., 2006. Differential gene expression of bone anabolic factors and trabecular bone architectural changes in the proximal femoral shaft of primary hip osteoarthritis patients. *Arthritis Research & Therapy* 8, R188.
- Turnbull, G., Clarke, J., Picard, F., Riches, P., Jia, L., Han, F., Li, B., Shu, W., 2018. 3D bioactive composite scaffolds for bone tissue engineering. *Bioactive Materials* 3, 278–314.
- Upmeier, H., Brüggjenjürgen, B., Weiler, A., Flamme, C., Laprell, H., Willich, S.N., 2007. Follow-up costs up to 5 years after conventional treatments in patients with cartilage lesions of the knee. *Knee Surg Sports Traumatol Arthrosc* 15, 249–257.
- Vallet-Regi, M., Salinas, A.J., 2021. Mesoporous bioactive glasses for regenerative medicine. *Materials Today Bio* 11, 100121.
- Varghese, S., Hwang, N.S., Canver, A.C., Theprungsirikul, P., Lin, D.W., Elisseeff, J., 2008. Chondroitin sulfate based niches for chondrogenic differentiation of mesenchymal stem cells. *Matrix Biol* 27, 12–21.
- Vasiliadis, H.S., Danielson, B., Ljungberg, M., McKeon, B., Lindahl, A., Peterson, L., 2010. Autologous Chondrocyte Implantation in Cartilage Lesions of the Knee: Long-term Evaluation with Magnetic Resonance Imaging and Delayed Gadolinium-Enhanced Magnetic Resonance Imaging Technique. *Am J Sports Med* 38, 943–949.
- Vyas, C., Mishbak, H., Cooper, G., Peach, C., Pereira, R.F., Bartolo, P., 2020. Biological perspectives and current biofabrication strategies in osteochondral tissue engineering. *Bio-manuf Rev* 5, 2.

- W. M. S. Russell and R. L. Burch, 1960. The Principles of Humane Experimental Technique. *Medical Journal of Australia* 1, 500–500.
- Wang, C., Huang, W., Zhou, Y., He, L., He, Z., Chen, Z., He, X., Tian, S., Liao, J., Lu, B., Wei, Y., Wang, M., 2020. 3D printing of bone tissue engineering scaffolds. *Bioactive Materials* 5, 82–91.
- Wang, S., Li, R., Xu, Y., Xia, D., Zhu, Y., Yoon, J., Gu, R., Liu, X., Zhao, W., Zhao, X., Liu, Y., Sun, Y., Zhou, Y., 2020. Fabrication and Application of a 3D-Printed Poly-ε-Caprolactone Cage Scaffold for Bone Tissue Engineering [WWW Document]. *BioMed Research International*. URL <https://www.hindawi.com/journals/bmri/2020/2087475/> (accessed 3.8.21).
- Wang, S.-J., Jiang, D., Zhang, Z.-Z., Huang, A.-B., Qi, Y.-S., Wang, H.-J., Zhang, J.-Y., Yu, J.-K., 2016. Chondrogenic Potential of Peripheral Blood Derived Mesenchymal Stem Cells Seeded on Demineralized Cancellous Bone Scaffolds. *Sci Rep* 6, 36400.
- Wasti, S., Adhikari, S., 2020. Use of Biomaterials for 3D Printing by Fused Deposition Modeling Technique: A Review. *Front. Chem.* 8.
- Wei, W., Dai, H., 2021. Articular cartilage and osteochondral tissue engineering techniques: Recent advances and challenges. *Bioactive Materials* 6, 4830–4855.
- Wilusz, R.E., Sanchez-Adams, J., Guilak, F., 2014. The structure and function of the pericellular matrix of articular cartilage. *Matrix Biology* 39, 25–32.
- Won, J.-Y., Park, C.-Y., Bae, J.-H., Ahn, G., Kim, C., Lim, D.-H., Cho, D.-W., Yun, W.-S., Shim, J.-H., Huh, J.-B., 2016. Evaluation of 3D printed PCL/PLGA/β-TCP versus collagen membranes for guided bone regeneration in a beagle implant model. *Biomed Mater* 11, 055013.
- Woodruff, M.A., Hutmacher, D.W., 2010. The return of a forgotten polymer—Polycaprolactone in the 21st century. *Progress in Polymer Science* 35, 1217–1256.
- Wu, C.-S., Liao, H.-T., Cai, Y.-X., 2017. Characterisation, biodegradability and application of palm fibre-reinforced polyhydroxyalkanoate composites. *Polymer Degradation and Stability* 140, 55–63.
- Wu, G.-H., Hsu, S., 2015. Review: Polymeric-Based 3D Printing for Tissue Engineering. *J. Med. Biol. Eng.* 35, 285–292.
- Wu, X., Zhou, M., Jiang, F., Yin, S., Lin, S., Yang, G., Lu, Y., Zhang, W., Jiang, X., 2021. Marginal sealing around integral bilayer scaffolds for repairing osteochondral defects based on photocurable silk hydrogels. *Bioactive Materials* 6, 3976–3986.
- Xia, B., Di Chen, Zhang, J., Hu, S., Jin, H., Tong, P., 2014. Osteoarthritis Pathogenesis: A Review of Molecular Mechanisms. *Calcif Tissue Int* 95, 495–505.
- Yamanlar, S., Sant, S., Boudou, T., Picart, C., Khademhosseini, A., 2011. Surface functionalization of hyaluronic acid hydrogels by polyelectrolyte multilayer films. *Biomaterials* 32, 5590–5599.
- Yang, J., Zhang, Y.S., Yue, K., Khademhosseini, A., 2017. Cell-laden hydrogels for osteochondral and cartilage tissue engineering. *Acta Biomater* 57, 1–25.
- Yang, S., Leong, K.F., Du, Z., Chua, C.K., 2001. The design of scaffolds for use in tissue engineering. Part I. Traditional factors. *Tissue Eng* 7, 679–689.
- Yao, Q., Wei, B., Guo, Y., Jin, C., Du, X., Yan, C., Yan, J., Hu, W., Xu, Y., Zhou, Z., Wang, Y., Wang, L., 2015. Design, construction and mechanical testing of digital 3D anatomical data-based PCL-HA bone tissue engineering scaffold. *J Mater Sci Mater Med* 26, 5360.
- Yh, J., Jh, C., Jk, S., Tk, K., Bc, C., Hy, C., 2007. Different effects of PLGA and chitosan scaffolds on human cartilage tissue engineering. *J Craniofac Surg* 18, 1249–1258.
- Yourek, G., Hussain, M.A., Mao, J.J., 2007. Cytoskeletal Changes of Mesenchymal Stem Cells During Differentiation. *ASAIO J* 53, 219–228.
- Yu, H., Matthew, H., Wooley, P., Yang, S.-Y., 2008. Effect of porosity and pore size on microstructures and mechanical properties of poly-ε-caprolactone- hydroxyapatite composites. *Journal of biomedical materials research. Part B, Applied biomaterials* 86, 541–7.
- Zadpoor, A.A., 2015. Bone tissue regeneration: the role of scaffold geometry. *Biomater. Sci.* 3, 231–245.
- Zak, L., Albrecht, C., Wondrasch, B., Widhalm, H., Veksler, G., Trattig, S., Marlovits, S., Aldrian, S., 2014. Results 2 Years After Matrix-Associated Autologous Chondrocyte Transplantation Using

- the Novocart 3D Scaffold: An Analysis of Clinical and Radiological Data. *Am J Sports Med* 42, 1618–1627.
- Zamanlui, S., Mahmoudifard, M., Soleimani, M., Bakhshandeh, B., Vasei, M., Faghihi, S., 2018. Enhanced chondrogenic differentiation of human bone marrow mesenchymal stem cells on PCL/PLGA electrospun with different alignments and compositions. *International Journal of Polymeric Materials and Polymeric Biomaterials* 67, 50–60.
- Zarrintaj, P., Manouchehri, S., Ahmadi, Z., Saeb, M.R., Urbanska, A.M., Kaplan, D.L., Mozafari, M., 2018. Agarose-based biomaterials for tissue engineering. *Carbohydr Polym* 187, 66–84.
- Zhang, L., Hu, J., Athanasiou, K.A., 2009. The Role of Tissue Engineering in Articular Cartilage Repair and Regeneration. *Crit Rev Biomed Eng* 37, 1–57.
- Zhang, W., Hu, J., Huang, Y., Wu, C., Xie, H., 2021. Urine-derived stem cells: applications in skin, bone and articular cartilage repair. *Burns Trauma* 9, tkab039.
- Zhang, W., Ling, C., Haoyang, L., Zhang, A., Mao, L., Wang, J., Chao, J., Backman, L., Yao, Q., Chen, J., 2020. Tannic Acid-Mediated Dual Peptide-Functionalized Scaffolds to Direct Stem Cell Behavior and Osteochondral Regeneration. *Chemical Engineering Journal* 396, 125232.
- Zhao, C., Jiang, W., Zhou, N., Liao, J., Yang, M., Hu, N., Liang, X., Xu, W., Chen, H., Liu, W., Shi, L.L., Oliveira, L., Wolf, J.M., Ho, S., Athiviraham, A., Tsai, H.M., He, T.-C., Huang, W., 2017. Sox9 augments BMP2-induced chondrogenic differentiation by downregulating Smad7 in mesenchymal stem cells (MSCs). *Genes Dis* 4, 229–239.
- Zhao, X., Hu, D.A., Wu, D., He, F., Wang, H., Huang, L., Shi, D., Liu, Q., Ni, N., Pakvasa, M., Zhang, Y., Fu, K., Qin, K.H., Li, A.J., Hagag, O., Wang, E.J., Sabharwal, M., Wagstaff, W., Reid, R.R., Lee, M.J., Wolf, J.M., El Dafrawy, M., Hynes, K., Strelzow, J., Ho, S.H., He, T.-C., Athiviraham, A., 2021. Applications of Biocompatible Scaffold Materials in Stem Cell-Based Cartilage Tissue Engineering. *Frontiers in Bioengineering and Biotechnology* 9.
- Zhou, G., Zheng, Q., Engin, F., Munivez, E., Chen, Y., Sebald, E., Krakow, D., Lee, B., 2006. Dominance of SOX9 function over RUNX2 during skeletogenesis. *Proc Natl Acad Sci U S A* 103, 19004–19009.
- Zhou, J., Xu, C., Wu, G., Cao, X., Zhang, L., Zhai, Z., Zheng, Z., Chen, X., Wang, Y., 2011. In vitro generation of osteochondral differentiation of human marrow mesenchymal stem cells in novel collagen-hydroxyapatite layered scaffolds. *Acta biomaterialia* 7, 3999–4006.
- Zhou, X., Esworthy, T., Lee, S.-J., Miao, S., Cui, H., Plesiniak, M., Fenniri, H., Webster, T., Rao, R.D., Zhang, L.G., 2019. 3D Printed scaffolds with hierarchical biomimetic structure for osteochondral regeneration. *Nanomedicine* 19, 58–70.
- Zhu, Y., Kong, L., Farhadi, F., Xia, W., Chang, J., He, Y., Li, H., 2019. An injectable continuous stratified structurally and functionally biomimetic construct for enhancing osteochondral regeneration. *Biomaterials* 192, 149–158.
- Zia, K.M., Tabasum, S., Khan, M.F., Akram, N., Akhter, N., Noreen, A., Zuber, M., 2018. Recent trends on gellan gum blends with natural and synthetic polymers: A review. *Int J Biol Macromol* 109, 1068–1087.
- Zuliani, C.C., Damas, I.I., Andrade, K.C., Westin, C.B., Moraes, Â.M., Coimbra, I.B., 2021. Chondrogenesis of human amniotic fluid stem cells in Chitosan-Xanthan scaffold for cartilage tissue engineering. *Sci Rep* 11, 3063.
- ŻYLIŃSKA, B., SILMANOWICZ, P., SOBCZYŃSKA-RAK, A., JAROSZ, Ł., SZPONDER, T., 2018. Treatment of Articular Cartilage Defects: Focus on Tissue Engineering. *In Vivo* 32, 1289–1300.

LIST OF PUBLICATIONS

1. Amrita Natarajan, VP Sivadas and Prabha D Nair. 3D-printed biphasic scaffolds for the simultaneous regeneration of osteochondral tissues. *Biomed Mater.* 2021 Jul 29;16(5). doi: 10.1088/1748-605X/ac14cb. PMID: 34265754.
2. Amrita Natarajan and Prabha D Nair; “3D printed based Osteochondro mimetic gradient constructs for enhancing articular joint regeneration” -to be communicated – *Biomaterials*
3. Manuscript entitled “Efficacy Of 3D Printed Personalized Biomimetic Substitutes For Osteochondral Tissue Regeneration: : An In vivo Study” to be communicated.

AWARDS

1. Received **best Poster** prize in 3D printing session sponsored by Biomaterials Science for the poster entitled “**Osteochondro mimetic gradient 3D printed based constructs for enhancing tissue regeneration**” in an International conference on BioMaterials, BioEngineering & Bio Theranostics, BIOMET -2018 at Vellore institute of Technology from 26th to 28th July organized by CBCMT, VIT, Vellore in association with STERMI and SBAOI
2. Received **second best poster** award for the poster entitled “**Efficacy Of 3D Printed Personalized Biomimetic Substitutes for Osteochondral Tissue Regeneration: An In vivo Study**”; Amrita Natarajan, Sachin J Shenoy and Prabha D Nair in the 11th India-Japan science and technology seminar- Nobel Laureate S&T Seminar Series” organized by Indian JSPS Alumini association (IJAA) and SCTIMST, Trivandrum on 6-7 December 2021.
3. Received the **best oral presentation** award for the abstract entitled “**Recapitulating the Microarchitecture of Native Tissues: Customizable 3D printed Biphasic Substitutes for Augmenting Osteochondral Tissue Regeneration**”; by Amrita Natarajan, Lynda V Thomas and Prabha D Nair in the International Conference on Polymeric Materials in Medicine (ICPMM 2022) held from 25 - 26 February 2022 and organized jointly by the Society for Polymer Science India (SPSI) and SCTIMST, Trivandrum

SYLLABUS AND SEMINAR TOPICS

Syllabus

Module I: Functional anatomy of musculo-skeletal system

Module II: Osteochondral defects

Module III: Extracellular matrix

Module IV: Biomaterial scaffolds for osteochondral regeneration

Module V: Stem cells

Module VI: In vivo animal models

SEMINAR TOPICS

Seminar 1: Functional anatomy of musculo skeletal system

Seminar 2: Osteochondral defects: Etiology, Pathogenesis, Diagnosis, Treatment strategies

Seminar 3: Biomaterial scaffolds for osteochondral tissue engineering

Seminar 4: Mesenchymal stem cells for osteochondral regeneration

Seminar 5: Invivo animal models for osteochondral implantation studies

Seminar 6: Characterization of biomaterial scaffold

CURRICULUM VITAE

Education

Ph.D. Scholar- Division of Tissue Engineering and Regeneration Technologies, Biomedical Technology Wing, Sree Chitra Institute for Medical Sciences and Technology, India. 2016-2022

Post-Graduation- MTech in Nano Medical Sciences, Amrita Viswavidyapeedham/ Amrita centre for Nanosciences and Molecular medicine, Cochin. Kerala, 2009-2011, CGPA 9.06/10

Graduation- BDS (Bachelor of Dental Surgery), Army college of Dental Sciences, Dr NTRUHS, 2003-2007, 73% and Internship from Army college of Dental Sciences, January 2008-December 2008)

Additional qualification- Advanced Diploma in Forensic Biotechnology and DNA Fingerprinting (International Forensic Science), 2015, 61%.

Achievements:

1. CSIR has awarded direct Senior Research Fellowship.
2. ICMR has awarded direct Senior Research Fellowship.

APPENDIX

PBS (1000ml) pH 7.4

NaCl	-8g
KCl	-0.2g
Na ₂ HPO ₄	-1.44g
KH ₂ PO ₄	-0.24g

SBF (1000ml) pH 7.4

NaCl	-8.035g
NaHCO ₃	-0.355g
KCl	-0.225g
K ₂ HPO ₄ .3H ₂ O	-0.231g
MgCl ₂ .6H ₂ O	-0.311g
1 M HCl	-39.0g
CaCl ₂	-0.292g
Na ₂ SO ₄	-0.072g
((HOCH ₂) ₃ CNH ₂)	-6.118g
1 M HCl	Appropriate amount for adjusting the pH~7.4

(1,9 DIMETHYLMETHYLENE BLUE) (DMMB) 10X

1,9 Dimethyl methylene blue	16 mg in 5 ml ethanol
Sodium formate	-2g
Formic acid	-2g

Made upto 100 ml, filtered and stored at RT

The dye is diluted to 1x using distilled water and used for the assay

Document Information

Analyzed document	complete thesis final for plagiarism check.docx (D141051515)
Submitted	6/23/2022 6:33:00 AM
Submitted by	Lynda Velutheril Thomas
Submitter email	lyndavt@sctimst.ac.in
Similarity	1%
Analysis address	lyndavt.sctims@analysis.orkund.com

Sources included in the report

W	URL: https://www.ncbi.nlm.nih.gov/pmc/articles/PMC3823419/ Fetched: 3/25/2020 10:35:02 PM	4
W	URL: https://www.jstage.jst.go.jp/article/dmj/40/2/40_2020-005/_pdf Fetched: 6/23/2022 6:34:16 AM	5
W	URL: https://www.ncbi.nlm.nih.gov/pmc/articles/PMC8271621/ Fetched: 9/10/2021 1:37:05 AM	4
W	URL: https://www.nature.com/articles/srep42556 Fetched: 12/2/2021 9:47:56 PM	5
J	Electrospinning of PCL/PVP blends for tissue engineering scaffolds URL: 791f3f3e-35d8-4a1b-906f-a8264ae79216 Fetched: 2/26/2020 7:50:03 PM	2
W	URL: https://pubmed.ncbi.nlm.nih.gov/23468162/ Fetched: 6/23/2022 6:33:12 AM	2
W	URL: https://www.science.gov/topicpages/p/polycaprolactone+pcl+scaffolds.html Fetched: 12/20/2019 6:06:34 AM	1

Entire Document

SYNOPSIS Human diarthrodial joint consists of osteochondral tissue, comprising superficial articular cartilage layered on the surface of subchondral bone. Osteochondral defects (OCDs), caused by multifactorial pathology which include lesions that penetrate the entire thickness of the articular cartilage, extend beyond the calcified zone, and into the subchondral bone. The condition may progress to osteoarthritis if not treated, which is the third most common musculoskeletal disease in the world, resulting in chronic physical disabilities. OCDs are difficult to treat because of the avascular nature and poor inherent regenerative capacity of the cartilage layer. The current treatment methodologies including osteochondral grafts have various limitations. Thus, simultaneous regeneration of dual tissues with disparate biomechanical properties for potential applications in treating OCDs is a target in regenerative medicine and an unmet clinical need.